Development and Characterization of a Biomimetic Passive Diffusion Membrane and *In Vivo* Relevant Dissolution Methodology

by

Patrick Donald Sinko

A dissertation submitted in partial fulfillment
of the requirements for the degree of
Doctor of Philosophy
(Pharmaceutical Sciences)
in the University of Michigan
2019

Doctoral Committee:

Professor Gordon L. Amidon, Co-Chair
Professor Gregory E. Amidon, Co-Chair
Professor Duxin Sun
Professor Robert Ziff

Patrick Donald Sinko

sinkopd@umich.edu

ORCID iD: 0000-0002-0304-7918

ACKNOWLEDGEMENTS

To my wife: 陈晓梅。谢谢你的耐心，我爱你。

To my Dad: Thank you for making science a part of my daily life, for supporting me and guiding me to become the person I have become, and for giving me the tools to carve out my best future personally and professionally.

To my Mom: Thank you for making sure I do not forget about the other things in life and for supporting me in everything I do.

I would like to dedicate this work to my family: Xiaomei, Kathryn, Noreen, Patrick, Patrick, Patricia, Don, Ann, Yong, and Chaoxia. To all my extended family: Jeff, Lisa, Laura, Alyssa, Sean, Chris, Angel, Michael, Brendan, Kiersten, Sue, Bill, Ed, and Flo. I hope that you see this work and understand that none of this was possible without all of you.

I would also like to dedicate this work to the members of my family who cannot read, but were just as important: Kaylee, Margaret, Fred, Barney, and the newest addition Malcolm. If you could read, I would hope you appreciate all the time that this work took was not just me ignoring you when you wanted to go outside and play. I love you all very much.

I would also like to thank Emily and Lesa, for taking care of my baby girl when I needed to travel or spend crazy hours in lab. Both Kaylee and I are extremely grateful.

This body of work would not be possible without the support of Ping Gao, Eric Schmidt, and Yi Shi at Abbvie Pharmaceuticals in North Chicago. I cannot express the amount of gratitude I have for you all believing in my idea and me as person. I cannot imagine a better way to start a career as you have shown me the best parts of collaboration, provided a great environment for this work, and allowed my skills as a scientist to develop.

To my co-adviser Greg: Thank you for all of the support in lab and life that you have given to me over these past six years. It is hard for me to come up with all the right words to thank you for everything you have done for me. It is my honor to have been able to study with you. To my co-adviser Gordon: Thank you for never letting me forget the big picture.

To the many collaborators and friends who have all contributed to this work, I specifically acknowledge your contributions in the following chapters. But I would like to thank more personally here, Bob and Niloufar, for all the pleasant and insightful conversation of fluid dynamics, mass transport, and many other things. To David, for indulging my curiosity and allowing me to participate in some of the coolest experiments I have ever done. Troy, Sarah, Angel, and Meagan for being great undergraduate researchers who made working in lab fun. I am proud to see how you have transitioned into the next steps of your careers. I would like to thank my lab mates in both Amidon laboratories; Deanna, Arjang, Nicholas Waltz, Nicholas Job,

Vikram, Hiro, Pamela, and members past for making lab fun to come into and be able to leave with confidence.

I would also like to thank my funding sources; 2015/11/01-2018/10/31 Abbvie Pharmaceuticals. Modernization of in vivo-in vitro Oral Bioperformance Prediction and Assessment: Development of an improved in vitro methodology to simulate the simultaneous dissolution and absorption of drugs. Sponsored Research Agreement contract number C99549, 2015/09/30-2020/09/29 HHSF223201510157C, Food and Drug Administration Innovations in Regulatory Science: In vivo Predictive Dissolution (IPD) to Advance Oral Product Bioequivalence (BE) Regulation, Norman Wiener Fellowship 2018-2019, College of Pharmacy Graduate Student Instructor Program, and The University of Michigan College of Engineering for financial support and the Michigan Center for Materials Characterization for use of the instruments and staff assistance.

TABLE OF CONTENTS

LIST OF TABLES

LIST OF FIGURES

LIST OF APPENDICES

ABSTRACT

Preclinical evaluation of modern solid oral dosage forms requires more advanced *in vitro* devices due to the trend of formulating low solubility, high permeability compounds for commercial therapeutics. Current compendial dissolution methodologies may not be suitable for such compounds due to high fluid shear rates, heterogeneity of shear rates, suboptimal fluid flow, unrealistic fluid volumes, and ultimately the lack of an experimental component that represents the absorption process. Here a dissolution apparatus is introduced that overcomes some limitations of the compendial apparatus using poly(dimethyl siloxane) (PDMS) as an *in vitro* biomimetic analogue that simulates the passive drug absorption process. PDMS is biomimetic because of similarities in small molecule transport such as mechanism, ionization selectivity, and lipophilicity. Nine molecular probes were used to evaluate the transport pathways and properties of PDMS to simulate human oral absorption rates. The transport pathways through PDMS are analogous to transcellular (TCDT) and paracellular (PCDT) drug transport pathways. PDMS PCDT was assessed using positronium annihilation life-time spectroscopy (PALS) and partition experiments; TCDT was assessed using diffusion and partition experiments. PALS determined that PDMS pores were uniform (diameter~0.85nm), isolated, and void volume was unaffected by drug accumulation. A strong linear correlation exists between predicted octanol-water partition coefficients and PDMS partition coefficients

($LogP_{PDMS}$=0.736 x $LogP_{O-W}$–0.971, R^2=0.981). The characteristics of an ultra-thin large area PDMS membrane (UTLAM) dissolution/absorption system with respect to pH, partition coefficient (K), aqueous boundary layer (ABL), drug particle size, and administered dose were measured. A pH dependent solution diffusion model and a particle size-dose dependent particle dissolution-absorption model were derived. A 1.5" hydrofoil design was implemented to reduce particle coning, promote particle re-suspension, and control bulk fluid shear. PDMS membranes were successfully fabricated to thicknesses of 11.2 ± 0.5μm to 12.5± 0.2μm, and a UTLAM active surface area of 21.8-25.2cm^2 (44.4cm^2 total area) was achieved. Experiments between pH 1.9-12.5 were investigated using ibuprofen as a model weak acid drug. Partition coefficient (K) is the dominant factor determining absorption and the ABL played a significant role in absorption when the drug is mostly non-ionized. In aqueous and membrane limited diffusion absorption, there was a significant shift towards higher pH in the half of maximum absorption rate caused by K and ABL. Number and mass particle size distributions (PSD) measured and dissolution was studied. Particle dissolution was determined to occur in the ABL adjacent to the PDMS membrane and has a significant effect on flux of drug across the PDMS membrane. Suspension experiments conducted with ibuprofen particle size radii of 3.7μm, 18μm, 117μm at doses of 0.2, 1, 10, and 40mg/mL. Significant enhancements in flux were observed with increasing dose and decreasing particle size in accordance with theoretical predictions of particle dissolution within the ABL. In all PSD's, an unaccounted increase in flux was observed at high doses and was attributed to particle settling on the horizontal PDMS membrane. In conclusion, the UTLAM PDMS diffusion cell

exhibits improved hydrodynamics in the donor phase and the PDMS membrane mimics *in vivo* relevant passive absorption kinetics through PDMS membranes.

CHAPTER 1

Research Objectives

There is a movement to adopt in vitro preclinical practices, methods, and experimental parameters that better reflect the critical parameters observed in the human oral absorption pathway. The adoption of in vitro methods that include a medium that performs as an "absorption" compartment has been used in industry to enhance the in vitro-in vivo correlations made by preclinical formulators.[1] It is anticipated by the author that due to the fact that the majority of compounds coming out of the discovery pipeline are highly lipophilic and low solubility, that the wide spread need to adopt in vitro dissolution tests include "absorption" mediums are essential to both the economic stream-lining of solid oral drug product development as well as capturing the true performance of enabling formulation technologies used for these highly lipophilic/low solubility compounds. The current organic fluid-based absorption system used has demonstrated that the absorption medium is necessary, however, being an organic fluid presents some experimental difficulties. To mitigate the aforementioned experimental challenges (see chapter 2), a solid, synthetic polymer membrane was proposed to substitute the organic fluid.

The purpose of this work is to establish an in vitro experiment that incorporates absorption kinetics into a dissolution method, with the intention to eventually

biomimic the human gastrointestinal passive diffusion absorption process. Absorption into a synthetic membrane is not a novel concept however, developing an ultra-thin large area membrane that partitions pharmaceutical molecules is an advancement. Engineering the permeability and absorption rate of diffusion cell to emulate BCS II absorption rates is key to achieving *in vivo* relevant results is a novel application. This results in the following specific aims:

Aim 1: Perform an *In Vitro* Characterization of the Biomimetic Properties of Poly(dimethyl siloxane)

Aim 2: Fabricate an Ultra-Thin, Large-Area Poly(dimethyl siloxane) Membrane and Diffusion Cell

Aim 3: Model the pH-Dependent Absorption in an Ultra-Thin, Large-Area Poly(dimethyl siloxane) Membrane Diffusion Cell

Aim 4: Model the Particle-Size and Dose Effects on Diffusion Flux Through an Ultra-Thin, Large-Area Poly(dimethyl siloxane) Membrane

Aim 5: Measure the Effects of Common Oral Excipients on Flux Through an Ultra-Thin, Large-Area Poly(dimethyl siloxane) Membrane: Beginnings of a Hierarchical Model for Predicting Formulation Dissolution Performance (pH + particle size + dose)

CHAPTER 2

Introduction to the State of the Art: Enabling Formulations and *In Vivo* Relevant – *In Vitro* Dissolution Methodologies: Literature Review

2.1 Introduction to *in vivo* relevant dissolution

The pharmaceutical industry is one of the most regulated industries in the market, and the magnitude of proof (safety/toxicology studies, *in vitro* dissolution performance, phase I-III clinical trials) required to assure the general population of the label guarantee is very costly.[2] In an article published in June 2015 by the head of the European Medicines Agency, it was estimated that $60 billion USD in research and development (R&D) was spent globally on the R&D of new molecular entities which never became marketable products. Drug product development organizations need to be focused, agile, and lean to stay competitive. The rising costs of drug development creates an environment where mitigating risk is necessary, but time, resources, and the threat of regulatory rejection limit the rapid development and implementation new solutions.[3]

Major pharmaceutical companies recognize that understanding the delivery mechanisms, reliably predicting efficacy, and enhancing safety would enhance productivity. A more efficient method of conducting impactful R&D is to adopt *in vitro* systems that more accurately represent the route of administration conditions in human beings, thus leading to

more physiological meaningful predictions.[3-6] This idea is not novel; scientists in this field have been attempting to synthesize the complex aspects of drug product design and drug delivery since the 1950's.[7-9] Yet, in modern industrial practice we primarily rely on simplistic methods developed in the middle of the last century (USP 2 dissolution).

The first globally recognized system to categorize active pharmaceutical ingredients was the biopharmaceutical classification system (BCS), which categorizes drug molecules based on their solubility and permeability.[10-12] This system gave the pharmaceutics community a common framework to engage in drug product and *in vitro* methodology design. The BCS is now commonly used in drug product development to guide selection and inform the development team of potential formulation challenges.[13] Additionally, deeper understanding of the BCS has allowed innovator and generic companies to expedite production of generic products via the Food and Drug Administration's (FDA) biowaivers system.[14] Further application of the BCS has recently inspired efforts, including this one, to design *in vitro* experiments that reflect a mechanistic understanding of the *in vivo* situation. The route which dissolution methodologies have progressed, driven by FDA compliance and quality control does not elucidate the true *in vivo* performance of the drug product.[15] There is no argument that well-defined standards of *in vitro* performance must be established, but a distinction between quality control and drug product design *in vitro* methods must recognized and maintained.

The United States Pharmacopeia (USP) is an entity that established some of the most ubiquitous dissolution methodologies, equipment, and standards used today around the world. In 1950 the USP's only official test for tablet and capsules was the disintegration test, but this test was known to be indirectly related to drug bioavailability and product

performance. It was shortly later in 1962 that dissolution testing was beginning to gain support as a more discriminating test for drug bioavailability and drug product performance. Finally, in 1968, the USP 1 basket stirred flask apparatus was introduced and by 1975 through a collaborative effort of industry and government there was convincing evidence that the USP 1 could provide an *in vivo-in vitro* correlation. This same study provided momentum towards the movement away from an *in vitro- in vivo* USP bioavailability standard. The USP 1 was complemented by the USP paddle apparatus (USP 2) in 1978 and in the same time frame the USP adopted the sink condition (3 times volume required to saturate a solution (~500mL – 1000mL; typically, 900mL), in simple aqueous media to eliminate the use of enzymes in simulated intestinal fluid) and 50RPM paddle speed to maximize product discrimination. Between 1985-1990, after the advent of multiple more complex dosage forms (enteric coated, extend/delayed release), the USP implemented an official system for accounting *in vivo-in vitro* correlations (level A, B, C, D).[16] This development provided a framework to compare how well or poorly a drug product performed relative to a pharmacokinetic clinical study. The trend of using dissolution testing as a method to discriminate between formulations, which is the primary use in industry to date, is contrary to the original intentions of the implementation of dissolution testing. However, this development was well intentioned and rational, due to need to quantify formulation consistency and ensure product safety & efficacy for the general public. This report and others in the recent past have begun to question the utility of the USP dissolution test and significant scientific effort is being put forth to make the dissolution test more physiologically meaningful. The most prevalent strategy has been to make the content of the dissolution

medium biomimetic, while fewer reports focus on the apparatus or *in vivo* mechanical/hydrodynamic forces.[17-26]

A recent clinical and computational study performed between the University of Michigan, University of Nottingham, and Pennsylvania State University/Colorado State University, human gastrointestinal phenomena have been more accurately described than ever before at the time of this report. Through a combination of intubation studies (obtaining, pH, pressure wave motility, gastric contents), real time magnetic resonance imaging (MRI) manometry (real time free water flow, motility patterns), and computational fluid dynamic simulations (CFDS) of peristaltic fluid and mass flow, a unique scientific perspective for developing guidelines for orally administered dissolution testing has been achieved. With the ability to understand the distinct segmental nature of the gastrointestinal tract, it is possible to capture the most critical parameters (pH, fluid volume, shear rates, secretion rates, intercompartmental transfer rates, antero-retrograde flow rates, etc.) in each segment and in between segments and transform these parameters into an apparatus that accurately simulates the current understanding of gastrointestinal dissolution processes. These measured and predicted values will govern the philosophy of design, simulation, evaluation, and implementation of the PDMS UTLAM device presented in the report.

Table 2-1 A brief description of the human parameters measured or simulated that affect gastrointestinal dissolution and absorption.

Human Parameter	Clinical, Literature, Simulation Value	
Aqueous Volume in Stomach[27]	35mL ± 7mL (fasted)	242mL ± 9mL (2min post 240mL glass of water dosing)
Total Aqueous Volume in Lower GI[27]	5-159mL (range, fasted) 43mL ± 14mL (fasted)	15-264mL (range, 12min post-water dose) 92mL ± 24mL (12min post 240mL glass of water dosing) 15-172mL (range, 45min post-water dose) 77mL ± 15mL (45min post 240mL glass of water dosing)
Bulk Fluid Properties[28-30] (CFDS)	$S^*_{USP\ II} < 250 – 500$ $Re_{Shear\ USP\ II} < 0.25 – 0.5$	$S^*_{Human\ GI} = 10 – 25$ $Re_{Shear\ Human\ GI} < 0.0007 – 0.003$
pH in Stomach[31]	1.1 – 7.47 (range, fasted) 2.50 (mean, fasted) 2.25 (median, fasted)	1.1 – 7.39 (range, fed) 4.04 (mean, fed) 3.95 (median, fed)
pH in Duodenum[31]	1.71 – 7.57 (range, fasted) 4.93 (mean, fasted) 4.91 (median, fasted)	
pH in Jejunum[31]	2.2 – 6.75 (range, fasted) 5.55 (mean, fasted) 5.62 (median, fasted)	

2.2 Dissolution

Traditionally, drug dissolution and permeation has been described using the film model (Film Theory). The origin of this type of model comes from the seminal study done in 1897 by Noyes-Whitney, who developed a simple relationship between dissolving solids and the mass in solution. Their equation was the first mathematical description of the dissolution process.

$$\frac{dX}{dt} = C(S - x) \qquad \text{Eq (2.1)}$$

S is the solubility, x is the concentration, and C is a constant.[32] Later, Nernst-Brunner found that C is a function of the surface area of the dissolving mass, the solutes diffusion coefficient and the hydrodynamic boundary layer thickness.

$$\frac{dX}{dt} = A \cdot \frac{D}{h}(S - x) \qquad \text{Eq (2.2)}$$

Since 1897, there have been many modifications of the Nernst-Brunner equation that attempt to capture different aspects of the dissolution process. The Higuchi-Hiestand model particle dissolution model assumes that the dissolution rate is diffusion controlled, the hydrodynamic boundary layer is equal to the radius of the particle and the same size for all particles of the same size, that the change in mass of the dissolved mass in the bulk is negligible, and that the geometry of the dissolving solids are a sphere.[33, 34] Hintz- Johnson developed a mass-based modification approach to Noyes-Whitney that predicts dissolution under changing surface area, particle size distribution, and particle radius. One important development that their model contributed to the understanding of dissolution sciences was how to treat the hydrodynamic boundary layer. Briefly, the hydrodynamic boundary layer physically arises from a phenomenon known as the "no-slip" boundary condition. This boundary condition states that there is no tangential motion of the fluid at the solid-liquid interface (arising from weak interactions such as hydrogen bonding/London dispersion forces), thus the velocity of the fluid immediately at the interface is equal to zero. This surface fluid does not move with the bulk until some distance away, at which point the fluid-fluid boundary is defined as the aqueous boundary/aqueous diffusion/hydrodynamic boundary layer. The fluid "within" the boundary layer is not stagnant, however, it does not move the same way the bulk fluid moves.[35-37] Hintz-Johnson postulated that there is a critical thickness of the hydrodynamic boundary layer that which the layer will not increase in thickness (h_{ABL} = r, for r ≤ 30μm; for r > 30μm h_{ABL} = 30μm).[38] Niebergall et al. proposed that the aqueous boundary layer is proportional to the square root of particle radius.[39] Sheng et al. make a distinction that Hintz-Johnson's approach is based of the Levich rotating disk experiments

involving a powder compact not free particles in solution.[40] One possible way to predict the hydrodynamic boundary layer is to use hydrodynamic theory. To include the hydrodynamic effects of slip, shear, etc. the film equation can be re-written in terms of the mass transfer coefficient, h:

$$\frac{dX}{dt} = A \cdot h(S - x) \quad \text{Eq (2.3)}$$

$$Sh = \frac{h \cdot D}{L} \quad \text{Eq (2.4)}$$

$$Sh = 2 + 0.6Re^{\frac{1}{2}}Sc^{\frac{1}{3}} \quad \text{Eq (2.5)}$$

$$Sh = 1 + \Delta_{Slip} + \Delta_{Confinement} + \Delta_{Shear} \quad \text{Eq (2.6)}$$

Sh is the Sherwood number and the characteristic length (L) is the hydrodynamic boundary layer thickness (δ) (Eq. 2.4). Relating the the boundary layer thickness to the Sherwood number allows for other hydrodynamic effects to be included in the calculation of the boundary layer thickness. The Ranz-Marshall correlation (Eq. 2.5) has been used to predict the Sherwood number for particle dissolution *in vitro* for particles undergoing flow and is a function of the particle Reynold's number and the Schmidt number.[41, 42] The Wang-Brasseur quasi-steady state model diffusion-controlled model's key advantage over well known traditional models (Hixon-Cromwell, Hintz-Johnson, Wang-Flannigan, etc.) is that it considers the change in the diffusion layer thickness with hydrodynamic effects such as slip, confinement, and shear effects on the Sherwood number for particles under pure diffusion (Eq. 2.6).[43, 44] The Sherwood number is used to calculate the hydrodynamic boundary layer thickness which is critical to determining mass transport (flux) from dissolving particles. From Wang-Brasseur the Sherwood number is defined as,[43]

$$Sh = \frac{r}{\delta} \quad \text{Eq (2.7)}$$

Where r is the particle radius, and δ is the hydrodynamic boundary layer thickness. Since this definition is valid for cases of pure diffusion, the Sherwood number can be modified for

cases in which agitation occurs in the fluid to Eq. 2.8 & 2.9. The Sherwood number is now a function of the fluid convection, particle confinement, and hydrodynamic effects.[45]

$$Sh_{Ranz-Marshal} = 1 + \Delta_{conv} \quad \text{Eq (2.8)}$$

$$Sh_{Wang-Brass} = 1 + \Delta_{confine} + \Delta_{hydr} \quad \text{Eq (2.9)}$$

Ranz-Marshall described convection enhancement (Δ_{Conv}) around spherical particle as in Eq 2.10.

$$\Delta_{conv} = 0.424 \cdot \sqrt[3]{Pe_{\Delta U}}\sqrt[6]{Re_{\Delta U}} \quad \text{Eq (2.10)}$$

Wang-Brasseur derived an analytical solution describing the particle confinement effect (Eq. 2.11 & 2.12)

$$\Delta_{confine} = \frac{\gamma}{1-\gamma} \quad \text{Eq (2.11)}$$

$$\gamma = \frac{3}{2}\frac{\left(\frac{r_c}{r_p}\right)^{2/3} - 1}{\frac{r_c}{r_p} - 1} \quad \text{Eq (2.12)}$$

For heat transport Ranz-Marshall defined mass transport from spherical droplets described in Eq 2.13.[46, 47]

$$Nu = 2 + 0.6 \cdot \sqrt[3]{Sc}\sqrt{Re} \quad \text{Eq (2.13)}$$

$$Nu = \frac{hL}{k} \quad \text{Eq (2.14)}$$

The Nusselt number is defined as the ratio of the convective to conductive heat transfer. h is defined as the heat transfer coefficient, L is characteristic length, and k is the thermal conductivity. This correlation was also valid for the mass transport analogue of the Nusselt Number, which is known as the Sherwood number. The Sherwood number is defined as the ratio of the convective to conductive (diffusive) mass transfer. h is the mass transfer coefficient, D the diffusion coefficient, and L the characteristic length. The Sherwood number

(Eq 2.14) is the direct mass transport analogue to the Nusselt number from heat transport (2.12).

$$Sh = 2 + 0.6 \cdot \sqrt[3]{Sc} \cdot \sqrt{Re} \qquad \text{Eq (2.15)}$$

$$Sh = \frac{hL}{D} \qquad \text{Eq (2.16)}$$

In Ranz-Marshall's derivation the characteristic length was described to be the diameter of the spherical droplet (particle) (Eq. 2.11 & 2.13). In Wang-Brasseur's derivation (Eq 2.8 & 2.7) of the Sherwood number the characteristic length is described as the radius of the spherical particle. These two relationships are equivalent as demonstrated via the following procedure. For Rans-Marshall:

$$Sh = 2 + 0.6 \cdot \sqrt[3]{Sc} \cdot \sqrt{Re} \qquad \text{Eq (2.17)}$$

Where the Schmidt and Reynolds number are defined as $Sc = \frac{\nu}{D}$ and $Re = \frac{d \cdot u}{\nu}$. D is the diffusion coefficient, ν is the kinematic viscosity, u is the fluid velocity, and d is the diameter of the spherical droplet/particle. Substituting the definitions of the Schmidt and Reynolds number into Eq. 2.17 yields Eq. 2.18, and when the terms are simplified Eq. 2.19.

$$Sh = 2 + 0.6 \cdot \sqrt[3]{\frac{\nu}{D}} \sqrt{\frac{d \cdot u}{\nu}} \qquad \text{Eq (2.18)}$$

$$Sh = 2 + 0.6 \cdot d^{\frac{1}{2}} \cdot u^{\frac{1}{2}} \cdot D^{-\frac{1}{3}} \cdot \nu^{-\frac{1}{6}} \qquad \text{Eq (2.19)}$$

For Wang-Brasseur:

$$Sh = 1 + 0.424 \cdot \sqrt[3]{Pe} \cdot \sqrt[6]{Re} \qquad \text{Eq (2.20)}$$

Where the Peclet and Reynold's numbers are defined as $Pe = \frac{u \cdot r}{D}$ and $Re = \frac{u \cdot r}{\nu}$. D is the diffusion coefficient, ν is the kinematic viscosity, u is the fluid velocity, and r is the radius of the spherical droplet/particle. Simplifying all terms in equation 2.20 yields equation 2.21.

$$Sh = 1 + 0.424 \cdot \sqrt[3]{\frac{u \cdot r}{D}} \cdot \sqrt[6]{\frac{u \cdot r}{\nu}} \quad \text{Eq (2.21)}$$

$$Sh = 1 + 0.424 \cdot u^{\frac{1}{2}} \cdot r^{\frac{1}{2}} \cdot D^{-\frac{1}{3}} \cdot \nu^{-\frac{1}{6}} \quad \text{Eq (2.22)}$$

If we change radius to diameter,

$$Sh = 1 + 0.424 \cdot u^{\frac{1}{2}} \left(\frac{d}{2}\right)^{\frac{1}{2}} D^{-\frac{1}{3}} \nu^{-\frac{1}{6}} \quad \text{Eq (2.23)}$$

$$Sh = 1 + \frac{0.424}{\sqrt{2}} \cdot u^{\frac{1}{2}} d^{\frac{1}{2}} D^{-\frac{1}{3}} \nu^{-\frac{1}{6}} \quad \text{Eq (2.24)}$$

Which simplifies to equation 2.25,

$$Sh = 1 + 0.3 \cdot u^{\frac{1}{2}} \cdot d^{\frac{1}{2}} \cdot D^{-\frac{1}{3}} \cdot \nu^{-\frac{1}{6}} \quad \text{Eq (2.25)}$$

Remembering the definitions of the Reynolds and Schmidt numbers, we can regroup the terms to form equation 2.26.

$$Sh_{WB} = 1 + 0.3 \cdot Sc^{\frac{1}{3}} Re^{\frac{1}{2}} \quad \text{Eq (2.26)}$$

Wang-Brasseur define flux as,

$$J_{WB} = Sh \cdot \frac{D}{r} \cdot \Delta C = k_c \Delta C \quad \text{Eq (2.27)}$$

Where k_c is the mass transfer coefficient and delta C is the concentration gradient. When Sh_{WB} is substituted into equation 2.27, the final particle dissolution flux is described in equation 2.28.

$$J_{WB} = \left(1 + 0.3 \cdot Sc^{\frac{1}{3}} Re^{\frac{1}{2}}\right) \cdot \frac{D}{r} \cdot \Delta C \quad \text{Eq (2.28)}$$

Ranz-Marshall define flux as,

$$J_{RM} = Nu \cdot \frac{D}{d} \cdot \Delta C \quad \text{Eq (2.29)}$$

From Equation 2.13 the Nusselt number which is equivalent to the Sherwood number (Eq. 2.15) when discussing mass transfer processes can be substituted into Equation 2.29 yielding,

$$J_{RM} = \left(2 + 0.6 \cdot \sqrt[3]{Sc}\sqrt{Re}\right) \cdot \frac{D}{d} \cdot \Delta C \qquad \text{Eq (2.30)}$$

To see the equivalence of Wang-Brasseur to the Ranz-Marshall simply change the d to 2r in Eq. 2.30 and compare Eq. 2.32 to Eq 2.33.

$$J_{RM} = \left(2 + 0.6 \cdot \sqrt[3]{Sc}\sqrt{Re}\right) \cdot \frac{D}{2r} \cdot \Delta C \qquad \text{Eq (2.31)}$$

$$J_{RM} = \left(1 + 0.3 \cdot \sqrt[3]{Sc}\sqrt{Re}\right) \cdot \frac{D}{r} \cdot \Delta C \qquad \text{Eq (2.32)}$$

$$J_{WB} = \left(1 + 0.3 \cdot Sc^{\frac{1}{3}} Re^{\frac{1}{2}}\right) \cdot \frac{D}{r} \cdot \Delta C \qquad \text{Eq (2.33)}$$

It is recognized that the hydrodynamic approach to calculating the aqueous boundary layer thickness is the most accurate approach for large particles, while particles with radii in the micron range are less affected by hydrodynamic parameters in the USP II apparatus.[40]

2.3 Absorption

Intestinal absorption is known to occur in four main ways: paracellular, transcellular passive diffusion, transcellular endocytosis, and transcellular carrier-mediated transport. Endocytosis and carrier-mediated transport are active transport mechanisms and have no immediate bearing on this work. Of the two remaining ways drug can enter the blood stream, the dominating type is passive diffusion. Paracellular junctions are the tight junctions in between individual cells and make up a significantly less portion of available transport surface area than the main cell body. The tightness of the junction also limits the size molecules and the rate of absorption through these sites. Therefore the *in vitro* membrane should reflect the transport that occurs in the transcellular passive diffusion case because of the high probability that transport is occurring through the apical main cell membrane and that the dominating transport rate will be through the apical cell membrane. Passive diffusion in the GI essentially only allows hydrophobic molecules to easily permeate through

the lipid bilayer. Ions, small uncharged polar molecules, and large uncharged polar molecules are greatly impeded during absorption. While a small fraction may pass through the barrier, much of that mass will be rejected. Carrier mediated and endocytosis are the only ways that can move ions, polar molecules, and large molecules across the membrane without disrupting the membrane.[48]

The effect of particle size and dose on dissolution/absorption was reported on recently, 1995-2010, by Sugano, Doyle-McCullough, Hodges, Limpanussorn, Norris. Sugano published a paper describing what he termed "particle drift", where particles could "drift" into the mucosal and "unstirred water layer" to enhance the amount of mass absorbed.[49] The other mentioned references specifically describe microparticles being able to penetrate into the mucous layer and gastrointestinal wall and entering systemic circulation through a paracellular route.[49-53] In principle and mathematical treatment, the concept of microparticles being able to enhance flux through the membrane was first written down (to this author's best knowledge) in 1979 in the thesis work on Gregory E. Amidon at the University of Michigan. Unlike in Sugano's film theory analysis of the particle size-dose effect, which attempts to calculate an effective thickness of the "unstirred water layer" based on surface areas, Amidon proposed a convection-diffusion model (Eq. 2.7) which treats the hydrodynamic boundary layer as it would naturally form.

$$\frac{\partial C}{\partial t} = D\frac{\partial^2 C(y)}{\partial y^2} - \frac{\partial C}{\partial y}v + R \qquad \text{Eq (2.7)}$$

However, in Amidon's original derivation, there was a mistake in the description of the boundary conditions. As Amidon and Sugano both suggest, particles can diffuse into the hydrodynamic boundary layer. When a particle approaches the absorption surface it continues to dissolve as it moves. The original boundary conditions for the convection-

diffusion model state that there is a continuity of flux between all regions (bulk fluid phase, aqueous boundary layer, membrane, and receiver).[54] However, by the definition of the phenomena being described this cannot be true. For a dissolving particle in the hydrodynamic boundary layer, mass is generated and diffuses into solution. This is the generation (R) term in the convection diffusion model and since mass is generated in bulk fluid and within the boundary layer flux between the bulk and the boundary layer does not equal the flux between the boundary layer and the membrane. This flux discontinuity is the origination of the "particle drift" effect or as was originally described "shorting out" the diffusion layer. The net effect is the same though, through a combination of particle micronization and increasing dose, fluxes above the the diffusion limited film theory maximum flux are possible. In Sugano's 2010 paper, he suggests the implications for this effect *in vivo*. In Sugano's analysis, which considered the surface area ratio of the particles to the "unstirred water layer", he noted that particles could exist in "villi interspace" as observed by Norris and Doyle-McCullough.[50, 53] One of the most common questions in the absorption modeling space is how to treat the intestinal surface area. Many consider the simple tube, or "flattened tube" whereby some scaling factor or ellipse calculation is considered, while others calculate the total surface area based on the microvilli and villi.[5] The issue with all of these interpretations is that physiologically, the intestine is not a fluid filled tube. The stomach releases fluid in pulsatile packets, which combine with excreted fluids from the gastrointestinal wall.[55] These fluid packets carry the pharmaceutical particles and were found to be effectively two types of fluid pockets, 0.5-2mL and >20mL. The smaller pockets made up ~ 75% of the number of fluid pockets observed.[27] Considering the discreet nature of these pockets, and the flattened nature of the unfilled intestine, it would be impossible for

such small pockets of fluid to experience surface contact areas which are commonly calculated. The small pockets of fluid would experience the villi and microvilli surface area, most likely form a spherical fluid domain (from peristalsis of the MMC), and when particles become trapped in the crypts of the villi and microvilli, they likely experience the flux enhancement as described by the convection diffusion model (depending on particle size and amount of solid drug per packet). This implies that while the total surface area of the intestine is impressive, the bigger influence on absorption of drug in the oral pathway is the ability for drug particles to access to these confined spaces where the aqueous diffusion limit can be superseded.

2.3.1 The Organic-Water Partitioning System

Biphasic systems or organic solvent based absorption systems (OSAS) have been utilized in the pharmaceutical industry to incorporate a passive absorption compartment into ivR *in vitro* dissolution systems.[1, 6, 56-58] However, systems such as octanol-water, can be challenging to use. The boundary that occurs between the aqueous and organic phases is more dynamic than a physical barrier.[59] Large agitations can create mixing between the organic and aqueous layers, which can result in a poorly defined interface. A significant challenge in OSAS systems is adjusting the surface area to volume ratio to modulate the interfacial mass transfer rate to accurately simulate human oral absorption.

2.3.2 The Caco-2 Cell Monolayer Permeability Assay

Another popular system for simultaneous dissolution and absorption studies are the cell-based membrane systems. Yamashita et al. have done extensive work with Caco-2 and MDCK II monolayer cell membranes in side-by-side diffusion cells in an effort to include absorption kinetics in dissolution tests for the purpose of *in vitro-in vivo* correlation and evaluation of

drug candidates during the early discovery phase of drug development.[60-63] They also have examined formulation effects (micelle transport and food effect) *in vitro* on Caco-2 membrane transport.[64-66] The donor and receiver volumes (on the order of 1-10mL) make these assays attractive to industry and academia for higher throughput permeation studies (used in well-plate assays), in addition to containing biological drug transporters in some systems which allow for active transport to occur in an *in vitro* environment. However, Caco-2 cell membrane assays to date have not attempted to achieve the correct membrane surface area to dissolution volume ratio to replicate human absorption rates. In balance, there are significant challenges in using Caco-2 or similar systems. Caco-2 cells are known for their significant inter-laboratory variability, which requires an external system of validation to verify any results generated in the use of Caco-2 permeability assays. In the recent past a clone of Caco-2 (TC7) was developed to increase the consistency of Caco-2 assays. Cell based systems require prolonged periods of time prior for cells to culture prior to use, unlike a synthetic membrane like PDMS or PAMPA. Additionally, drug molecules tend to be retained in the Caco-2 membrane when drug is solubility challenged, and the hydrodynamic boundary layer severely affects the permeation of drug molecules through the membrane. [67, 68]

2.3.3 The Parallel Artificial Membrane Permeability Assay

PAMPA is another tool that was developed in the late 1990's to improve and expedite the evaluation of new chemical entities permeability and estimate oral absorption rates. The development of PAMPA focused on high throughput screening which gives PAMPA a distinct advantage over Caco-2 or other cell-based assays. Particularly, in the pharmaceutical industry where the rapid pace of early discovery phase pharmaceutical development demands robust, repeatable, and fast/real time analytical techniques in data analysis.[69] There

are a range of structural configurations for different routes of drug administration i.e. oral, brain, skin, and different combinations of polymer/organic/phospholipid phases) for PAMPA systems.[70-73] PAMPA has even been used in parallel studies with Caco-2 assays to determine effects of reflux and efflux transporters on permeability and oral absorption.[74] These characteristics make PAMPA a powerful tool for permeability screening and mechanism determination, but a poor method for incorporating realistic human GI absorption kinetics into dissolution methods. PAMPA suffers the same limitations as cell-based assays where interfacial area is determined artificially by the micro well-plates used in the assay, and the available volumes for dissolution are not scaled to match the human GI situation. The hydrodynamic boundary layer can also significantly affect the permeation of lipophilic drugs.[75]

2.4 Polymer films for separations processes

Selection of an appropriate polymer for passive diffusion "absorption" began with identifying classes of polymers that were used in separations applications and the mechanism of molecular transport. From Table 2-2, Polysiloxanes were found to be used in gas separations, pervaporation, and nanofiltration of organophilic molecules. Polysiloxanes are also already commonly used in an industrial capacity at thicknesses of 0.1-110μm. The purpose of the absorption medium is to separate organophilic pharmaceuticals from an aqueous medium. Polysiloxanes would be insoluble in aqueous media, not allow aqueous infiltration of the polymer network, and could be made extremely thin, thus presented a class of polymers for ideal starting point to biomimic human oral passive diffusion-based absorption.

Table 2-2 Legend for Industrial established separation materials & processes.

Legend for table 2-3 which describes the mass transfer processes for which the polymers are currently used for industrial applications.[76]

Membrane Process	Description
GS	Gas Separation (Air separation, natural gas separation)
RO	Reverse Osmosis (Ultrapurification of water, water treatment)
UF	Ultrafiltration (Concentration, fractionation, or purification processes)
D	Dialysis, Blood purification and plasma separation
ED	Electrodialysis
MF	Microfiltration
NF	Nanofiltration
PV	Pervaporation
Anisotropic	Asymmetric
Isotropic	Symmetric
Mesoporous	2-50nm pores
Macroporous	100-300-micron pores
Non-porous	No pores

Table 2-3 Polymers used in industrial mass transport applications

A description of the barrier type, cross section, typical thickness, and application for a variety of polymers used as membranes.[76]

Polymer	Morphology			Membrane Process
	Barrier Type	Cross Section	Barrier Thickness (μm)	
Cellulose Acetates	Non-porous	Anisotropic	~0.1	GS, RO
	Mesoporous	Anisotropic	~0.1	UF
	Macroporous	Isotropic	50-300	MF
Perfluorosulfonic acid polymer	Non-porous	Isotropic	50-500	ED, Fuel Cell
Polyphenylene oxide	Non-porous	Anisotropic	~0.1	GS
Poly(styrene-codivinylbenzene), sulfonated or aminated	Non-porous	Isotropic	100-500	ED
Polytetrafluoroethylene	Macroporous	Isotropic	50-500	MF
	Non-porous		~0.1	GS
Polyamide, aromatic, in situ synthesized	Non-porous	Anisotropic/ composite	~0.05	RO, NF
Polycarbonates, aromatic	Non-porous	Anisotropic	~0.1	GS
	Macroporous	Isotropic track etched	6-35	MF
Polyether, aliphatic crosslinked, in situ synthesized	Non-porous	Anisotropic/ composite	~0.05	NF
Polyimides	Non-porous	Anisotropic	~0.1	GS, NF
Polysiloxanes	Non-porous	Anisotropic/ composite	~0.1 < 110	GS, PV, NF (organophilic)
Polysulfones	Non-porous	Anisotropic	~0.1	GS
	Mesoporous			UF
Polyvinyl alcohol, crosslinked	Non-porous	Anisotropic/ composite	< 1-10	PV (hydrophilic)

2.5 Structure-Based Predictions of poly(dimethyl siloxane) permeability compared to Predicted Human Oral Permeability

There are many software-based molecular characterization tools available to scientists, including chemicalize.org, chemspider.com, drugbank.ca, etc., which can take a molecular structure and provide basic predictions about its physical-chemical properties. The octanol-water system, as a measure of equilibrium partitioning, has also been well characterized and modeled, a non-exhaustive list of relatively recent work: [77-80]. Knowing the K x D_{PDMS} product relationship with $LogP_{octanol\text{-}water}$ we can then predict the permeability of any drug which we know the $LogP_{octanol\text{-}water}$ ($LogD_{octanol\text{-}water}$). Sinko P.D. et al shows that PDMS permeability scales inversely proportionally with membrane thickness, which means that if we know K x D_{PDMS} we can scale the permeability to any thickness we can manufacture.[81] We can predict a drugs non-ionized PDMS permeability from $LogP_{octanol\text{-}water}$ ($LogD_{octanol\text{-}water}$) (Figure 2-1-A). Mathematically, our procedure for utilizing PDMS membranes for *iv*R dissolution/absorption tests does not discriminate between dissolution under non-ionizing, partially ionizing, or fully ionizing conditions. The intrinsic measurements in Figure 2-1-A show the broadest behavior of the partition coefficients and should be valid for any experimental condition if there are some non-ionized molecules present. If the LogD for the molecular entity is known in PDMS then that value can be used to obtain the PDMS permeability through the relationship found in Sinko PD et al.[81] The following figures show the K x D_{PDMS} product predicting permeability in PDMS at a theoretical thickness. The actual data (in light blue) are the measured K x D product for that molecule scaled by the target thickness in each plot. The membrane can be relatively thick and achieve permeation magnitudes of non-ionized molecules like those observed in humans under physiologic conditions (Figure 2-1-A).

However, thinning the membrane allows for a more exact match on the 1:1 line. It is not necessary to have a 1:1 match for PDMS and human GI permeability. However, the closer the two permeabilities are, the less compensation in the $(A/V)_{in\ vitro}$ is required. Thin membranes allow for higher partially ionized absorption rates because the magnitude of the non-ionized increases (Figure 2-1-B). To maintain *iv*R, the physiological pH range must be defined and incorporated into the prediction for permeability. For example: in Figure 2-1-C & D, assuming a pH of 5.5 and 6.5 (both expected pHs in the human GI), the LogD at each pH was calculated and converted into a $LogK_{PDMS}$. Wherein those values were used to calculate the permeability at each pH in PDMS. This type of approach allows for easy estimation of dynamic permeability in an experiment where the pH changes as a function of distance down the "GI tract". This provides the first part of the solution, $K_{in\ vitro}$, but the more difficult human absorption component needs to be quantified.

The Winiwarter et al. 1998 model was found amongst several other models for human permeation and absorption rate prediction in a paper by Linnankoski et al. published in 2008, (Uppsala, Sweden).[82, 83] This model was selected to predict human oral permeation, because it was derived from the physical-chemical properties of the molecule (see equation 4, R^2 = 0.93 and Q^2 = 0.90).

$$logP_{effective\ in\ humans} = -2.883 - 0.010 \times Polar\ surface\ area + 0.192 \times logD_{pH\ 5.5} - 0.239 \times Hydrogen\ bond\ donors \quad \text{Eq (2.8)}$$

Winiwarter's model used 22 structurally diverse molecular entities, measured real human jejunal permeability, and measured/calculated molecular descriptors. The human permeation data was obtained using a regional *in vivo* perfusion system in the proximal jejunum, and was the permeability data used in the foundation of the BCS. These data were the training set which was then validated with an additional 136 compounds from the

Pomona College Medicinal Chemistry Project. The training set molecules were amoxicillin, antipyrine, atenolol, carbamazepine, creatinine, desipramine, enalaprilat, fluvastatin, furosemide, D-glucose, hydrochlorothiazide, ketoprofen, L-leucine, L-dopa, α-methyldopa, metoprolol, naproxen, piroxicam, propranolol, terbutaline, urea, and verapamil. They measured the pKa, LogP and LogD (pH 5.5 and 6.5) using the pH metric technique. SYBYL was used to calculate HOMO, LUMO, dipole moments, molecular weight, number of atoms, hydrogen bonding capacity (H-bond count & atom specific bonding), molecular volume, molecular surface area, H-bond donors, H-bond acceptors, and polar surface area. After their rigorous analysis, Winiwarter et al. determined that the best model was the one shown in equation 4. More complex models achieved slightly higher correlation coefficients, but not so much better that they were worth pursuing.[83]

Figure 2-1-B suggests that using a thin membrane will allow for human magnitude of permeabilities to be measured from PDMS membranes. It should be noted that PDMS membranes can be fabricated down to single micron thicknesses, and that the ability to achieve a better match in PDMS permeability would be possible via a more advanced casting procedure (

Table 2-3). The only limitation to fabrication is the elastic modulus of the material and the precision of the casting procedure. It is possible to replicate, *in vitro*, the *in vivo* permeability by modifying the current casting procedure to obtain thinner membranes.

To determine if PDMS is a viable material to achieve absorption rates at the same magnitude as observed/predicted in the human gastrointestinal tract, measurements of the partition coefficient were made (see chapter 3.4.2 1). Once the PDMS partition coefficients were measured, a correlation between PDMS partitioning and octanol-water partitioning was established. This allowed for the prediction of PDMS permeabilities of many different BCS class drugs. In Figure 2-1-A, the permeability relationship between PDMS and Human oral is compared. PDMS is amenable to many fabrication methods, and the permeability is inversely proportional to the thickness of the membrane the plots in Figure 2-1-B look at the effect of thickness. Partitioning is also significantly affected by pH, so Figure 2-1-C & D also examines the affects on PDMS permeability of the pH at physiologically relevant pH.

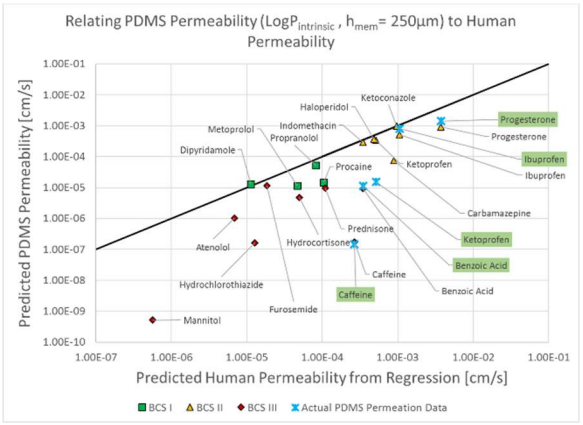

A

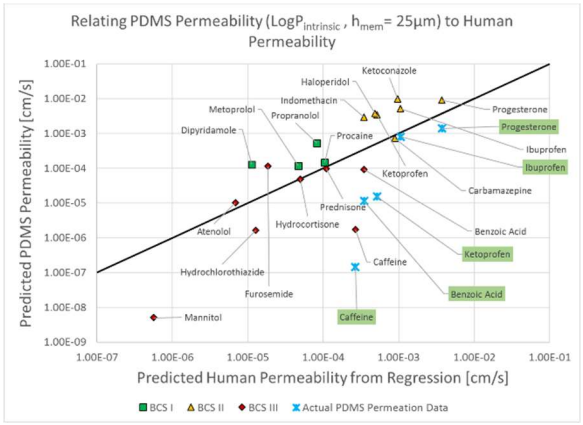

B

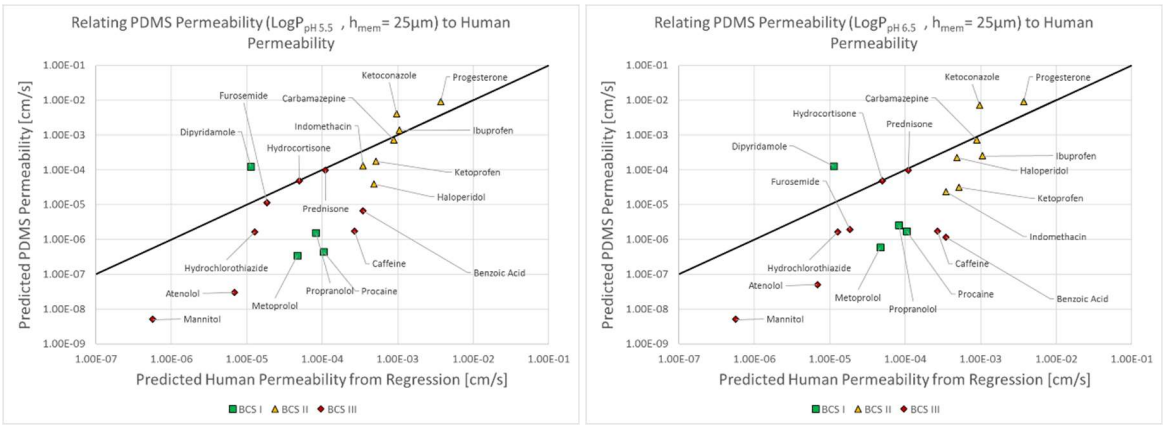

C D

Figure 2-1 Predicting the utility of PDMS for biomimetic *in vitro* oral pharmaceutical absorption.

A) Direct prediction from the octanol-water partition coefficient (computationally determined) yields a predicted PDMS permeability in a theoretical 250µm thick PDMS membrane. PDMS permeability was predicted in two ways 1) assuming an average of the measured diffusion coefficients in PDMS 2) using the correlation betweeen measured $LogK_{PDMS}$ and the thickness independent permeability (K x D). The method of using the drugs intrinsic K xD can be used to predict permeability at any thickness. Demonstrating that PDMS membranes at a reasonable thickness can nearly human magnitude permeabilitys for high permeabilty drugs under their intrinsic non-ionizing conditions. The black line in this plot is a 1:1 line, therefore if a drug falls near this line, it can be said (within the confidence of the methods used to generate these data) that the permeability in humans would be equal to the intrinsic permeability in PDMS membrane at 250µm thickness. B) Since the thickness independent permeability, we can easily change our model to accommodate any thickness. The thickness is reduced by 10x from 250µm to 25µm, to show that a tighter fit to the 1:1 line can be achieved with changes to the thickness of the membrane. A 1:1 fit is not necessary, but it does reduce the amount of compensation in the *in vitro* variables required to maintain ivR absorption kinetics. For the ivR methodology, we do not expect that all drugs under duodenal and jejunal pHs will be in their intrinsic state. This plot shows: C) the effect that the "duodenal" pH =5.5 has on the predicted PDMS permeability; D) the effect that the "jejunal" pH 6.5 has on the predicted PDMS permeability. Drugs will be in various states of ionization under duodenal and jejunal pHs and possibly not in their intrinsic state.

It was determined that based on this, albeit small, sample of measured partition coefficients, it would be possible based on PDMS permeability alone (ignoring the effects of the aqueous boundary layer) that it would be possible to achieve permeability through a PDMS membrane that is within the same order of magnitude as the human oral permeability. This study also confirmed that very thin PDMS membranes would be requires to achieve the permeability needed.

CHAPTER 3

In Vitro Characterization of the Biomimetic Properties of Poly(dimethyl siloxane) to Simulate Oral Absorption

3.1 Abstract

The potential use of poly(dimethyl siloxane) (PDMS) as an *in vitro* biomimetic analogue of the passive drug absorption process in the human gastrointestinal tract (GI) is assessed. PDMS is biomimetic because of similarities in small molecule transport such as mechanism, ionization selectivity, lipophilicity. Ten molecular probes are used to evaluate the transport pathways and properties used to predict human oral absorption rates. The transport pathways through PDMS (bulk/pore) are analogous to transcellular (TCDT) and paracellular (PCDT) drug transport pathways. PDMS PCDT is assessed using positronium annihilation life-time spectroscopy (PALS) and partition experiments; TCDT using diffusion and partition experiments. PALS determined that PDMS pores were uniform (Diameter~0.85nm), isolated, and void volume was unaffected by drug accumulation after equilibrium partitioning. Therefore, there is no PCDT or convective flow through PDMS. A strong linear correlation exists between predicted octanol-water partition coefficients and PDMS partition coefficients ($LogP_{PDMS}=0.736xLogP_{O\text{-}W}-0.971$, $R^2=0.981$). The pH-partition hypothesis is confirmed in PDMS using ibuprofen over pH 2-12. Diffusivity through PDMS is a function of lipophilicity and polar surface area was found to be:

$K \times D_{PDMS} = 4.46 \times 10^{-8} \times e^{2.91 \times LogP_{PDMS}}$ (R^2=0.963) & $K \times D_{PDMS} = 4.61 \times 10^{-6} \times \left(\frac{PSA}{K_{PDMS}}\right)^{-1.20}$ (R^2=0.973). Varying the mass% of curing agent changed the lipophilicity and diffusivity ($p<0.02$), but not practically ($KxD = 2.23x10^{-5} cm^2 s^{-1}$ vs $2.60x10^{-5} cm^2 s^{-1}$) and does affect elastic modulus (3.2%=0.3MPa to 25%=3.2MPa).

3.2 Introduction

Table 3-1 Variables and Definitions for Chapter 3.

Variable	Definition
A_{G-I}	Effective Gastrointestinal Surface Area (cm^2)
$A_{o/w}$	Organic-Aqueous Interfacial Surface Area (cm^2)
A_m	Membrane Surface Area (cm^2)
D	Molecule's Diffusion Coefficient (cm^2/s)
D_{Aq}	Aqueous Diffusion Coefficient (cm^2/s)
D_{N-I}	Intrinsic Non-Ionized Diffusion Coefficient of Molecule in the Membrane (cm^2/s)
D_I	Intrinsic Ionized Diffusion Coefficient of Molecule in the Membrane (cm^2/s)
P_m	Total Membrane Permeability (cm/s)
P_{PDMS}	Drug Permeability through PDMS subtracting the influence of the Aqueous Boundary Layer (cm/s)
$P_{o/w}$	Total Octanol-Water Permeability (cm/s)
P_{eff}	Effective Total Permeability (cm/s)
P_{N-I}	Intrinsic Non-Ionized Partition Coefficient of Molecule in the Membrane (cm/s)
P_I	Intrinsic Ionized Partition Coefficient of Molecule in the Membrane (cm/s)
h	Characteristic length of the diffusion process, a.k.a the boundary layer, membrane thickness, liquid-liquid interfacial thickness (cm)
h_{Aq}	Aqueous Boundary Layer Thickness (cm)
h_m	Thickness of the PDMS membrane (cm)
K	Equilibrium Partition Coefficient
C_{Aq}^*	Equilibrium Concentration of drug in the aqueous media at a specific pH (g/cm^3)
C_m^*	Equilibrium Concentration of drug in the membrane at a specific pH (g/cm^3)
K	Equilibrium Partition Coefficient (unitless)
K_{N-I}	Intrinsic Non-Ionized Partition Coefficient of Drug in PDMS (unitless)
K_I	Intrinsic Ionized Partition Coefficient of Drug in PDMS (unitless)
$f_{Aq\ N-I}$	Fraction of Drug that is non-ionized (unitless)
f_E	Fraction of Drug Extracted from Extraction Theory (unitless)

Variable	Definition
$LogK_{N-I}$	Logarithm of the Intrinsic Non-Ionized Partition Coefficient of Drug in PDMS (unitless)
LogD	Logarithm of the pH Distributed Partition Coefficient (unitless)
A_m	Membrane Surface Area (cm^2)
$V_{in\ vitro}$	Volume of the fluid in the *in vitro* experiment donor compartment (cm^3)
$V_{in\ vivo}$	Volume of the fluid available for drug dissolution *in vivo* (cm^3)
V_m	Volume of the Membrane (cm^3)
S	Saturation Concentration of Drug in Donor Fluid at a particular temperature and pH (g/cm^3)
$k_{in\ vivo}$	Apparent first order absorption rate *in vivo* (s^{-1})
$k_{in\ vitro}$	Apparent first order rate *in vitro* (s^{-1})
$\dot{m}$	mass transfer coefficient ($g\ s^{-1}$)
Q_T	mass per unit area from the slope of the receiver concentration profile multiplied by $V_{aq}/A_{membrane}$ ($g\ cm^{-2}$)
pKa	pH at which the drug is 50% ionized
pH	- log of of the hydrogen concentration

3.2.1 *In vivo* relevant dissolution and absorption

3.2.1 1 The *in vivo* relevant (ivR) Hypothesis for Realistic *in vitro* Absorption Kinetics

For orally administered drugs, dissolution methodologies should examine the drug product in an ivR *in vitro* experimental system that accurately simulates the critical parameters of the *in vivo* environment and kinetic processes of the human GI. The ivR hypothesis is that using physiologically relevant fluids (e.g.: pH, volumes, temperature, buffer, buffer capacity, surfactants), hydrodynamic conditions (e.g.: shear, advection), and mass transfer rates (e.g.: diffusion, permeation to simulate the absorption process) in an *in vitro* system can better simulate *in vivo* performance than current and common compendial dissolution methodologies.[4, 27, 84, 85] This report is primarily concerned with determining if PDMS can be used to replicate the passive absorption kinetics of the human GI so that it can be applied to a device that meets the criteria for ivR dissolution. PDMS was characterized using a rotating membrane diffusion cell (Figure 3-1) to determine if it meets the

requirements as a robust, semipermeable, and *in vivo* relevant *in vitro* membrane. By measuring the fundamental transport properties of the membrane system, its potential to act as an ivR membrane can be easily evaluated for a variety of drug molecules.

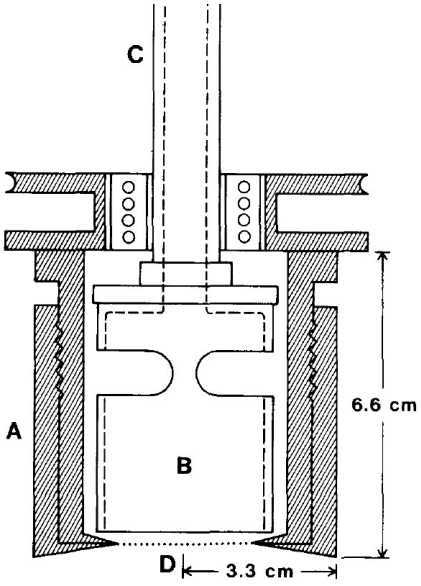

Figure 3-1: A schematic diagram of the rotating diffusion cell[54]

Cross section "A" shows the outer housing of the diffusion cell, which is freely rotating. Section "B" is the inner housing, which is connected to the support structure and is non-moving. Within "B" two large fillets allow for media to cascade over the edge creating a well mixed environment. Section "C" shows the upper portion of the support structure where, lab clamps hold the diffusion cell in place during an experiment. "C" also contains a hollow tube that enters "B", allowing for sampling mechanisms (probes or pipettes) to access the inner chamber. Section "D" is membrane interphase.

Mudie et al. laid the experimental ground work for the ivR absorption hypothesis.[5] The goal of which is to construct an *in vitro* system in which the partition rate coefficient ($k_{abs_{in\ vitro}}$) is approximately equal to the *in vivo* absorption rate coefficient ($k_{abs_{in\ vivo}}$).

$$k_{in\ vivo} \approx k_{in\ vitro} \quad \text{Eq (3.1)}$$

$$P_{in\ vivo} \frac{A_{G-I}}{V_{in\ vivo}} = P_{\frac{o}{w}} \frac{A_{\frac{o}{w}}}{V_{in\ vitro}} \quad \text{Eq (3.2)}$$

Renaming the variables to Mudie et al.'s hypothesis, for the PDMS based absorption system these authors propose that:

$$P_{in\ vivo} \frac{A_{G-I}}{V_{in\ vivo}} = P_m \frac{A_m}{V_{in\ vitro}} \quad \text{Eq (3.3)}$$

Where Equation (3.3) allows for the human absorption kinetics, either measured or predicted, to be replicated *in vitro* by scaling the $A_{in\ vitro}/V_{in\ vitro}$ to make $K_{abs\ in\ vivo} \approx K_{abs\ in\ vitro}$.

However, various *in vitro* systems have been used in the past to attempt to integrate absorption kinetics into dissolution methods, such as the octanol-water system, Caco-2 cell membrane permeability assay, parallel artificial membrane permeability assay (PAMPA). Yet these systems fall short in way or another to providing realistic human GI absorption kinetics in a robust and facile *in vitro* setting.

3.2.1 2 PDMS as an *in vivo* relevant membrane

The current report has investigated the use of a PDMS membrane to overcome the experimental challenges encountered in other *in vitro* permeation assays/devices/methods. A properly selected material can yield a membrane that mitigates or eliminates the experimental challenges found in other *in vitro* absorption systems. However, the selection of an optimal polymer membrane is more than a question of lipophilicity. There are *in vitro* aspects that must be considered as well such as erosion, degradation, and physical stability. Water intrusion/swellability, creation of aqueous pores, diffusion of drug, diffusion of polymer degradation products, micro-environmental pH changes, diffusion through pores, hydrogen/hydroxide ion transport into the membrane causing micro-environment pH changes, osmotic effects, convection, adsorption/desorption, and partitioning behavior may all affect mass transport.[86]

Since there is no significant convective passive drug transport through the human GI, polymers that were known to have convective transport behaviors such a sieving or size exclusion were eliminated from consideration for the biomimetic *in vitro* membrane. For robust and simple *in vitro* mass transport analysis, the membrane needs to be stable across

the pH spectrum and be unaffected by the solution conditions present in the donor and receiver compartments. Selecting the polymer to not include highly reactive functional groups ensures physical and chemical stability. Polymers containing carboxylic anhydrides, ketal-, and ortho ester functional groups were excluded because they have been reported to be some of the most reactive functional groups. The type of drug (acid or base) and the drug's interaction with the membrane can contribute to degradation or hydrolysis of the membrane. Acidic and basic drugs can autocatalyze degradation by changing the micro-environment pH in the polymer.[86] These reasons excluded the use of hydrogels and other common control released polymers. While employed in other pharmaceutical applications, the use of these types of polymers in ivR absorption applications would be problematic due to the diffusion coefficient becoming dependent on the aqueous content in the membrane, as well as a time dependent interfacial surface area. PDMS was selected for the current studies because it is non-swelling, non-interconnected porosity, lipophilic/organophilic, and pH stable. In addition, PDMS's selection was favorable due to ease of fabrication, low cost, and availability.

PDMS was commercialized in 1943 by the Dow Corning company and was obtained for these studies as the Sylgard 184 elastomer kit.[87] This kit contains two components, the polymer base and the polymer curing agent. The polymer base contains 60% dimethylsiloxane which is dimethylvinyl terminated, 30%–40% dimethylvinylated and trimethylated silica, and 1–5% tetra(trimethylsiloxy)silane. The base material is viscous, η_{base} = 5000 cS. The curing agent contains dimethyl methylhydrogen siloxane that through a platinum catalyst, initiates a step-wise polymerization using a hydrosilation reaction at the vinyl groups in the base material.[88, 89] At room temperature (RT) PDMS forms a transparent, colorless, elastomeric polymer, see Figure 3-2.

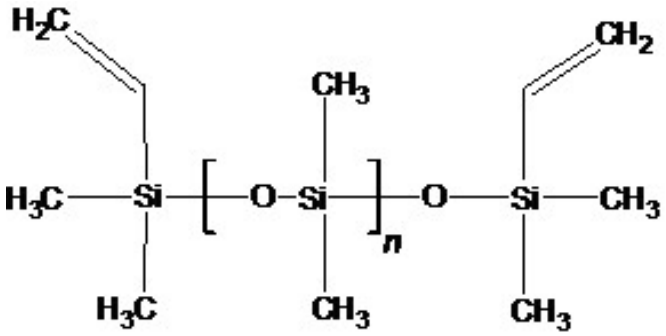

Figure 3-2 Chemical structure of Sylgard 184® base material.[89]

The density of the cured polymer (at 10:1, mass of base: mass of curing agent) is 1.03-1.05 g cm^{-3} at 25°C (measured in this work and [89]). The glass transition temperature of PDMS is -127°C, which according to Sperling's textbook implies that at RT the polymer is in the viscous-flow regime.[87] PDMS has a critical molecular mass of Mc = 24,500g mol^{-1}, an average molecular weight of chain segment between intermolecular junctions of Me =12,293g mol^{-1}, and reptation tube diameter of d_t = 78.6Å.[87] PDMS obeys steady state and pseudo steady state Fick's law for diffusion and is impermeable to hydrochloric acid, phosphate buffer salts, protonated aminophenones, charged organic molecules, inorganic ions, and does not readily transport water and mineral oil. However ethanol is transported without modifying the membrane.[90]

3.3 Materials & Methods

3.3.1 Materials

Agilent 1100 High Performance Liquid Chromatography (HPLC), Eclipse Plus C 18 Column (3.5µm x 4.6µm x 150mm), Acetonitrile (EMD Millipore, HPLC grade), deionized water (Milli-Q purified), trifluoroacetic acid (Fisher Scientific, Optima Grade), triethylamine (Fisher Scientific, Optima Grade), methanol (Fisher Scientific, HPLC grade), Ibuprofen

(Albemarle Lot No. 2050-0032F), Progesterone (Sigma Aldrich, CAS 57-83-0), Benzoic Acid (Fisher Scientific CAS 65-85-0), Metoprolol Tartrate (Sigma Aldrich, CAS 56392-17-7), Caffeine (Sigma Aldrich, CAS 58-08-2), Atenolol (Sigma Aldrich, CAS 29122-68-7), Ketoprofen (TCI Tokyo, Japan, CAS 22071-15-4), Hydrochloric acid buffer pH 2.0 (USP guideline), Acetate Buffer 5.0 (USP guideline), Phosphate buffer pH 6.5 (USP guideline), Sodium Hydroxide Buffer pH 12 (NaOH + KCl), Poly(dimethyl siloxane), (Sylgard 184 elastomer kit, Dow Corning), Hexane (Fisher, reagent grade), Instron uniaxial press, Fisher-Scientific accuSpin micro17 Centrifuge, Wenesco Inc. HP1212-D cure plate with glass cover.

3.3.2 Experimental Methods

3.3.2 1 Generic membrane casting procedure

Sylgard 184 base was weighed in a glass container and moved to a vacuum chamber where a -750mbar vacuum was pulled for 25min to remove gas. Separately, an appropriate amount of Sylgard 184 curing agent was weighed on an analytical balance. A 1:1 ratio (total mass:volume) of hexane was measured in a graduated cylinder. The hexane was used to dissolve the catalyst component and then was added to the container containing the base polymer. Manual mixing was done until the base was completely dissolved (easily observed by a change in the index of refraction). An appropriate volume of solution was drop cast into polyethylene weigh boats using a pipette. The PDMS solution cured at the desired temperature and time with solvent evaporating into a lab hood.

3.3.2 2 Strain rate effect in PDMS mechanical samples

Three strain rates were tested: 1, 0.1, 0.01 mm s^{-1} strain rates in uniaxial compression

3.3.2 3 PDMS Elastic modulus and cure temperature sample preparations

PDMS cylinders were prepared at 3mm thickness and 6mm diameter. For the elastic modulus samples, the ratio of the polymer base to curing agent was varied (3, 7, 10, 15, 20, 30):1. For cure temperature samples, the base to curing agent ratio was 10:1. Each sample was cured at a different temperature for 9 days. Samples cured above 40°C were allowed to cure at RT until the hexane was evaporated (< 1 day) until the film was semi-solid, and then the remainder of the nine-day cure was completed. This prevented boiling hexane from forming bubbles within the sample.

3.3.2 4 Effect of curing temperature on elastic modulus

The curing temperatures studied were 20°C, 40°C, 60°C. Five samples were prepared using a 6mm diameter surgical punch (L/D ~0.5). The modulus was calculated from the linear slope on the compression stress-strain curve at a strain rate of 0.01mm s^{-1}.

3.3.2 5 Elastic modulus versus composition ratio

Five samples were prepared using a 6mm diameter surgical punch (L/D ~0.5). The modulus was calculated from the linear slope on the compression stress-strain curve.

3.3.2 6 HPLC methods

For acidic drugs 0.085%v/v trifluoro acetic acid was used in both water and acetonitrile. For basic drugs 0.1%v/v triethylamine was used in both water and acetonitrile. See Table 3-2 for details. For HPLC Standard Curves, limit of detection (LOD) and limit of quantitation (LOQ), a five-point standard curve (two-fold dilution per step) was created for each drug in the buffer used for the experiment.

Table 3-2 A brief description of the HPLC methods, including the mobile phase composition used and the average elution time of the molecule.

Drug	Mobile Phase Composition (Acetonitrile/H2O)	Average Elution Time (min)
Progesterone	60/40	6.63
Ibuprofen	60/40	5.04
Benzoic Acid	29/71	4.52
Ketoprofen	49/51	4.48
Caffeine	17/83	2.62
Atenolol	19/81	4.52
Metoprolol Tartrate	41/59	4.28

3.3.2 7 Partition coefficient measurements

For each drug, five membranes were prepared. Each membrane was prepared with 10 parts base to 1 part curing agent and cured at 20°C for at least 72 hours. Once cured, the membranes were sectioned using a template and razor blade. The dimensions of the perimeter and thickness were measured using a caliper to determine the volume of membrane. After determining membrane density, subsequent volume measurements were made using the density relationship. Stock solution was distributed to 5 sample vials with 1 membrane-free vial to serve as a control. The time zero point was measured from the blank vial and time points and 1mL samples were taken at 12 and 24 hours. The collected samples were assayed in duplicate by HPLC.

3.3.2 8 Distribution Partition Coefficient measurements

This experiment was conducted in a similar manner described in 3.3.2.7. The model drug, ibuprofen, was exposed to R_T 13mM HCl at pH 2.00, 50mM acetate at pH 5.00, 50mM phosphate at pH 6.50, and 39mM NaOH at pH 12.00.

3.3.2 9 Non-ionized thermodynamic solubility determination at 37°C

Five 1.5mL centrifuge tubes were labeled and prepared with 1mL of the appropriate non-ionizing buffer (see Table 3-5). Solid drug in powder form was added to each individual vial and then vortexed. The addition of drug and vortex mixing was repeated until there was visible undissolved drug powder present. The centrifuge tubes were then put into a hot box where they remained at an aqueous temperature of 37°C (set point 43°C). The internal temperature was determined by measuring the temperature of a "blank" tube in the rack. Once the internal temperature reached 37°C, the tubes were held at 37°C for 48 hours. The tubes were removed from the hot box and centrifuged at 17,000G for 3 hours. The tubes cooled below 37°C during the centrifugation so the tubes were re-inserted into the hot box and allowed to reach 37°C over the course of 1 hour. Supernatant was then extracted directly from the tube in the hot box without disturbing the pellet. The supernatant was appropriately diluted for HPLC analysis. The limit of quantification and limit of detection were calculated to ensure the validity of the dilution scheme.

3.3.2 10 Rotating membrane diffusion cell experiments

Thickness of the sample membrane was measured using a caliper at the center of the membrane and then at four additional points within the circumference of the membrane in the region which was exposed to the drug saturated aqueous phase. The initial mass of the membrane was weighed prior to drug exposure. A recirculating bath warmed the beaker containing the donor aqueous suspension (sodium dodecyl sulfate 0.9mM) of drug to 37°C. A rotating membrane diffusion cell was utilized, as shown in Figure 3-1.[54] Seventy mL of the appropriate receiver phase was then added into the inner chamber of the diffusion cell. This receiver phase was a medium that ionizes the drug once drug passes completely through the

membrane, creating sink conditions and preventing reverse transport. For drugs that were non-ionizable, the receiver phase and donor phase were compositionally equivalent except for any surfactant and drug, which was solely present in the donor phase. The dip probe was calibrated in situ for each experiment and recorded one measurement every 60 seconds (five spectra averaged per measurement). Donor phase volume of 250mL was added to the warmed jacketed beaker, and then raised into contact with the diffusion cell. Air that was present in between the membrane and the aqueous phase was removed using a syringe. The diffusion cell was rotated at 150RPM during the experiment. An additional procedure was used for permeation measurements of metoprolol tartrate as this compound is a salt form of the drug metoprolol. Tartrate salt is acidic and upon dissociation in the aqueous environment, the pH will undergo an acidic shift. To maintain intrinsic pH, the donor phase was monitored in real time with a pH dip probe and the pH was maintained at pH = 12 by titrating 2N sodium hydroxide.

3.3.2 11 Positron Annihilation Lifetime Spectroscopy (PALS)

Radioactive ^{22}Na deposited and sealed in a thin kapton film was used as the positron source. This source was placed between two 41mm x 41mm x 1.3mm sheets of PDMS. This configuration was found to effectively stop the majority of positrons (excluding the 8% stopped in the kapton film) in the sample PDMS. Lifetime measurements were initially taken in both air and vacuum. There was a lower event acquisition rate in the vacuum setup due to the increased distance necessary to fit the vacuum chamber between the detectors. With the ability to mathematically compensate for the pick-off annihilation, the characterization of the free volume voids was primarily run in air at and above 20°C, while the sub 20°C was run under vacuum.

The lifetime of the particle called positronium (Ps) is most important in analyzing the pore properties of PDMS. Ps is analogous to a hydrogen atom, but with no nucleus and a positron (anti-matter electron) that orbits with an electron in a triplet state energy configuration. Since Ps can trap in open volume voids this positronium is directly sensitive to the pore size in which it resides. The other two short lifetimes are related to singlet Ps and positrons that annihilate with an electron without forming Ps and will not be considered further. All fitting of the PALS spectra were done using a customized version of the Posfit program.[91]

PDMS membranes were not returned into hexane to remove any non-crosslinked material nor did was the cured membrane put into vacuum to attempt to remove any latent hexane as proposed in other papers.[88] However, high vacuum was used during a PALS measurement to see if there was any change in the lifetime as any hexane was "extracted" from the membrane. There was no irreversible change in positronium lifetime when the vacuum and air samples (after compensating for known air effects on the positronium life, data not shown) were compared.

3.3.2 12 PALS thermal expansion series

A PDMS membrane was sectioned for PALS analysis. The R_T positronium lifetime was measured. The same sample was then heated to a target temperature and held at that temperature until sufficient data was gathered for a positronium measurement at the target temperature. The same sample was then brought back to R_T, where the positronium lifetime was measured again. This cycle was repeated until all the temperature values were measured. For measurements at cryogenic temperatures, the sample was cycled between R_T & -230°C with data taken at selected temperatures in between.

3.3.2 13 Error bars

All error bars are reported as the standard error of the mean unless n < 5, in which no summary statistic is given (mean, SEM).

3.4 Results & Discussion

3.4.1 Paracellular Type (Pore) Drug Transport in PDMS

Pore transport in PDMS was measured by PALS to evaluate whether pores play a significant role in the overall conduction of drug molecules from donor to receiver phases. Positron Annihilation Spectroscopy has been used for 40-50 years to characterize single vacancies and vacancy clusters. Positronium Annihilation Lifetime spectroscopy (PsALS or PALS), over the same time course, has been used to measure sub-nanometer and intermolecular voids in polymers, making this technique a robust method for probing the porous part of the PDMS polymer network. When a positron is injected into materials, it will eventually annihilate with an electron with the complete conversion of the pair's combined mass, m, into high-energy photons with total energy E, given by Einstein's famous formula $E = mc^2$. There are two types of particles that are examined during PALS analysis, free positron annihilation (with electrons in the target material) and Positronium (Ps) annihilation. Both positrons and Ps seek out and localize in vacancies/voids in metals and insulators. Simple coulomb attraction forces positrons into electron-decorated vacancies in metals, whereas in insulators the reduced dielectric interaction in a void energetically favors trapping neutral Ps in low-density regions. Ps has two states, singlet (para-) and triplet (ortho-), depending on the relative spin state of the positron and electron. The self-annihilation lifetime of para-Ps is short, 125 ps, and this rapid singlet annihilation occurs with the emission of two back-to-back gamma rays of 511 keV. However, ortho-Ps (o-Ps) in vacuum is required to annihilate

into at least three photons to conserve angular momentum, and this slower, triplet process has a long, characteristic lifetime of 142 ns. Lifetime spectroscopy can easily distinguish this long-lived triplet state of Ps; therefore o-Ps plays the key role in probing porous materials.[91, 92]

To determine whether the voids in PDMS form an interconnected porous network or are isolated voids a "beam PALS" spectrometer, in which a low energy focused beam of positrons is used to shallowly implant positrons and form Ps close to the PDMS sample surface, was used to resolve pore connectivity.[91] Ps can diffuse in an interconnected porous network and escape into vacuum producing a readily distinguishable 140 ns lifetime component. Using beam energies (mean positron implant depths) of 1.2 keV (40 nm), 3.2 keV (180 nm) and 4.2keV (280 nm), the telltale 140 ns vacuum component was not found, indicating no Ps diffusion. It is conclusive that the voids of PDMS are isolated. Positronium lifetimes were converted into a spherical pore diameter over the range of interest using the time-honored Tao-Eldrup model (assuming a simple spherical pore model).[91, 93, 94] In Figure 3-3, the ability to detect very small changes in void size by positronium PALS is demonstrated by measuring the void size in the membrane at different temperatures. The result of which is that physical changes in PDMS, such as thermal expansion transition points can be easily detected using PALS.

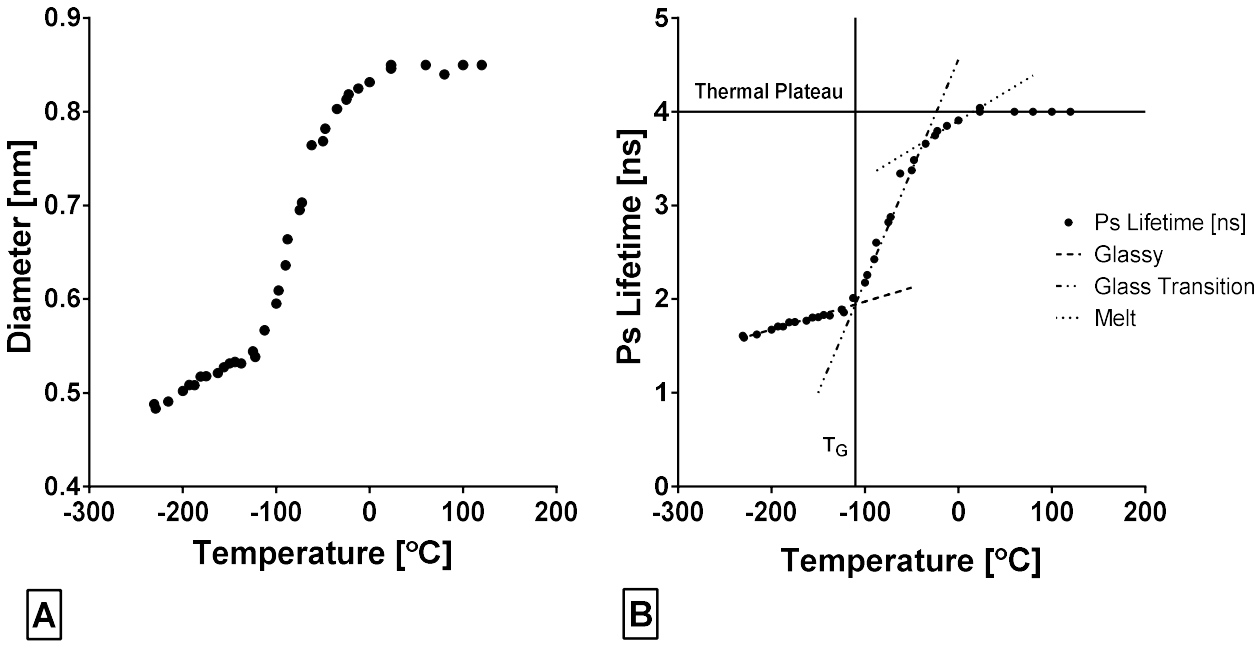

Figure 3-3 Thermal Expansion of Free Volume Pore Structure in PMDS.

A) Measuring the PDMS pore diameter as a function of temperature it is demonstrated that very small changes in void morphology can be accurately measured. **B)** The temperature was cycled between RT and the target temperature, to see if there is any evidence of permanent thermal history. PDMS recovered both R_T Ps lifetime and signal intensity after being exposed to different temperatures. Four distinct regions were fit; -240°C to -122°C (glassy), T_G = -110°C ± 8°C; -100°C to -47.5°C (glass transition region), T_{melt} = -44°C ± 7°C; -25°C to 25°C (rubbery plateau/flow); 25°C to 150°C (viscous flow); The flat region is actual a thermal plateau that originates from the competitive phenomena of linear thermal expansion of the pore and increased oscillation of the pore due to increased thermal energy. The Ps particle will be annihilated upon the pore contracting during an inward oscillation so the true maximum pore size cannot truly be measured. This is typically described as the "roll-over" region. It was assumed that any changes in the morphological structure caused during experimentation would be detectable, but it is recognized that future experiments should be done at lower temperatures for clearer results. The application of this system, to replicate human body temperatures, requires that analysis is conducted at 37°C. The PALS measured T_G and T_m are consistent with [87] & [95] respectively for PDMS. N = 1 membrane, 2-3x10^5 events on average per run at each temperature.

To see whether drug accumulated in the pores of the membrane, PALS was used to measure a PDMS membrane before and after equilibrium partitioning with ibuprofen (Figure 3-4). Ibuprofen was chosen as a model drug because of its high lipophilicity and the ability

to measure the difference in mass of drug in the membrane before and after the partitioning experiment. There was no statistical difference in the positronium lifetimes, but there was a 1.76mg ± 0.12mg (n = 7) mass increase in 25% by mass curing agent PDMS membranes, and a 2.90mg ± 0.38mg (n = 6) mass increase in 3.2% by mass curing agent PDMS membranes. This mass increase agrees with the measured partition coefficient for ibuprofen in PDMS.

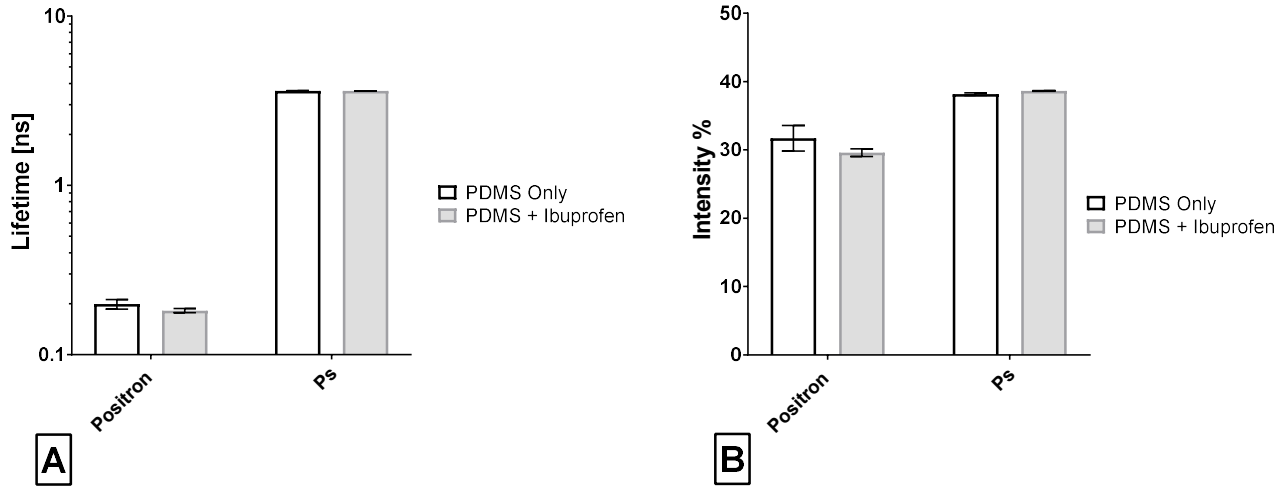

Figure 3-4 Ibuprofen accumulation in the Free volume pores.

A) The primary goal in utilizing PDMS was to partition drug molecules from drug and drug product containing phase into a reservoir compartment at magnitudes comparable to rates observed in humans. At equilibrium partitioning, it was hypothesized that drug or other components that partition into the membrane may accumulate in the PDMS pores thereby affecting the Ps lifetime. A highly lipophilic drug, ibuprofen, was chosen because a large amount of drug would be retained by the membrane, increasing the probability that a change in the lifetime could be observed. A change in Ps lifetime was not observed. **B)** A statistical change was observed in the positron lifetime. It is unclear if this change is physically significant to the authors. N = 1 membrane per condition, 3-5x10^6 events on average per run.

3.4.2 Transcellular Type (Bulk) Drug Transport in PDMS

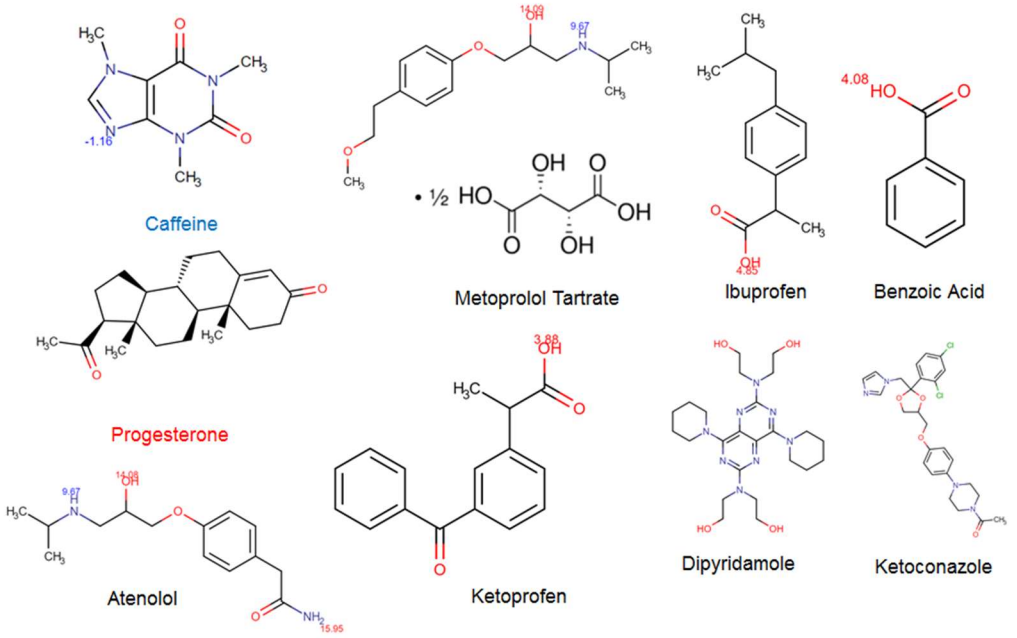

Figure 3-5 Nine molecular probes used to study the partition coefficient and diffusion coefficient in PDMS.

3.4.2 1 Partitioning of Molecular Probes into PDMS

Bulk transport properties of PDMS were measured to evaluate PDMS fitness for the mimicking human oral absorption. The partition coefficient was calculated according to Equation 3.4.

$$K = \frac{C_m{}^*}{C_{Aq}{}^*} \qquad \text{Eq (3.4)}$$

The first study conducted was to determine if process variations in fabrication would lead to differences in the equilibrium partition of the model drug, ibuprofen (Figure 3-6**-A)**. Four different mass % of curing agents (4.9%, 9.1%, 16%, and 25%) were examined at two different pH conditions (2.00 HCl 13mM & 6.50 phosphate 50mM). The $\text{LogD}_{\text{PDMS}}$ was

measured as a function of pH at pH 2.00, 5.00, 6.45, and 12.00 using 13mM HCl, 50mM acetate, 50mM phosphate, and 39mM NaOH buffers, respectively, at R_T (Figure 3-6-**C**).

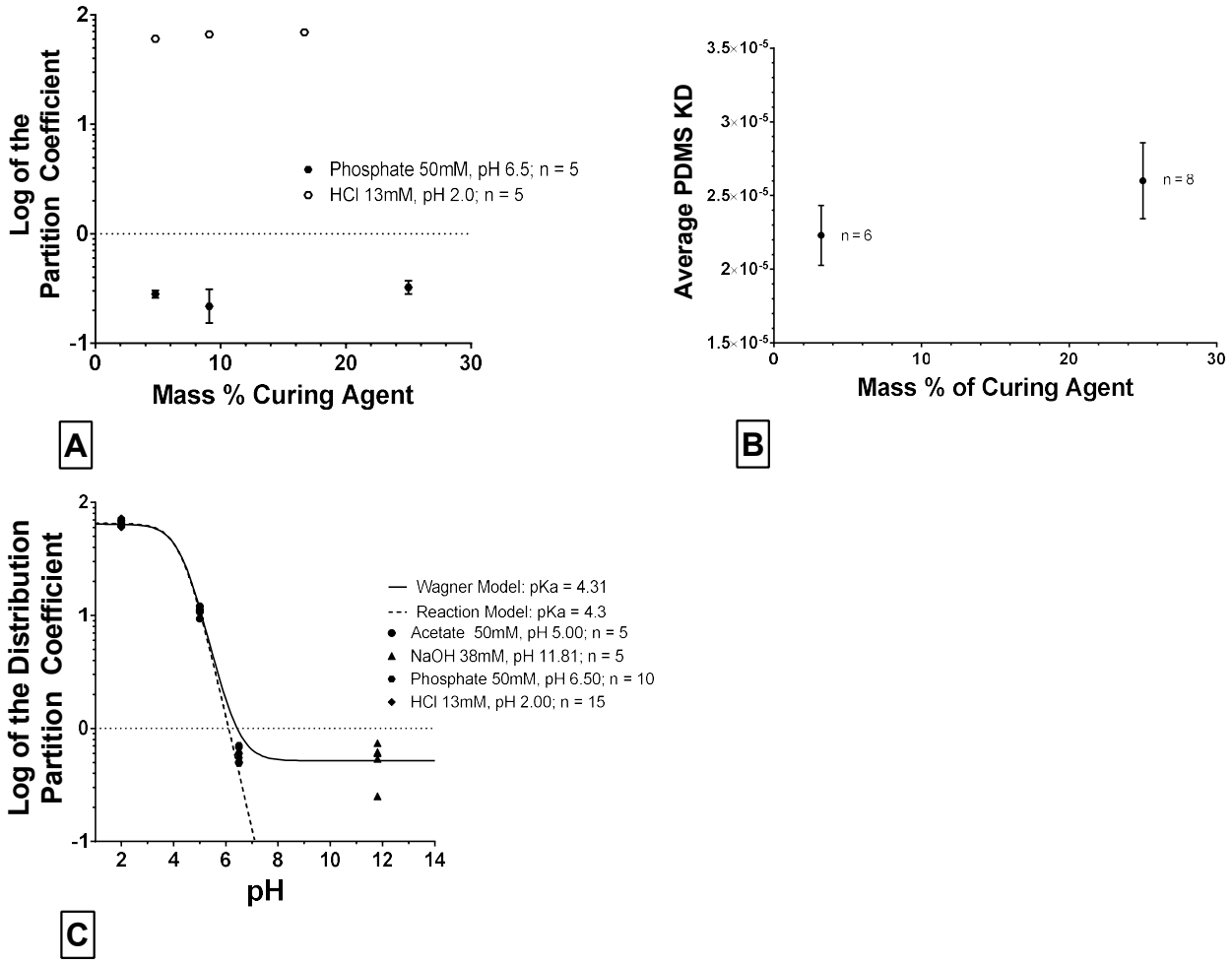

Figure 3-6 Membrane fabrication variability on Partition and Diffusion Coefficient/pH distributed Partition Coefficient for Ibuprofen in PDMS.

A) pH distributed partition coefficients in pH 2.0 HCl buffer and pH 6.50 50mM phosphate buffer with model drug ibuprofen. Three different concentrations of curing agent in membranes were measured to see if the curing agent provided any lipophilic difference to the final cured membrane. There was no practical difference between the partition coefficient of the varied concentration of curing agent in the membranes. N = 5 membranes per curing agent condition per pH condition. N_{total} = 30. **B)** Varying the amount of curing agent of PDMS was hypothesized to be a simple method to modulate the permeability and add another mechanism of permeation control. The extreme concentrations of curing agent were used to elucidate differences in the permeability behavior. There was a statistical difference according to a two tailed t-test ($p < 0.02$) with N = 6 for the low extreme concentration of 3.2% and N = 8 for the high extreme concentration of curing agent. However, the practical difference in the context of the ivR methodology is negligible. This also implies that permeability will not be significantly affected by minor process variations during fabrication. The permeand was the model drug, ibuprofen under intrinsic non-ionizing conditions (pH = 2.0 HCl) with receiver phase pH 6.5 50mM phosphate, 37°C, 150RPM in the rotating diffusion cell. **C)** Distribution partition coefficient experiments were conducted confirm that Equation 3.5-3.6 were valid in PDMS. These equations are useful in predicting absorption rate over a range of pH.

The LogD relationship is given in Equation 3.5 for a monoprotic acid (model 1).[96] In Table 3-3the LogD was also calculated using the Wagner model which accounts for ionized drug partitioning (Equation 3.6, model 2) and the pKa of ibuprofen was back calculated to confirm the validity of the fit for both models (for model 2, equation 3.8 was used to transform the shifted pKa from Equation 3.6 back to the true pKa).[97]

Model 1:

$$logD = logK_{N-I} - log(10^{pH-p} \quad + 1) \qquad \text{Eq (3.5)}$$

Model 2:

$$logD = log(P_{N-I}f_E) = log\left[P_{N-I}\frac{f_{N-I}P_{N-I}+(1-f_{N-I})P_I}{1+f_{N-I}P_{N-I}+(1-f_{N-I})P_I}\right] \qquad \text{Eq (3.6)}$$

$$f_{N-I} = \frac{1}{1+10^{pH-pK}} \qquad \text{Eq (3.7)}$$

$$pH_{from\ fit} = pKa_{actual} - log(P_{N-I} - 1) \qquad \text{Eq (3.8)}$$

Where $pH_{from\ fit}$ is input pKa in the LogD equation and pKa_{actual} is the un-shifted pKa from fit, the true pKa of the molecule

Table 3-3 Comparing the reaction model and the Wagner model, for estimating the distribution of partition coefficients as a function of pH, also used to predict the pKa of Ibuprofen using PDMS.

Ibuprofen pKa			**Measured PDMS**			
Lit. pKa value	**Model 1**	**Model 2**	**$LogP_u$ ± SE**	**$LogP_i^{I}$ ± SE**	**P_u ± SE**	**$P_{i\ Eq.\ 6}^{II/III}$**
4.4[5]	4.3	4.31	1.81 ± 0.01 N = 15	-0.286 ± 0.080 N = 15	65 ± 1.05 N = 15	0.008

[I]experimentally determined at pH 11.81

[II]using the experimental data at pH 11.81 and fu ~ 0, Pi was calculated to fit equation 3.6

[III]In later work (chapter 5) the intrinsic ionized partition coefficient was measured to be 0.245. This table is published in [81] prior to the preparation of this dissertation.

Since permeability is a function of the partition coefficient (**Equation 3.9**), generally

$$P = \frac{KD}{h} \qquad \text{Eq (3.9)}$$

it was important to see if the partition coefficient could be predicted for any drug in PDMS. A simple correlation was created between the predicted partition coefficient of drugs

in the octanol-water system (the standard reference system for partitioning) and the PDMS system. Figure 3-7 suggests that a linear correlation can be used to translate the well-established octanol-water partition coefficients to the PDMS system. Ketoprofen consistently deviated from the expected lipophilicity correlation. *In vivo*, ketoprofen has a large human GI permeability even though its pKa (3.89) is lower than ibuprofen (4.4).[5, 83] Based on ketoprofen's pKa alone, it would be expected that it would be more ionized in the human GI than ibuprofen thus less well absorbed. This suggests that ketoprofen's lipophilicity is high enough to drive the drug across the human GI membrane as explained by Wagner et al.[97] However, it is possible that the deviation in PDMS partitioning comes from ketoprofen's high polar surface area. Due to the methyl groups that decorate the backbone of PDMS, the polar-non-polar interaction at the solid-liquid interface would be stronger for molecules that have a more polar surface area.

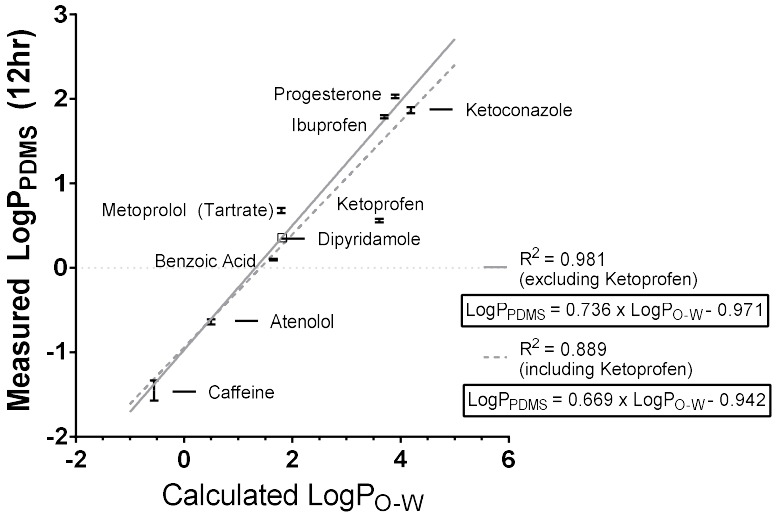

Figure 3-7 Octanol-Water to PDMS Partition Coefficient Correlation Curve.

A correlation of the predicted octanol-water intrinsic non-ionized partition coefficient and the measured PDMS intrinsic non-ionized partition coefficient. It was determined that there was no practical difference between the partitioning of most drugs into the PDMS membrane at 12 and 24 hours, in which the 12-hour time point more accurately represents "equilibrium" in the context of the time scale for typical human GI motility patterns. Partition coefficient was calculated using equation 7. N = 5 membranes per drug except dipyridamole where N = 1. N_{total} = 41.

3.4.2 2 Diffusion of Molecular probes through PDMS Membranes

Membrane permeability was calculated from the linear slope of the concentration vs time curve for each experiment. This pseudo steady-state linear region was determined by calculating the linear regression coefficient of the slope and optimizing the range to achieve a R^2 as close to 1 as possible. The slope of this line, when multiplied with the receiver volume, gave the mass transfer coefficient (Equation 3.10).

$$\dot{m} = m_{pseudo-steady} \times V_R \quad \text{Eq (3.10)}$$

Where $\dot{m}$ = mass transfer coefficient [µg s^{-1}]; $m_{pseudo\text{-}steady}$ = slope of concentration vs time plot in the pseudo-steady state region [µg mL^{-1} s^{-1})]. The effective permeability was calculated using permeability layer theory (Equation 3.11) and as a check, diffusion coefficient was calculated using Crank's uniform initial distribution & surface concentration different for diffusion in a plane sheet (Equation 3.9, 3.12-13).[98] Permeability layer theory considers every layer in the diffusion system (solid and liquid interfaces), while Crank's approach examines diffusion only within the membrane itself.

$$\frac{1}{P_{eff}} = \frac{A_m(S)}{\dot{m}} \quad \text{Eq (3.11)}$$

$$Q_T = \frac{DC_2}{h}\left(t - \frac{(h)^2}{6D}\right) \quad \text{Eq (3.12)}$$

$$D = \frac{Q_T h}{C_2} \quad \text{Eq (3.13)}$$

Where C_2 = concentration of the molecule at the inner surface of the membrane ($C_{aq\ total}$ * K) [µg cm^{-3}] and t = time [s]. The membrane permeability from permeability layer theory is Equation 3.14 and Crank's membrane permeability is Equation 3.15.

$$\left[\frac{A_m \times S}{\frac{dC}{dt} \times V_R} - \frac{h_{Aq}}{D_{Aq}}\right]^{-1} = P_{PDMS} \quad \text{Eq (3.14)}$$

$$\frac{\frac{dC}{dt} \times V_R}{\frac{A_m}{C_2}} = \left(\frac{Q_T}{K \times C_{aq}}\right) = P_{PDMS} \quad \text{Eq (3.15)}$$

The difference in the permeability when the aqueous boundary permeation is assumed to be of negligible importance and when the contribution is accounted for was examined. For drugs with a $LogK_{PDMS} \leq 1.5$ the permeability difference is ≤ 10% and for higher partitioning drugs ($1.5 < LogK_{PDMS} < 2.1$) results were found to have up to a 25% difference. The lag time (time to steady state transport) was calculated by solving the pseudo-steady state linear regression equation for Y = 0, where Y = concentration and X = time. This lag time can be predicted by Equation 3.16. [98, 99]

To derive the time to pseudo steady state first

$$Q_T = \frac{dc}{dt}\frac{V}{A} = \frac{DC_2}{h}\left(t - \frac{h^2}{6D}\right) \quad \text{Eq (3.16)}$$

$$Q_T = \frac{DC_2}{h}\left(t - \frac{h^2}{6D}\right) \equiv y = mx + b \quad \text{Eq (3.17)}$$

$$where\ y = Q_T; m = \frac{DC_2}{h}; and\ b = -\frac{DC_2}{h}\frac{h^2}{6D} \quad \text{Eq (3.18)}$$

If we take the limit of Q_T as t → infinity

$$\lim_{t\to\infty} Q_T = \left(\frac{DC_2}{h}t - \frac{C_2 h}{6}\right) \quad \text{Eq (3.19)}$$

The behavior of the equation is dominated by the slope of the line, so the steady steady transport behavior is described as

$$Q_T = \frac{DC_2}{h} \quad \text{Eq (3.20)}$$

$$D = \frac{Q_T h}{C_2} \quad \text{Eq (3.21)}$$

The unit analysis of equation 3.21 above confirms that D has the correct units.

$$D = \frac{Q_T h}{C_2} \equiv \frac{\left[\frac{g}{cm^3 s}\right]\left[cm^3\right]}{\left[\frac{g}{cm^3}\right]}[cm] = \frac{\left[\frac{g}{s}\right]\frac{[1]}{[cm]}}{\left[\frac{g}{cm^3}\right]} = \left[\frac{g}{s}\right]\left[\frac{cm^3}{g}\right]\frac{1}{[cm]} = \left[\frac{1}{s}\right]\left[\frac{cm^2}{1}\right]\frac{1}{1} = \left[\frac{cm^2}{s}\right] \quad \text{Eq (3.22)}$$

Now time to steady state can be derived.

$$\frac{dc}{dt}\frac{V}{A} = \frac{DC_2}{h}\left(t - \frac{h^2}{6D}\right) \quad \text{Eq (3.23)}$$

$$\frac{dc}{dt}\frac{V}{A} = \left(\frac{DC_2}{h}t - \frac{DC_2}{h}\frac{h^2}{6D}\right) \quad \text{Eq (3.24)}$$

$$\frac{dc}{dt}\frac{V}{A} = \left(\frac{DC_2}{h}t - \frac{C_2}{1}\frac{h}{6}\right) \quad \text{Eq (3.25)}$$

$$0 = \left(\frac{DC_2}{h}t - \frac{C_2}{1}\frac{h}{6}\right) \quad \text{Eq (3.26)}$$

$$\frac{DC_2}{h}t = \frac{C_2 h}{6} \quad \text{Eq (3.27)}$$

$$\frac{DC_2}{h}t = \frac{C_2 h}{6} \quad \text{Eq (3.28)}$$

$$t = \frac{C_2 h}{6}\frac{h}{DC_2} \quad \text{Eq (3.29)}$$

$$t = \frac{h^2}{6D} \quad \text{Eq (3.30)}$$

To calculate t from experimental quantities, substitute equation x into equation x…

$$t = \frac{h^2}{6D} = \frac{h^2 C_2}{6Q_T h} = \frac{h(KS)}{6\frac{dcV}{dtA}} = \frac{h(KS)A}{6\frac{dc}{dt}V} \equiv \frac{[cm]\left[\frac{g}{cm^3}\right][cm^2]}{\left[\frac{g}{cm^3 s}\right][cm^3]} = \frac{1\left[\frac{g}{1}\right][1]}{\left[\frac{g}{s}\right][1]} = [s] \quad \text{Eq (3.31)}$$

Where $t_{pseudo\text{-}s.s.}$ is the time to pseudo steady state transport [s]. This measurement is highly sensitive to the measured values of partition coefficient, diffusion coefficient within the membrane, and solubility. It is key to determine these as accurately as possible to achieve valid predictions. In table 5 in Sinko et al. 2017 there was a mistake in reporting the time to steady state transport calculations. In this dissertation, the times have been corrected in Table 3-6.

It was hypothesized that modulating the elastic modulus of PDMS could modulate the drug permeability. Figure 3-6-B and Table 3-4 show that the difference in permeability when the curing agent (and by association, Elastic modulus) is varied. There is a statistical difference in permeability between membranes with 3.2% and 25% by mass curing agent, but in practice is of negligible importance. This is most likely because PDMS is in the viscous flow regime at 37°C, making backbone chain movement relatively easy to accommodate diffusing species. The permeation data is presented as the K x D product (P x h). This eliminates experimental variability from the membrane thickness and allows for more accurate comparisons of permeability with the added benefit of permeation prediction at any membrane thickness. Additionally, the apparent diffusion coefficient through the silastic membranes, such as PDMS, is reported in the literature as the product of the intrinsic

diffusion coefficient of the drug through the polymer network and the apparent partition coefficient of the uncharged species between the solvent and the membrane. Knowledge of the partition coefficient should permit for prediction of the relative diffusion through PDMS membranes.[90] So, the K x D product can be thought of as both the diffusivity of molecule through PDMS and a normalized by thickness permeability.

Table 3-4 The tabulated results of the two-tailed t-test to determine if the null hypothesis (no difference in the permeation between the 3.2% and 25%w/w curing agent membranes) was valid. The null hypothesis is rejected based on the t-statistic, however the practical difference in permeation is negligible for the intended application of *iv*R absorption.

Composition [mass%]	**Average K x D [x10^{-5}cm^2 s^{-1}]**	**Total Standard Error [x10^{-6}cm^2 s^{-1}]**	**Two Tail T-Test Statistic**	**p -value 0.0103**
25	2.60 N = 8	2.58 N = 8	-3.04	df = 12 (11.9)
3.2	2.23 N = 6	2.03 N = 6		98.97% confidence to reject null hypothesis

The K x D product was measured for the same set of drugs for which the partition coefficient was measured (Figure 3-8-A and **Equation 3.32**).

$$K \times D_{PDMS} = 4.46 \times 10^{-8} \times e^{2.91 \times LogP_{PDMS}} \quad \text{Eq (3.32)}$$

$$K \times D_{PDMS} = 4.61 \times 10^{-6} \times \left(\frac{PSA}{K_{PDMS}}\right)^{-1.20} \quad \text{Eq (3.33)}$$

The permeation of model drug, ibuprofen, behaved per Equation 3.9 which demonstrates that permeability can be predicted over a wide range membrane thicknesses, as seen in Figure 3-8-B. The deviation of ketoprofen in the octanol-water partition coefficient to PDMS partition coefficient is not observed in the PDMS permeability vs PDMS partition coefficient correlation. Therefore, it possible that ketoprofen has a lower affinity for PDMS than octanol due its high polar surface area relative to its partition coefficient (Figure 3-8-C and **Equation 3.33**).

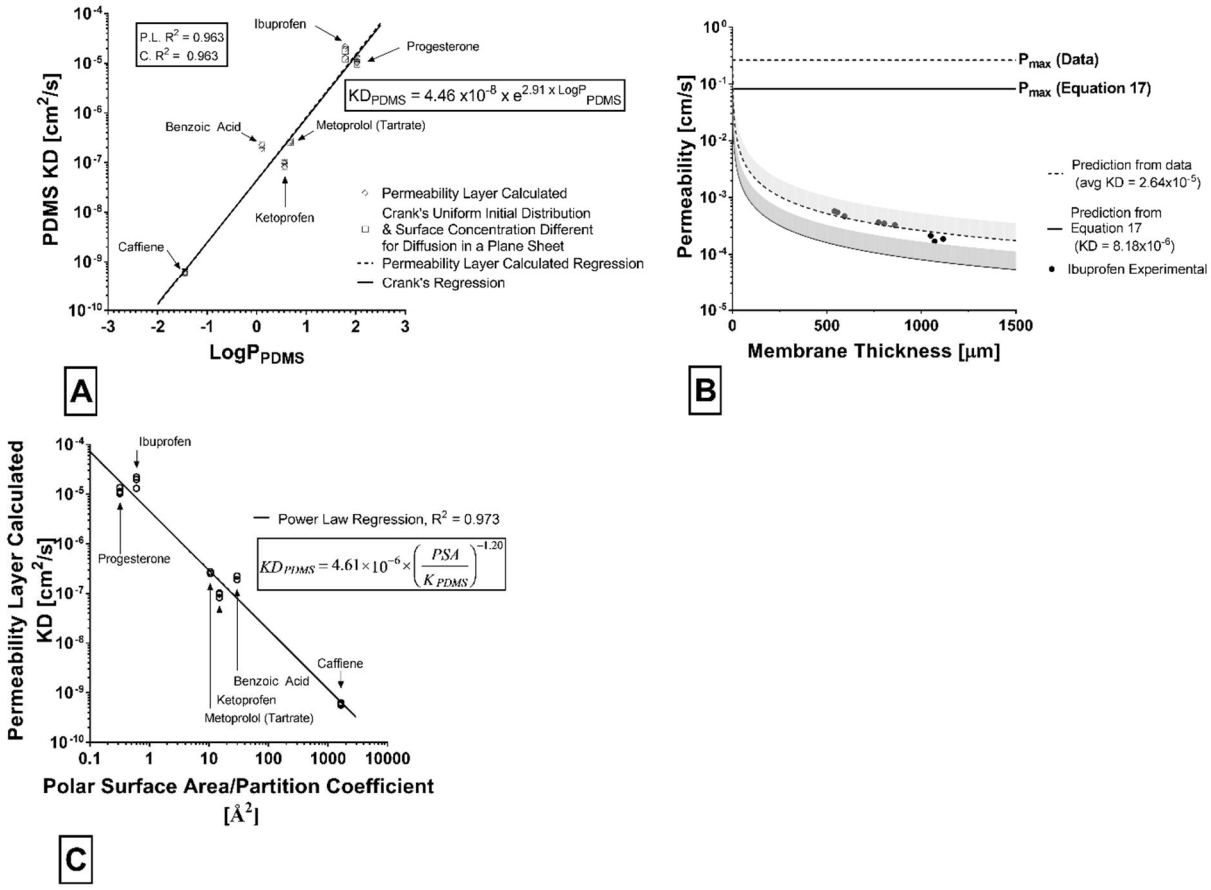

Figure 3-8 Transport Properties Correlations for PDMS.

A) The correlation between octanol-water & PDMS partitioning was established to allow for a prediction directly from the chemical structure to the permeation through a PDMS membrane at any nominal thickness. Looking at Figure 6 and Figure 7A, a clear path to an initial rational based dissolution-simultaneous absorption (ivR) experiment can be designed for any drug molecule. **B)** PDMS permeability scales with thickness ($1/h_{mem}$) and the permeability of a drug can be predicted from the K x D product at any thickness. The K x D product was calculated at each thickness and the average was used in P = (K x D)/h. N = 1 membrane per thickness (data). The K x D relationship measured in Figure 7A was used to predict ibuprofen-PDMS permeability (Equation 17). Ibuprofen under intrinsic non-ionizing conditions (pH = 2.0 HCl) with receiver phase pH 6.5 50mM phosphate, 37°C, 150RPM in the rotating diffusion cell. Gray bands on each trend indicate the positive 95% confidence interval. **C)** PDMS is resistant to transporting polar entities, and it was reasonable to suspect that the polar surface area of a molecule would influence the overall diffusivity of the species. PDMS diffusion is also a function of the molecule's lipophilicity towards PDMS. Ketoprofen deviates from the visually observable trend in Figure 6, but when the polar surface area is accounted for, ketoprofen aligns as expected. Based on the strong power law relationship, D_{PDMS} is inversely proportional to the molecules polar surface area.

In each permeation experiment, the donor phase containing drug was at a non-ionizing pH if the drug was ionizable and the receiver phase was at a completely ionizing (>99%) pH.

The the non-ionized thermodynamic solubility at 37°C value used in the permeation calculations were reported in Table 3-5. Progesterone solubility is reported twice, the second time as an analytical check. This check shows that the method used to determine solubility was unaffected by the amount of dilution used to obtain the solubility (diluted 3.5x and 10.5x respectively).

Table 3-5 For each rotating diffusion cell experiment, the donor side concentration was ~3x the solubility reported from drugbank.ca. The actual solubilities were then measured for each molecule in the donor solution conditions present during the permeation experiments. These solubility values were used in all permeation calculations. Metoprolol Tartrate solubility was not measured.

Drug	Dilution Factor	Non-Ionized Solubility [µg mL^{-1}]	Standard Error [µg mL^{-1}]
Ibuprofen	N = 5 Rep = 2	60 I	1.18
Ketoprofen	N = 5 Rep = 2	147 I	2.3
Benzoic Acid	N = 5 Rep = 2	69.8x10^{2} I	2.31x10^{2}
Caffeine	N = 3 Rep = 2	47.0x10^{3} II	0.332x10^{3}
Progesterone	N = 4 Rep = 2	21.3 I	0.26
Progesterone (Analy. Comp.)	N = 4 Rep =2	20.9 I	0.21

I = pH 2.00 13mM hydrochloric acid buffer at 37°C
II = pH 6.45 50mM phosphate buffer at 37°C
N = number of individual samples
Rep = number of times replicated

Table 3-6 shows the experimentally measured permeability, diffusion coefficient, lag time, and experimental conditions used to generate them for each drug. These permeability measurements are in the intrinsic ionization state (completely non-ionized), and it is expected for *iv*R testing to occur at pH values where many drugs will have some fraction of ionized molecules. The Wagner models and Winne models for pH dependent absorption

show that significant absorption occurs *in vivo* even under pH conditions were there is a large fraction of ionized drug.[97, 100] However, from a characterization standpoint the use of the relationship between $LogK_{PDMS}$ and PDMS permeability is valid for any $LogD_{PDMS}$. An experimental compound may be partially ionized under physiologic pH conditions, but if the $LogD_{PDMS}$ can be measured or predicted, so can the correct PDMS permeability. PDMS reflects the *in vivo* situation, where ionized drug is present in the absorption pathway and absorption rate will be a function of pH. A quantitative analysis of the relationship between pH and absorption rate will be presented in chapter 5.

Table 3-6 The tabulated results of the rotating diffusion cell experiments.

The average membrane thickness, average PDMS permeability, and average PDMS KD are calculated as discussed. The partition independent diffusion coefficient was calculated by dividing the average PDMS KD by the 10^{LogK} for PDMS. To compare the diffusivities in the polymer with the aqueous, the Hayduk-Laudie diffusion coefficient was calculated.[101] Lag times were measured using linear regression of the concentration vs time profile and represent the time to steady state transport. The predicted lag times from Crank's method (Equation 3.30).

Drug	Donor / Receiver Buffer	Avg. Membrane Thick. [μm]	Avg. PDMS Perm. [cm s^{-1}]	Avg. PDMS (K*D) [cm^2 s^{-1}]	Partition Indep. Diff. Coeff. (K*D)/$10^{LogK_{PDMS}}$ [cm^2 s^{-1}]	Aqueous Hayduk-Laudie Diff. Coeff. [cm^2 s^{-1}]	PDMS LogK	Lag Time (exp.) [min]	Lag Time (pred.) [min] [IV]	$\frac{t_{Lag_{pred.}}}{t_{Lag_{exp.}}}$ [IV]
Ibuprofen	I/III	651 N = 3	2.82×10^{-4} N = 3	1.83×10^{-5} N = 3	2.404×10^{-7} N = 3	8.41×10^{-6}	1.81 N = 5	68 N = 3	55 N = 3	0.9 N = 3
Progesterone	I/III	662 N = 4	1.73×10^{-4} N = 4	1.14×10^{-5} N = 4	1.07×10^{-7} N = 4	6.72×10^{-6}	2.03 N = 5	115 N = 4	125 N = 4	1.09 N = 4
Benzoic Acid	I/III	676 N = 2	3.10×10^{-6} N = 2	2.08×10^{-7} N = 2	1.66×10^{-7} N = 2	1.28×10^{-5}	0.10 N = 5	25 N = 2	78 N = 2	3.04 N = 2
Ketoprofen	I/III	653 N = 3	1.45×10^{-6} N = 3	9.46×10^{-8} N = 3	2.58×10^{-8} N = 3	8.02×10^{-6}	0.56 N = 5	232 N = 3	460 N = 3	2.65 N = 3
Metoprolol Tartrate	II/III	502 N = 2	5.25×10^{-6} N = 2	2.64×10^{-7} N = 2	5.46×10^{-8} N = 2	7.20×10^{-6}	0.68 N = 5	161 N = 2	128 N = 2	0.79 N = 2
Caffeine	I/III	703 N = 3	8.59×10^{-9} N = 3	6.02×10^{-10} N = 3	1.70×10^{-8} N =3	9.63×10^{-6}	-1.45 N = 5	115 N = 3	808 N = 3	7.19 N = 3

I = pH 2.00 13mM hydrochloric acid buffer at 37°C
II = pH 12.00 39mM sodium hydroxide buffer at 37°C
III = pH 6.45 50mM phosphate buffer at 37°C
IV = Corrected mistake in published table to correct values

3.4.2 3 Mechanical Properties and Microstructural Analysis

At the onset of this work, it was hypothesized that the stiffness of the polymer (crosslinking) may govern the transport of drug molecules. Additionally, modulating the stiffness of the network was hypothesized to be a secondary method to modulating permeability in PDMS membranes. It was also necessary to understand the material's mechanical properties for fabrication of an *in vitro* absorption device. Before any mechanical testing was conducted, a study of the strain rate effect was conducted. The initial studies were performed in tension, but the material was found to be too soft for use in the testing cell. Therefore, all mechanical measurements presented in this report were completed in compression. Figure 3-9-A shows there is a minimal effect of strain rate on the elastic modulus of PDMS, and the smallest strain rate was used for the remainder of the mechanical testing (0.01mm/s). The aforementioned hypothesis was prompted by the data shown in [102], and the elastic modulus versus mass percent of curing agent experiment was recreated in Figure 3-9-B. This relationship was measured to examine the difference in the elastic modulus between hexane solubilized- drop cast PDMS produced in this work and PDMS created by simply mixing the two parts of the Sylgard 184 kit.[102] The PDMS produced by hexane homogenization was less stiff across all concentrations of curing agent as compared to the non-hexane method. Additionally, in the hexane casting method, there is an apparent critical point at which the addition of curing agent no longer enhances the elastic modulus. This was not demonstrated in the non-hexane method in [102]. Finally, the effect of curing temperature was measured to see if the

elastic modulus could be altered during curing. Figure 3-9-C suggests that a small increase in the elastic modulus can be achieved by curing at temperatures above R_T.

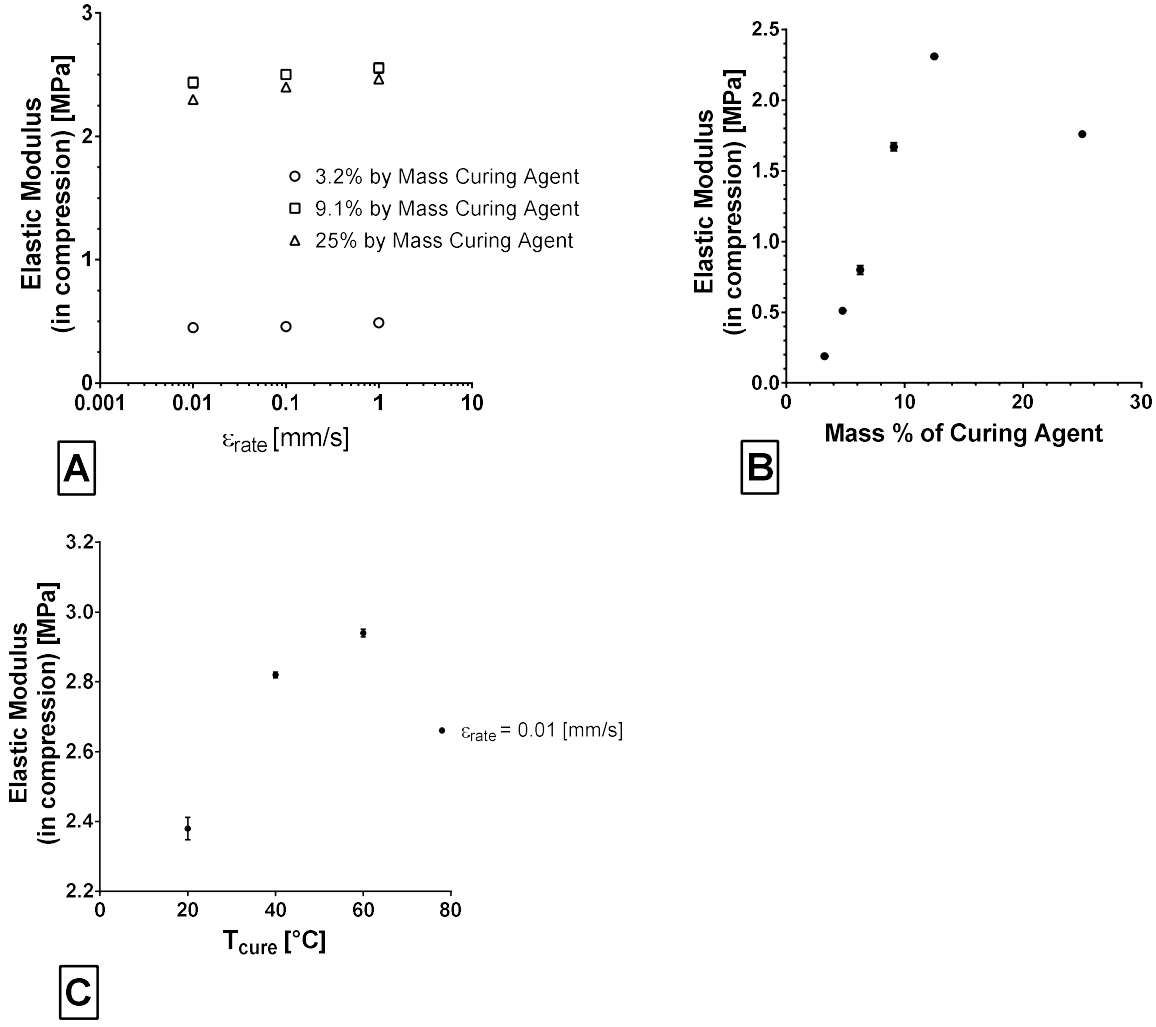

Figure 3-9 Mechanical Properties of Bulk PDMS.

A) Shows the effect of (0.01, 0.1, 1)mm/s strain rate on three different PDMS blends (25, 9.1, 3.2)% curing agent by mass or (3:1, 10:1, 30:1) Mass base : Mass Curing agent. It was determined that the smallest strain rate would be suitable for the remaining mechanical characterization. N = 5 per strain rate per PDMS blend. N_{total} = 45 **B)** When the concentration of curing agent is varied, the elastic modulus can be manipulated. This property is important for eventual processing & manufacturing of PDMS into thin hollow tubes or sheets for drug partitioning processes. PDMS made using the hexane drop-cast method, shows a similar trend observed in [102]. A critical point exists at which the addition of curing agent no longer stiffens the material. Comparing the overall magnitude of the elastic modulus between the simple mix and hexane drop cast method, hexane produces a lower elastic moduli polymer. N = 5 PDMS cylinders per concentration, L/D ~ 0.5. N_{total} = 30 **C)** PDMS was prepared in hexane and allowed to cure at various temperatures. PDMS can be made stiffer by increasing the cure temperature. These data are using 9.1% mass curing agent PDMS. N = 5 membrane cylinders per temperature, L/D ~0.5. N_{total} = 15.

To evaluate RT pore stability the PDMS void structure was quantified via PALs at 3, 103, and 193 days after casting (Figure 3-10-A), and no statistical change was observed in the positronium lifetime over this time course. For accelerated casting procedures (above 20-25°C and faster than 3-7 days), PDMS membranes were cured at 70°C to determine the effect elevated curing temperature had on the final R_T void structure. There was no change in the positronium lifetime between 20°C and 70°C cure temperatures (Figure 3-10-B). 70°C was chosen as the upper limit because that was the temperature at which hexane boils. Boiling hexane produces bubbles within the final cured membrane which was potentially undesirable. Membranes were cured at 60°C without significant bubbles forming. Finally, PALS was used to measure if a change occurred in the void structure due to process variation (Figure 3-10-C). The amount of curing agent was varied from 0% (pure base material) to 25% curing agent by mass. There was no statistical difference in the positronium lifetime in any composition measured.

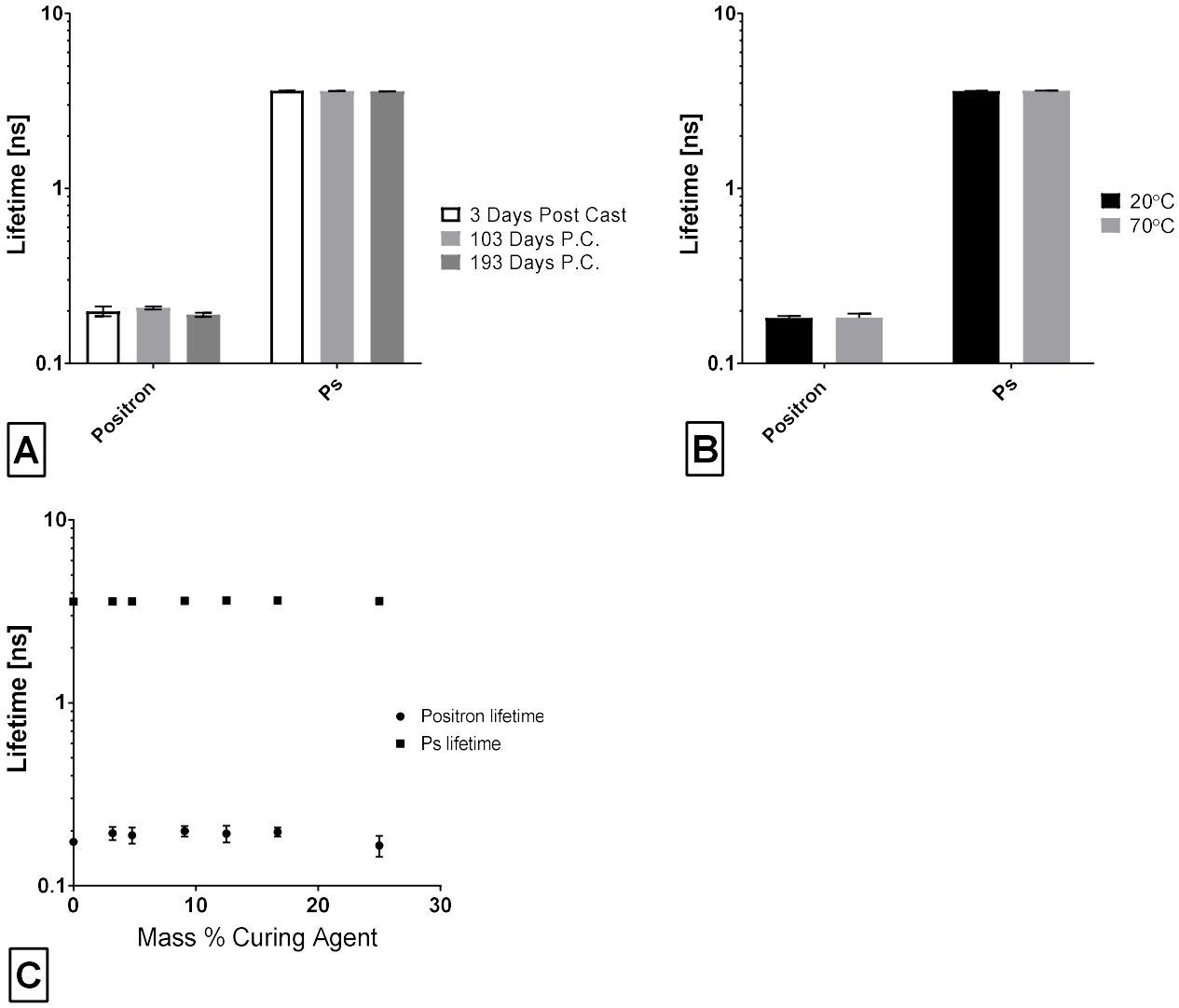

Figure 3-10 PALS Characterization of Potential Variation in PDMS Fabrication.

A) The void size was measured via Ps-ALS at R_T (20°C) to show that the void structure had long term stability. There was no statistical difference between pore sizes measured at 3 days and 193 days post-casting, 3-5x10^6 events on average per run. **B)** Higher curing temperature was examined to see if the pore structure formed at higher temperature was physically different than when cured at R_T. Using Ps lifetime as an analogue for pore size, the void structure was unaffected by the curing temperature. N = 1 membrane per temperature, 3-5x10^6 events on average per run **C)** To gauge the effect of process variability on the void structure, Ps lifetimes were measured over a wide range of mass% of curing agent. Where 0% is the neat base material in its viscous fluid state. There was no significant change in Ps lifetimes over the range of curing agent mass % studied. N = 1 PALS run per concentration, 3.6 - 7.2x10^5 events per run.

3.4.3 Latent Hexane and Possible Effect of Hexane on Mass Transport Through Poly(dimethyl siloxane)

A potential concern with using hexane as a solubilizing agent to create PDMS membranes is that hexane could be retained post fabrication and alter the permeability of the PDMS membrane. A gas-chromatography experiment was conducted to determine the amount of residual hexane remaining in a PDMS UTLAM within a day of coming out of the annealing oven.

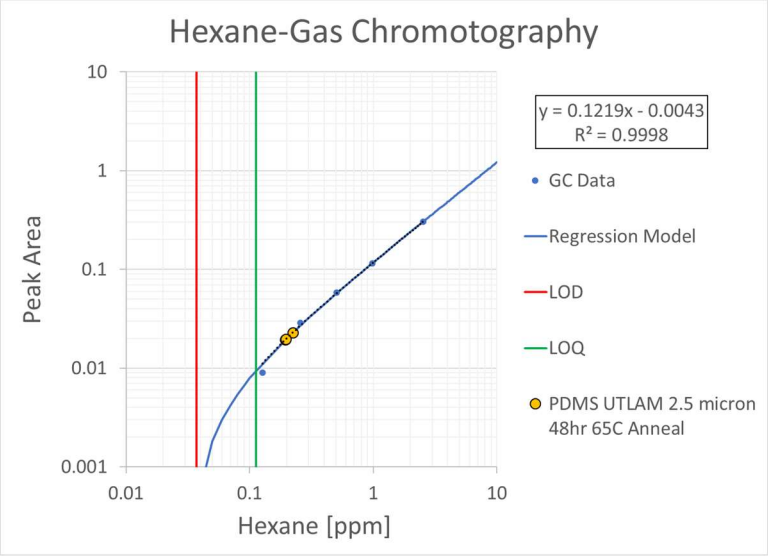

Figure 3-11 Latent Hexane in PDMS UTLAM.

Gas-Chromatography of hexane performed by Jennifer Walker. The standard curve's limit of detection and quantification were determined using standard methods. Measured hexane retained within the PDMS UTLAM were between the two lowest concentrations on the standard curve. Thank you Jenna Walker of the Steve Schwendeman laboratory at U-M for performing this measurement.

In Figure 3-11 standard curve was developed and then PDMS UTLAM samples were measured against the standard curve. It was determined that PDMS retained 5.75 nanogram of hexane per milligram of sample. The samples analyze had a mass of approximately 120mg, meaning that less than 1 microgram of hexane was retained

with the PDMS UTLAM. The sample was chosen because during fabrication it had the highest ratio of hexane to PDMS (producing the thinnest UTLAM).

The next study was to soak the PDMS membranes in hexane and other media and perform a diffusion experiment. The soaked membranes were weighed prior to insertion into the rotating diffusion cell, and post diffusion experiment. Soaking the PDMS membrane in hexane caused a drop in the pre-experimental mass of the PDMS membrane. This is likely due to the ability for hexane to swell the PDMS membrane (like a hydrogel) and remove any unreacted/non-crosslinked components. The mass of the membrane post diffusion experiment with ibuprofen shows that there is a still a net loss of mass from fabrication, however the loss decreases as ibuprofen accumulates in the membrane. In parallel to the hexane study, other liquids (octanol, decanol, silicon oil, and mineral oil) were studied to see if the PDMS membrane could be impregnated with another lipophilic phase to enhance flux performance.

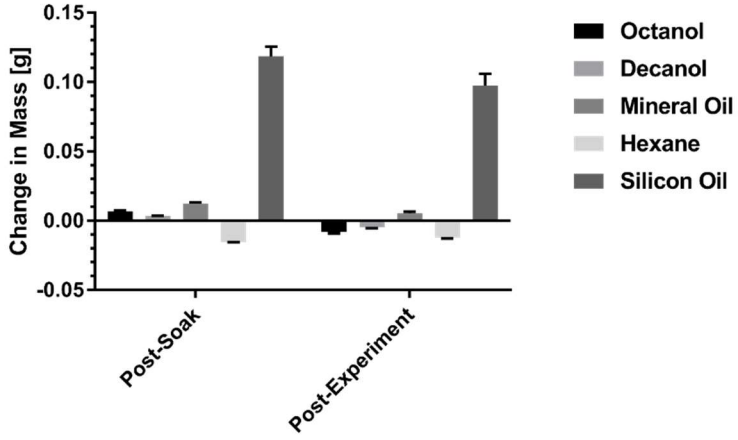

Figure 3-12 Partitioning of various lipophilic fluids into PDMS.

PDMS membranes (h_m > 100μm) were soaked in various fluids for 48 hours. The mass pre-soak, and post-soak were recorded. Membranes were lightly patted with a kimwipe to remove surface fluid before mass measurement. All fluids produce a $p < 0.01$ difference comparing the to the as fabricated PDMS membrane.

As seen in Figure 3-12, the the fluid that had the largest uptake into the PDMS membrane was silicon oil, yet the mass uptake was significant ($p < 0.01$) for all fluids. This is not entirely surprising as PDMS is an organophilic/lipophilic material. In Figure 3-13 below, the pseudo steady state flux of ibuprofen was measured for PDMS membranes soaked into the same fluids in Figure 3-12. The control sample was an as fabricated PDMS membrane, while the rest were soaked in the respective fluid for 48 hours prior to measurement.

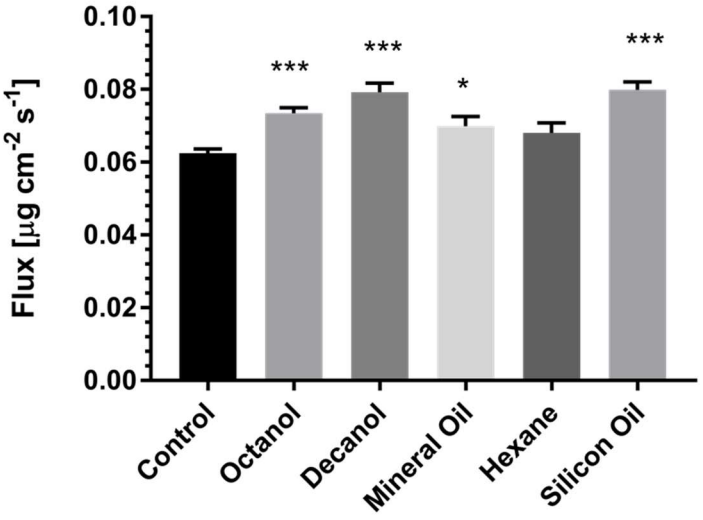

Figure 3-13 Flux Enhancement of various lipophilic fluids into PDMS.

The steady state flux of ibuprofen was measured post-soak of various fluids with PDMS membranes.*** indicates a p-value of $p < 0.01$ and * indicates a p-value of $p < 0.05$ from a T-test to compare the mean values of the flux relative to the as fabricated PDMS membrane.

It was observed that the octanol, decanol, mineral oil, and silicon oil that partitioned into the PDMS membrane enhanced the flux, while hexane that did not partition into the PDMS membrane was not able to enhance the flux. However, it is unclear what caused the flux enhancement. Examining which fluids were retained by the PDMS during the entire course of the experiment as opposed to diffusing back out

into solution, only mineral oil and silicon oil were retained in the membrane post experiment. Octanol and decanol re-partitioned most likely into both the donor and receiver phases. The flux enhancement from the silicon and mineral oil may be due to a complex partition coefficient which is a function of ibuprofen solubility in PDMS + silicon oil/mineral. While the flux enhancement from the octanol and decanol may be due to increased solubility in the donor phase from octanol/decanol leakage and dissolution into the donor aqueous medium.

3.5 Conclusions

PDMS does not have interconnected porosity as measured by beam PALS. No drug was quantified in the PALS void volume (as measured by a change in lifetime), nor was any change in mass of the membrane measured when soaked in pure water (data not shown). The effective diffusive flow of drug appears to transport within the densely packed-domains in the polymer network. PDMS is pH stable, as shown in the $LogD_{PDMS}$ experiments for ibuprofen over a pH range of 2.0-12.0. The K x D product successfully predicted ibuprofen permeability over a 500μm difference in thickness of PDMS membrane. The authors believe that the use of the K x D product (Diffusivity) to predict PDMS-drug permeability would be valid at any thickness that PDMS membranes are currently produced. Large area (>5cm^2), ultra-thin (1□m) membrane fabrication is possible and will be the main type of geometry required for absorption rates of pharmaceutical at rates comparable to human GI absorption rates.[103] However, PDMS can be fabricated to have a 3 dimensional surface area, which could accommodate even larger surface area to volume ratios without sacrificing the

physiologically relevant volumes required by the ivR methodology.[104] The pure diffusion coefficients in PDMS are significantly slower ($\sim 10^2$) than those in water, but the true diffusion coefficients for PDMS must account for the partitioning behavior into PDMS and the polar surface area of the solute molecule ($K \times D \propto K_{PDMS}$; $K \times D \propto \frac{1}{PSA}$). Knowing the thickness independent permeability (K x D) behavior allows for *iv*R modeling of the absorption kinetics in an *in vitro* test. This relationship also allows for the design of an *iv*R absorption compartment to be addressed in a future publication. PALS characterization at room and physiologic temperature of the PDMS membrane shows that the physical structure of the membrane is not significantly affected by any processing or experimental parameters that a membrane would be exposed to in *iv*R dissolution & absorption experiments. Dissolving the PDMS components in hexane appears to produce softer (lower Young's modulus) membranes than PDMS that is fabricated with no solvent. The Young's modulus can be modulated between ~0.3MPa and ~2.3MPa by changing the amount of curing agent added to the base material during fabrication. Even though high temperature curing is limited to ~60°C in hexane during polymerization ($T_{Boiling\ hexane}$ = ~70°C), exposing the polymer solution to temperatures above R_T can result in up to a 0.5MPa increase in the Young's modulus. While these mechanical differences may be significant in fabrication of the *in vitro* absorption component, the mechanical differences do not affect the drug permeation performance significantly nor does the latent hexane present in the PDMS membranes.

3.6 Acknowledgements

I would like to thank Thomas Killeen from Grand Valley State University for his contributions on the cryogenic PALS measurements and Troy Halseth for obtaining some of the solubility and distribution coefficient data, Nicholas Job for proof reading the original publication and assistance in the HPLC development in this chapter. I would also like to thank Jenna Walker for performing the gas-chromatography on the PDMS UTLAM.

CHAPTER 4

Fabrication of an Ultra-Thin, Large-Area Poly(dimethyl siloxane) Membrane and Diffusion Cell

4.1 Abstract

PDMS membranes needed to be in the 10's of micrometer of thickness, based on the estimates for the permeability through PDMS to biomimic passive diffusion oral absorption. A diffusion cell and stirring device were created to meet the need of housing an UTLAM and attempt to incorporate knowledge from literature about better stirrer methods. The diffusion cell was successfully fabricated at the University of Michigan Chemistry Glass Blowing Shop, and a commercial triple blade hydrofoil with a diameter of 50% of the donor side tank diameter was purchased. In addition to developing a diffusion cell to house and test the UTLAM, the UTLAM itself was selected after an exploration of the fabrication parameters and physical limitations of the UTLAM. Solution viscosity (mass % of PDMS in solution) and terminal rotational speed of the wafer significantly affected the final thickness of the UTLAM as measured by freeze fracture scanning electron microscopy. A method was developed to make PDMS UTLAM separation from the casting substrate, using a polyvinyl alcohol sub layer. Polyvinyl alcohol films were characterized using ellipsometry. The effort to design a composite spin cast film resulted in reliable separation of the function PDMS

layer. The diffusion cell was then easily assembled and installed into the benchtop setup. The hydrofoil was able to keep particles well suspended based on the results of chapter 6.4.

4.2 Introduction

Early predictions of the permeability, absorption rate, and feasible geometry indicated that the rotating membrane diffusion cell would be insufficient as an apparatus to achieve absorption rates on the scale observed/measured/predicted in human's oral absorption pathway for BCS II/IV. It was determined that PDMS had enough affinity for pharmaceutical molecules to still be utilized, however the ability to mimic *in vivo* absorption rates was limited effectively to only the BCS II compounds, with limited feasible options to mimic BCS IV compounds. One definite requirement to make PDMS suitable for ivR absorption was to increase the permeability observed in the characterization experiments by at least 1 if not 2 orders of magnitude ($1 \cdot 10^{-4} cm \cdot s^{-1} \rightarrow 1 \cdot 10^{-3} cm \cdot s^{-1}$ or $1 \cdot 10^{-2} cm \cdot s^{-1}$). The rationale being that if the PDMS could not be rate limiting than the maximum absorption performance could be achieved in terms of the membrane. To achieve permeabilities in the desired order of magnitude, it was predicted that a PDMS membrane would have to be ~40μm in thickness or less. This would make the membrane permeability at least equal to the permeability of a ~30μm aqueous boundary layer, which is a reasonable hypothetical thickness for an aqueous system stirred at about 150RPM (predicted using Levich's Rotating Disk Equation). The other aspect of designing the diffusion cell was to keep the membrane surface area to donor volume ratio as high as possible (to further increase the

absorption rate potential). This led to the need for an ultra thin and large area membrane.

Attempting keep fabrication costs low, a prefabricated 3" glass tube with Viton O-ring and clamp kits was obtained. The total cross cross-sectional area was significantly larger than the rotating membrane diffusion cell (44.4cm^2 compared to 6.41cm^2). The target volume for the receiver chamber was about 110mL to reduce the amount of fluid needed per test. However, due to physical limitations in the glass blowing process the cylindrical portion of the lower glass piece needed to be significantly longer than 15mm. The total volume in each of the two diffusion cells created was about 211mL and 229mL. Figure 4-1 shows the idealized schematic version of the UTLAM diffusion cell. The truncated cone was utilized to promote fluid mixing and reduce the lower chamber volume. A glass pipette was fused onto the slant of the truncated cone to allow for a sampling device to access the lower chamber. For the proceeding experiments a glass tube with a cannula was attached to the lower chamber port to allow for syringes to pull samples for offline HPLC analysis. However, the as fabricated port is potentially compatible with standard UV-VIS dip probes. This is advantageous because the membrane should not allow particles through, which typically obscure UV-VIS dip probes.

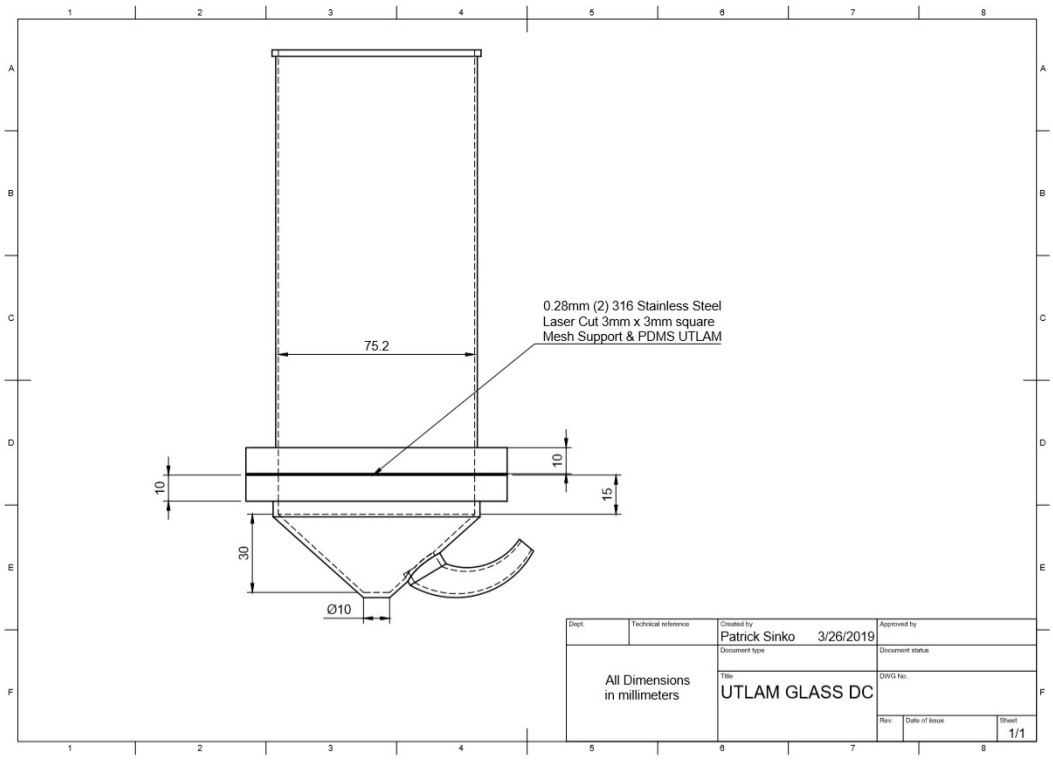

Figure 4-1 Engineering Drawing of PDMS UTLAM Diffusion Cell.

An engineering sketch of the idealized UTLAM diffusion cell. Practically, the lower chamber's cylindrical portion was extended by 10-15mm so that the glass blower could handle the part during shaping. This resulted in a volume increase from about 110mL to about 230mL. The sampling port in the lower compartment is threaded at the exposed end allowing for a threaded cap with a hole to attach either a glass sampling tube containing a cannula. It is postulated that a standard UV-VIP dip probe could also be secured into place. The curvature of the sample port is exaggerated in this diagram, the glass blower was able to produce nearly any shape desired.

In addition to the diffusion cell being redesigned, significant amount of though went into designing the stirring implement for this new diffusion cell. Computational fluid dynamic simulations of two types of impellers where conducted to examine the geometry of both hydrofoil and anchor style impellers. The effect of impeller diameter on average bulk fluid velocity and shear were metrics used to evaluate to suitability of the impeller. These results (data not shown) where consistent with the literature on hydrofoil and anchor stirrers. Due to an incompatibility of materials with 3D prototyped parts, the hydrodynamics of the modeled impellers in this

diffusion cell could not be experimentally verified. Commercial hydrofoils were then purchased to meet the experimental demand. Hydrofoils were ultimately chosen due to their ability to promote particle resuspension and provide homogeneous shear rates within the diffusion cell. Both of which are classic problems with the USP II dissolution apparatus. In Figure 4-2 below, shows the hydrofoil impeller in detail that was used for the UTLAM diffusion cell studies in this dissertation. Ideally, more CFD work will be done in the near future to understand the flow patterns, bulk velocity, and bulk shear rates imposed by this impeller as those are critical pieces of evidence to making the claim for *in vivo* relevance or being compatible with the *in vivo* relevant philosophy.

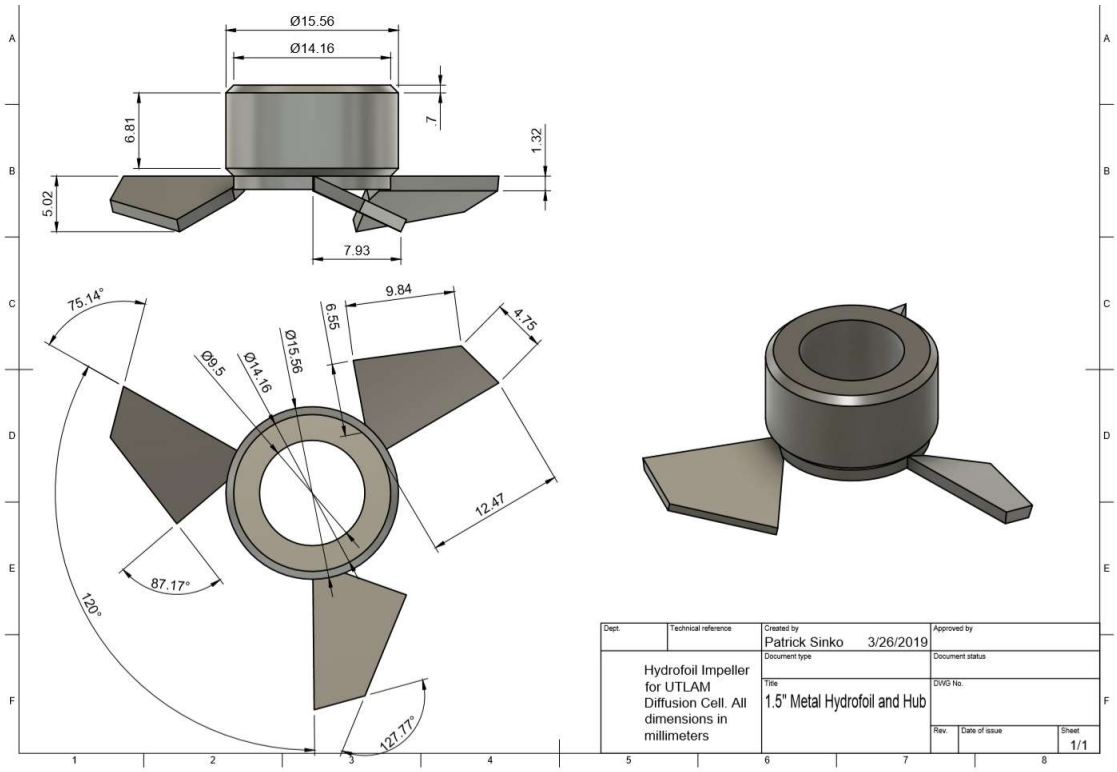

Figure 4-2 Engineering drawing of the 1.5" commercial hydrofoil used to stir the PDMS UTLAM diffusion cell.

This impeller was rotated counterclockwise to push fluid down, to aid in resuspension of particles.

4.3 Materials

Sylgard 184 Elastomer Kit (Dow Corning), Hexane, Polyvinyl alcohol, polytetrafluoroethylene (PTFE) tape, Viton -O-rings, MIRA3 FEG Scanning Electron Microscope, Liquid Nitrogen, Undoped silicon wafers with native silicon oxide, Ellipsometer

4.4 Methods

4.4.1 Casting the Polyvinyl Alcohol Film

Deionized water was heated to 85°C and polyvinyl alcohol was added to create a 3% by mass solution. The water was vigorously mixed throughout the addition of the polymer due to the polymers tendency to gel as it collected at the bottom of the flask. The mixture was stirred overnight (>6hrs) until a solution formed. The temperature was dropped to 65°C and was then ready for casting. A 100mm diameter silicon wafer was washed 5 times with milliQ purified deionized water. The spin coater was set to a speed of 5000RPM and an acceleration of 5000 RPS. 65°C PVA solution was then deposited onto the wafer in place with a pipette filler using a 14mL stereological pipette. After the solution was deposited onto the silicon wafer, the spin coater sequence was engaged and ran for 75 seconds. Coated Wafers were transfer to a vacuum oven set to 65°C and vacuum annealed for 24 hours.

4.4.2 Casting the poly(dimethyl siloxane) Film

A 10:1 mass ratio of base and catalyst components from the Sylgard 184 kit were mixed together on an analytical balance. Various mass to volume rations of pre-polymer PDMS to hexane were mixed on an analytical balance. Using the same pipette

and pipette filler from section 4.4.1 room temperature PDMS-hexane solution was deposited onto a stationary PVA coated, silicon wafer. The spin sequence was then engaged (various speeds and accelerations) for 75 seconds. Coated wafers were transferred to a 65°C vacuum oven for 48 hours.

4.4.3 Measuring poly(dimethyl siloxane) ultra-thin films

Wafers coated in PVA-PDMS were dipped into liquid nitrogen for 5-6 minutes, allowing the PDMS to become glassy. The wafer was then fractured by hand along pre-scribed scratches on the back of the wafer. The freeze-fractures edges were marked and then at room temperature final separation of the sample occurred. Freeze fracture was required because PDMS is sticky, especially as the film decreases in thickness. When fractured at room temperature, the film tended to stretch out onto the exposed edge of the silicon wafer. Thus, creating an artificially thinner cross-sectional thickness.

4.4.4 Creating the membrane support structure

The first support structure was fabricated in house from two 2mm opening sonic sieves. The mesh was separated from the side walls and edges of the mesh was sealed with Gorilla Glue® 6-minute epoxy. Once cured, the edges were sanded flat and wrapped with polytetrafluoroethylene (PTFE) tape. The UTLAM was floated off the casting substrate directly onto one of these supports, where is was sealed in between with many layers of PTFE tape. This formed the white disk structure observed in Figure 4-7. The PTFE tape served three purposes 1) create a seal between the diffusion cell O-rings and the upper/lower chamber 2) Prevent leaks from upper to

lower chamber 3) PTFE could be partially melted, so the fully wrapped membrane and sieve mesh were vacuum heated to 65°C for 30min prior to assembly of the diffusion cell. When rapidly clamped into position, the PTFE tape melted to the diffusion cell O-rings sealing any leaks that could form due to uneven contact between the sieve mesh edges.

The second support structure was 0.28mm thick 316 stainless steel cut with a laser to form a circumscribed rectangular mesh pattern. The rectangles were 2.9mm x 2.9mm and the spacing was about 0.99mm. These supports were also wrapped in PTFE tape for the same reasons described above. Additionally, a large buildup of PTFE tape was required at the edge of the support's diameter to create a leak proof seal.

4.5 Results

The polyvinyl alcohol layer was characterized, to be thorough, but the actual deposition thickness was not engineered. Enough polyvinyl alcohol needed to be deposited to ensure that the entire silicon wafer was coated for repeatable release of the PDMS film. The polyvinyl alcohol layer was sufficiently thin to be measured via ellipsometry and was measured at five different intervals along the major diameter (indicated in Figure 4-3). The mean thickness of the layer was found to about 60nm with a minimum thickness of about 55nm and a maximum thickness of about 70nm. During the casting process, undissolved polyvinyl alcohol was suspected to be the cause of post- "scarring" on the film. To confirm that polyvinyl alcohol was deposited in these "scar" atomic force microscopy (AFM) was performed (data not shown). The

AFM experiment was designed to trace across a scar and compare the depth profile to a control scratch and known ellipsometric thickness. While the "scar" indicated a severe drop in the polyvinyl alcohol thickness, AFM confirmed that there was still a significant amount of polyvinyl alcohol present, enough polyvinyl alcohol to act as a barrier to PDMS adhesion to the silicon wafer.

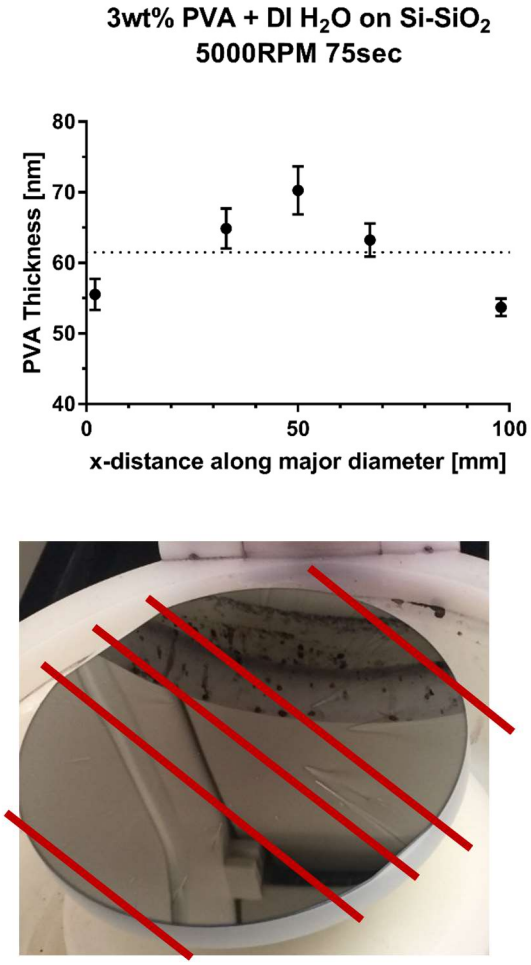

Figure 4-3 Polyvinyl Alcohol Sacrificial Film Layer.

The results of the ellipsometric measurement of polyvinyl alcohol films on silicon wafers. The films were produced at a terminal rotational speed and acceleration of 5000 (RPM/RPS) out of solution with deionized water. Average value of the thickness of the film was approximately 60nm. It was found that the amount of deposited polyvinyl alcohol was sufficient to separate PDMS from the silicon wafer. PDMS solution was not expected to affect the polyvinyl alcohol layer because of orthogonal solvents used to create both layers. The red lines in the photograph indicate the positions at which the polarized beam spot was placed during ellipsometric measurements, the measurement was taken as close to the mid-line of each marked position as possible.

The next step in developing the PDMS diffusion cell was determining what spin parameters were needed to achieve a PDMS membrane 40μm or less. A survey of reasonable solution concentrations of PDMS and terminal rotational speed were attempted to create a design space.[103] The reference literature provided a range for both variables however, because those authors used a different intermediary layer (PEG) the trends of rotational speed and viscosity will be different due to the a difference in interfacial conditions.

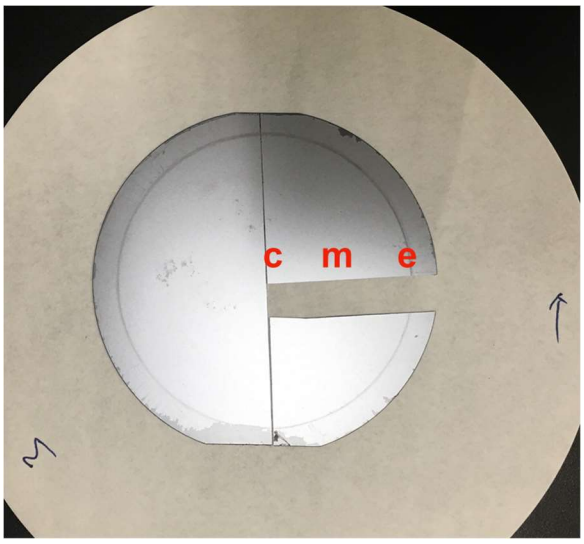

Figure 4-4 SEM Sample Preparation of PDMS UTLAM.

A photograph of the 100mm wafer processed for SEM image analysis. The view is of the back of the silicon wafer. A diamond scriber is used to pre-notch the major diameter and a 90° pre-notch is made so that a rectangular sample can be extracted and then mounted into the SEM. The pre-notched wafers were submerged into a liquid nitrogen bath to embrittle the polymers so that they could be brittlely fractured, which would preserve the as cast thickness of the PDMS. Liquid nitrogen was required due to PDMS's low glass transition temperature.

In Figure 4-4, the sample for SEM can be seen (as a negative) as described in 4.4.3. C, m, e, indicate the center, middle, and edge of the wafer. A total of 6 measurements across all three areas per wafer were used to describe the average membrane thickness in the survey study and 40 in the confirmation study.

Figure 4-5 SEM Images of the PDMS UTAM Samples.

The SEM image on the left is a low magnification view of the SEM sample holder with PDMS UTLAM wafers mounted in measurement position. The SEM image on the right is of the PDMS UTLAM still attached to the silicon wafer after the freeze-fracture sample preparation. MIRA3 FEG SEM was outfitted with an image analysis platform and the yellow lines indicate the measured thickness of the PDMS UTLAM.

Figure 4-5 shows the view of sample PDMS UTLAM in the MIRA3 FEG SEM and how the image analysis derived the thickness of the membrane film.

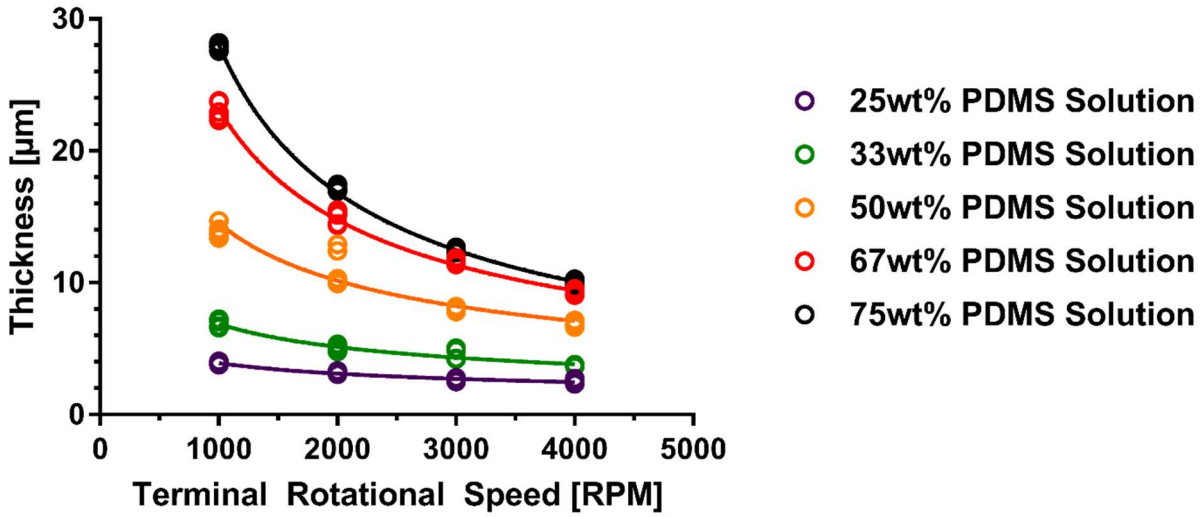

Figure 4-6 Spin Cast PDMS on PVA Thickness Regime.

From literature it was known that rotational speed and viscosity would affect the film thickness, however, no literature was found specifically for the PVA-PDMS system. The resulting data shows similar power law-type relationships observed in the literature for PDMS and other substrate polymers. Once the screening study was performed, a proof of concept study to determine the thinnest membrane possible for use in the UTLAM diffusion cell was conducted. The results indicated that a 12.5µm PDMS membrane would be able to survive experimental loaded during assembly and execution of the experiment. (See **Error! Reference source not found.**)

Table 4-1 Comparison of the screening study and confirmation study results for the final casting parameters of the PDMS UTLAM used in this dissertation.

3000/3000 RPM/RPS	Avg. h_m [µm]	Std. Dev. [µm]
Screening (N = 1) (Count = 6)	12.5	0.2
Confirmation (N = 4) (Count = 40)	11.2	0.5

N indicates the number of wafers produced, and count indicated the total number of thickness measurements.

Figure 4-6 shows the results of the screening survey of the effect of solution viscosity (analogue of solution concentration of PDMS) and terminal rotational speed showed a power law dependence of rotational speed. The more viscose the solution the thicker the resulting membrane would be. Additionally, the slower the rotational speed the thicker the membrane would be. In an effort to challenge what was possible, 2.5, 5, 12.5, 17, and 28μm membranes were made, floated, and loaded in the diffusion cell to see if they could survive experimental conditions.

Table 4-2 PDMS A record of the proof of concept experiments to determine if a UTLAM of certain thickness could support 0.26kg in the lower chamber and up to at least 0.54kg in the upper chamber. Successful floating means that the PDMS was separated from the silicon intact, loading implies that the UTLAM supported the masses completed unsupported by fluid on the opposite side of the diffusion cell.

Target Thickness [μm]	[RPM] [RPS]	f_{PDMS}	Successful Float	Successful Loading
27.9	1000	0.75	✔	✔
17.15	2000	0.75	✔	✔
12.51	3000	0.75	✔	✔
5.02	2000	0.33	X	X
2.48	4000	0.25	X	X

4.6 Discussion

Ultimately, the PDMS spin parameters chosen to produce UTLAM for the proceeding studies were 3000 RPM and an initial acceleration of 3000 RPS. This produced a thickness of ranging from 10.7-12.7 micron (Table 4-1). There was some batch to batch variability, most likely due to the length of time the PVA solution had sat, effectively the dissolved concentration of PVA. Another potential source of

variability is the batch to batch differences in the exact concentration of PDMS in solution.

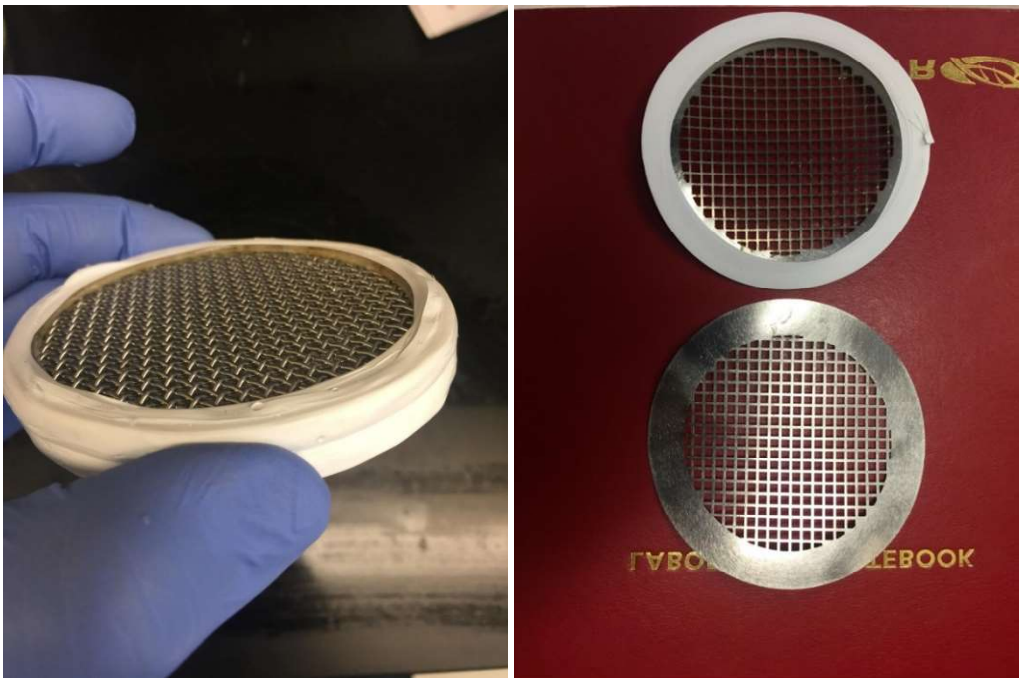

Figure 4-7 Photographs of UTLAM Support Structures.

Photographs of the two types of mesh membrane supports used in this dissertation. The left image is of homemade 2mm sonic sieve mesh and the right image is of laser cut 316 stainless steel. The major difference between the two was that the thickness of the metal mesh was 0.9-1.8mm and 0.28mm respectively. The laser cut support had slightly increased available surface area for drug transport (25.2cm^2 as compared to 21.8cm^2). The warping in the laser cut supports, termed "oil canning", was not limited to achieving a flat membrane surface in the UTLAM diffusion cell. However, the residual stresses in the steel do cause the diffusion cell to unscrew after a period of time. It is recommended that annealing of the steel is performed to reduce the oil canning.

It was found to be critical that each support was wrapped in PTFE tape and then the component sealed (support/membrane/support) in a thick wrapping of PTFE tape. This created a consistent water proof seal. The PDMS UTLAM survives at least 0.54 kg of water completely unsupported by fluid in the lower chamber using either support structure (Figure 4-7).

4.7 Acknowledgements

None of the following chapters would be possible without Roy Wentz, University of Michigan LSA Chemistry Glass Blower. The sincerest thanks are extended to him for the ease and speed with which he works. I would like to thank Haiping Sun for performing the SEM characterization and MC^2 at the University of Michigan for use of the staff and equipment. I would also like to thank Booby Kerns, center manager of MC^2 for all of the help coordinating AFM (data not shown) and SEM work.

CHAPTER 5

pH-Dependent Absorption in an Ultra-Thin, Large-Area Poly(dimethyl siloxane) Membrane Diffusion Cell

5.1 Abstract

Preclinical evaluation of modern solid oral dosage forms requires more advanced *in vitro* devices due to the trend of formulating low solubility, high permeability compounds for commercial therapeutics. Current compendial dissolution methodologies maybe not always be suited for such compounds due to excessive fluid volume, high fluid shear rates, heterogeneity of shear rates, suboptimal fluid flow, and ultimately the lack of absorption ability.[105] Here a dissolution apparatus is introduced that overcomes some limitations of the compendial apparatus. In this report the characteristics of the ultra-thin large area polydimethylsiloxane (PDMS) membrane (UTLAM) absorption system with respect to pH, partition coefficient (K), aqueous boundary layer (ABL). A pH dependent solution diffusion model is presented. For all experiments, the diffusion cell was warmed to 37°C and stirred at 150RPM with a 1.5" hydrofoil. A 12.5µm thick, 100mm diameter PDMS membrane was fastened between two mesh supports. Experiments between pH 1.9-12.5 were investigated using ibuprofen as a model weak acid drug. A model was established to predict pH dependent solution diffusion based on film theory. K is the dominant force for

absorption and can overcome pH limitations to absorption imposed by the drug's natural pKa. The ABL played a significant role when the drug is mostly non-ionized. In the aqueous and membrane limited diffusion cases, there was an observed shift in the natural drug pKa caused by K and ABL. A diffusion-controlled polymer membrane was incorporated into a dissolution apparatus to mimic the passive *in vivo* absorption pathway. A hydrofoil was implemented to reduce coning, promote particle re-suspension, and homogenize bulk fluid shear. High rates of transport across the membrane are possible for drugs with high partition coefficients. This is important because with increasingly low solubility/high permeability drugs in development, dissolution performance will differ greatly between a compendial apparatus and an apparatus with absorption. The UTLAM will be a valuable tool to achieving human scale drug permeabilities in PDMS for future IVIVC. Ultimately, the UTLAM PDMS diffusion cell provides a more realistic dissolution experiment by improving the hydrodynamic properties in the donor phase and including absorption kinetics. This device could be easily standardized for use as industrial preclinical development dissolution apparatus.

5.2 Introduction

5.2.1 Absorption Modeling *in vitro*

The purpose of this work is to establish the foundation for a mass transport model to include effects of solubilized drug, solid polydisperse particles in solution, pH, aqueous boundary layer, excipient effects and diffusion-controlled membrane absorption. When complete, this model will provide a comprehensive mechanistic

frame work to predicting dissolution performance of formulated products. The authors propose that modeling pH-dependent absorption of the soluble drug as the first simplest solution parameter to define.

When considering the effects of pH on absorption the pH-partition hypothesis is recognized as the basis for modeling. In the pH-partition hypothesis, the claim that only non-ionized drug permeates a membrane is stated.[106] Thus, by knowing the fraction of non-ionized drug and the partition coefficient, the absorption rate should be easily predicted. The rate should also seemingly be proportional to the fraction of drug that is "available" for partitioning. At the pKa, 50% of the drug is ionized, which means that the absorption should be at 50% of maximum absorption rate in an even comparison. Wagner and Sedman proposed a model backed up with experimental data that in fact the absorption rate is not directly proportional to the fraction of non-ionized drug.[97] They observed a shift in the 50% of maximum absorption (referred to as a "shift" in the pKa, and in this work "an apparent shift in pKa"). They observed that the lipophilicity of a molecule could extend the pH a which the maximum absorption rate could be achieved as long as the lipophilicity was significantly high. An important implication is that many drugs administered orally become partially ionized in some portion if the gastrointestinal tract and yet are absorbed well. Depending on the degree of ionization and the degree of the partition coefficient, drugs may behave to the absorbing surface, as if they are non-ionized. Essentially, the ionization reaction in solution is extremely fast compared to the rate of absorption into the membrane (biological or synthetic). Since the the rate of absorption of the non-ionized species is still orders of magnitude higher than the

ionized form, the membrane effectively only sees the non-ionized form. The non-ionized form is rapidly removed from solution, thus changing the balance of non-ionized to ionized drug. The pH is not significantly changed and thus resets the dissolved drugs population balance of non-ionized to ionized molecule. It is only when the pH shift from massive amounts of drug leaving (no buffer, weak buffer, low amount of drug present) that the absorption rate will slow due to the increased total amount of ionized drug present. Winne later described the Wagner-Sedman model as a special conditions of a more general model that included the effect of the microclimate pH and aqueous boundary layer.[100]

5.2.2 Rotating Membrane Diffusion Cell (RMDC) and Ultra-Thin Large-Area Membrane (UTLAM) Diffusion Cell

A rotating membrane diffusion cell (Figure 2-1) was used to measure membrane-controlled mass transport. This cell housed PDMS membranes from 150μm-1000μm in thickness with an aperture area of 6.419cm^2. Due to the thicknesses of the membranes, no support structure was needed to keep the membrane in place during the diffusion experiment. Fresh membranes were used for each replicate in each experimental condition, and the diffusion cell was disassembled each time for cleaning post-experiment. The diffusion cell is rotated via an elastic band on a groove in section C. For the RMDC, laminar fluid flow develops at the inner and outer surfaces of the section D. The inner section is mixed through fluid passing over baffles cut into section B allowing for homogeneous sampling of the interior compartment. For these experiments, the RMDC was rotated at a constant 150RPM.

The UTLAM diffusion cell (Figure 4-1) was used to measure aqueous boundary layer-controlled mass transport. This cell housed a 12.5μm thick 44.4cm^2 PDMS membrane. The PDMS UTLAM's were reused in every experiment, after a minimum of 15 minutes where a pH 12 NaOH bath extracted ibuprofen from the previous experiment. The UTLAM was washed thoroughly with deionized water pre and post NaOH bath. While PDMS's stiffness increases with decreasing domain size (~2MPa → ~8MPa) it is unable to resist deformation across 75.2mm span at 12.5μm thickness.[103] Due the support the UTLAM diffusion cell was able to with stand at least 0.54kg of water placed in the upper chamber in the normal operating position, and 0.26kg of water in a completely inverted operating position. Since the membrane deflects significantly upon loading fluid into the diffusion cell, the volume of the receiver and donor will influence each other. This is specific to the experiments where a sonic sieve mesh was used as a membrane support. A correction to the surface area available due to mesh interference was made, yielding 21.8cm^2. Unlike the RDMC, the stirring for the upper chamber was controlled by a 1.5" hydrofoil rotating in the push down configuration at 150RPM, and the lower chamber was stirred as fast as possible while maintaining steady rotation of a 10mm magnetic stir bar.

5.3 Materials & Methods

5.3.1 Materials

Agilent 1100 High Performance Liquid Chromatography (HPLC), Eclipse Plus C 18 Column (3.5μm x 4.6μm x 150mm), Acetonitrile (EMD Millipore, HPLC grade),

deionized water (Milli-Q purified), trifluoroacetic acid (Fisher Scientific, Optima Grade), Ibuprofen (Albemarle Lot No. 2050-0032F), Poly(dimethyl siloxane), (Sylgard 184 elastomer kit, Dow Corning), Hexane (Fisher, reagent grade), Acetone, Isopropanol, Methanol (Fisher Scientific, HPLC grade), Monobasic Potassium Phosphate, Potassium Phthalate, Sodium Hydroxide, Potassium Chloride, Hydrochloric Acid.

5.3.2 Experimental Methods

5.3.2 1 Thick membrane casting procedure

Sylgard 184 base was weighed in a glass container and moved to a vacuum chamber where a -750mbar vacuum was pulled for 25min to remove gas. Separately, an appropriate amount of Sylgard 184 curing agent was weighed on an analytical balance. A 1:1 ratio (total mass: volume) of hexane was measured in a graduated cylinder. The hexane was used to dissolve the catalyst component and then was added to the container containing the base polymer. Manual mixing was done until the base was completely dissolved (easily observed by a change in the index of refraction). An appropriate volume of solution was drop cast into polyethylene weigh boats using a pipette. The PDMS solution cured at the desired temperature and time with solvent evaporating into a lab hood.

5.3.2 2 UTLAM Casting Procedure

For this work a 12.5μm thick PDMS membrane was required to achieve sufficient permeability so that the membrane was not rate limiting. To achieve such a thin structure a separate casting method was developed. Silicon wafers were cleaned

using deionized water, methanol, acetone, isopropanol, hexane, and then a triple deionized water rinse. A 3%w/w polyvinyl alcohol solution at 65°C was deposited onto the wafer while stationary. The wafer was accelerated to 5000RPM at 5000 rotations per second and held at 5000RPM for 75 seconds. The wafer was then placed in a vacuum oven, purged of atmosphere, and the cured at 65°C for 24 hours. A 1:10 mixture of Sylgard 184 was dissolved in hexane to create a 75%w/w solution of PDMS in hexane. The solution was deposited on the polyvinyl alcohol coated silicon wafer and accelerated to 3000RPM at 3000 rotations per second. The final composite wafer was then placed in the vacuum oven, purged, and cured at 65°C for 48 hours. PDMS UTLAM were released from the casting substrate using deionized water to dissolve the polyvinyl alcohol, allowing the UTLAM to float to the surface for insertion into the diffusion cell.

5.3.2 3 HPLC methods

For ibuprofen 0.1%v/v trifluoro acetic acid was used in both water and acetonitrile. See

Table 5-1for details. For HPLC Standard Curves, limit of detection (LOD) and limit of quantitation (LOQ), a five-point standard curve was created for each drug in the buffer used for the experiment.

Table 5-1 A brief description of the HPLC methods, including the mobile phase composition used and the average elution time of the molecule.

Drug	Mobile Phase Composition (Acetonitrile/H_2O)	Average Elution Time (min)
Ibuprofen	70/30	2.89

5.3.2 4 Partition coefficient measurements

Five membranes were prepared in a similar manner to chapter 3.2.1. The dimensions of the perimeter and thickness were measured of the sectioned samples using a caliper to determine the volume of membrane. After determining membrane density, subsequent volume measurements were made using the density relationship. Stock solution was distributed to 5 sample vials with 1 membrane-free vial to serve as a control. The time zero point was measured from the blank vial and time points and 1mL samples were taken at 12 and 24 hours. The collected samples were assayed in duplicate by HPLC. This was procedure was conducted for the intrinsic non-ionized partition coefficient of ibuprofen at pH 2. The intrinsic ionized partition coefficient was determined from a pH 7 solution diffusion experiment. 50µg/mL ibuprofen in pH 7.0 phosphate 50mM buffer was used as the donor phase. The aqueous boundary layer for the UTLAM diffusion cell had been characterized allowing for the deconvolution of the required ionized intrinsic partition coefficient to fit the measured flux. As ibuprofen is over 99% ionized at pH 7, it is an acceptable pH value to make the intrinsic measurement.

5.3.2 5 Rotating membrane diffusion cell experiments

Thickness of the sample membrane was measured using a caliper at the center of the membrane and then at four additional points within the circumference of the membrane in the region which was exposed to the drug saturated aqueous phase.

The initial mass of the membrane was weighed prior to drug exposure. A recirculating bath warmed the beaker containing the donor aqueous suspension (sodium dodecyl sulfate 0.9mM) of drug to 37°C. A rotating membrane diffusion cell was utilized, as shown in Figure 3-1.[54] Seventy mL of the appropriate receiver phase was then added into the inner chamber of the diffusion cell. This receiver phase was a medium that ionizes the drug once drug passes completely through the membrane, creating sink conditions and preventing reverse transport. For drugs that were non-ionizable, the receiver phase and donor phase were compositionally equivalent except for any surfactant and drug, which was solely present in the donor phase. The dip probe was calibrated in situ for each experiment and recorded one measurement every 60 seconds (five spectra averaged per measurement). Donor phase volume of 250mL was added to the warmed jacketed beaker, and then raised into contact with the diffusion cell. Air that was present in between the membrane and the aqueous phase was removed using a syringe. The diffusion cell was rotated at 150RPM during the experiment.

5.3.2 6 UTLAM Diffusion Cell Experiments

50µg/mL solution was created of ibuprofen at specified donor pH (see appendix for complete composition and properties). The receiver media was a NaOH + KCl buffer 38mM at pH 12.5. This would act to completely ionize any ibuprofen that permeated the membrane, preventing reverse flux as long as the difference in the degree of ionization between the donor and receiver was significant. Just as in the RMDC experiments, the diffusion cells were warmed to 37°C, however stirring was achieved using a hydrofoil impeller. The hydrofoil was a 1.5" diameter (D_{HF}/D_{Tank} =

0.5), rotated at 150RPM, and was composed of three pitched flat blades. Samples were pulled via a cannula and diluted 1:1 with 1N hydrochloric acid, to assist in neutralizing the pH prior to injection on the HPLC.

5.3.2 7 Table of Variables and Definitions

Table 5-2 A brief description of the variables for chapter 5

Variable	Definition
J	Flux ($\mu g/cm^2 \cdot s$)
J_{exp}	Experimentally Measured Flux ($\mu g/cm^2 \cdot s$)
J_{Total}	Total Flux ($\mu g/cm^2 \cdot s$)
J_{ABL}	Flux through the aqueous boundary layer ($\mu g/cm^2 \cdot s$)
J_{Mem}	Flux through the membrane ($\mu g/cm^2 \cdot s$)
$J_{Receiver}$	Flux (appearance) in bulk receiver ($\mu g/cm^2 \cdot s$)
J_{Donor}	Flux from bulk donor ($\mu g/cm^2 \cdot s$)
D	Molecule's Diffusion Coefficient (cm^2/s)
D_{Aq}	Aqueous Diffusion Coefficient (cm^2/s)
D_{N-I}	Intrinsic Non-Ionized Diffusion Coefficient of Molecule in the Membrane (cm^2/s)
D_I	Intrinsic Ionized Diffusion Coefficient of Molecule in the Membrane (cm^2/s)
P_m	Total Membrane Permeability (cm/s)
P_{eff}	Effective Total Permeability (cm/s)
$P_{Aq\text{-}Donor}$	Effective Aqueous Boundary Layer Permeability in Donor Phase (cm/s)
$P_{Aq\text{-}Receiver}$	Effective Aqueous Boundary Layer Permeability in Receiver Phase (cm/s)
P_{N-I}	Intrinsic Non-Ionized Partition Coefficient of Molecule in the Membrane (cm/s)
P_I	Intrinsic Ionized Partition Coefficient of Molecule in the Membrane (cm/s)
h_{Aq}	Aqueous Boundary Layer Thickness (cm)
h_m	Thickness of the PDMS membrane (cm)
K_{N-I}	Intrinsic Non-Ionized Partition Coefficient of Drug in PDMS (unitless)
K_I	Intrinsic Ionized Partition Coefficient of Drug in PDMS (unitless)
$f_{Aq\ N-I}$	Fraction of Drug that is non-ionized
A_m	Membrane Surface Area (cm^2)
V_R	Volume of the Receiver Phase (cm^3)
V_m	Volume of the Membrane (cm^3)
S	Saturation Concentration of Drug in Donor Fluid at a particular temperature and pH (g/cm^3)
dm/dt	The change in mass with respect to time
dC/dt	The change in concentration of drug with respect to time
$k_{app\ exp}$	Experimentally measured apparent first order rate (s^{-1})
k_{app}	Apparent first order rate (s^{-1})
pKa	pH at which the drug is 50% ionized
pH	- log of of the hydrogen concentration

$m_{mem\ N\text{-}I}$	mass of non-ionized drug in membrane
$m_{mem\ I}$	mass of ionized drug in membrane
$m_{Aq\ N\text{-}I}$	mass of non-ionized drug in aqueous phase
$m_{Aq\ I}$	mass of ionized drug in aqueous phase
Ξ	Ratio of membrane permeability to aqueous boundary layer permeability

5.3.2 8 Experimental Determination of the Apparent Absorption Rate

Flux is defined as:

$$J = \frac{1}{A_m}\frac{dm}{dt} = \frac{1}{cm^2}\frac{g}{s} \quad \text{Eq (5.1)}$$

Measuring the concentration against time profile dC/dt can be determined, and receiver volume and membrane area are known.

$$J_{exp} = \frac{V_R}{A_m}\frac{dC}{dt} = \frac{1}{cm^2}\frac{g}{s} \quad \text{Eq (5.2)}$$

To calculate the absorption rate the effective permeability must be determined…

$$J_{exp} = P_{eff}\Delta C \quad \text{Eq (5.3)}$$

Assuming that sink conditions apply

$$P_{eff} = \frac{J_{exp}}{\Delta C} = \frac{J_{exp}}{C_{Donor_{final}} - C_{Receiver_{final}}} \approx \frac{J_{exp}}{C_{Donor_{final}}} \quad \text{Eq (5.4)}$$

Resulting in

$$k_{app_{Exp}} = \frac{A_{mem}}{V_{receiver}} \cdot P_{eff} \quad \text{Eq (5.5)}$$

5.3.2 9 Determination of UTLAM Diffusion Cell Aqueous Boundary Layer Thickness

$$J_{exp} = \frac{V_R}{A_m}\frac{dC}{dt} \quad \text{Eq (5.6)}$$

$$P_m = \frac{K_{N-I}D_{N-I}}{h_m} = \frac{65{\cdot}2.404\times10^{-7}cm^2\ s^{-1}}{12.51\times10^{-4}cm} = 1.25\times10^{-2}cm\ s^{-1} \quad \text{Eq (5.7)}$$

$$\frac{V_R}{A_m}\frac{dC}{dt} = \left(\frac{1}{P_{Aq-Donor}} + \frac{1}{P_{UTLAM}}\right)^{-1} C_{Final} \quad \text{Eq (5.8)}$$

$$\frac{1}{P_{Aq-Donor}} = \left(\frac{V_R}{\sim 48.1\frac{\mu g}{cm^3}\times 21.8cm^2}\frac{dC}{dt}\right)^{-1} - \frac{1}{1.25\times10^{-2}} \quad \text{Eq (5.9)}$$

$$P_{Aq-Donor} = 2.13\times10^{-3} \pm 2.35\times10^{-4}cm\ s^{-1} \rightarrow \frac{8.41\times10^{-6}cm^2\ s^{-1}}{h_{Aq}} \quad \text{Eq (5.10)}$$

$$\overline{h_{Aq}} = 39.5\times10^{-4} \pm 4.53\times10^{-4}cm\ (\mathrm{n} = 5) \quad \text{Eq (5.11)}$$

5.3.2 10 Determination of Rotating Membrane Diffusion Cell Levich Aqueous Boundary Layer Thickness

$$h_{Aq} = 1.61\left(\frac{D_{Aq}}{\nu}\right)^{\frac{1}{3}}\left(\frac{\nu}{\omega}\right)^{\frac{1}{2}} \quad \text{Eq (5.12)}$$

$$h_{Aq} = 1.61\left(\frac{8.41\times10^{-6}cm^2\,s^{-1}}{\frac{0.692cp}{100\cdot0.9933g\,cm^{-3}}}\right)^{\frac{1}{3}}\left(\frac{\frac{0.692cp}{100\cdot0.9933g\,cm^{-3}}}{\frac{2\pi}{60}\cdot150RPM}\right)^{\frac{1}{2}} = 36.1\times10^{-4}cm \quad \text{Eq (5.13)}$$

5.4 Results

5.4.1 *In Vivo* Extraction Model

To determine the absorption rate in the UTLAM diffusion cell, the literature was reviewed and an absorption model that demonstrated clinical success was produced by Wagner and Sedman.[97] This model predicted absorption rates as a function of luminal pH. The key assumptions of this model are that: 1) both the non-ionized and ionized forms of the drug can partition into the GI cell membrane. 2) No chemical reactions (metabolism) of drug occurred in the GI lumen, cell membrane or immediately on the interface between cell membrane and bloodstream. 3) Mass is distributed based on equilibrium assumptions (extraction theory).[97] Equation 5.14 shows the final change in mass equation and Equation 5.15 shows the apparent first order absorption rate, which is simply the coefficient in front of the mass term in Equation 5.14.

$$-\frac{dm_{Aq\,Donor}}{dt} = m_{Aq\,Donor}\frac{A_m}{h_m V_m}\frac{D_{N-I}P_{N-I}f_{Aq_{N-I}}+D_I P_I\left(1-f_{Aq_{N-I}}\right)}{\left(1+P_{N-I}f_{Aq_{N-I}}+P_I\left(1-f_{Aq_{N-I}}\right)\right)} \quad \text{Eq (5.14)}$$

$$k_{app} = \frac{A_m}{h_m V_m}\frac{D_{N-I}P_{N-I}f_{Aq_{N-I}}+D_I P_I\left(1-f_{Aq_{N-I}}\right)}{\left(1+P_{N-I}f_{Aq_{N-I}}+P_I\left(1-f_{Aq_{N-I}}\right)\right)} \quad \text{Eq (5.15)}$$

Where,

$$P_{N-I} = \frac{m_{mem_{N-I}}}{m_{Aq_{N-I}}} \quad \text{Eq (5.16)}$$

$$P_I = \frac{m_{mem_I}}{m_{Aq_I}} \quad \text{Eq (5.17)}$$

For monoprotic acids,

$$f_{Aq_{N-I}} = \frac{1}{1+10^{pH-p}} \quad \text{Eq (5.18)}$$

For monoprotic bases,

$$f_{Aq_{N-I}} = \frac{1}{1+10^{pKa-}} \quad \text{Eq (5.19)}$$

5.4.2 Derivation of *In vitro* Film Theory model

For pseudo-steady-state pH dependent absorption based on film theory for non-ionized & ionized molecular transport, Fick's first law states that

$$J = -D\frac{\partial C}{\partial y} \quad \text{Eq (5.20)}$$

Rewriting the partial derivative yields

$$J = -\frac{D\Delta C}{\Delta y} \quad \text{Eq (5.21)}$$

The coordinate system is defined in Figure 6-1 where the donor side is negative y and going towards the receiver is positive y. Therefore

$$\Delta y = 0 - h = -h \quad \text{Eq (5.22)}$$

Substituting the value of Δy in to Fick's Law

$$J = -\frac{D\Delta C}{-h} \quad \text{Eq (5.23)}$$

The permeability coefficient is defined as

$$P = \frac{diffusivity}{characteris \quad lengt} = [\frac{cm}{s}] \quad \text{Eq (5.24)}$$

Thus, simplifying Fick's Law to

$$J = P\Delta C \quad \text{Eq (5.25)}$$

In film theory, diffusion layers are defined at the surface of dissolving particles, at the donor and receiver surfaces of the membrane, and the membrane itself. The simplest mass transport case would be no particles and only molecular drug exists in

solution. Film theory provides a way to predict flux through each diffusion layer (Equation 5.3). As suggested by the definition of absorption rate in Equation 3.3, determining an effective permeability of dissolved drug would allow for prediction of the apparent absorption rate. It is assumed that there is a continuity of flux between diffusive regions because there is no mass generation in any region due to the drug being fully dissolved.

$$J_{Donor} = J_{ABL} = J_{Mem} = J_{Receiver} \quad \text{Eq (5.26)}$$

To predict the total flux from bulk donor to bulk receiver phase, the diffusion layers can be treated like capacitors in series from electrical theory and mathematically this is modeled as an inverse of an an inverse sum. Rewriting Equation (5.25) as…

$$J_{Total} = P_{eff}\Delta C \quad \text{Eq (5.27)}$$

Through continuity of flux, the change in concentration is only dependent on the start and end point. The donor side concentration is labeled total concentration, implying that the sum of the populations of non-ionized and ionized forms of the drug constitute the total amount of drug in the system. The effective permeability is defined by the resistances to diffusion from the start to the end point. In between the bulk donor fluid and the bulk receiver fluid, there are two aqueous boundary layers, and a membrane. The effective permeability is written in combination with the new definition of ΔC as…

$$J_{Total} = \left(\frac{1}{P_{Aq_{Donor}}} + \frac{1}{P_m} + \frac{1}{P_{Aq_{Receiver}}}\right)^{-1} (C_{Total} - C_{Receiver}) \quad \text{Eq (5.28)}$$

Each permeability must be defined, and for aqueous diffusion layers permeability is defined as

$$P_{Aq} = \frac{D_{Aq}}{h_{Aq}} \qquad \text{Eq (5.29)}$$

There is an implicit assumption that the non-ionized and ionized forms of the drug diffusion through the aqueous medium at the same rate and can be modeled with a singular constant. For chemical entities which have a large difference in the non-ionized and ionized diffusion coefficients, this definition is insufficient. Based on recognition of the pH-partition theory, it is understood that ionization affects partitioning and that ionized species can partition into lipophilic media (even if it is to a significantly lower extent than the non-ionized counterpart). In film theory total permeabilities are considered in series because they are dependent on each other, but for describing partial permeabilities within a single diffusion region, the total regional permeability is modeled as a capacitor in parallel. A simple sum of all the constituent permeabilities for that species yields the total regional permeability. In this work only a monoprotic acid is considered, so only two species exist across the pH spectrum. Multi-protic systems would need to adjust accordingly.

$$P_m = P_{\mathrm{N-I}} + P_I = \frac{K_{N-I}D_{N-I}}{h_m} + \frac{K_I D_I}{h_m} \qquad \text{Eq (5.30)}$$

Considering each diffusion layer independently, the definition of "total" varies. For the aqueous boundary layer on the donor side, it has been reported in literature that the diffusion coefficient of a partially ionized species in an aqueous medium is best estimated by a single diffusion coefficient. Presumably this is the non-ionized diffusion coefficient. The permeability term for the aqueous boundary layer is effectively pH-independent, realizing this the C_{Total} that the diffusion layer is affected by is the sum of concentrations of all the species of drug molecules present. For the membrane, it is understood that both the diffusion coefficient and partition

coefficient depend on the form of ionization and the degree of ionization. For a molecule with a single pKa, this means that there are two diffusion coefficients and the spectrum of partition coefficients that will determine membrane transport. For the membrane permeability, it becomes clear that the non-ionized and ionized permeabilities are affected by the fraction of the total molecular population of interest in which the equilibrium constants respectively represent. This distinction is made so that the flux equation can be modified to include a variable pH by way of calculating the fraction of drug that is non-ionized.

$$J_{Total} = \frac{(C_{Total} - C_{Receiver})}{\frac{1}{P_{Aq_{Donor}}} + \frac{1}{P_m} + \frac{1}{P_{Aq_{Receiver}}}} \quad \text{Eq (5.31)}$$

Applying the logic of the previous paragraph, the change in concentration is rewritten in each component to reflect the appropriate mass transport…

$$\frac{1}{C_{Total}} \frac{\frac{dm_{Aq_{Donor}}}{dt}}{A_m P_{Aq_{Donor}}} + \frac{1}{C_{Total}} \frac{\frac{dm_{Aq_{Donor}}}{dt}}{A_{Mem}\left(\frac{K_{N-I} D_{N-I}}{h_m} + \frac{K_I D_I}{h_m}\right)} + \frac{1}{\left(C_{Mem_{Receiver}} - C_{Bulk_{Receiver}}\right)} \frac{\frac{dm_{Aq_{Donor}}}{dt}}{A_{Mem} P_{Aq_{Receiver}}} = 1 \quad \text{Eq (5.32)}$$

If it is assumed that the fluid flow is vigorous enough because the stirring is high enough on the receiver side in the *in vitro* device, it is valid to assume that the receiver side boundary layer does not play a significant role in the total resistance to diffusion. Equation 5.32 then simplifies to

$$\frac{1}{C_{Total}} \frac{\frac{dm_{Aq_{Donor}}}{dt}}{A_m P_{Aq_{Donor}}} + \frac{1}{C_{Total}} \frac{\frac{dm_{Aq_{Donor}}}{dt}}{A_m P_m} = 1 \quad \text{Eq (5.33)}$$

Extracting the dm/dt term and breaking the total concentration the membrane sees into constituent non-ionized and ionized total concentrations simplifies Equation 5.33 to Equation 5.34.

$$\frac{dm_{Aq_{Donor}}}{dt} = \left(\frac{1}{A_m P_{Aq_{Donor}} C_{Total}} + \frac{1}{A_m \left(C_{N-I} \frac{K_{N-I} D_{N-I}}{h_m} + C_I \frac{K_I D_I}{h_m} \right)} \right)^{-1} \quad \text{Eq (5.34)}$$

By the definitions for non-ionized concentration and ionized concentration

$$C_{N-I} = C_{Aq\ Donor\ total} \cdot f_{Aq_{N-I}} \quad \text{Eq (5.35)}$$

$$C_I = C_{Aq\ Donor\ total} \cdot \left(1 - f_{Aq_{N-I}}\right) \quad \text{Eq (5.36)}$$

The pH dependent term is now properly accounted for in each membrane permeability, and the total concentration re-enters the equation. Now total concentration can be factored out yielding

$$\frac{dm_{Aq_{Donor}}}{dt} = \left(\frac{1}{A_m P_{Aq_{Donor}} C_{Total}} + \frac{1}{A_m\left(C_{Total} f_{Aq_{N-I}} \frac{K_{N-I} D_{N-I}}{h_m} + C_{Total}\left(1-f_{Aq_{N-I}}\right)\frac{K_I D_I}{h_m}\right)}\right)^{-1} \quad \text{Eq (5.37)}$$

$$\frac{dm_{Aq_{Donor}}}{dt} = A_m C_{Bulk_{Total}} \cdot \left(\frac{1}{P_{Aq_{Donor}}} + \frac{1}{\frac{f_{Aq_{N-I}} K_{N-I} D_{N-I}}{h_m} + \frac{\left(1-f_{Aq_{N-I}}\right) K_I D_I}{h_m}}\right)^{-1} \quad \text{Eq (5.38)}$$

Equation 5.37 simplifies to Equation 5.38, when all the definitions for permeability are substituted.

$$\frac{dm_{Aq_{Donor}}}{dt} = A_m C_{Bulk_{Total}} \cdot \left(\frac{h_{Aq}}{D_{Aq}} + \frac{h_m}{K_{N-I} \mathrm{D_{N-I}} f_{Aq_{N-I}} + K_I \mathrm{D_I}\left(1-f_{Aq_{N-I}}\right)}\right)^{-1} \quad \text{Eq (5.39)}$$

The penultimate step is to convert the bulk donor concentration into mass, thereby completing the derivation of the mass transfer equation for a diffusion-controlled absorption rate, where only solubilized drug is present.

$$\frac{dm_{Aq_{Donor}}}{dt} = m_{Aq_{Donor_{Total}}} \cdot \frac{A_m}{V_{Bulk_{Donor}}}\left(\frac{h_{Aq}}{D_{Aq}} + \frac{h_m}{K_{N-I} \mathrm{D_{N-I}} f_{Aq_{N-I}} + K_I \mathrm{D_I}\left(1-f_{Aq_{N-I}}\right)}\right)^{-1} \quad \text{Eq (5.40)}$$

Unit analysis confirms that the derived mass transfer equation has the units of mass per unit time.

$$\frac{dm_{Aq_{Donor}}}{dt} = g\,\frac{cm^2}{cm^3} \cdot \left(\frac{s}{cm}\right)^{-1} = \frac{g}{s} \quad \text{Eq (5.41)}$$

Recognizing that the equation is mass times rate, the first order apparent rate constant is defined as

$$k_{app} = \frac{A_m}{V_{Bulk_{receiver}}}\left(\frac{h_{Aq}}{D_{Aq}} + \frac{h_m}{K_{N-I} \mathrm{D_{N-I}} f_{Aq_{N-I}} + K_I D_I\left(1-f_{Aq_{N-I}}\right)}\right)^{-1} \quad \text{Eq (5.42)}$$

5.4.3 Theoretical Predictions

5.4.3 1 Predicting Ibuprofen Absorption Performance

There are two physical situations that are pertinent to solution absorption *in vitro*, aqueous boundary layer rate-limited and membrane diffusion rate-limited. To fully examine both theories, they should be tested at the extremes and ideally a model would satisfy the resulting experimental data. Based on the characterization work done by Sinko et al. 2017, it is possible to design two diffusion cells to capture the extrema in solution diffusion process.[81] If the diffusion cells can be made different enough to represent the both rate limiting cases, the model's extremes should be measurable. Figure 5-1 & Figure 5-2 shows the pH dependence for a feasible membrane-controlled and aqueous boundary layer-controlled diffusion cell. The ordinate axis is Ξ, is defined as the ratio of total membrane permeability to aqueous permeability.

$$\Xi = \frac{\left(K_{N-I}D_{N-I}f_{Aq_{N-I}} + K_I D_I\left(1-f_{Aq_{N-I}}\right)\right){h_m}^{-1}}{D_{Aq}{h_{Aq}}^{-1}} \qquad \text{Eq (5.43)}$$

If Ξ < 1, then the aqueous boundary layer permeability is larger than the membrane permeability meaning the system is limited by the membrane and is membrane controlled. If Ξ > 1, then the membrane permeability is greater than the aqueous permeability, meaning the system is limited by the aqueous boundary layer and is aqueous boundary layer controlled. When the stirring conditions area held constant (i.e. boundary layer thickness), the effect of pH can be observed. It is reasonable to suspect that the partition coefficients are much more sensitive and significant variables to examine than the aqueous boundary layer as partition

coefficients can change by multiple orders of magnitude and boundary layer thicknesses may vary by 1/100 to ½ an order of magnitude. Ibuprofen's intrinsic non-ionized partition coefficient is ~65, so estimating from Figure 5-1 & Figure 5-2 the absorption rate under non-ionized conditions the RMDC should be valid for extraction theory (membrane controlled) and the UTLAM diffusion cell should be valid for film theory (aqueous boundary layer controlled). As the pH increases, both cells Ξ will drop exponentially.

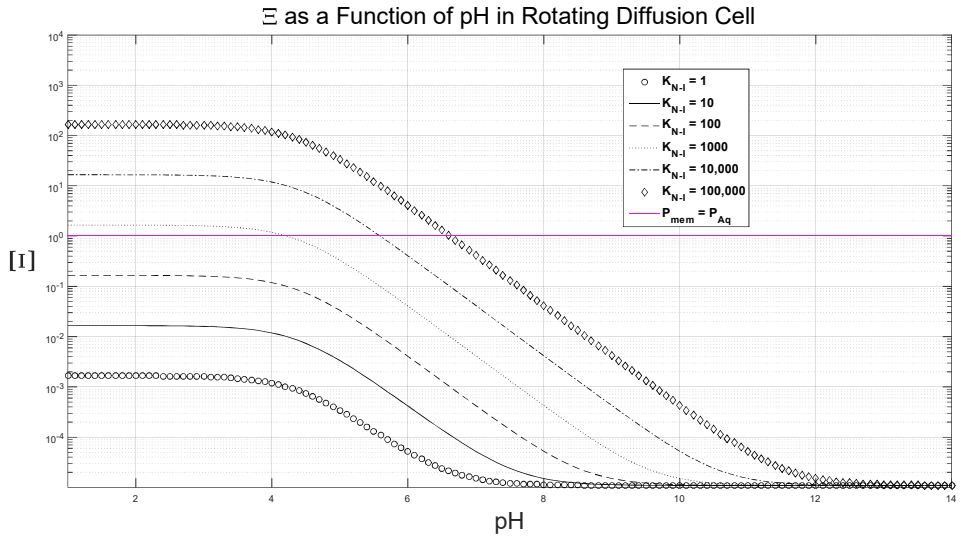

Figure 5-1 Examining the relative permeability of the PDMS UTLAM compared to the permeability of the aqueous boundary layer as a function of pH.

When the trend is above the magenta line, the permeability of the membrane is greater than the aqueous boundary layer. When the trend is below the magenta line, the membrane is less permeable than the aqueous boundary layer. Examining the pH of interest, the rate limiting step to diffusion can be determined at a glance. In the rotating membrane diffusion cell, the thickness of the membrane is intentionally much thicker than the UTLAM diffusion cell. The ratio of h_{Aq} to h_m is constant in this plot, only the pH dependent partition coefficient is varied.

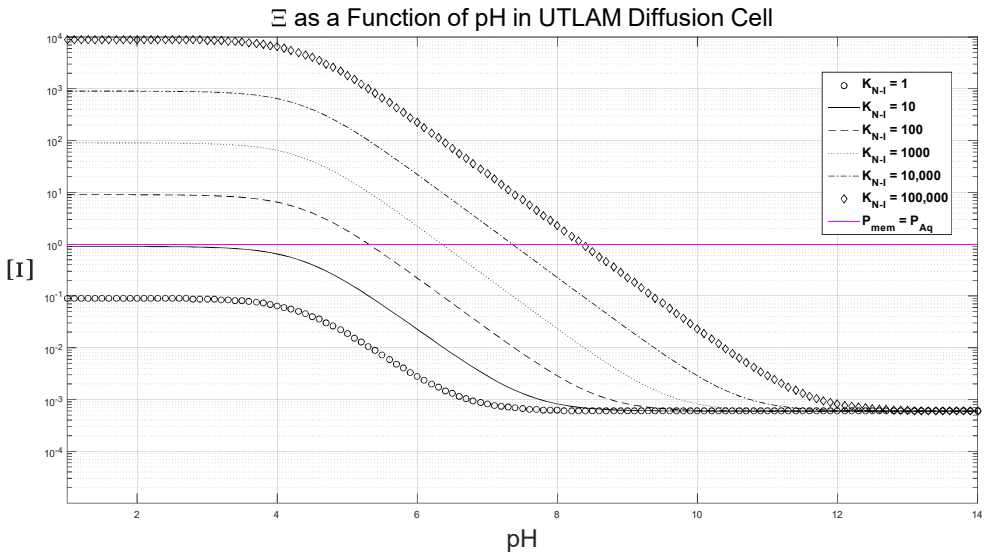

Figure 5-2 Examining the relative permeability of the PDMS RMDC compared to the permeability of the aqueous boundary layer as a function of pH.

This is the same plot as in Figure 5-1, however performed at a different ratio of h_{Aq} to h_m that is consistent with the ratio in the UTLAM diffusion cell.

5.4.3 2 Membrane rate limited diffusion

To test whether extraction and film theory apply under experimental conditions feasible to create in the lab, two types of diffusion cells are tested. The first, with a membrane permeability much lower than the permeability of the aqueous boundary layer. This setup allows for the membrane to dominate diffusion. Theoretically, if extraction theory is valid in the PDMS diffusion system, this membrane-controlled diffusion cell should meet the most important criteria for Wagner's model, "The rate at which drug leaves the membrane dominates absorption". A prediction using both extraction theory and film theory using the actual, independently measured parameters for the RMDC are shown in Figure 5-3. The differences in the apparent absorption rate in Figure 5-3 are the effect of the aqueous boundary layer and a consequence of how the extraction theory model calculates the first order rate of

appearance from the membrane. The difference between the two theories is the volume over which the first order rate constant acts. In extraction theory membrane volume is chosen and in film theory the fluid phase of interest (donor or receiver) is chosen.

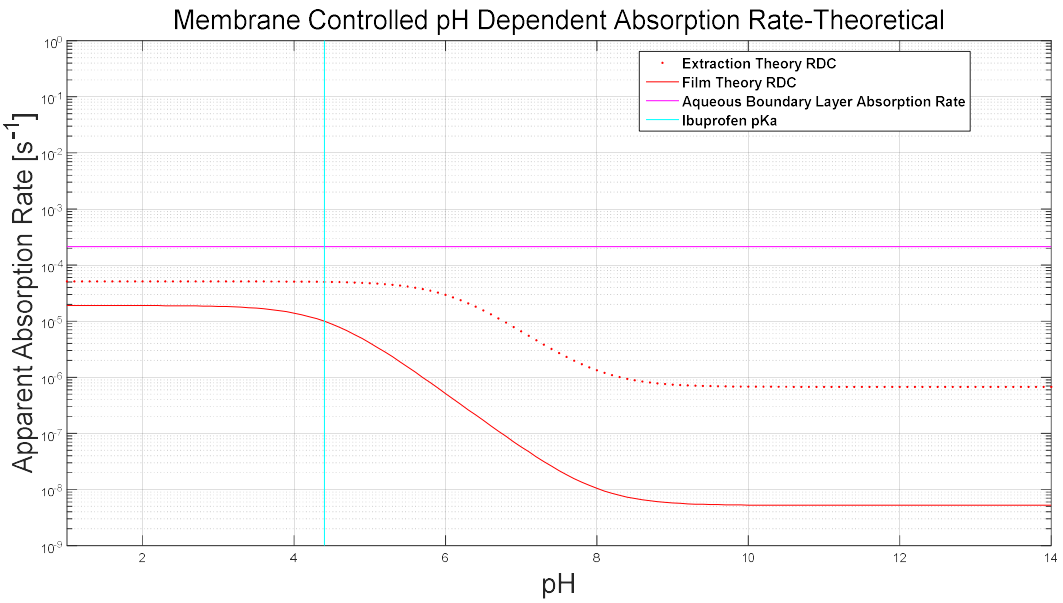

Figure 5-3 Comparison of Extraction Theory to Film Theory for RMDC.

Theoretical prediction of the pH dependent absorption behavior of ibuprofen based on extraction and film theory for the rotating membrane diffusion cell. The magenta line is the predicted aqueous boundary layer absorption rate. The blue line indicates ibuprofen's pKa. The red dotted line is Wagner and Sedman's extraction theory absorption rate, while the solid red line is the film theory absorption rate.

Neither the apparent absorption rate for extraction or film theory can achieve rates as high as the known aqueous boundary layer absorption rate.

5.4.3 3 Aqueous Boundary Layer Limited Diffusion

One of the most challenging aspects to implementing *in vivo* relevant dissolution methodologies with absorption abilities is how to set the absorption rate to a realistic rate. The most direct method is to change parameters such as surface areas, or

membrane thicknesses to increase or decrease the absorption rate as desired. The challenge is doing so without having to redesign the diffusion cell for every molecule that makes it into preclinical evaluation. One potential solution is to create polymer membrane that is more permeable than the aqueous diffusion layer, thus absorption rate could be controlled by stirring or lack of stirring in addition to hardware modification. However, extraction theory tells us that since the membrane controls the flux, it would be possible to have absorption rates greater than the absorption rate through the aqueous boundary would permit if the intrinsic non-ionized partition coefficients are sufficiently high. Film theory contradicts this assertion, and claims that as the membrane permeability becomes infinite, the flux is limited by the aqueous boundary layer thickness. As in section 2.3.2. a prediction using independently measure parameters for the UTLAM diffusion cell are made for both extraction theory and film theory in Figure 5-4.

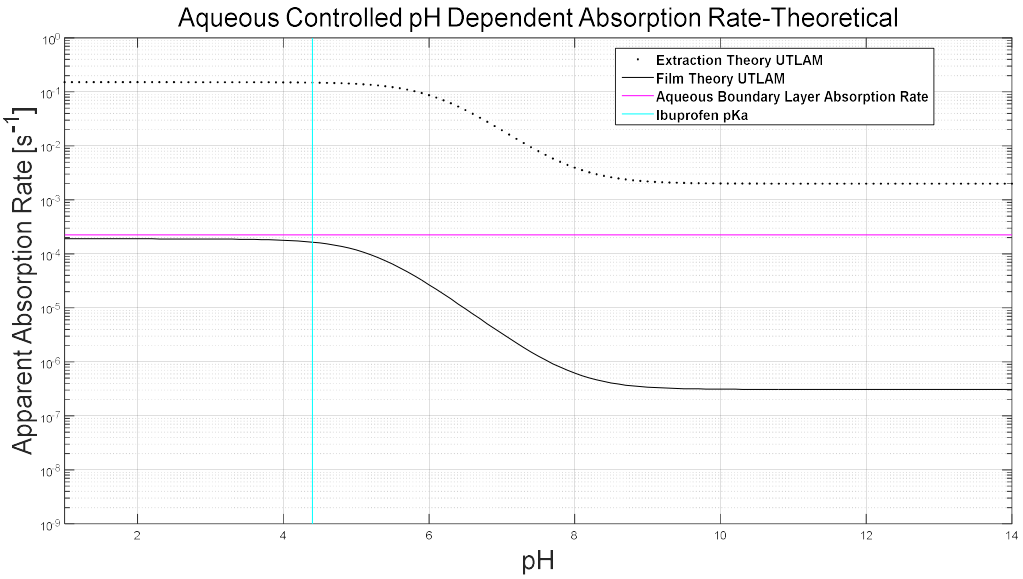

Figure 5-4 Comparison of Extraction Theory to Film Theory for UTLAM Diffusion Cell.

Theoretical prediction of the pH dependent absorption behavior of ibuprofen based on extraction and film theory for the UTLAM diffusion cell. The magenta line is the predicted aqueous boundary layer absorption rate. The blue line indicates ibuprofen's pKa. The black dotted line is Wagner and Sedman's extraction theory absorption rate, while the solid black line is the film theory absorption rate. It should be noted that extraction theory posits that the absorption rate is governed by the membrane. For ultra thin membranes, the permeability can be much higher than the aqueous boundary layer, leading to predictions of absorption that supersede the absorption rate of the aqueous boundary layer.

5.4.4 Experimental Result

5.4.4 1 Experimental Constants

Table 5-3 A brief description of the quantities used in the MATLAB code to produce the model predictions.

Property	UTLAM	RDC
PDMS K_{N-I}	64.56	64.56
PDMS K_I	0.245	0.245
$h_{Membrane}$	12.5 $x10^{-4}$ cm	680$x10^{-4}$ cm
$h_{Aqueous}$	37.3 $x10^{-4}$ cm	36.1 $x10^{-4}$ cm
$V_{Membrane}$	0.0273 cm^3	0.4359 cm^3
$V_{Receiver}$	219 cm^3	70 cm^3
$A_{Membrane}$	21.8 cm^2	6.41 cm^2
$D_{Aqueous}$	8.41 $x10^{-6}$ cm^2 s^{-1}	8.41 $x10^{-6}$ cm^2 s^{-1}
$D_{Membrane\ N-I}$	2.404 $x10^{-7}$ cm^2 s^{-1}	2.404 $x10^{-7}$ cm^2 s^{-1}
$D_{Membrane\ I}$	1.586 $x10^{-8}$ cm^2 s^{-1}	1.586 $x10^{-8}$ cm^2 s^{-1}
pKa	4.4	4.4

5.4.4 2 Extraction Theory vs Experimental

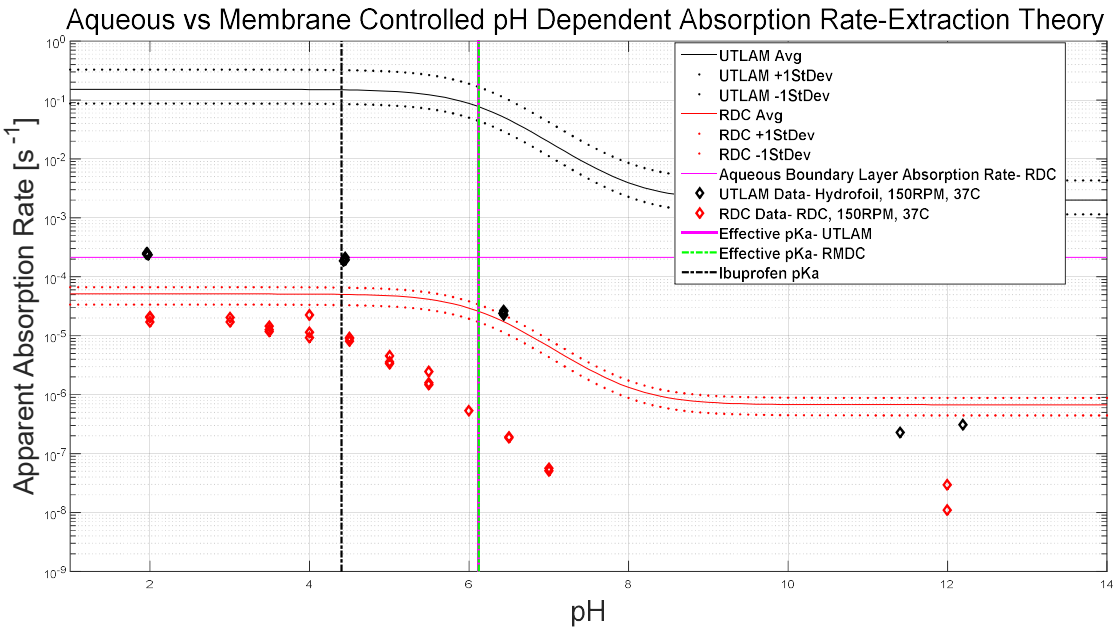

Figure 5-5 Extraction Theory Prediction of Absorption Rate compared to Experimental Data.

Experimental data produced along the pH spectrum in both the rotating diffusion cell and UTLAM diffusion cell. The most noticeable feature of this figure is that the experimental results do not exceed the predicted aqueous boundary layer absorption rate. This proves that the equilibrium extraction model does not apply in the two *in vitro* devices tested. The dotted lines indicate ne standard deviation on the membrane thickness. The standard deviation of the UTLAM (black curves) thickness was only 0.2μm however at that length scale the permeability is very sensitive to small changes in thickness, thus the seemingly large error bars.

In Figure 5-5, comparisons are made between the rotating membrane diffusion cell and the UTLAM diffusion cell experimental data, and the theoretical predictions for extraction theory. One notable quality is that the UTLAM permeability is not able to achieve the extreme absorption rates which are predicted by the the UTLAMs extreme thinness. There is clearly another physical factor limiting the flux of drug through the membrane, thus proving that the rate at which drug leaves the membrane governs the rate of appearance is not a valid assumption for this system. Surprisingly, the rotating membrane diffusion cell also fails to obey extraction theory. It is most

likely due to the same physical factor that enabled the UTLAM diffusion cell to fail, as there were very little experimental differences that could cause this type of behavior to happen. Another observation is that the apparent shift in the pKa is significantly larger in the model than what appears to be the shift in the experimental data for both diffusion cells.

5.4.4 3 Film Theory vs Experimental

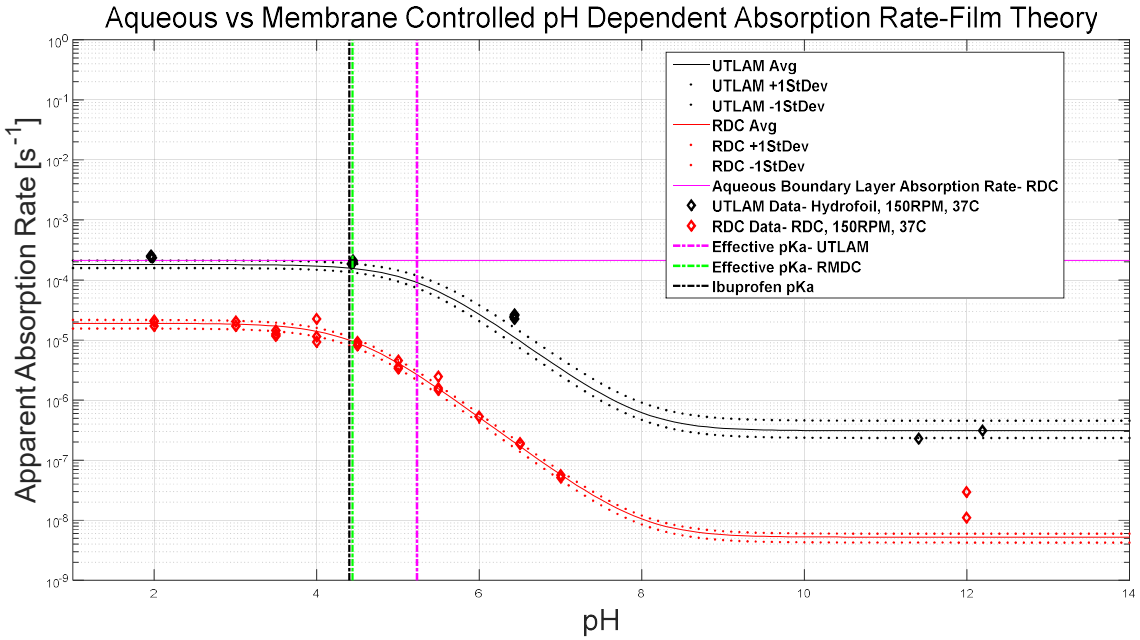

Figure 5-6 Film Theory Prediction of Absorption Rate compared to Experimental Data.

With the same comparison as Figure 5-5, this figure shows the data compared to film theory. The two diffusion cells have slightly different shaped curves. This is indicated by the distance between the vertical dashed lines, which is the inflection point of the curve (second derivative with respect to pH set equal to zero). For both vertical lines, a shift away from the natural solution pKa occurs, which means that the range of pH that ibuprofen (in this case, but applicable to all lipophilic molecules) is absorbed at at less 50% of the maximum absorption rate is extended. The implication is that drug can experience variable pH along the gastrointestinal tract, and if the absorption was assumed to be proportional only to the non-ionized fraction, it is very likely that the absorption rate is underestimated. This is particularly important for BCS II acidic drugs where the solution solubility is increased as the pH transitions from the stomach to the duodenum/jejunum. In this case, the driving force for dissolution goes up, more drug is in solution, and depending on the lipophilicity, the absorption rate may not significantly decrease from maximum absorption rate.

The same experimental data generated on both diffusion cells now plotted against the film theory models in Figure 5-6. There appears to be good agreement between the models and data, implying that the aqueous boundary layer is a significant part of the absorption process. In the case of the UTLAM diffusion cell it proves to be the limiting factor. Extraction theory and film theory results in a very different behavior of the apparent shift in the pKa. In film theory both the aqueous boundary layer and non-ionized partition coefficient affect the magnitude of the apparent shift in the pKa. The apparent shift in the pKa in the UTLAM data is 5.234 from 4.4 and 4.441 from 4.4 for the RMDC.

5.5 Variation of Parameters/Sensitivity Analysis

5.5.1 Apparent Absorption Rate

5.5.1 1 Membrane Limited Apparent Absorption Rate

When the permeability of the membrane is much lower than the aqueous boundary layer, it is expected that hydrodynamic effects have less influence on the absorption rate. In Figure 5-7 & Figure 5-8, the model inputs (such as ibuprofen pKa, etc.) are held constant except for pH, non-ionized partition coefficient, and aqueous boundary layer thickness. It becomes clear from Figure 5-7 & Figure 5-8, that the only difference between the RMDC and UTLAM is a matter of membrane thickness. As the non-ionized partition coefficient is increased, the maximum apparent absorption rate increases until it approaches the aqueous boundary layer absorption rate which the membrane cannot overcome. As the maximum absorption rate approaches the upper limit, the shift of the whole curve steadily moves towards the right. This indicates

that the increased partition coefficient is allowing for not only higher maximum absorption rates, but also higher rates over a wider range of pH.

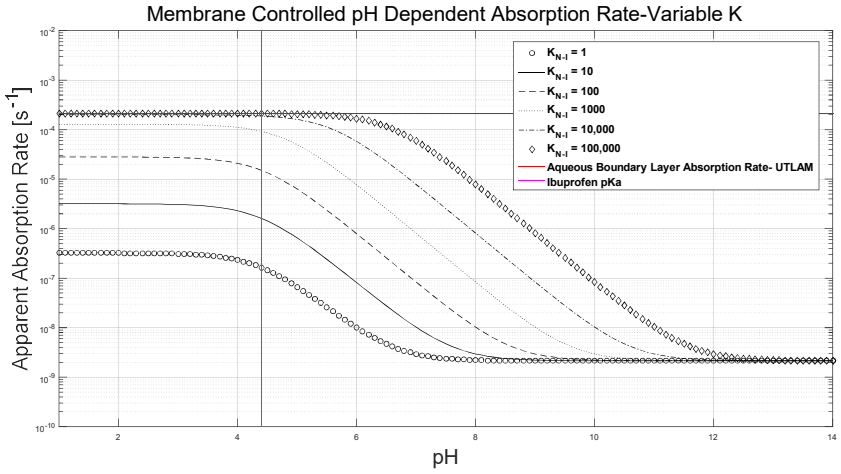

Figure 5-7 Effect of Varying Partition Coefficient in Membrane Diffusion Limited Regime.

When the membrane limited the diffusion of drug into the receiver chamber, the partition coefficient dominates the absorption rate. To achieve absorption rates that approach the maximum in this case, the molecule needs to have a very large intrinsic non-ionized partition coefficient.

As expected, when the aqueous boundary layer thickness is varied to a reasonable degree there is little sensitivity in the membrane-controlled absorption rate.

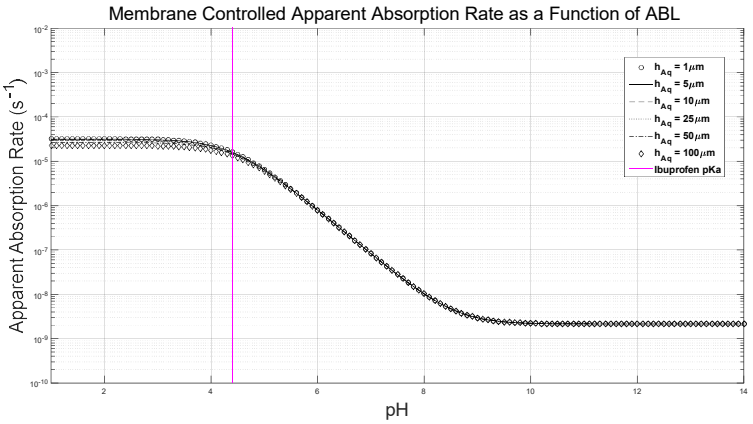

Figure 5-8 Effect of Varying Aqueous Boundary Layer Thickness in Membrane Diffusion Limited Regime.

When the membrane limits drug diffusion into the receiver chamber, the aqueous boundary layer of this physical situation should not significantly alter the absorption rate.

5.5.1 2 Aqueous Diffusion Layer Limited Apparent Absorption Rate

At the other extreme, where the permeability of the membrane is greater than the aqueous boundary layer, the responses to aqueous boundary layer thickness and partition coefficient differ are examined in Figure 5-9 & Figure 5-10. In the first case where only the partition coefficient is varied, it was observed that even at low partition coefficients, significant absorption occurs. At moderate partition coefficients, the maximum absorption rate is achieved, and the only thing gained by a higher partitioning affinity is a shift in the apparent pKa. The degree of the shift is much greater in the aqueous diffusion layer limited case as compared to the membrane limited case.

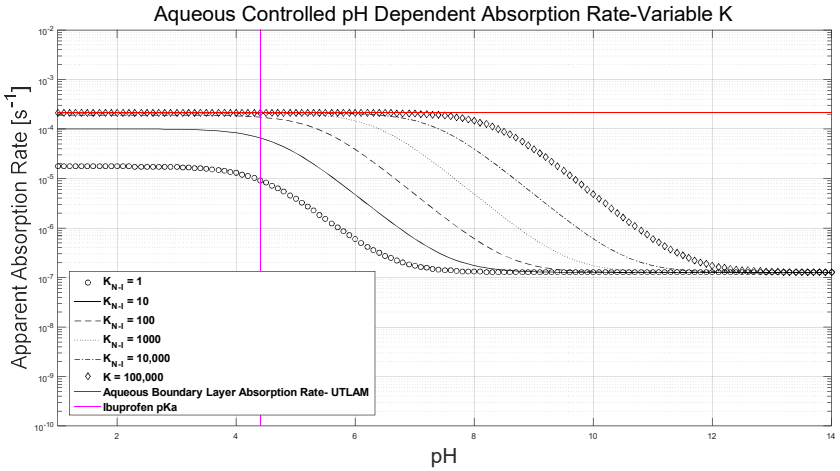

Figure 5-9 Effect of Varying Partition Coefficient in Aqueous Diffusion Limited Regime.

This figure shows the absorption rate when the membrane permeability is much higher than the aqueous boundary layer permeability. It does not take much lipophilicity to achieve maximum absorption rates, and lipophilicity of the molecule increases, the shift in the apparent pKa increases much more than was observed in the membrane limited response to increasing partition coefficient. For very oily acidic drugs, this will allow for more complete absorption along the entire length of the intestinal tract.

When the aqueous boundary layer is varied the effect is essentially only visible in the intrinsic non-ionized absorption rate. As the boundary layer thickness

decreases, the maximum absorption rate increases. Interestingly, as the boundary layer thickness decreases, the apparent shift in the pKa does not shift to the right as it has in the other three cases presented. In fact, as the boundary layer decreases, the apparent pKa converges on the natural pKa of the molecule in solution. This proves that the shift in the pKa is an aqueous boundary layer phenomenon. Mathematically, as the series permeability of the aqueous contribution increases so much, that the only significant term left is the pH dependent membrane permeability. It is the influence of the aqueous boundary permeability term which causes the deviation from the expected pKa. It is also worth noting that as the boundary layer increases, that the apparent shift in the pKa also increases, while the maximum absorption rate decreases. This occurs because the aqueous boundary layer permeability drops to a level which affects the total permeability (lowering the rate and suppressing the pH effect on the total effective partition coefficient).

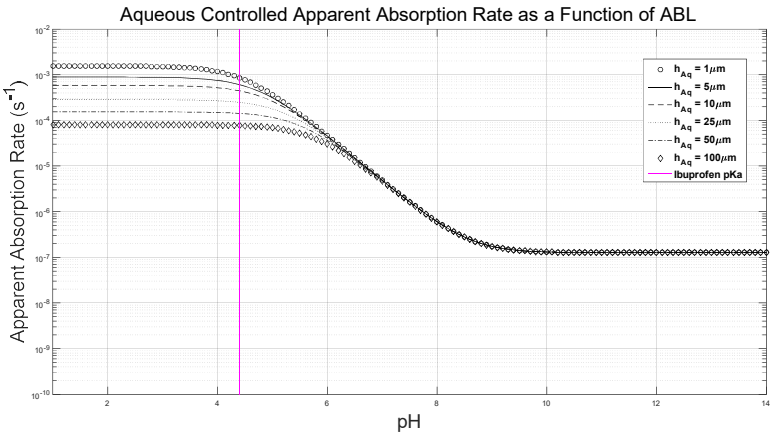

Figure 5-10 Effect of Varying Aqueous Boundary Layer Thickness in Aqueous Diffusion Limited Regime.

It is only when the membrane is not rate limiting that the effect of the aqueous boundary layer on absorption rate can be observed. As the aqueous boundary layer thickness decreases the permeability increases leading to faster absorption rates. However, because the aqueous component of the permeability begins to dominate the effect permeability term, the effective pH-dependent permeability of the film model loses its ability to overcome solution pH affect on the molecule's absorption ability. The term that is affected by pH is the membrane permeability so as the aqueous boundary layer thickness decreases, the apparent shift in the pKa returns to the natural pKa in solution.

5.5.2 Absorption Function

5.5.2 1 Membrane Limited Absorption Function

To better illustrate the trend of the shift in apparent pKa, the absorption rates area normalized by the maximum absorption rate and defined as the "absorption function". This procedure was also performed by Winne when he analyzed the extraction theory models.[100] Maximum absorption rate occurs at $f_{\text{Aq N-I}} = 1$, resulting the following equation.

$$AF = \frac{k_{app(pH)}}{k_{app_{MAX}}} = \frac{\left(\frac{h_{Aq}}{D_{Aq}} + \frac{h_m}{K_{N-I}D_{N-I}f_{Aq_{N-I}} + K_I D_I\left(1-f_{Aq_{N-I}}\right)}\right)^{-1}}{\left(\frac{h_{Aq}}{D_{Aq}} + \frac{h_m}{K_{N-I}D_{N-I}}\right)^{-1}} \qquad \text{Eq (5.44)}$$

Figure 5-11 & Figure 5-12 show that at 0.5 absorption function a clear response of the pKa to partition coefficient and a lack of response to the aqueous boundary layer.

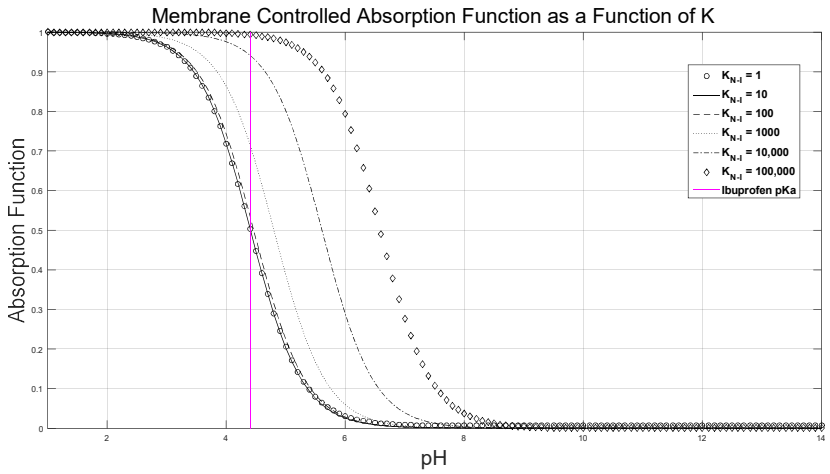

Figure 5-11 Effect of Varying Partition Coefficient in Membrane Diffusion Limited Regime on Absorption Function.

Calculating the absorption function allows for an easy comparison of the shift in the apparent pKa of the absorption rate curves. In this figure, the shift in the absorption curve for the membrane-controlled system with variable partition coefficients are plotted. Tracing a line at the ordinate axis value of 0.5, and examining the corresponding pH tells you at what pH the absorption rate has dropped to half of maximum.

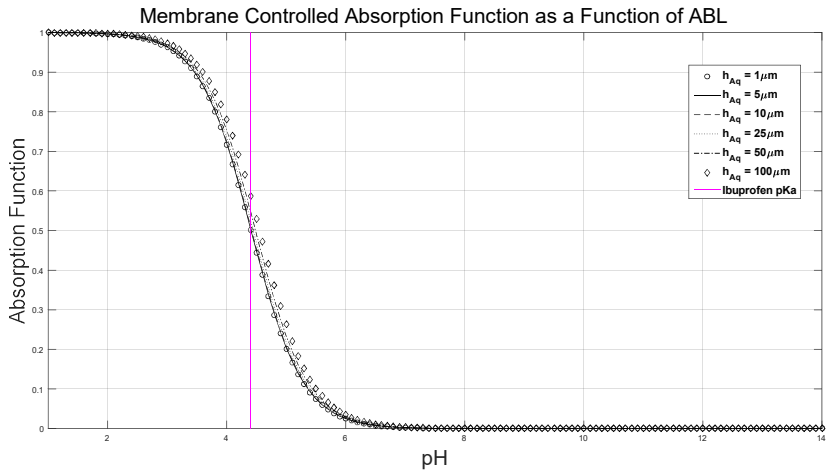

Figure 5-12 Effect of Varying Partition Coefficient in Membrane Diffusion Limited Regime on Absorption Function.

The same a Figure 5-11, but varying aqueous boundary layer thickness instead of partition coefficient.

5.5.2 2 Aqueous Boundary Layer Limited Absorption Function

Similar to section 5.5.2.1 in calculation, the absorption function plots in **5-13** & **5-14** instead shows that aqueous limited absorption has a much greater sensitivity to partition coefficient and aqueous boundary layer thickness.

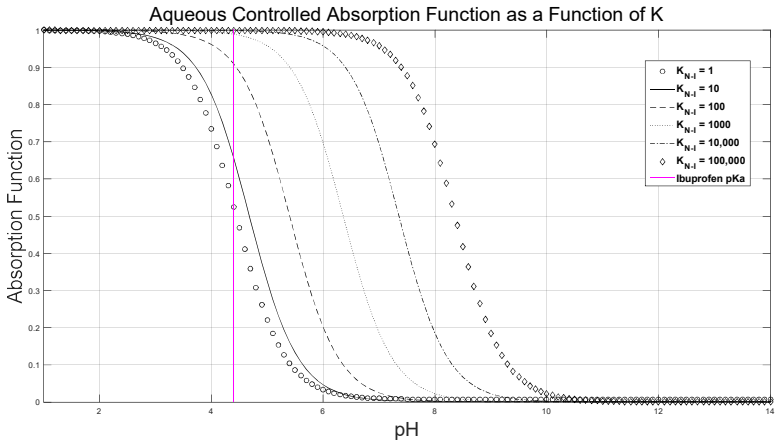

Figure 5-13 Effect of Varying Partition Coefficient in Aqueous Diffusion Limited Regime on Absorption Function.

This figure can be compared to Figure 5-14 to demonstrate the potential of implications of using UTLAM as an absorption medium in dissolution methodologies.

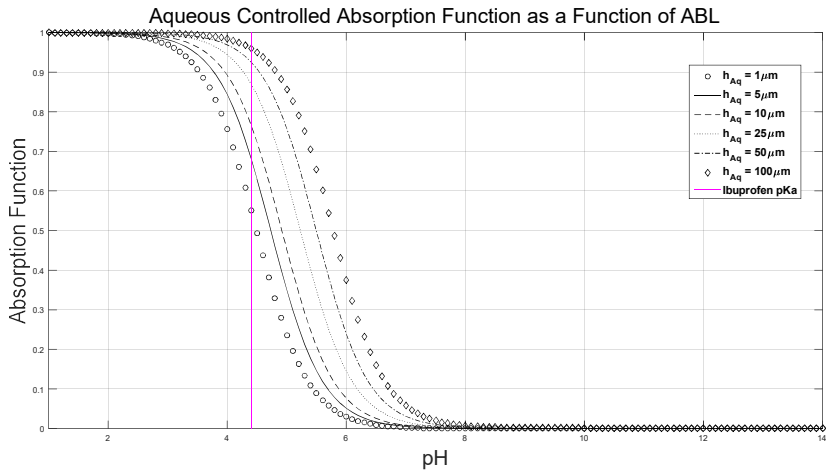

Figure 5-15 Effect of Varying Aqueous Boundary Layer Thickness in Aqueous Diffusion Limited Regime on Absorption Function.

As expected from the absorption rate figures, the aqueous boundary layer in the aqueous controlled system shows a shift to the left in apparent pKa as the boundary layer thickness decreases.

5.5.3 Apparent Shift in pKa

5.5.3 1 pKa shift as a function of Aqueous Boundary Layer Thickness

To determine the exact value of the apparent shift in pKa the second derivative of the absorption rate function was calculated in MATLAB. The second derivative is defined as the inflection point, which occurs at the pKa or 50% of maximum absorption rate.

$$\frac{\partial^2}{\partial pH^2} AF(pH) = \frac{\partial^2}{\partial pH^2}\left[\frac{\left(\frac{h_{Aq}}{D_{Aq}}+\frac{h_m}{K_{N-I}D_{N-I}f_{Aq_{N-I}}+K_I D_I\left(1-f_{Aq_{N-I}}\right)}\right)^{-1}}{\left(\frac{h_{Aq}}{D_{Aq}}+\frac{h_m}{K_{N-I}D_{N-I}}\right)^{-1}}\right] \quad \text{Eq (5.45)}$$

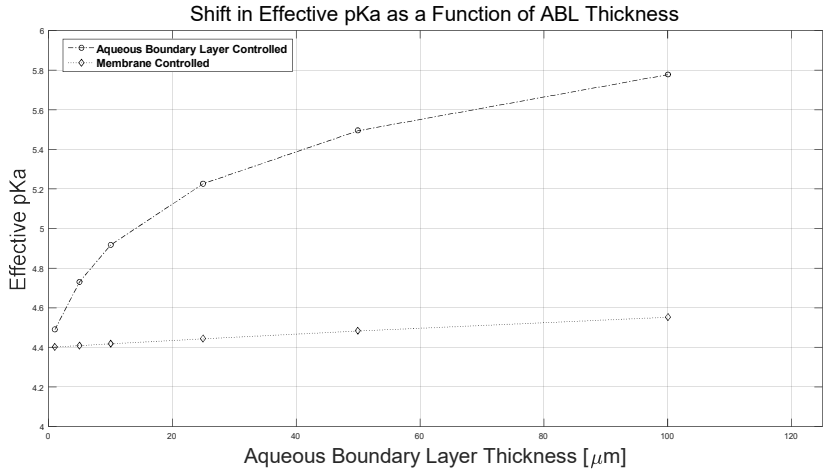

Figure 5-16 Apparent pKa Shift as a Function of Aqueous Boundary Layer Thickness.

Quantification of the apparent pKa shift in both the rotating diffusion cell and UTLAM diffusion cell as a function of aqueous boundary layer thickness. This figure demonstrates the significant affect that stirring can have on the absorption rate of a molecule at pH near or above its natural pKa.

Typically, the aqueous boundary layer at the absorption surface can be altered by agitation. Figure 5-16 provides an idea of how the the maximum absorption rate can be influenced by the experimental setup. Faster stirring leads to a faster absorption rate, but the molecule becomes more susceptible to pH. The difference between the two predicted lines is that the diffusion is membrane limited or aqueous boundary layer limited.

5.5.3 2 pKa shift as a function of Intrinsic Non-Ionized Partition Coefficient

It is not usually possible to change a molecules lipophilicity in relationship to a specific polymer. However, it is possible to change polymer systems or chemically modify the drug molecule of interest, and the result of this is shown in Figure 5-17. Thinking from the perspective of drug candidate selection for preclinical evaluation, drug candidates could be designed to resist the affects of pH by estimating their necessary PDMS partition coefficient for maximum absorption, and then chemically

tailoring the molecule to that partition coefficient. Another approach would be to change polymer systems, and if the membrane behaves according to the *in vivo* relevant hypothesis and transports drug at a physiological rate, the substitution for PDMS could be made. As has been discussed, there is a limit (aqueous boundary layer) for solutions in absorption that can only be overcome by some external modification of either the solubility of the drug or affinity for the membrane. PDMS is not the only polymer that can meet the mechanical, physical, and chemical demands for an appropriate *in vivo* relevant membrane material.

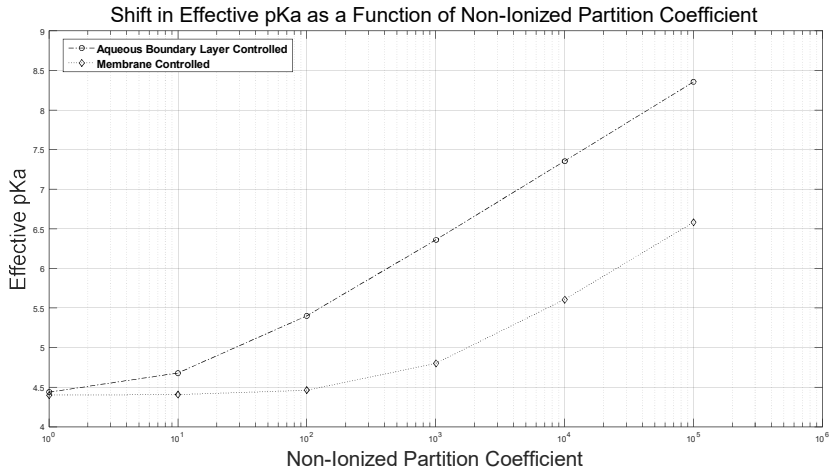

Figure 5-17 Apparent pKa Shift as a Function of Aqueous Boundary Layer Thickness.

Quantification of the apparent pKa shift in both the rotating diffusion cell and UTLAM diffusion cell as a function of intrinsic non-ionized partition coefficient. This figure shows that different polymer systems or different drugs (depending on how you modulate the partition coefficient) will have a large affect on the absorption rate.

5.6 Discussion

It is clear from the experimental data that the film theory model is able to predict solution diffusion at both the membrane diffusion limited and aqueous boundary layer limited threshold of pure solution diffusion. The apparent first order absorption rate for solutions is limited by the non-ionized partition coefficient and to a lesser

extent the thickness of the aqueous boundary layer thickness. The aqueous boundary layer thickness can suppress the pH effects on absorption rate when the boundary layer is relatively large, however the gain in the range of pH that maximum absorption occurs is directly traded off as the magnitude of the maximum absorption rate drops. It is possible to begin to select drug candidates for specific lipophilicities which can enhance the absorption performance for specific regions of the oral absorption pathway.

5.7 Acknowledgments

I would like to especially thank Sarah Harris for generating the rotating diffusion cell data. I would like to thank Niloufar Salehi for assisting in writing the MATLAB code to determine the second derivative of the apparent absorption rate in MATLAB and Pamela Meyer for assisting in preparing/conducting some of the UTLAM diffusion cell experiments.

CHAPTER 6

Particle-Size and Dose Effects on Diffusion Flux Through an Ultra-Thin, Large-Area Poly(dimethyl siloxane) Membrane

6.1 Abstract

As mentioned in chapter 2, interest in modeling the effect of particle size and dose on the flux through the membrane is critical to understanding how disintegrating and dissolving formulated products interact with the gastrointestinal environment. A dissolution apparatus was introduced that overcomes some limitations of the compendial apparatus and demonstrate the characteristics of the ultra-thin large area polydimethylsiloxane (PDMS) membrane (UTLAM) absorption system. A particle size-dose dependent particle dissolution-absorption model are presented. Two methods of supporting the UTLAM are investigated, one of which is designed to trap particles at the surface of the membrane and the other designed to allow particles to flow freely past the membrane surface. For all experiments, the diffusion cell was warmed to 37°C and stirred at 150RPM with a 1.5" hydrofoil. A 11.2 ± 0.5μm thick, 25.2cm^2 (44.4cm^2 total) PDMS membrane was fastened between two mesh supports. Experiments were conducted at pH 1.9-2.0 in the donor and pH 12.5 in the

receiver using ibuprofen as a model weak acid drug. An ImageJ routine was used to analyze microscopic images of particles and calculate equivalent spherical diameters to generate mass distributions with respect to drug particle radius. Dissolution occurs in the ABL and has significant affects on the flux. In non-pre-saturated suspension experiments conducted with PSD $r_{50\text{-mass}}$ = 3.7μm, 18μm, 117μm ($r_{50\text{-number}}$ = 1.2μm, 5.4μm, 64μm) at doses (0.2, 1, 10, and 40mg/mL) achieved flux enhancements relative to the maximum solution flux of $(-17\% \text{ to } 265\%)|_{R_{50}} =$ 3.7μm, $(-6\% \text{ to } 159\%)|_{R_{50}} = 18$μm, $(-79\% \text{ to } 74\%)|_{R_{50}} = 117$μm. In all PSD's, an unaccounted for increase in flux was observed at high doses and was most likely due to particles settling. In thick mesh experiments it was observed that particles larger than the ABL experienced flux enhancement because they were pinned to the membrane surface. In all three PSD tested, increasing dose lead to a flux enhancement. The UTLAM PDMS diffusion cell improved the hydrodynamics in the donor phase, and mimics *in vivo* relevant absorption kinetics. In all particle size distributions, an unaccounted effect was observed at high doses, an increase in flux, and is most likely due to particles settling on the membrane surface. Additionally, in thick mesh experiments it was observed that particles larger than the ABL experienced flux enhancement when pinned to the membrane surface. In all three particle size distributions tested, increasing dose lead to an enhancement in flux through the membrane. A diffusion-controlled polymer membrane was incorporated into a dissolution apparatus to mimic the passive *in vivo* absorption pathway. A hydrofoil was implemented to reduce coning, promote particle re-suspension, and homogenize bulk fluid shear. Micronization of particles and large doses has been

demonstrated to contribute to the "shorting-out" of the ABL. Particle size is dominant in the interplay between particle size and dose, but high doses can induce settling which can increase the flux more than particle size would normally allow. Even though the PSD fractions used had a wide range of particles, it seems that the average radius is sufficient to predict performance. Particles smaller than the average most likely contribute more to saturating the solution while larger particles contribute to the steady state dissolution due to smaller changes in radius with respect to time. Ultimately, the UTLAM PDMS diffusion cell provides a more realistic dissolution experiment by improving upon the hydrodynamic and kinetics aspects of the compendial dissolution apparatus.

6.2 Introduction

Dissolution is a critical process for solid oral dosage forms because only molecular drug can permeate the gastrointestinal membrane and enter systemic circulation.[12, 13] For BCS II and IV (low solubility/high permeability & low solubility/low permeability) orally administered solid dosage forms there are significant challenges with solubilizing drug for intestinal absorption. Ultimately, many formulation practices such as, micronization, suspensions, addition of surfactants (micelles & colloids), amorphous solid dispersions, self emulsifying drug dispersions, salt forms, and co-crystals have been introduced to increase the drug exposure to the gastrointestinal lumen in order to increase the flux across the gastrointestinal membrane.[107-110] Some of these methods work by kinetically altering the solubility of the drug molecule while others work by changing the diffusion and

convection processes that occur. This work focuses on the technique of micronization of solid drug particles to enhance dissolution *in vitro* and *in vivo*. We propose a model to analytically describe the process which has been informally referred to for many years as "shorting-out" the aqueous boundary layer.

The aqueous boundary layer or stagnant diffusion layer is a concept that originates from the Navier-Stokes incompressible fluid flow concept of "no-slip" at the interface of a fluid and a solid. When fluid is in contact with a solid surface, the viscose force (frictional forces between fluid molecules), and weak attractive forces (hydrogen bonding/London dispersion forces) between the liquid and solid molecules can overcome convection forces at the surface of a microscopically rough surface. This leads the velocity components of the fluid dropping to zero in the directions tangential to the solid surface, which in classical fluid mechanics is defined as the "no-slip" boundary condition. Similarly, when the velocity of the fluid perpendicular to the solid surface drops to zero, the boundary condition is called an "impermeable wall".[35] This stagnation of the fluid at the solid surface has been described as far back as 1904 by Nernst-Brunner as an extremely thin film that coats the solid surface. The implication is that there is some balance point some distance from the solid surface where the combination of the fluid viscosity and the weak attractive forces are overcome by the convection forces of the "bulk" fluid. This balance point is considered to be the thickness of the stagnant fluid layer. In this approach, Nernst & Brunner assumed that there is no fluid convection and only molecular diffusion motion acts to transport mass within the boundary layer (i.e. that the fluid is static). However, Levich was able to understand that the tangential

convection plays an important role in the convection-diffusion transport of the solute.[111] He famously derived the equations for determining the hydrodynamic boundary layer thickness for the popular rotating disk apparatus, now commonly used in pharmaceutics to determine dissolution rates of solid drug powders.

$$J_{Lev} = 0.62 \cdot D^{\frac{2}{3}} \cdot \nu^{-\frac{1}{6}} \cdot \omega^{\frac{1}{2}} \cdot \Delta C \quad \text{Eq (6.1)}$$

$$\delta_{Levich_{rotating\ dsk}} = 1.61 \left(\frac{D}{\nu}\right)^{\frac{1}{3}} \left(\frac{\nu}{\omega}\right)^{\frac{1}{2}} \quad \text{Eq (6.2)}$$

A commonly held belief in the pharmaceutics field is that the hydrodynamic boundary layer only contains molecular solute and no solid particles exist within that layer. This maybe because in the Nernst-Brunner static boundary layer (film theory) it is believed that the hydrodynamic boundary layer is a physical barrier in which particles cannot flow in or out. However, there is no actual physical barrier formed. The only physically valid reason to believe that particles will not act within the hydrodynamic boundary "layer" is if the particles are physically longer than the thickness of the boundary layer. Even so, the particle is not prevented from contacting the solid surface, it would be partially interacting with the surface fluid and bulk fluid. Now since large particles longer than the length scale of the boundary layer will have a lower chance of being able to perform dissolution within the boundary layer, the assumption is that they mostly act in the bulk fluid and the static Nernst-Brunner boundary layer convention is satisfied. However, there are two ways to overcome the maximum diffusion limited flux from a conceptual stand-point. 1) Change the length scale of the dissolving particles to a length that is less than or equal to the length of the hydrodynamic boundary layer. This would allow dissolving particles a higher probability to be located within the "stagnant" diffusion layer. 2) By

increasing the population of particles, the interparticle distance decreases and ultimately forces particles to the solid surface. This approach literally pushes particles into the "stagnant" boundary layer. The net effect of both scenarios is that the mean free path for diffusion is shortened below the conventional diffusion limit of the hydrodynamic boundary layer. By assuming that particles exist in mode 1, 2, or a combination of mode 1 & 2, the resistance to diffusion processes significantly changes and a flux enhancement is achieved. The following derivation describes this process analytically. It is assumed that the change in radius with respect to time of the dissolving particles must be very small, thus satisfying the pseudo-steady-state assumption. We examine the flux of monodisperse particles on a system of polydisperse particles.

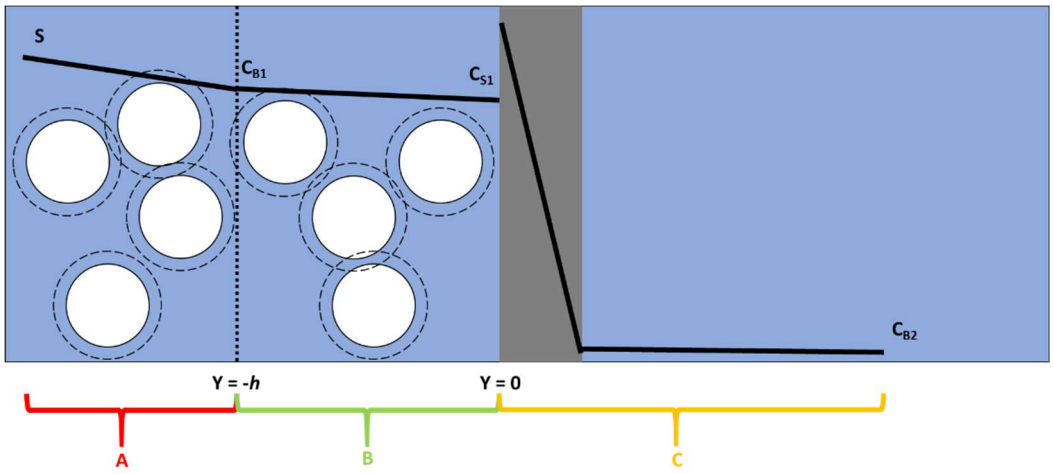

Figure 6-1 Schematic of the physical situation when particles are dissolving in a test apparatus with a diffusion-controlled membrane barrier.

The white circles represent mono-sized spherical drug particles, the dashed lines surrounding the indicate dissolution (not the boundary layer, the boundary layer in Higuchi Hiestand dissolution model is not well defined). The vertical dashed line represents the aqueous boundary layer thickness and is dashed to indicate that it is a theoretical construct not a physical barrier. The solid black lines indicate solution/solid concentrations of dissolved drug.

Figure 6-1 describes the physical situation. Region A in red is the bulk fluid containing the majority of solid drug particles. These particles produce a concentration gradient from the surface concentration, which is equal to drug solubility, to a concentration just below drug solubility at the point defined as (- h). - h is the interface of the bulk fluid region and the aqueous boundary layer. Particles are allowed to flow in and out of this interface. Region B is defined as the aqueous boundary layer. At steady state it is expected for a linear concentration profile to develop between points -h and 0 (the membrane surface). At 0, Region C begins. Region C includes the membrane and the entirety of the receiver phase. This assumption is valid when the receiver side aqueous boundary layer permeability is extremely high thus not contributing a resistance to diffusion. This can be easily achieved by vigorous stirring and completely ionizing the drug in the receiver compartment.

6.3 Materials & Methods

6.3.1 Preparation of Materials

1N hydrochloric acid (HCl) was diluted to 0.01N HCl and titrated to a pH of 2. 50mL of 0.2M of potassium chloride (KCl) was added to 26mL of 0.01N HCl and QS to 200mL of MilliQ purified deionized water. 0.9mM of sodium lauryl sulfate was added to the solution to aid in wetting the ibuprofen surface, to create optimal suspensions. 0.9mM sodium lauryl sulfate is below the critical micellar concentration, thus micelle formation is not expected to occur.

Ultra Thin Large Area Polydimethylsiloxane Membranes (UTLAM PDMS) were prepared on a Laurell Spin processor with 100mm diameter vacuum chuck. Undoped polished silicon wafers (diameter = 100mm) were coated with a 3% w/w solution of polyvinyl alcohol (PVA) in deionized water at 5000RPM (acceleration 5000), and vacuum annealed for 24 hours at 65°C to create a ~60nm film. The PVA coated silicon wafers were then coated with a 75% w/w solution of PDMS in hexane at 3000RPM (acceleration 3000) to produce a 11.2μm thick membrane. The PDMS coating was vacuum annealed at 65°C for 48 hours. The UTLAM PDMS was then floated from the wafer in 2-3L of deionized water (3 hours) and transferred onto a support screen. The support screen was a 2000μm sonic sieve with woven stainless-steel screen with 0.9mm diameter wire (max thickness = 1.8mm). Two of these sieves were cut down to flat disks and Gorilla Glue brand 5min epoxy was used to seal the outer diameters as well as smooth any defects from cutting. The upper and lower surfaces of the support screens were then sanded flat. Polytetrafluoroethylene (PTFE) tape was then used to seal each screen, covering the epoxy but not the stainless-steel mesh. The UTLAM PDMS was then scooped onto a screen in the float bath, and once removed and patted dry the other screen was gently placed on top to create a compact. This compact was wrapped tightly with PTFE tape and then vacuum heated at 65°C for 30min. The hot compact was then transferred to the glass diffusion cell and screw tightened while hot to ensure a tight seal. The second type of support was a laser cut 316 stainless steel (0.28mm thick). A similar PTFE wrapping procedure was performed to create the membrane component.

6.3.2 Methods

6.3.2 1 Determining the Diffusion Limited Flux Experiments.

A solution of 50μg/mL ibuprofen was created in 0.01N HCl. Appearance of ibuprofen was measured in the lower chamber, "receiver side", at 0, 2.5, 5, 7.5, 10, 12.5, and 15 minutes. The donor side concentration was measured at time 0 and 15 minutes to determine C_{Final}.

6.3.2 2 Determining Flux not limited by the Aqueous Boundary Layer.

A suspension of varying total concentration (solid + dissolved drug) was created using a slurry method. Dry Ibuprofen powder was weighed into a beaker, then 5-8 drops of hydrochloric acid buffer was dropped to wet the powder. Mixing with a spatula was performed until a dry paste was formed. Pre-warmed non-saturated buffer was then added to the beaker to form the suspension, and immediately deposited into the diffusion cell donor compartment to begin the experiment. Using non-saturated buffer results in some initial dissolution of the particles, however smaller particles dissolve faster than the large particles, so it is less likely that the average radius changed significantly during the preparation process.

6.4 Results

6.4.1 Variables & Definitions

Table 6-1 A brief description of the variables used in chapter 6.

Variable	Definition
D_{Aq}	Aqueous Diffusion Coefficient (cm^2/s)
M	Mass of particles (g)
V	Volume of fluid in the Donor side (cm^3)
r	Radius of a sphere (cm)
a or a_0	Average Radius of the spherical particle (cm)
ρ	Density of the drug (g/cm^3)
A_P	Surface area of the spherical particle (cm^2)
h	Aqueous Boundary Layer Thickness (cm)
K_{PDMS}	Partition Coefficient of Drug in PDMS (unitless)
D_{PDMS}	Diffusion Coefficient of Drug in PDMS (cm^2/s)
h_m	Thickness of the PDMS membrane (cm)
S	Saturation Concentration of Drug in Donor Fluid at a particular temperature and pH (g/cm^3)
Region A	The bulk fluid containing a saturated solution and solid drug particles
Region B	The donor side aqueous boundary formed assuming the no slip condition at the surface of the membrane
Region C	The membrane surface + receiver side boundary layer + the receiver side bulk fluid
P_A	Permeability of Drug through Region A a.k.a. particle dissolution into Bulk (cm/s)
P_C	Permeability through Region C (cm/s)
P_{eff}	The series sum of the permeability resistances or experimentally determined permeability (cm/s)
C_{B1}	The interfacial concentration between Region A and Region B (g/cm^3)
C_{B2}	The bulk concentration of the receiver side (g/cm^3)
C_{S1}	The concentration at the surface of the membrane (a.k.a. the interfacial concentration between Region B and Region C) (g/cm^3)
λ	Characteristic Length of a dissolving particles (cm^{-1})
v	viscosity in (cp)
ω	rotational speed of the disk (radians/sec)
$J_{Diffusion\ limited}$	The maximum possible flux assuming no particle dissolution in the aqueous boundary layer and a saturated solution ($g\ cm^{-2}\ s^{-1}$)
J_{max}	The maximum flux possible assuming that particles are dissolving at the membrane surface (within the aqueous diffusion layer) ($g\ cm^{-2}\ s^{-1}$)
J_C	The flux predicted across the PDMS membrane (Region C) assuming particles dissolving in the bulk and within the aqueous boundary layer ($g\ cm^{-2}\ s^{-1}$)
J_p	Flux from the population of particles ($g\ cm^{-2}\ s^{-1}$)
J_T	Total flux from Region A to Region C ($g\ cm^{-2}\ s^{-1}$)
dm/dt	The change in mass with respect to time
dC/dr	The change in concentration of drug with respect to the change in radius of the spherical drug particle
dC_p/dt	Change in bulk concentration from particle dissolution with respect to time
w	Width of a rectangle
l	Length of a rectangle
P	Perimeter of a rectangle

6.4.2 Derivation of the Convection Diffusion Model

6.4.2 1 Higuchi-Hiestand Particle Dissolution

The first component of this model requires that a model for the change in concentration from dissolving particles. Describing the change of concentration of a particle with respect to its radius using the Higuchi-Hiestand particle dissolution model. This model essential assumes that the diffusion layer around the particles is the same for all particles and is equal to the radius of the particle. Sheng et al. and Wang-Brasseur state that particle dissolution is highly dependent on the boundary thickness of the dissolving particle. Fick's 1st law states,

$$J = -D\frac{dC}{dr} \qquad \text{Eq (6.3)}$$

Considering the units of flux (mass per unit area per unit time) we re-write Fick's 1st Law as

$$\frac{dm}{dt}\frac{1}{A} = -D\frac{dC}{dr} \qquad \text{Eq (6.4)}$$

To define the change of mass (dm/dt) with respect to time we must know the particle geometry. We make a simplifying assumption that the particles are spherical and when the actual drug particles are measured for size and distribution of size, they are converted from their rectangular prismatic shape into an "equivalent" sphere. The weighted average of the radius is used as the "average" spherical radius in the proceeding calculations.

Since the volume of a sphere is defined as

$$V_{sphere} = \frac{4}{3}\pi r^3 \qquad \text{Eq (6.5)}$$

And the surface area of a sphere can be determined by taking the first derivative of volume with respect to the radius…

$$\frac{d}{dr}V = A = 4\pi r^2 \quad \text{Eq (6.6)}$$

We define the change in mass with respect to time of a single spherical particle as the diffusivity multiplied by the surface area of the particle times the concentration gradient…

$$\frac{dm}{dt}\frac{1}{A} = -D\frac{dC}{dr} \quad \text{Eq (6.7)}$$

$$\frac{dm}{dt} = -DA\frac{dC}{dr} \quad \text{Eq (6.8)}$$

$$\frac{dm}{dt} = D4\pi r^2\frac{dC}{dr} \quad \text{Eq (6.9)}$$

As radius changes with respect to time, collect the radius and time dependent variables…

$$\frac{dm}{dt}\frac{dr}{r^2} = 4\pi D dC \quad \text{Eq (6.10)}$$

Integrate the left-hand side (LHS) with respect to radius and the right-hand side (RHS) with respect to concentration assuming steady state where dm/dt is constant…

$$\frac{dm}{dt}\int_{a_0}^{\infty}\frac{dr}{r^2} = 4\pi D\int_{S}^{C_0} dC \quad \text{Eq (6.11)}$$

Where a_0 is the average spherical radius and S and C_0 typically defined as the surface (solubility) and bulk concentration respectively but their meaning is also understood to mean from high and low concentration respectively…

$$\frac{dm}{dt}\frac{-1}{a_0} = 4\pi D(S - C_0) \quad \text{Eq (6.12)}$$

The change in mass can then be simplified as follows.

$$\frac{dm}{dt} = -4\pi a_0 D(S - C_0) \quad \text{Eq (6.13)}$$

We now describe the change in the concentration from particles with respect to time:

$$\frac{dC_p}{dt} = \frac{M}{{}^4/_3\pi a^3\rho V}\frac{dm}{dt} \quad \text{Eq (6.14)}$$

$$\frac{dC_p}{dt} = \left(\frac{3M}{4\pi a^3\rho}\right)\left(\frac{1}{V}\right)\frac{dm}{dt} \quad \text{Eq (6.15)}$$

The first part of the RHS expression determines the number of particles given an average radius, drug density, and mass (dose, total amount of drug weighed). The second part of the expression in combination with the first gives the number of particles per volume of donor fluid. Which when multiplied by the change in mass will yield the change in the concentration attributed to particle dissolution with respect to time.

We substitute the expression for dm/dt derived above into dCp/dt

$$\frac{dC_p}{dt} = \frac{3M}{4\pi a^3 \rho V}\left(-4\pi a_0 D(S - C_0)\right) \quad \text{Eq (6.16)}$$

Where a = a_0 = the average spherical radius…

$$\frac{dC_p}{dt} = \frac{-12\pi a_0 DM}{4\pi a^3 \rho V}(S - C_0) \quad \text{Eq (6.17)}$$

Simplifying the equation yields…

$$\frac{dC_p}{dt} = \frac{-3DM}{a^2 \rho V}(S - C_0) \quad \text{Eq (6.18)}$$

Flux from the dissolving particle surface is again described using Fick's 1st law.

$$J_p = -\frac{V}{A}\frac{dC_p}{dt} \quad \text{Eq (6.19)}$$

Substituting the expression for dCp/dt we obtain the the dose dependent flux from a population of monodisperse spherical particles.

$$J_p = \frac{V}{A}\frac{3D}{a^2 \rho V}(S - C_0) \quad \text{Eq (6.20)}$$

Simplifying the expression yields the final flux equation for a monodisperse distribution of spherical particles as a function of both the dose administered and the particles equivalent spherical radius.

$$J_p = \frac{3DM}{a^2 \rho A}(S - C_0) \quad \text{Eq (6.21)}$$

The diffusion cell is comprised of a donor (drug containing at time = 0) and receiver (drug free at time = 0), as well as a diffusion-controlled membrane (non-

porous, pure diffusion). With agitation on both sides of the membrane, this yield 5 distinct zones. Ideally, zone 1 is particles dissolving into the bulk, zone 2 is the donor side "aqueous boundary layer", zone 3 is the diffusion-controlled membrane, zone 4 is the receiver side "aqueous boundary layer", and finally zone 5 is the receiver bulk fluid.

Therefore, to calculate the total flux

$$J_T = P_{eff}\Delta C \qquad \text{Eq (6.22)}$$

Where the effective permeability is the series summation of each zones or layer permeability

$$P_{eff} = \left(\sum \frac{1}{P_i}\right)^{-1} \qquad \text{Eq (6.23)}$$

From Zone 1 to Zone 2 the permeability of drug is governed by the permeability of the drug from the particles dissolving surface to the interface of the stagnant diffusion layer (a.k.a. the "aqueous boundary layer"). From Zone 2 to Zone 3 the permeability is governed purely by the diffusion of the drug across the "aqueous boundary layer". From Zone 3 to Zone 4 the drug's permeability is a function of partition coefficient, ionization state, polar surface area, diffusivity, and membrane thickness. From Zone 4 to Zone 5 the drug permeability is governed by the receiver side "aqueous boundary layer", and then is accumulated in the bulk fluid of the receiver phase. Formally writing the complete quaternary resistance to diffusion as…

$$P_{eff} = \left(\frac{1}{P_p} + \frac{1}{P_{Aq_D}} + \frac{1}{P_m} + \frac{1}{P_{Aq_R}}\right)^{-1} \qquad \text{Eq (6.24)}$$

Where size and dose dependent population particle permeability is expressed as from the derivation above...

$$P_p = \frac{3D_{Aq}M}{a^2\rho A_p} \qquad \text{Eq (6.25)}$$

The membrane permeability is defined as…

$$P_m = \frac{K_{PDMS} D_{PDMS}}{h_m} \quad \text{Eq (6.26)}$$

And the donor side and receiver side stagnant fluid layer permeabilities are expressed as…

$$P_{Aq_D} = \frac{D_{Aq}}{h_{Aq}} \quad \text{Eq (6.27)}$$

$$P_{Aq_R} = \frac{D_{Aq}}{h_{Aq}} \quad \text{Eq (6.28)}$$

Inserting them into the effective permeability expression yields…

$$P_{eff} = \left(\frac{1}{\frac{3DM}{a^2 \rho A}} + \frac{1}{\frac{D}{h}} + \frac{1}{\frac{K_{PDMS} D_{PDMS}}{h_m}} + \frac{1}{\frac{D}{h}} \right)^{-1} \quad \text{Eq (6.29)}$$

Describing the flux of drug from the bulk donor fluid to the bulk receiver fluid across the membrane is as follows…

$$J_T = \left(\frac{1}{\frac{3D}{a^2 \rho A}} + \frac{1}{\frac{D}{h}} + \frac{1}{\frac{K_{PDMS} D_{PDMS}}{h_m}} + \frac{1}{\frac{D}{h}} \right)^{-1} \left(S - C_{B_2} \right) \quad \text{Eq (6.30)}$$

However, we can create an electrochemical sink for an ionizable drug to create both a mass sink and significantly reduce the amount of reverse transport. By having the donor side under completely non-ionizing conditions we will also not need to worry about molecular species relative mobility in the boundary and its effect on transport. The receiver compartment completely ionizing the aqueous boundary layer is effectively shorted out because the drug molecule instantly is charged upon contact with the receiver fluid thus significantly decreasing its affinity for the membrane and lowering its' permeability. The benefit is that ionized drug solubilities tend to be significantly higher than the non-ionized form creating the mass sink conditions, all of which yield suitable experimental conditions for measuring steady state transport conditions as proposed in this model.

Now applying the receiver side conditions to the total flux expression, the receiver side permeability becomes very large, as long as the receiver is well buffered and stirred. Thus, the limit of 1/ x towards infinity goes towards 0, and can be ignored from the expression yielding…

$$J_T = \left(\frac{1}{\frac{3DM}{a^2 \rho A}} + \frac{1}{\frac{D}{h}} + \frac{1}{\frac{K_{PDMS} D_{PDMS}}{h_m}} \right)^{-1} \left(S - C_{B_2} \right) \qquad \text{Eq (6.31)}$$

Since the receiver side is ionizing the non-ionized drug concentration goes to 0 immediately upon extraction from the receiver side surface of the membrane, thus no diffusion layer.

$$J_{diffusion\ limited} = \left(\frac{1}{\frac{3DM}{a^2 \rho A}} + \frac{1}{\frac{D}{h}} + \frac{1}{\frac{K_{PDMS} D_{PDMS}}{h_m}} \right)^{-1} (S) \qquad \text{Eq (6.32)}$$

This flux is defined as the diffusion limited flux.

If we expect that at high doses and/or very small particle sizes that the particles would be within the length scale of the “aqueous boundary layer” then the “aqueous boundary layer” permeability would not govern the flux of drug from the donor side to the receiver. In the configuration described above, the only remaining resistance to diffusion is the membrane permeability. Additionally, if the particles permeability was significantly high due to very small radii and surface area, that permeability resistance would go to zero by the same limit of 1/x. So, the maximum flux is described as

$$J_{max} = \left(\frac{1}{\frac{K_{PDMS} D_{PDMS}}{h_m}} \right)^{-1} (S) \qquad \text{Eq (6.33)}$$

6.4.2 2 Convection-Diffusion Model for Monodisperse Particle Flux across a PDMS UTLAM

Figure 6-1 describes the physical situation to be modeled in this section. To determine particle dissolution processes in the aqueous boundary layer (Region B) we write the convection-diffusion equation…

$$\frac{\partial C}{\partial t} = D\frac{\partial^2 C(y)}{\partial y^2} - \frac{\partial C}{\partial y}v + R \qquad \text{Eq (6.34)}$$

We describe the change in concentration with respect to time as the diffusional component, convection component, and the generation (dissolution) component respectively. Since there is no fluid convection across the membrane the convection term can be ignored…

$$\frac{\partial C}{\partial t} = D\frac{\partial^2 C(y)}{\partial y^2} + R \qquad \text{Eq (6.35)}$$

Where R (the generation term), is describing the concentration generated from the particle dissolution process…

$$R = \frac{dC_p}{dt} = \frac{3D}{a^2\rho V}(S - C_0) \qquad \text{Eq (6.36)}$$

But in this context C_0 which meant the bulk concentration an "infinite" distance away from the dissolving surface now means the concentration as a function of y distance from the membrane surface. We also drop the negative sign to match the coordinate convention of the system as positive flux is defined from left to right. Drug concentration will drop from the particle surface to the membrane surface. The following equation describes diffusion of drug from the bulk fluid and particle dissolution within the aqueous boundary layer.

$$\frac{\partial C}{\partial t} = D\frac{\partial^2 C(y)}{\partial y^2} + \frac{3DM}{a^2\rho V}(S - C(y)) \qquad \text{Eq (6.37)}$$

with the boundary conditions…

$$J_A = J_B \qquad \text{Eq (6.38)}$$

$$J_B = J_C \quad \text{Eq (6.39)}$$

Due to the generation of mass from dissolution in the aqueous boundary layer the continuity of flux is disturbed in region B (aqueous boundary layer) and therefore the we cannot set $J_A = J_B = J_C$ to solve for the concentration at the surface of the membrane.

$$J_A \neq J_C \quad \text{Eq (6.40)}$$

For the ordinary second order differential equation (SODE) with the form below we recognize that:

$$D\frac{\partial^2 C(y)}{\partial y^2} + \frac{3D}{a^2 \rho V}(S - C(y)) \quad \text{Eq (6.41)}$$

$$D\frac{\partial^2 C(y)}{\partial y^2} + \frac{3DM}{a^2 \rho V}S - \frac{3DM}{a^2 \rho V}C(y) \quad \text{Eq (6.42)}$$

Approximately equals the following…

$$\frac{\partial^2 w(y)}{\partial y^2} - w(y) = w''(z) - w(z) = c_1 e^{r_1 x} + c_2 e^{-r_2 x} \quad \text{Eq (6.43)}$$

Where r_1 and r_2 are the roots of the quadratic characteristic equations.

Ultimately, we need to solve for the concentration at the surface of the membrane therefore we evaluate C(y) @ y = 0 to solve for C_{S1} and manipulate the SODE to be able to use the simplest integration as described above…

$$\frac{\partial C}{\partial t} = D\frac{\partial^2 C(y)}{\partial y^2} + \frac{3D}{a^2 \rho V}(S - C(y)) \quad \text{Eq (6.44)}$$

Divide the LHS and RHS by the aqueous diffusion coefficient of the drug…

$$\frac{1}{D}\frac{\partial C}{\partial t} = \frac{\partial^2 C(y)}{\partial y^2} + \frac{3M}{a^2 \rho V}(S - C(y)) \quad \text{Eq (6.45)}$$

We define…

$$\lambda^2 = \frac{3M}{a^2 \rho V} \quad \text{Eq (6.46)}$$

$$P_A = \frac{3DM}{a^2 \rho V} \quad \text{Eq (6.47)}$$

$$\frac{P_A}{D} = \frac{3M}{a^2 \rho V} = \lambda^2 \quad \text{Eq (6.48)}$$

Then substitute our definition into the SODE…

$$\frac{1}{D}\frac{\partial C}{\partial t} = \frac{\partial^2 C(y)}{\partial y^2} + \lambda^2(S - C(y)) \quad \text{Eq (6.49)}$$

Applying steady-state conditions dC/dt is equal to zero…

$$0 = \frac{\partial^2 C(y)}{\partial y^2} + \lambda^2(S - C(y)) \quad \text{Eq (6.50)}$$

We now define another function g to remove the constant from the SODE, arriving at the w''- w = 0 form. We define g, g', and g'' by dividing both sides of the equation by S…

$$g(y) = \frac{C(y)}{S} - 1 \quad \text{Eq (6.51)}$$

$$g'(y) = \frac{C'(y)}{S} = \frac{\partial}{\partial y}\frac{C(y)}{S} \quad \text{Eq (6.52)}$$

$$g''(y) = \frac{C''(y)}{S} = \frac{\partial^2}{\partial y^2}\frac{C(y)}{S} \quad \text{Eq (6.53)}$$

Rewriting the SODE in terms of the function g we obtain the w'' – w = 0 form and can perform the integration yielding…

$$g''(y) - \lambda^2 g(y) = 0 \quad \text{Eq (6.54)}$$

And since…

$$w''(z) - kw(z) = c_1 e^{\sqrt{k}z} + c_2 e^{-\sqrt{k}z} \quad \text{Eq (6.55)}$$

$$g(y) = c_1 e^{-\lambda y} + c_2 e^{\lambda y} \quad \text{Eq (6.56)}$$

$$\frac{\partial}{\partial y} g(y) = -c_1 \lambda e^{-\lambda} + c_2 \lambda e^{\lambda y} \quad \text{Eq (6.57)}$$

Now we evaluate the general solution at the boundary conditions.

$$@\ y = -h,\ P_A\big(S - C(-h)\big) = -D\ C'(-h) \quad \text{Eq (6.58)}$$

$$@\ y = 0\ ,\ P_C C(0) = -D\ C'(0) \quad \text{Eq (6.59)}$$

As we are trying to describe the diffusion and dissolution within region B (the aqueous boundary layer), the boundaries are defined at y = 0 (the membrane surface) & y = -h (the interface between the aqueous boundary layer and the bulk fluid). At y = -h…

$$J_A = J_B \quad \text{Eq (6.60)}$$

$$P_A(S - C(y))|_{y=-h} = -D\frac{\partial}{\partial y}C(y)\Big|_{y=-h} \quad \text{Eq (6.61)}$$

$$P_A\big(S - C(-h)\big) = -D\ C'(-h) \qquad \text{Eq (6.62)}$$

After establishing the continuity of flux between Region A and B in terms of the concentration equation we now determine the boundary conditions in terms of our arbitrary function g…

$$g(-h) = \frac{C(-h)}{S} - 1 \qquad \text{Eq (6.63)}$$

Multiply both sides of the equation by the solubility (S) to define C(y) in terms of g(y)…

$$Sg(-h) = C(-h) - S \qquad \text{Eq (6.64)}$$

$$C(-h) = S\ g(-h) + S \qquad \text{Eq (6.65)}$$

Since the boundary condition requires C(y) and C'(y), take the derivative of C(y)…

$$C(-h) = S\ g(-h) + S \qquad \text{Eq (6.66)}$$

$$C'(-h) = S\ g'(-h) \qquad \text{Eq (6.67)}$$

Substituting in the values derived for C(y) and C'(y) in terms of the g function from the boundary conditions into the boundary equation yields…

$$P_A\big(S - (S\ g(-h) + S)\big) = -D\ S\ g'(-h) \qquad \text{Eq (6.68)}$$

And simplify by distributing the -1 on the LHS…

$$P_A(S - S\ g(-h) - S) = -D\ S\ g'(-h) \qquad \text{Eq (6.69)}$$

$$P_A\big(-S\ g(-h)\big) = -D\ S\ g'(-h) \qquad \text{Eq (6.70)}$$

Dividing out the -1*S from the LHS to the RHS…

$$P_A\ g(-h) = D\ \ g'(-h) \qquad \text{Eq (6.71)}$$

And finally, isolating g(-h) yields…

$$g(-h) = D/P_A\ \ g'(-h) \qquad \text{Eq (6.72)}$$

$$\frac{P_A}{D} g(-h) = \ \ g'(-h) \qquad \text{Eq (6.73)}$$

And here we can define parameter "a" to be…

$$a = \frac{P_A}{D} \qquad \text{Eq (6.74)}$$

Yielding…

$$a\ g(-h) = \quad g'(-h) \qquad \text{Eq (6.75)}$$

At y = 0, the second boundary condition is satisfied by…

$$J_B = J_C \qquad \text{Eq (6.76)}$$

$$-D\frac{\partial}{\partial y}C(y)\Big|_{y=0} = P_C C(y)|_{y=0} \qquad \text{Eq (6.77)}$$

$$-D\ C'(0) = P_C C(0) \qquad \text{Eq (6.78)}$$

Using our definitions of the g function to determine the values at the membrane surface, y = 0…

$$g(0) = \frac{C(0)}{S} - 1 \qquad \text{Eq (6.79)}$$

$$C(0) = S\ g(0) + S \qquad \text{Eq (6.80)}$$

$$C'(y) = S\ g'(y) \qquad \text{Eq (6.81)}$$

Substituting in the values derived from the boundary conditions into the boundary equation…

$$-D\ S\ g'(0) = P_C(S\ g(0) + S) \qquad \text{Eq (6.82)}$$

$$-D\ S\ g'(0) = P_C S(\ g(0) + 1) \qquad \text{Eq (6.83)}$$

$$-D\ \ g'(0) = P_C(g(0) + 1) \qquad \text{Eq (6.84)}$$

$$-\frac{D}{P_C}\ \ g'(0) = g(0) + 1 \qquad \text{Eq (6.85)}$$

We then define the parameter “b” to be…

$$b = \frac{P_c}{D} \qquad \text{Eq (6.86)}$$

$$g'(0) = -b\ (g(0) + 1) \qquad \text{Eq (6.87)}$$

Now we are able to solve for the integration constants. Apply the boundary condition at the bulk fluid interface with the aqueous diffusion layer remembering that…

$$@\ y = -h \qquad \text{Eq (6.88)}$$

$$a\ g(-h) = \quad g'(-h) \qquad \text{Eq (6.89)}$$

And the g(-h) and g’(-h) are equal to…

$$g(y) = c_1 e^{-\lambda y} + c_2 e^{\lambda y} \rightarrow g(-h) = c_1 e^{\lambda h} + c_2 e^{-\lambda h} \qquad \text{Eq (6.90)}$$

$$\frac{\partial}{\partial y}g(y) = -c_1\lambda e^{-\lambda y} + c_2\lambda e^{\lambda y} \rightarrow \frac{\partial}{\partial y}g(-h) = c_1\lambda e^{\lambda h} - c_2\lambda e^{-\lambda h} \qquad \text{Eq (6.91)}$$

Now substitute the values of g(-h) and g'(-h)…

$$a\left(c_1\, e^{-\lambda h} + c_2\, e^{\lambda h}\right) = c_1\lambda e^{-\lambda h} - c_2\, \lambda e^{\lambda h} \qquad \text{Eq (6.92)}$$

We now gather like terms of c_1 and c_2 and separate them the LHS and RHS respectively…

$$\left(a c_1\, e^{-\lambda h} - c_1\lambda e^{-\lambda h}\right) = -c_2\, \lambda e^{\lambda h} - a\, c_2\, e^{\lambda h} \qquad \text{Eq (6.93)}$$

Factor out the common term on each side….

$$c_1 e^{-\lambda h}(a - \lambda) = -c_2 e^{\lambda h}(a + \lambda) \qquad \text{Eq (6.94)}$$

And solve for c_1…

$$c_1 = -\frac{c_2 e^{2\lambda h}(a+\lambda)}{(a-\lambda)} \qquad \text{Eq (6.95)}$$

Applying the second boundary condition results at the interface of the aqueous diffusion layer and the membrane surface yields…

$$@\ y = 0 \qquad \text{Eq (6.96)}$$

$$g(y) = c_1 e^{-\lambda y} + c_2 e^{\lambda y} \rightarrow g(0) = c_1 e^0 + c_2 e^0 \qquad \text{Eq (6.97)}$$

$$\frac{\partial}{\partial y} g(y) = -c_1\lambda e^{-\lambda y} + c_2\lambda e^{\lambda y} \rightarrow \frac{\partial}{\partial y} g(0) = c_1\lambda e^0 - c_2\lambda e^0 \qquad \text{Eq (6.98)}$$

Now substitute the values of g(0) and g'(0)…

$$-b\,(g(0) + 1) = \ g'(0) \qquad \text{Eq (6.99)}$$

$$-b(c_1\, e^0 + c_2\, e^0 + 1) = c_1\lambda e^0 - c_2\, \lambda e^0 \qquad \text{Eq (6.100)}$$

Since e^0 is equal to 1 we can simplify to…

$$-b(c_1\ + c_2\ + 1) = c_1\lambda - c_2\, \lambda \qquad \text{Eq (6.101)}$$

Now substituting the expression for c_1 into the expression above to solve for c_2…

$$-b\left(-\frac{c_2 e^{2\lambda h}(a+\lambda)}{(a-\lambda)}\ + c_2\ + 1\right) = \lambda(-\frac{c_2 e^{2\lambda h}(a+\lambda)}{(a-\lambda)} - c_2) \qquad \text{Eq (6.102)}$$

$$\left(\frac{c_2 e^{2\lambda h}(a+\lambda)}{(a-\lambda)} b - c_2 b - b\right) = \lambda(-\frac{c_2 e^{2\lambda h}(a+\lambda)}{(a-\lambda)} - c_2) \qquad \text{Eq (6.103)}$$

$$c_2\left(\frac{e^{2\lambda h}(a+\lambda)b}{(a-\lambda)} - b + \frac{\lambda e^{2\lambda h}(a+\lambda)}{(a-\lambda)} + \lambda\right) = b \qquad \text{Eq (6.104)}$$

$$c_2 = \frac{b}{\left(\frac{e^{2\lambda h}(a+\lambda)b}{(a-\lambda)} - b + \frac{\lambda e^{2\lambda h}(a+\lambda)}{(a-\lambda)} + \lambda\right)} \qquad \text{Eq (6.105)}$$

$$c_2 = \frac{b}{\left(\frac{e^{2\lambda h}(a+\lambda)b}{(a-\lambda)} - b + \frac{\lambda e^{2\lambda h}(a+\lambda)}{(a-\lambda)} + \lambda\right)} \qquad \text{Eq (6.106)}$$

$$c_2 = \frac{b\,(a+\lambda)}{\left(e^{2\lambda h}(a+\lambda)(\lambda+b)+(\lambda-b)(a-\lambda)\right)} \quad \text{Eq (6.107)}$$

Now that c_2 is determined we substitute c_2 back into the c_1 equation to solve for c_1…

$$c_1 = -\frac{c_2 e^{2\lambda h}(a+\lambda)}{(a-\lambda)} \quad \text{Eq (6.108)}$$

$$c_1 = -\frac{b\,(a+\lambda)}{\left(e^{2\lambda h}(a+\lambda)(\lambda+b)+(\lambda-b)(a-\lambda)\right)}\frac{e^{2\lambda h}(a+\lambda)}{(a-\lambda)} \quad \text{Eq (6.109)}$$

$$c_1 = -\frac{b(a+\lambda)^2\, e^{2\lambda h}}{\left(e^{2\lambda h}(a+\lambda)\,(b+\lambda)(a-\lambda)+(\lambda-b)(a-\lambda)^2\right)} \quad \text{Eq (6.110)}$$

Now that the integration constants have been solved for, we write the specific solution to the convection-diffusion equation in terms of the function g as…

$$g(y) = c_1\, e^{\lambda y} + c_2\, e^{-\lambda y} \quad \text{Eq (6.111)}$$

$$g(y) = \left(-\frac{b(a+\lambda)^2\, e^{2\lambda h}}{\left(e^{2\lambda h}(a+\lambda)\,(b+\lambda)(a-\lambda)+(\lambda-b)(a-\lambda)^2\right)}\right) e^{\lambda y} + \left(\frac{b\,(a+\lambda)}{\left(e^{2\lambda h}(a+\lambda)(\lambda+b)+(\lambda-b)(a-\lambda)\right)}\right) e^{-\lambda y} \quad \text{Eq (6.112)}$$

And converting the function g, back into the concentration…

$$g(y) = \frac{C(y)}{S} - 1 \quad \text{Eq (6.113)}$$

$$C(y) = S\, g(y) + S \quad \text{Eq 6.114)}$$

$$C'(y) = S\, g'(y) \quad \text{Eq (6.115)}$$

$$C(y) = S\left[\left(-\frac{b(a+\lambda)^2\, e^{2\lambda h}}{\left(e^{2\lambda h}(a+\lambda)\,(b+\lambda)(a-\lambda)+(\lambda-b)(a-\lambda)^2\right)}\right) e^{\lambda y} + \left(\frac{b\,(a+\lambda)}{\left(e^{2\lambda h}(a+\lambda)(\lambda+b)+(\lambda-b)(a-\lambda)\right)}\right) e^{-\lambda y}\right] + S \quad \text{Eq (6.116)}$$

$$C'(y) = -\frac{S\,\lambda b(a+\lambda)^2\, e^{2\lambda h}}{\left(e^{2\lambda h}(a+\lambda)\,(b+\lambda)(a-\lambda)+(\lambda-b)(a-\lambda)^2\right)}\, e^{\lambda y} - \frac{S\lambda b\,(a+\lambda)}{\left(e^{2\lambda h}(a+\lambda)(\lambda+b)+(\lambda-b)(a-\lambda)\right)}\, e^{-\lambda y}$$

Eq (6.117)

Using the definition at y = 0 that C(y) is the membrane surface concentration (C_{S1}), we evaluate C(0), by stating the flux through region C is equal to the flux coming from region B…

$$J_C = P_C C_{S_1} = -D\frac{\partial}{\partial y} C(y)\Big|_{y=0} \quad \text{Eq (6.118)}$$

$$J_c = -DC'(y=0) = -DS\, c_1\lambda\, e^{\lambda\times 0} + DS\, c_2\lambda\, e^{-\lambda\times 0} \quad \text{Eq (6.119)}$$

$$J_c = DS\lambda\ (-c_1\, e^0 + \ c_2\, e^0\ ) \quad \text{Eq (6.120)}$$

$$J_c = DS\lambda\ (-c_1\ +\ c_2\ ) \quad \text{Eq (6.121)}$$

Again, substituting the values of c_1 and c_2…

$$J_c = DS\lambda \left(\frac{b(a+\lambda)^2 e^{2\lambda h}}{\left(e^{2\lambda h}(a+\lambda)(b+\lambda)(a-\lambda)+(\lambda-b)(a-\lambda)^2\right)} + \frac{b(a+\lambda)}{\left(e^{2\lambda h}(a+\lambda)(\lambda+b)+(\lambda-b)(a-\lambda)\right)} \right) \quad \text{Eq (6.122)}$$

We notice that we can factor out (a – λ) from both c_1 and c_2 in the denominator…

$$J_c = DS\lambda \left(\frac{b(a+\lambda)^2 e^{2\lambda h}}{\left(e^{2\lambda h}(a+\lambda)(b+\lambda)+(\lambda-b)(a-\lambda)\right)} \frac{1}{(a-\lambda)} + \frac{b(a+\lambda)}{\left(e^{2\lambda h}(a+\lambda)(\lambda+b)+(\lambda-b)(a-\lambda)\right)} \right) \quad \text{Eq (6.123)}$$

Then we notice that c_1 and c_2 only differ by an $(a + \lambda)e^{2\lambda h}$ in the numerator, allowing factoring of the remaining terms to arrive at the final solution for the flux across the membrane…

$$J_c = DS\lambda \left(\frac{b(a+\lambda)}{\left(e^{2\lambda h}(a+\lambda)(b+\lambda)+(\lambda-b)(a-\lambda)\right)} \left(\frac{(a+\lambda)\, e^{2\lambda h}}{(a-\lambda)} + 1 \right) \right) \quad \text{Eq (6.124)}$$

Where…

$$a = \frac{P_A}{D} = \lambda^2 \quad \text{Eq (6.125)}$$

$$J_c = DS\lambda \left(\frac{b(\lambda^2+\lambda)}{\left(e^{2\lambda h}(\lambda^2+\lambda)(b+\lambda)+(\lambda-b)(\lambda^2-\lambda)\right)} \left(\frac{(\lambda^2+\lambda)\, e^{2\lambda h}}{(\lambda^2-\lambda)} + 1 \right) \right) \quad \text{Eq (6.126)}$$

$$J_c = DS\lambda \left(\frac{b(\lambda+1)\lambda}{\left(e^{2\lambda h}(\lambda+1)\lambda(b+\lambda)+(\lambda-b)(\lambda-1)\lambda\right)} \left(\frac{(\lambda+1)\lambda\, e^{2\lambda h}}{(\lambda-1)\lambda} + 1 \right) \right) \quad \text{Eq (6.127)}$$

Yielding the final equation for flux across the membrane for particles dissolving in the bulk and within the aqueous boundary layer…

$$J_c = DS\lambda \left(\frac{b(\lambda+1)}{\left(e^{2\lambda h}(\lambda+1)(b+\lambda)+(\lambda-b)(\lambda-1)\right)} \left(\frac{(\lambda+1)\, e^{2\lambda h}}{(\lambda-1)} + 1 \right) \right) \quad \text{Eq (6.128)}$$

$$b = \frac{P_c}{D} = \frac{K_{PDMS} D_{PDMS}}{h_m D} \quad \text{Eq (6.129)}$$

$$\lambda = \sqrt{\frac{3M}{r^2 \rho V}} \quad \text{Eq (6.130)}$$

6.4.3 Experimental Results

6.4.3 1 Particle Size Distributions

Ibuprofen particles were characterized using an optical microscope and laser diffraction to measure and confirm the particle size distribution. Both methods assume a spherical particle and ibuprofen forms a rectangular prism as a crystal. The

two particle size distributions are as follows. In the optical microscopy the perimeter and surface area of the particle was measured using ImageJ. Since Ibuprofen crystals are roughly rectangular prisms, the following equations were used to convert the actual measured surface area and perimeter into a rectangular width and length.

$$wl = A \quad \text{Eq (6.131)}$$

$$2(w + l) = P \quad \text{Eq (6.132)}$$

$$l = \frac{A}{w} \rightarrow 2\left(w + \frac{A}{w}\right) = P \quad \text{Eq (6.133)}$$

Multiply by both sides by w…

$$2(w^2 + A) = Pw \quad \text{Eq (6.134)}$$

$$2w^2 + 2A = Pw \quad \text{Eq (6.135)}$$

$$2w^2 - Pw + 2A = 0 \quad \text{Eq (6.136)}$$

$$w^2 - \frac{Pw}{2} + A = 0 \quad \text{Eq (6.137)}$$

Since…

$$w = \frac{\frac{P}{2} \pm \sqrt{\frac{P^2}{4} - 4A}}{2} \quad \text{Eq (6.138)}$$

Taking the positive root…

$$w = \frac{\frac{P}{2} + \sqrt{\frac{P^2}{4} - 4A}}{2} \quad \text{Eq (6.139)}$$

And defining…

$$l = \frac{A}{w} \quad \text{Eq (6.140)}$$

$$z = \frac{minimum(w,l)}{z-factor} \quad \text{Eq (6.141)}$$

These equations allow for a rectangular prism approximation of the ibuprofen particle. We then assume that the "height" of the prism is equal to the lesser of the values for "w" and "l". This estimate was based on rolling particles over under the optical microscope and measuring the z-dimension (Table 6-2). From this a rectangular volume is calculated, and then set equal to a spherical volume. It is from this equivalent spherical volume which we calculate the particle radius for the

Higuchi-Hiestand dissolution model. It is most likely that for ibuprofen that these particle sizes are overestimated.

$$V_{Rectangular\ Prism} = w \cdot l \cdot z = \frac{4}{3}\pi r^3 \quad \text{Eq (6.142)}$$

$$\frac{3}{4\pi} V_{Rectangular\ Prism} = r^3 \quad \text{Eq (6.143)}$$

$$r = \sqrt[3]{\frac{3}{4\pi} V_{Rectangular\ Prism}} \quad \text{Eq (6.144)}$$

Table 6-2 Table of ratios of the smallest measured particle dimension to calculate the thickness of the particle.

Particle Fraction	z-factor
High Shear Wet Sieve	1
53-63 micron	1
150-250 micron	2

Optical Microscopy Method

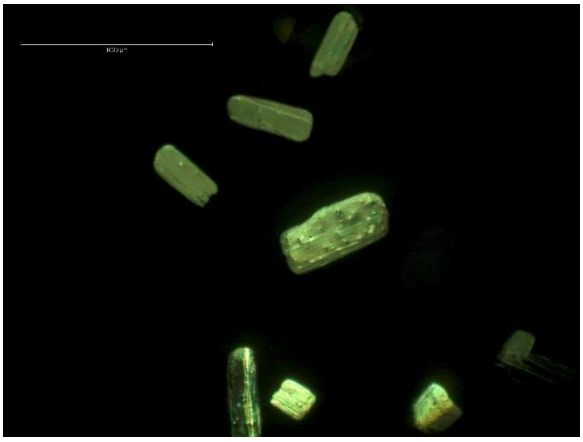

Figure 6-2 Optical Microscopic Image of Ibuprofen.

A micrograph taken with a 4x objective on a light microscope (light source underneath sample stage) of dry sieved ibuprofen particles from the 150-250μm sieve opening fraction in immersion oil.

Ibuprofen particles were imaged at a single objective (4x, 10x, 20x) using a polarized light microscope that was rotated to 90°. Ibuprofen crystals were

suspended in immersion oil on glass slides for imaging. An inline camera captured the images as exemplified in Figure 6-2.

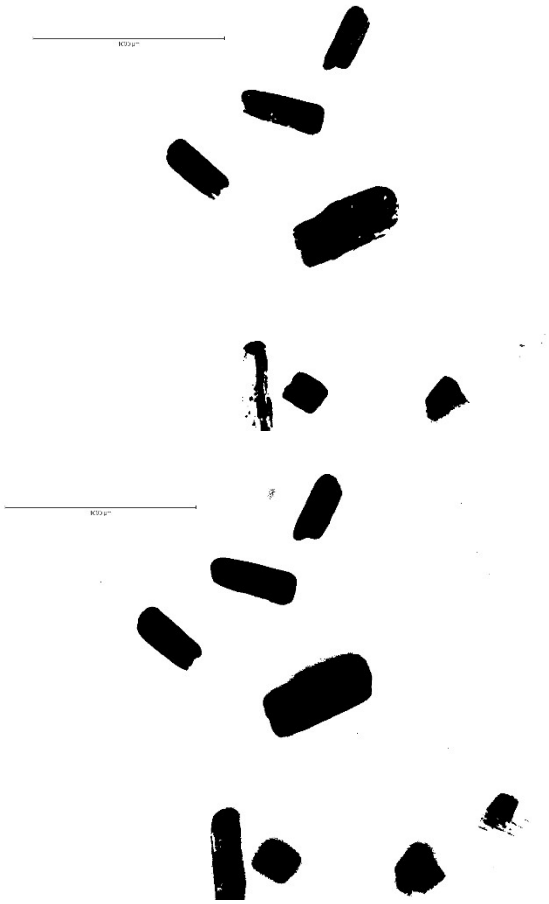

Figure 6-3 Comparison of Thresholding Methodologies for Image Analysis.

The top image is the same image in Figure 6-2, with the default isoData iterative binarization threshold protocol applied by ImageJ to separate the image background from particles within the image. The bottom image is the Renyi entropy threshold protocol.

In ImageJ, the entire series of images was imported converted to 8-bit images, then binarized using the isoData iterative (default) or Renyi entropy background threshold protocol to produce images for automated analysis (Figure 6-3). The analyze particles function was then used to generate surface area and perimeters for each particle. Each particle was manually examined against its original image to determine if it was a real particle, and if it was found to be non-representative

(stacked particles, background lighting issues, etc.) the particle was removed from the population. In one particle fraction, the ImageJ routine was compared to a manual counting (N ~ 10,000).

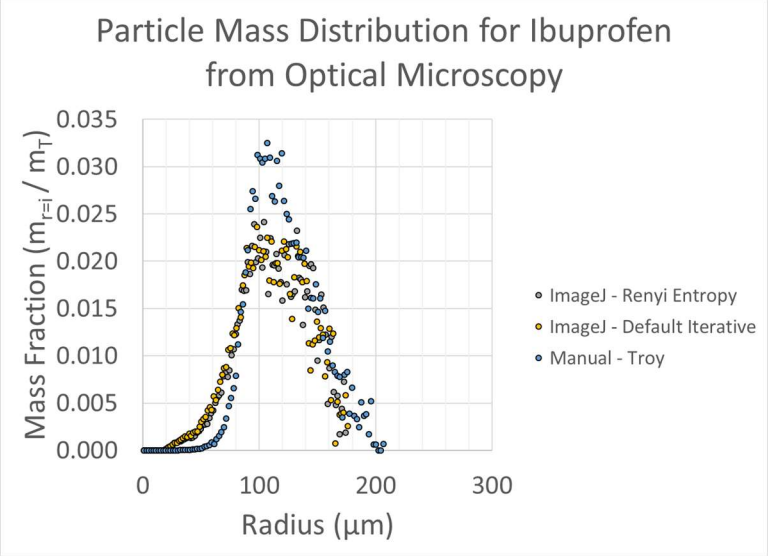

Figure 6-4 Manual versus Automatic Particle Counting.

A comparison of the two ImageJ threshold protocols to a manual counting of particles performed by Troy Halseth. The manual characterization was sharper most likely to some selectivity bias by the experimenter and the microscope objective used to capture the data. However, the results are not qualitatively that different.

Table 6-3 Tabulated results of the mass average radius for a three image processing methods from Figure 6-5.

Method	R @M_{50} [µm]
Renyi Entropy[112]	~113.04
IsoData Iterative[113]	~112.30
Manual (l · w)	~117.28

The resulting mass distributions were compared at r_{50}. The two ImageJ routines produced similar results for r_{50}, however the manual counting produced a slightly higher average. The higher average radius from the manual counting could be due to

selectively picking particles that look ideal and ultimately the manual count detected fewer smaller radius particles than the automated routine. This can be observed by the sharpness of the probability density function in the hand counted vs the relative broadness of the computer counted curves (Figure 6-4, Table 6-3). Once it was determined that the ImageJ routine would count particles with similar accuracy as a manual counting, the other powder fractions were counted. The resulting mass and number distributions are shown as probability density functions in Figure 6-6-A and cumulative density functions in Figure 6-6-B. In data not published in this thesis, these results were compared to laser diffraction measurements performed on a Malvern ® Mastersizer 2000. The Mastersizer measured that the optical microscopy method over-predicted the average mass particle size for the largest particles and the smallest particles. The results for the average mass particle for the middle distribution were within 1-2 micron. A potential reason for the larger values in the large particles was that a single optical objective was used to analyze each image, and it was low magnification. This most likely added bias to the analysis by unintentionally not capturing smaller particles in the sample. The Mastersizer flows a solution containing the same system of particles and would not be susceptible to the same bias.

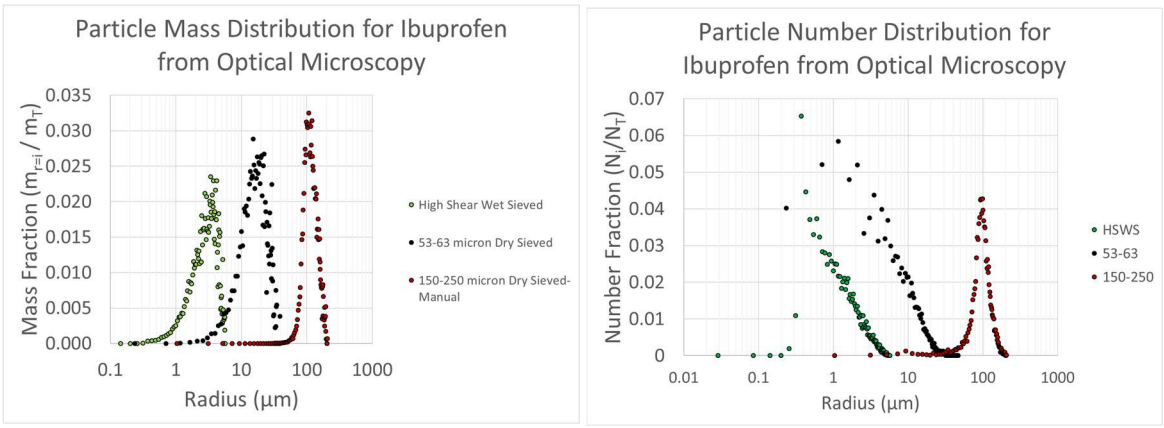

A

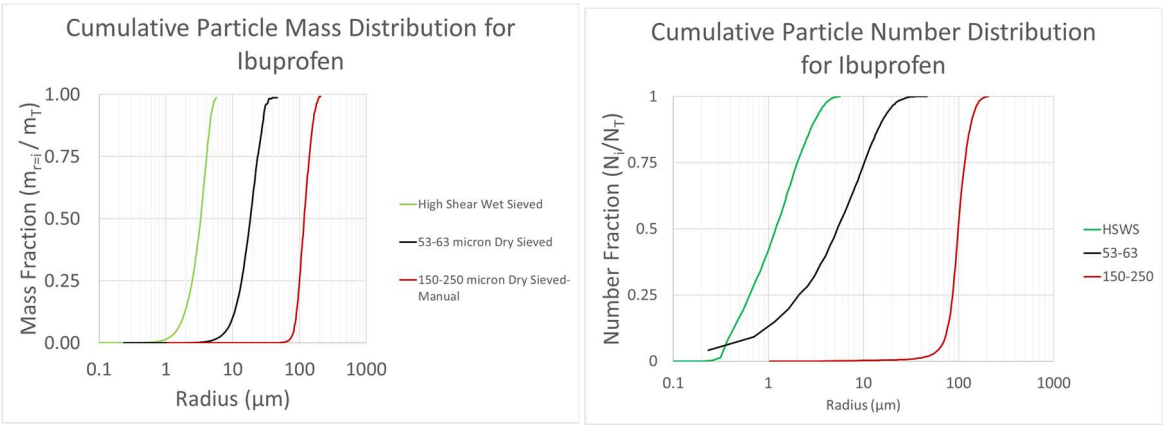

B

Figure 6-6 Statistical Characterization of Particle Size for Ibuprofen.

A) The probability density functions for both the mass distribution and number distribution of optically measure ibuprofen particles. B) The cumulative density functions for the mass and number distributions of the optically measured ibuprofen particles.

Table 6-4 Comparison of the optical microscopy determined mass average and number average radii from Figure 6-6.

Particle Fraction	Optical – Mass Distribution (µm)	Optical – Number Distribution (µm)
High Shear Wet Sieve	3.32	1.20
53 – 63 Dry Sieve	18.28	5.39
150 – 250 Dry Sieve	117.58	64.35

Traditionally in pharmaceutical sciences the mass average radius would be considered the appropriate choice to describe mass action. However, in this model of mono-sizing a polydisperse system, the total mass maybe better estimated by the particles which will dominate the flux, therefore a number average may be scientifically justified. Since smaller particles will have higher surface flux, they would drive the initial flux because of the faster dissolution rate.

6.4.3 2 Determination of the Donor Side Aqueous Boundary Layer

Based on the measurements from Sinko et al. ibuprofen could be used to measure aqueous boundary layer phenomena due to its high affinity to the PDMS membrane as long as the membrane thickness was small enough to shift the resistance to diffusion from the membrane to the aqueous diffusion layer.[81] It is well known that the convection of the fluid determines the aqueous boundary layer that forms at the solid surface, as shown by Levich et al. It is therefore critical in stirred systems to determine the aqueous boundary layer thickness. Without computationally expensive simulation, it is difficult to know what the convection pattern at the membrane surface looks like. The support mesh for the membrane is large compared to the membrane thickness (l_{mesh} = 23 x 10^{-3}cm / $h_{membrane}$ = ~ 10 x 10^{-4}cm). Therefore, the laminar Levich convection-diffusion rotating disk model for the boundary layer thickness may not be valid for this apparatus due to surface roughness. An estimate of the boundary layer thickness can be made using a solution experiment and the assumption of a stagnant layer. These results can be compared to the ideal Levich solution for the boundary layer. First, the area of the membrane was calculated, and all solution experiments performed at 37°C & 150RPM. We

calculate the surface area as a function of the wire thickness of the support and the gap distance between wires. The analytical equations were confirmed using a CAD representation of the support mesh, surface area calculated automatically in AutoCAD Fusion 360.

$$A_m = A_{ap} \times (1 - 2f + f^2) \quad \text{Eq (6.145)}$$

$$f = \frac{l_{beam} \times N}{D_{ap}} \quad \text{Eq (6.146)}$$

$$N = \frac{D_{ap}}{l_{beam} + l_{gap}} \quad \text{Eq (6.147)}$$

Where…

$D_{ap} = 7.62\ cm$; $l_{gap} = 2.8mm$; $l_{beam} = 0.99\ mm$; $A_{ap} = \pi r^2 = 44.4\ cm^2$; $A_{m_{analytical}} = 25.2\ cm^2$

Knowing the true surface area, we then can calculate the experimental flux, where V_R is the volume of the receiver fluid phase.

$$J_{exp} = \frac{V_R}{A_m}\frac{dC}{dt} \quad \text{Eq (6.148)}$$

Where V_R is to convert the concentration slope measured in the receiver into a mass transfer coefficient (dm/dt or $\dot{m}$)

Knowing that…

$$P_{PDMS\ UTLAM} = \frac{K_{PDMS} D_{PDMS}}{h_m} = \frac{65 \cdot 2.404 \times 10^{-7} cm^2\ s^{-1}}{12.51 \times 10^{-4} cm} = 1.24 \times 10^{-2} cm\ s^{-1} \quad \text{Eq (6.149)}$$

And…

$$\frac{V_R}{A_m}\frac{dC}{dt} = \left(\frac{1}{P_{Aq-Donor}} + \frac{1}{P_{UTLAM}}\right)^{-1} C_{Final} \quad \text{Eq (6.150)}$$

The donor side aqueous boundary layer is…

$$\frac{1}{P_{Aq-Donor}} = \left(\frac{V_R}{47.8\frac{\mu g}{cm^3} \times 21.8 cm^2}\frac{dC}{dt}\right)^{-1} - \frac{1}{9.7 \times 10^{-3}} \quad \text{Eq (6.151)}$$

$$P_{Aq-Donor} = 2.25 \times 10^{-3} \pm 2.45 \times 10^{-4} cm\ s^{-1} = \frac{8.41 \times 10^{-6} cm^2\ s^{-1}}{h_{abl}} \quad \text{Eq (6.152)}$$

$$\bar{h} = 37.3 \times 10^{-4} \pm 3.97 \times 10^{-4} cm\ (\text{n} = 5) \quad \text{Eq (6.153)}$$

6.4.4 Pseudo-Steady State Particle Flux Results

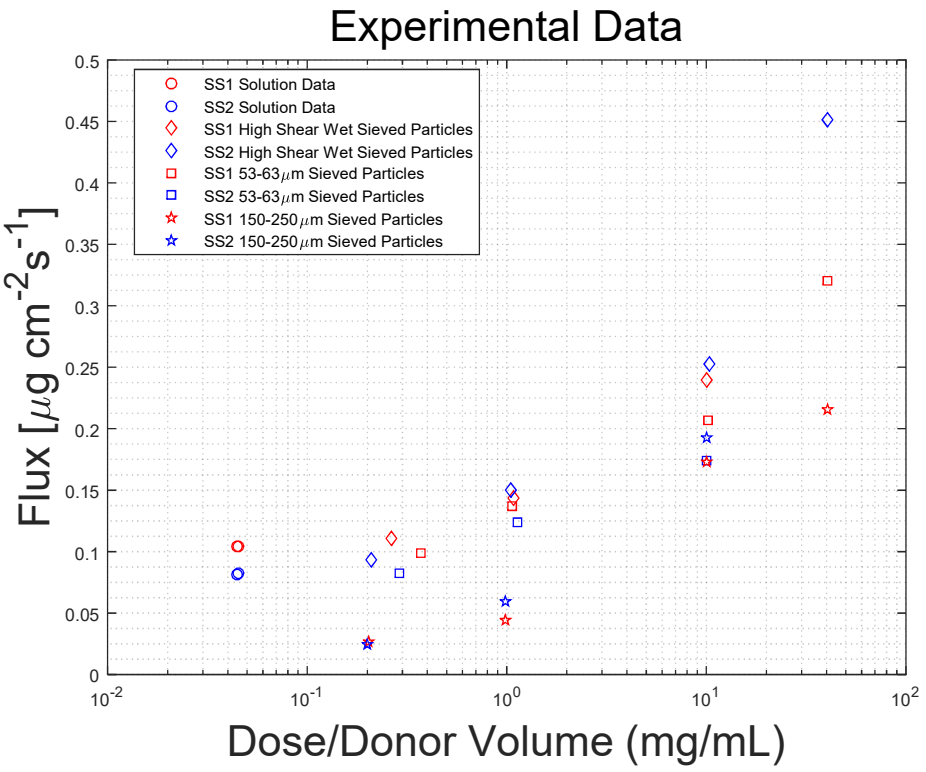

Figure 6-7 All Flux Data from Particle Size-Dose Experiments.

All three particle size distributions suspension dissolution experimental flux results as well as the solution flux experimental flux results. The general trend shows that it is possible to increase flux by increasing dose, but it is unclear if there is a particle size effect. Fluxes of the 150-250μm particles are noticeably lower than the other two fractions.

6.4.4 1 Experimental vs Optically Determined Average Mass Radius

The diffusion convection-model is only supposed to be valid when particles can exist within the aqueous diffusion layer. When the 150-250-micron sieve cut of particles were tested, it was expected that the average particle would not be able to experience flux enhancement, allowing these particles to serve as a control. The 150-250-micron sieve cut should obey the film theory diffusion limited model (equation 6.30), where the particles own diffusion layer and the donor aqueous boundary layer hinder molecular transport. The results as shown in Figure 6-8.

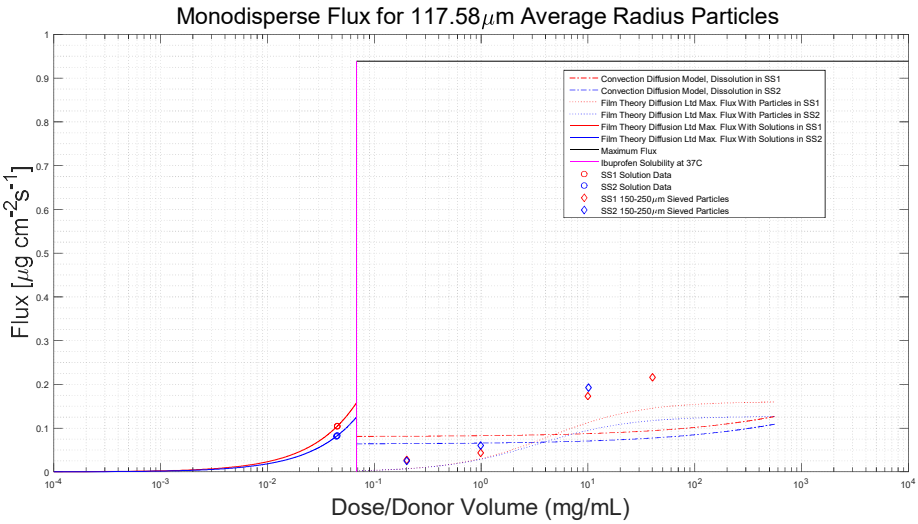

Figure 6-8 150-250-micron sieve cut Mass Average Radius Results.

Predictions of the particle-size and dose effects for the 150-250μm dry sieved particles based on the optically determined mass average radius. The shape of the curve indicates that these particles obey the film theory diffusion limited flux model.

The 53-63 sieve cut of particles was expected to obey the convection diffusion model as the average radius determined by microscopy determined that the average radius was below the aqueous boundary layer thickness. In Figure 6-9, a clear upward curve in the data is observed, however, the data does not align with the diffusion-convection model. This is most likely not a failure of the model, but a failure to capture the true average radius of the particles.

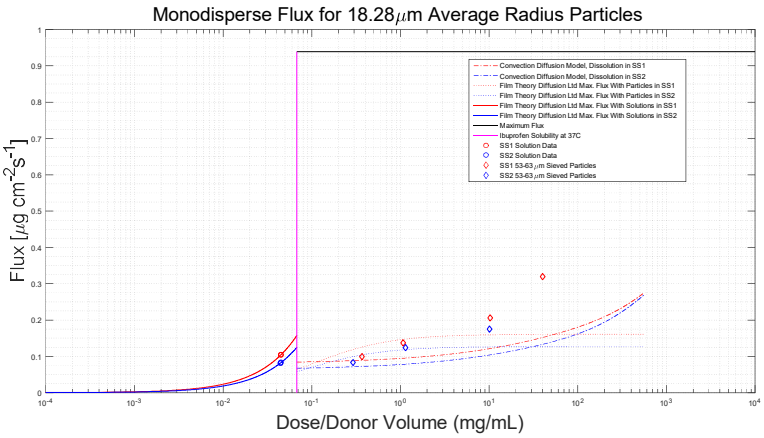

Figure 6-9 53-63-micron sieve cut Mass Average Radius Results.

Predictions of the particle-size and dose effects for the 53-63µm dry sieved particles based on the optically determined mass average radius. The shape of the curve indicates that these particles obey the convection-diffusion dissolution model.

Finally, the high shear wet sieved particles were observed to obey the convection diffusion model (Figure 6-10). The polydispersity of the particle size distribution was much narrower than the other two particle fractions. Combined with a reasonable estimate for the average radius, led to good agreement with the theoretical predictions. However, at the 40mg/mL dose there was a large flux increase. This was observed in all three PSD's and is thought to be the effect of particle settling. The density of particles in solution must have overcome the ability for the hydrofoil impeller to keep particles moving at the surface.

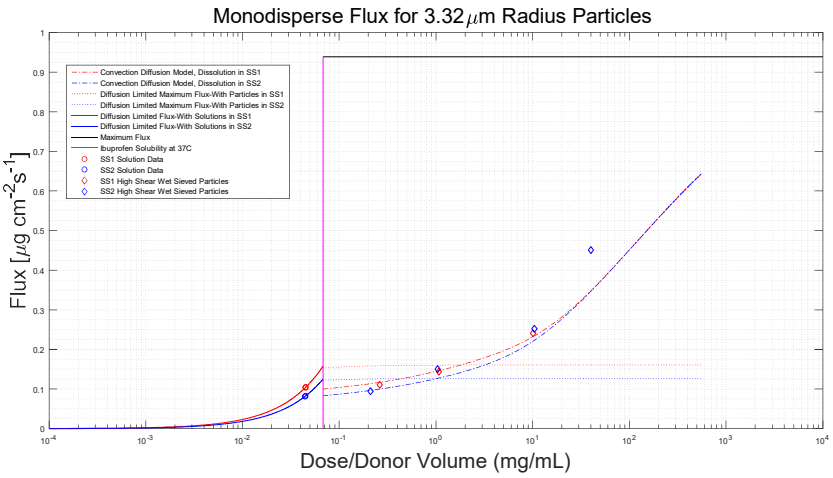

Figure 6-10 High Shear Wet-Sieved Mass Average Radius Results.

Predictions of the particle-size and dose effects for the high shear wet sieved particles based on the optically determined mass average radius. The shape of the curve indicates that these particles obey the convection-diffusion dissolution model.

6.4.4 2 Experimental vs Optically Determined Average Number Radius

The same comparison's in section 6.4.4.2 were made when using the number average-average radius to predict the flux of the three PSD's at the four doses. The agreement for the models themselves did not change, however the fits changed. For the largest PSD, the model fit went from underpredicting to overpredicting. It is likely that the true average radius falls somewhere in between the two measured radii, however, it is clear that flux behavior is clearly diffusion limited and particles of this size do not obey the convection-diffusion model. (see Figure 6-11)

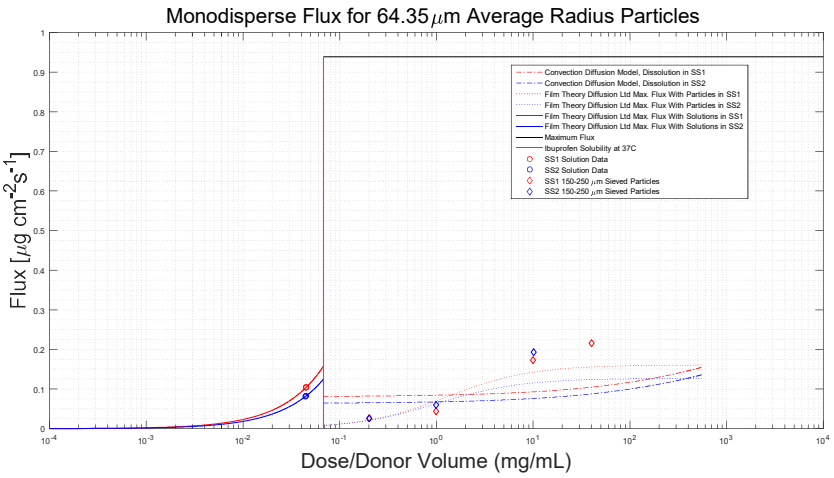

Figure 6-11 150-250-micron sieve cut Number Average Radius Results.

Predictions of the particle-size and dose effects for the 150-250μm dry sieved particles based on the optically determined number average radius. The shape of the curve indicates that these particles obey the film theory diffusion limited flux model.

The median PSD now clearly fits the convection-diffusion model, where as before the average radius failed to predict the use of a single model for the flux for all four doses. (see Figure 6-12) The possibility of the dissolution-absorption mechanics changing in between doses with the same particle size population seemed unlikely, therefore the radius determined in the mass distribution using the optical microscopy method needs refinement.

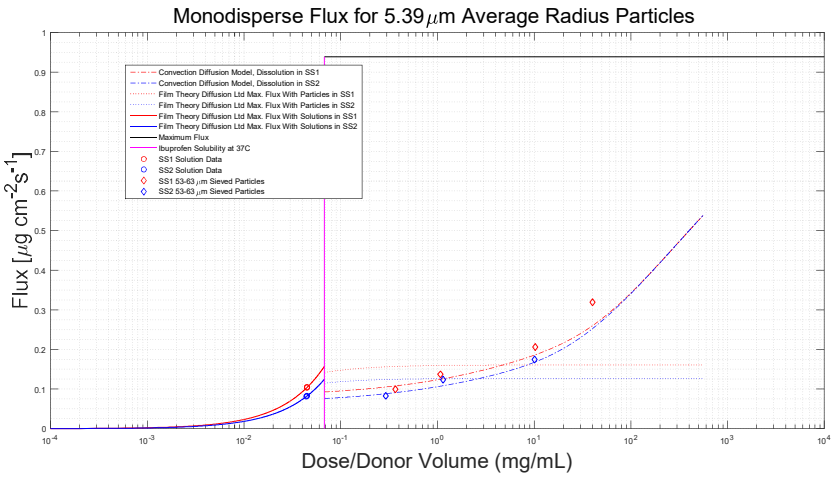

Figure 6-12 53-63-micron sieve cut Number Average Radius Results.

Predictions of the particle-size and dose effects for the 53-63μm dry sieved particles based on the optically determined number average radius. The shape of the curve indicates that these particles obey the convection-diffusion dissolution model.

Finally, the smallest and narrowest distribution of particles seems to be overpredicted using the number average radius. (see Figure 6-13) As with the other two distributions, it is likely that the optical microscopy method does not accurately capture the average particle size (mass/volume or number). Additional work for the publication of this work does use laser diffraction measurements from a Malvern ® Mastersizer to determine more accurate values for the average radii. Even though the optical characterization method proved to ultimately not be the most accurate method, it was accurate enough to provide credence to the validity of the convection-model, because reasonable estimates of the particle size distributions led to model estimates which are well represented by the data. It is recognized that the particle size measurements can and will be improved for final publication.

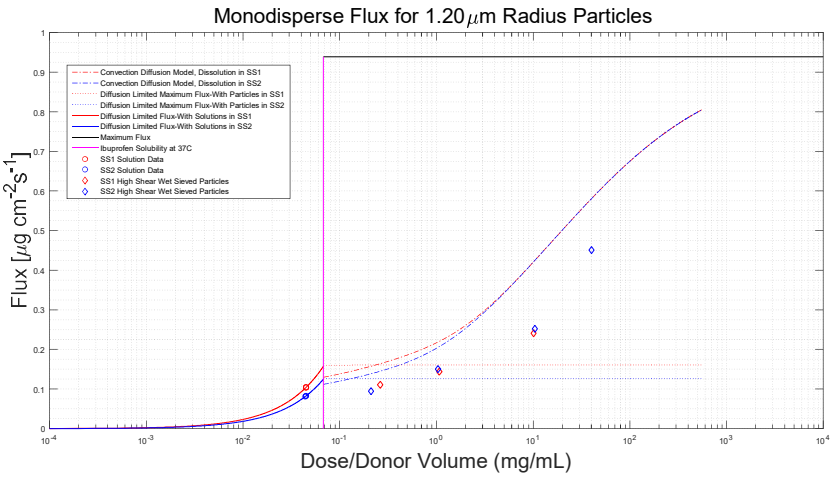

Figure 6-13 High Shear Wet Sieved Number Average Radius Results.

Predictions of the particle-size and dose effects for the high shear wet sieved particles based on the optically determined number average radius. The shape of the curve indicates that these particles obey the convection-diffusion dissolution model.

6.4.5 Flux Enhancement of Trapped particles at the Membrane Surface

One of the more interesting results of this study was that when a PDMS UTLAM support with very deep wells (0.9-1.8mm as opposed to the 0.28mm used in section 6.4.4). Particles were observed, post-test, to be located primarily in these wells. Even though in solution experiments the aqueous boundary layer was determined to be ~40μm, particles of all sizes seemed to experience a flux significantly higher than particles of the same size with a thinner support structure. In Figure 6-14, not only do all three particle size distributions experience the "shape" of the convection-diffusion model, but the flux relative to comparable doses could be at least twice the flux of optimally flowing particles.

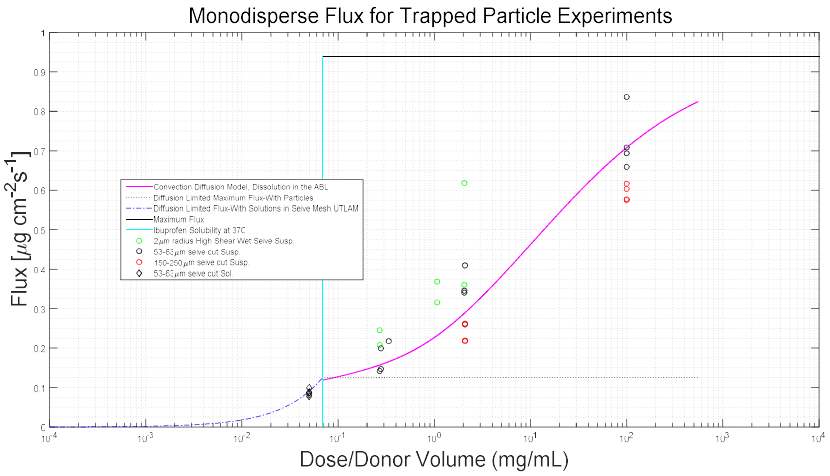

Figure 6-14 Particles Trapped at The Membrane Surface Results.

Results of the particle-size and dose effects for the high shear wet sieved, 53-63μm dry, and 150-250μm dry sieved particles. The shape of the curve indicates that these particles obey the convection-diffusion dissolution model. However, these all PSD at all dose produced fluxes at least double of the predicted flux. The magenta line indicates the convection-diffusion model's prediction for a monodisperse population of particles with a 1μm radius. Clearly the thicker mesh captured particles and pinned them to the membrane surface. This would explain how the larger particles could produce such a high flux, particles aggregating at the surface effectively dissolve right at the surface of the membrane. This is qualitatively predicted by the model as the model predicts that all particles are behaving like they are extremely small.

When considering the actual environment for particle dissolution and absorption, it is hard to escape the conclusion that the villi and microvilli play a critical role in concentrating particles within the droplet of luminal fluid at the surface of the epithelium to maximize absorption of luminal contents.

6.4.6 Flux through the membrane as a function of radius at constant doses

Examining the convection-diffusion model's flux as a function of radius allows for a unique perspective on formulation design. Figure 6-15 would allow for selection of a particle size for the active ingredient to determine the total dose that would need to be administered for a particular dose in the oral formulation. The trade off between particle size and dose can be used when deciding what amounts of active are needed

for the oral formulation, to achieve a certain absorption profile. Ideally, the combination of the convection-diffusion model and the pH-dependent film theory model would allow for the rational selection of a particle size by a formulator. This idea is being explored in the future work chapter of this dissertation.

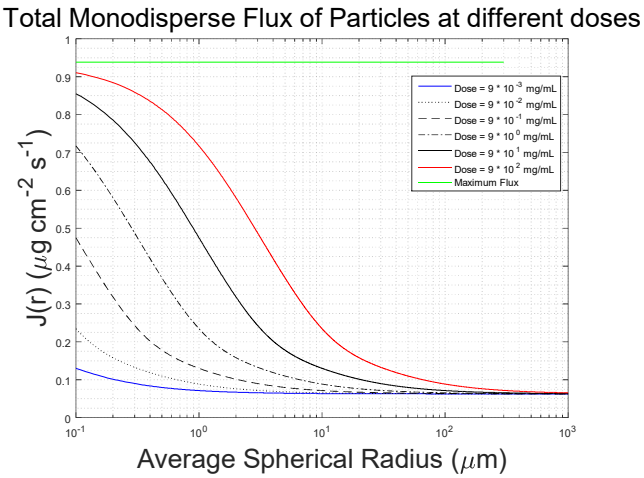

Figure 6-15 Effect of Particle Radius On Flux At Different Doses.

This shows that large particles are the least sensitive to flux enhancement by in creasing the dose. The large diameters do not allow for the packing in the diffusion layer that smaller particles can achieve. From this plot, it is easy to compare the length scale of the particle and the thickness of the diffusion layer. A common estimate for the diffusion layer in pharmaceutical systems is approximately 30μm, (in UTLAM 1 its was ~30μm and UTLAM 2 40μm). In this figure once the particles radius reaches about 30μm, an exponential increase in the flux is predicted. Hintz-Johnson's assumption about the particles aqueous boundary layer stated that the maximum thickness no matter the particle size was about 30μm, unless the particle was 30μm or less (at which the diffusion layer was noted to be equal to the radius). This is an interesting coincidence, but since Hintz-Johnson predicts a linear change in the particles permeability it does not quite match the exponential change predicted in the convection-diffusion model.

6.5 Discussion

The main conclusion from this study is that particles dissolve in the aqueous boundary layer and significantly enhance the flux through the absorptive surface. A convection-diffusion dissolution-absorption model based on the Higuchi-Hiestand dissolution model was proven to describe the effect of "shorting-out" the aqueous

diffusion layer. The characterization methods for measuring particle size in this dissertation were found to be adequate to prove the concepts of the dissolution-absorption model, however it is recognized that other standard particle size measurement techniques should be and are being applied for the final publication of this body of work. The physiological implications of this model should not be understated, as it is well known that the majority of simplifications about the physical reality of the drug dissolution-absorption process are not relevant to what actually occurs. The microenvironment of the gastrointestinal tract most likely functions on the principles established within this model. It is the combination of the local surface area and confinement of the dissolving solids in the crypt of the villi/microvilli which allow sufficient flux for drug delivery.

6.6 Acknowledgements

I would like to thank Troy Halseth for generating the data for the manual and ImageJ particle counting analysis for the high shear wet sieved particles and the 150-250 micron dry sieved. I would also like to thank Troy for his efforts in the early experimental development for this chapter. I would like to thank Niloufar Salehi for characterizing the 53-63-micron particles as well as for all the discussion about the theoretical framework, optimization of the derivation, and discussion of experimental procedures in the late stages of the project. I would also like to thank Pamela Meyer for completing the high dose experiments and for all the analytical methods discussions we have had.

CHAPTER 7

Future Work: Effect of Common Oral Excipients on Flux Through An Ultra-Thin, Large-Area Poly(Dimethyl Siloxane) Membrane: Beginnings of a Hierarchical Model for Predicting Formulation Dissolution Performance

7.1 Abstract

The purpose of this study is to qualitatively and quantitatively measure the affects of common excipients in solid oral dosage forms on dissolution rate, C_{Max}, AUC, and absorption rate (where applicable). A Plackett-Burman (PB) Design is used to efficiently detect main effects between Ibuprofen and an excipient. Performing the PB array of dissolution experiments on the USP II, USP II biphasic, and PDMS UTLAM diffusion cells will show the inter-apparatus affects, elucidating any device specific responses. Ultimately, a mechanistic hydrodynamics-based dissolution model in conjunction with the models for pH, particle size, and dose from chapter 5 & 6 will aid in isolating excipient effects from hydrodynamic and absorption effects.

7.2 Introduction

The PDMS UTLAM was proposed to be a tool for preclinical evaluation of candidate formulations. In an effort to begin understanding the possible effects of common excipients on PDMS-drug partitioning a study was designed to compare three dissolution techniques and 11 common excipients found in oral formulations to determine the influence of these excipients on the dissolution and absorption behavior of ibuprofen. The specific aims of this work are to; Aim 1: Determine the major effects (no 2nd order interactions) of 11 common oral excipients on the intra-apparatus dissolution and absorption performance of Ibuprofen. Aim 2: Determine the major effects (no 2nd order interactions) of 11 common oral excipients on the inter-apparatus dissolution and absorption performance of Ibuprofen. Aim 3: Utilize the results from the USP II and USP II biphasic experiments to isolate excipient effects specific to the PDMS UTLAM. Aim 4: Use a novel hydrodynamic dissolution model coupled with the models from chapter 5 and 6 to model particle dissolution. Aim 5: Use the mechanistic model to quantify difference of dissolution and absorption performance to describe the excipient effect. A plackett-burman design of experiments array was chosen to examine eleven factors in twelve experiments per dissolution apparatus. The plackett-burman (PB) partial factorial array is an efficient way to study main interactions between factors, however the second order and higher interactions are confounded.[114-116] In which case a different experimental design must be used once the main factors of interest are identified and further investigation of the higher order interactions becomes necessary. The responding variable was ibuprofen, which was held at a constant mass percentage of every

formulation except the negative control (pure ibuprofen). The negative control used the same target mass that each formulation should have contained.

The study design goal was to prove two main aims: 1) Absorption kinetics are important for API with significant lipophilicity and significant differences in *in vitro* parameters could be better measured by dissolution systems with absorption components. 2) The UTLAM method of incorporating absorption is easier, more cost effective (no need for filtering receiver phase samples, could be compatible with UV-dip probes which provide more data, real time, and reduce HPLC throughput demands), more environmentally friendly, and more pleasant to work with as compared to the biphasic aqueous-organic solvent test. To achieve these aims 11 common ubiquitous excipients in solid oral dosage forms were identified and the typical levels of each excipient were also identified. The marker was ibuprofen and ibuprofen's dissolution rate, area under the curve (AUC), and absorption rate (where applicable) were measured for each formulation in a standard USP 2 900mL dissolution test, a 200mL/200mL aqueous/1-octanol Biphasic dissolution test in USP 2 vessel, and the 130mL donor/100mL receiver UTLAM dissolution test with pH 6.5 50mM phosphate buffer.

The excipients chosen from this study represent most major excipient functions in modern solid oral dosage forms at typical compositional levels (chapter **7.3.2.4**). Microcrystalline cellulose, mannitol, anhydrous dibasic calcium phosphate, and anhydrous lactose are common structural excipient which can compose much of the formulation. Citric Acid was to acidify the local solution. Sodium croscarmellose and crospovidone are polymer based disintegrants which act via water uptake and

swelling to burst the compacted solid. The formulations in this study were uncompressed powders so the expected advantages of formulations with disintegrants will be muted because there is no tablet to break apart. However, there could be solution phenomena such as aggregation of polymer at the absorption interface (octanol or PDMS membrane) which could alter the partitioning rate. Sodium dodecyl sulfate is a surfactant which could also have the potential to interact with the absorption interface. Magnesium stearate and silicon dioxide are common lubricants/glidants respectively. HPMC-AS is a precipitation inhibitor polymer. For each iteration of the formulation, the non-structural excipients were held at a constant level which would be consistent for the typical amount of that excipient in a formulated product. The difference would be evenly distributed among any structural excipients in the formulation.

7.3 Materials & Methods

7.3.1 Materials

Agilent 1100 high-performance liquid chromatography (HPLC), Extend C 18 column (3.5 µm × 4.6 µm x 150 mm), acetonitrile (EMD Millipore, HPLC grade), deionized water (Milli-Q purified), trifluoroacetic acid (Fisher Scientific, Optima grade), methanol (Fisher Scientific, HPLC grade), Crospovidone (UM2012-085 Lot # K-H09074), Croscarmellose Sodium Non-GMP (Material # 10127157), HPMC-AS, LF (UM 2012-091 Lot #007), Microcrystalline Cellulose (PH102 UM2012-004), Mannitol, NF (Glaxo-Smith Klein UM2009-010), Dibasic Calcium Phosphate (JRS Lot# 2059X UM2011-049), Lactose Monohydrate-310-NF (UM2001-018), Magnesium

Stearate (UM2009-013), Sodium Dodecyl Sulfate for Electrophoresis 99% (Sigma-Aldrich), Citric Acid Anhydrous (Fisher A940-500), Ibuprofen (Albemarle Lot No. 2050−0032F), hydrochloric acid buffer pH 2.0 (USP guideline), phosphate buffer pH 6.5 (USP guideline), sodium hydroxide buffer pH 12 (NaOH + KCl), 1-Octanol, 99% pure (Acros Organics Lot# A0358670 CAS 111-87-5), polyvinyl alcohol MW = 25K, 88% hydrolyzed (Poly Sciences, Inc. #02975 Lot# 652279), poly(dimethylsiloxane), Sylgard 184 elastomer kit (Dow Corning), hexane (Fisher, reagent grade), Model WS-650MZ-23NPPB spin processor (Laurell Technologies), vacuum drying oven (Yamato ADP300C), 100mm Test Grade Silicon Wafers with native silicon oxide layer (Encompass Distribution Services), Stratasys J750 printer build size: 490 x 390 x 200 mm, VEROCLEAR RGD810 (material for J750), Dimension Elite 3-D printer build size 203 x 203 mm

7.3.2 Methods

7.3.2 1 USP II dissolution

5.4L of Phosphate buffer was degassed and then heated to 37°C in the USP 2 six station apparatus. During the heating process the motor was engaged allowing for the fluid to be stirred at 50RPM for no less than 30min prior to dosing the formulations. Formulations were weighed on an analytical balance prior to dosing and were administered through ports in lids on the USP 2 bowl. The experiments ran for 1 hour and at the end of the experiment 100mL of acetonitrile was added to solubilize any undissolved ibuprofen. The acetonitrile/phosphate was then allowed to run for an additional hour at which time the mass balance sample was taken. 2mL

samples were drawn and media was not replaced for the USP 2 monophasic experiments. 1mL of sample was discarded through a 0.45µm PVDF syringe filter and then 1mL of sample was captured and diluted 1:1 in acetonitrile for HPLC analysis (HPLC methods can be found in the appendix).

The HPLC data was converted from peak area to concentration with a standard curve and then the time course data was input to a MATLAB program that fit the data with a spline function. This allowed for better estimations of C_{max} & t_{max} when the C_{max} & t_{max} did not fall within the first 10min, as well as allowing for rapid calculation of the $AUC_{0\text{-}60min}$ via a numerical trapezoidal method. This program was applied to the data of all three apparatuses and a comparison of the manual and MATLAB method and concentration profiles for each formulation are not included in this dissertation (but will be shown in the final publication).

7.3.2 2 USP II Biphasic dissolution

200mL of phosphate buffer was degassed and heated in a single, water jacketed USP 2 bowl. A custom lid cover was created to house the sampling ports for the aqueous and organic phases, as well as house a large diameter tube to dose the solids directly to the aqueous phase after the organic phase has been poured on top. The advantage of this is that the two phases can equilibrate prior to the dosing of the solid, as opposed to having to rapidly fill the organic phase immediately post dose. The tip of the dosing tube was far enough under the aqueous surface that no organic could enter the tube (even under the pressure applied by the 1-octanol) and the tip was close enough to the top edge of the USP 2 paddle that a large shear could pull powder down into the vessel without any experimenter assistance. The dosing tube was

constructed from two 10mL pipette tips, which were wide enough to prevent any "rat holing" or other powder flow concerns. The aqueous media was gently poured down the sides of the dosing tube to replenish media removed from sampling to catch any solid that may have stuck to the tube during initial dosing, and the 1-octanol was carefully injected through the organic sampling cannula as to not disturb the organic-water interface with bubbles. Two milliliter samples were drawn from each phase and filtered with a 0.45µm PVDF syringe filter. The respective media was replaced in each phase post sampling.

7.3.2 3 PDMS UTLAM dissolution

To attempt to keep the A/V of both the USP II Biphasic and the PDMS UTLAM diffusion cell, 90mL was chosen to be the donor phase volume for all PDMS UTLAM diffusion cell experiments. The A/V in the USP II Biphasic is still greater than the PDMS UTLAM by about 0.1. The first 12 experiments conducted in the PDMS UTLAM were using 90mL of pH 6.5 50mM phosphate buffer, stirring at 150RPM. The second twelve experiments were conducted at 50RPM using the same buffer. The same sampling procedure for the USP II Biphasic experiments was employed in for the UTLAM diffusion cell experiments.

7.3.2 4 Plackett-Burman Design of Experiments Array (Mass % of Formulation)

Table 7-1 The Plackett-Burman Design of Experiments Array.

The units for this table are mass percent.

Entity	Factor	F - 1	F – 2	F - 3	F - 4	F - 5	F - 6	F - 7	F - 8	F - 9	F - 10	F - 11	F - 12	F - 13
Ibuprofen	N/A	35.9	35.9	35.9	35.9	35.9	35.9	35.9	35.9	35.9	35.9	35.9	35.9	100
Sodium Croscarmellose	1	5			5				5	5	5			
Silicon Dioxide	2	0.1	0.1			0.1				0.1	0.1	0.1		
HPMC-AS	3	10		10			10				10	10	10	
Microcrystalline Cellulose	4	10	20.7		19.4			28.1				48	24.1	
Mannitol	5	10	20.7	16.4		31			51.1				24.1	
Anhydrous Dibasic Calcium Phosphate	6	10	20.7	16.4	19.4		50.1			47				
Anhydrous Lactose	7	10		16.4	19.4			28.1			47			
Magnesium Stearate	8	1			1	1	1		1			1		
Sodium Lauryl Sulfate	9	1				1	1	1		1			1	
Crospovidone	10	2	2				2	2	2		2			
Citric Acid	11	5		5				5	5	5		5		

7.4 Results

7.4.1 USP 2 900mL Monophasic Dissolution Experiment

The USP 2 does not provide a lot of discrimination between the 13 formulations as seen in Figure 7-1 (positive control = all excipients + ibuprofen [F1], negative control = only ibuprofen [F13]). There are most likely at least two different groupings for the dissolution rate, and little understanding about the exposure differences between formulations (time and AUC). It was expected that maximum concentration would be similar for all formulations due to using similar initial masses and volumes.

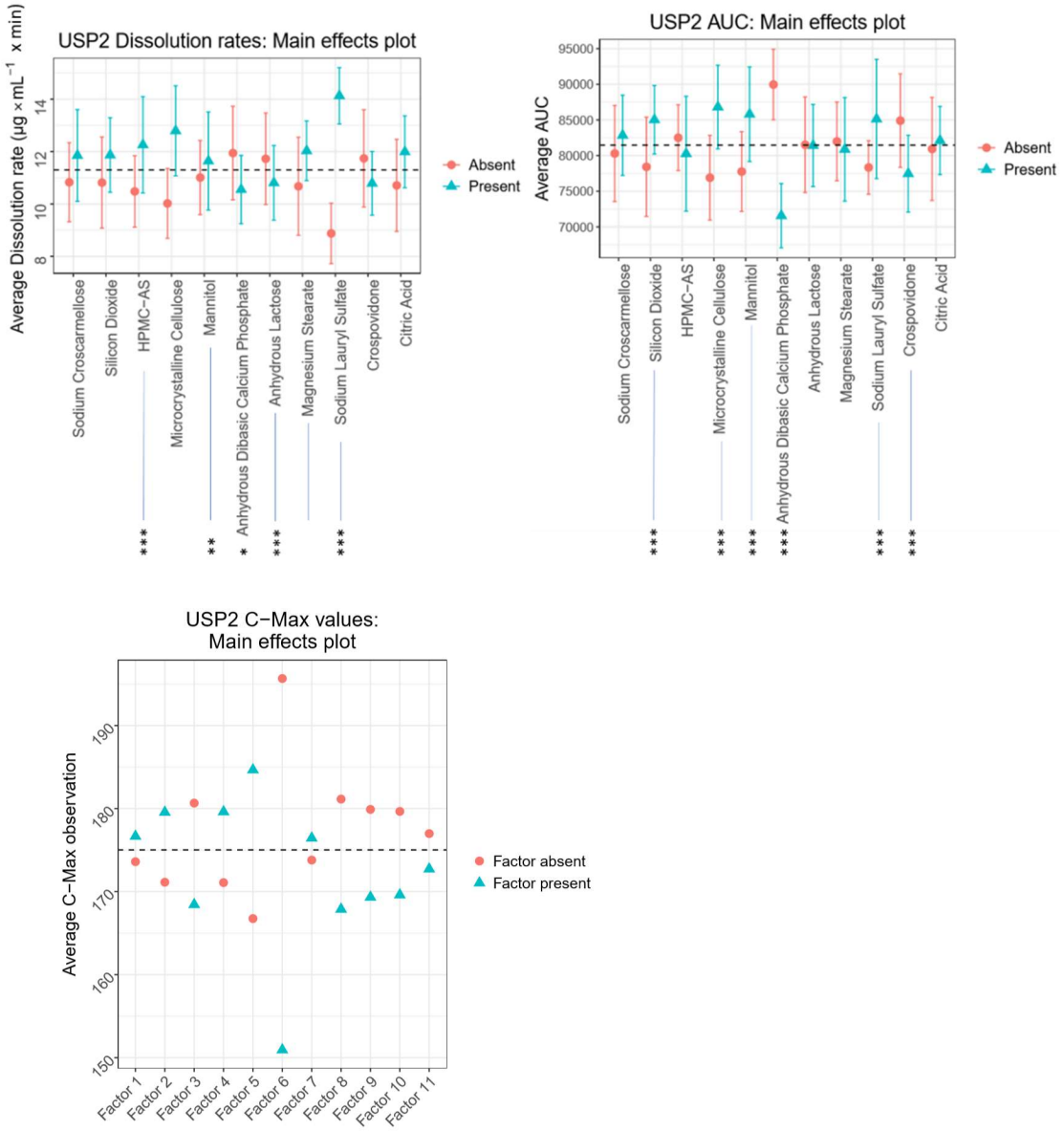

Figure 7-1 Main effects plots for the PB array conducted in the USP II device.

These plots examine the affect on the average value of the parameter (Dissolution rate, c-max, AUC) in the presence and absence of the factor. Statistical confidence intervals are calculated with $p < 0.001$ = ***, $p < 0.01$ = **, and $p < 0.05$ = *.

7.4.2 USP 2 200mL/200mL Biphasic 1-Octanol/Water Dissolution Experiment

The biphasic device had significantly varied performance when compared to the counterpart USP 2 experiments (Figure 7-2). Dissolution rate, maximum concentration, and AUC were significantly affected by each excipient in the formulation. This is expected when the volume of the dissolution phase was reduced to near physiological levels and with the addition of absorption kinetics. However, just because this is expected does not mean that these results are not novel. Even though this system is not the UTLAM it very clearly demonstrates that even simple formulations and simple drug molecules can have a drastically different performance in the *in vitro* dissolution device when comparing a traditional dissolution method to an *in vivo* relevant dissolution method. Another significant result of this type of comparison is that the not just the magnitude of rates and areas that are different, but the performance of the excipients themselves change in between test methods. For example; factor 6 (anhydrous dibasic calcium phosphate) in the USP 2 device is practically the only excipient that has an effect of the ibuprofen's performance, whereas in the biphasic device there is almost no response from anhydrous dibasic calcium phosphate.

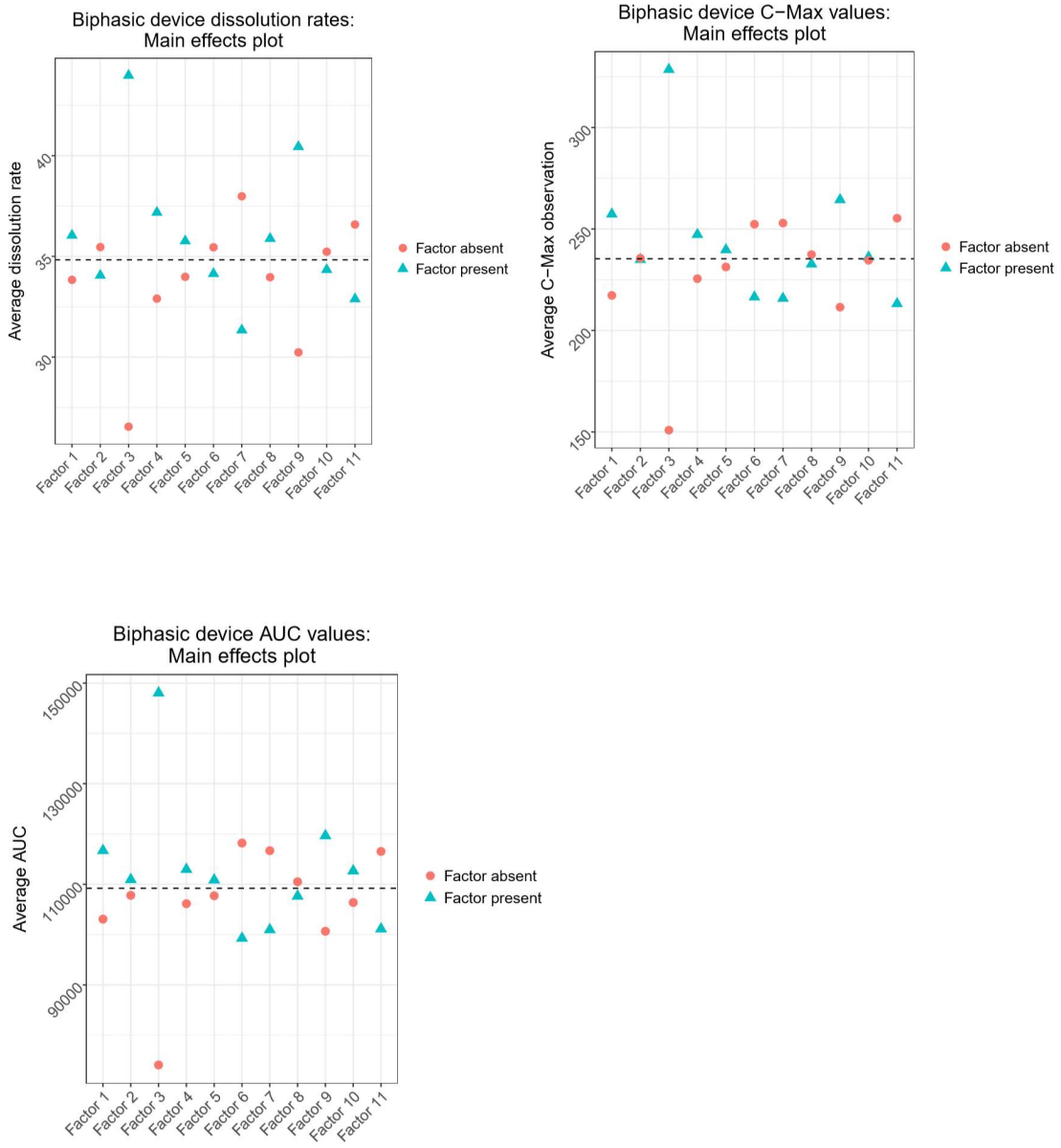

Figure 7-2 Main effects plots for the PB array conducted in the USP II Biphasic device.

These plots examine the affect on the average value of the parameter (Dissolution rate, c-max, AUC) in the presence and absence of the factor. Statistical confidence intervals are calculated with $p < 0.001$ = ***, $p < 0.01$ = **, and $p < 0.05$ = *.

7.5 Discussion

More in depth analysis is required to make strong conclusions about the data that has already been generated. Experiments are continuing in the PDMS UTLAM diffusion cell. Ultimately a comparison of the excipients effect on dissolution and

absorption parameters will be compared within an apparatus as well as between apparatuses.

APPENDICES

APPENDIX A

Ultra-Thin, Large-Area Membrane Diffusion Cell Design Considerations

A1. Rapid Prototyping: CAD and Additive Manufacturing for the Advancement of Pharmaceutical Science

Computer aided design (CAD) and additive manufacturing have been used since the 1980s to reduce the cost, effort, and production time of prototype models for engineered parts. CAD models of a part are made in a variety of commercially available software packages and exported into a ".stl" file (Standard Tessellation Language or STereoLithographic file). The stl file provides coordinates for triangular planes which represent small portions of surfaces of the CAD model. Higher tessellation translates to more resolution the surface has, which ultimately leads to smoother or more detailed printed parts. One of the most popular additive manufacturing techniques is stereolithography (SL), which is one method within the colloquial term "3D printing". SL uses photosensitive monomer resins that polymerize when exposed to ultraviolet light. The penetration of ultraviolet light is

shallow in the liquid monomer resin; thus the polymerization reaction occurs near the liquid surface. Once the photopolymerization is complete the build substrate is lowered into the reservoir of liquid monomer resin and then the photopolymerization process is repeated over the slice of the two-dimensional cross section until the part is completed. Another common additive manufacturing technique is fused deposited modelling (FDM). FDM relies on hot melt extrusion, specifically, heating the material 0.5°C above the melting temperature and then depositing it through a movable head. The material rapidly cools after the extrusion and cold welds in place to the adjoining layers. The resolution of the additive manufacturing device is described as a voxel, which is a three-dimensional pixel.[117-119] The resolution of the three-dimensional printers used in this work range from 16μm to 85μm for the SL resin printers (Projet 3500 HD Max/ Stratasys J750) and 178μm-500μm for the FDM ABS printer (Stratasys Dimension Elite).

CAD, FDM, and SL have recently begun to enter the field of pharmaceutical science in the form of drug delivery systems such as modified and immediate release tablets, caplets, and disks.[120-128] While there appears to be interest in using additive manufacturing to develop new ways to control dose weight and dissolution properties, there is no literature about using additive manufacturing to improve the science of dissolution itself. The ability to rationally design dissolution methodologies and equipment that are relevant to physiologic dissolution are now possible because of rapid prototyping simulated parts (vessels & impellers) from computational fluid dynamics simulations, and clinical studies.

From a parallel project, which involved designing new dissolution apparatus components the hydrofoil impeller was found to have many desirable properties as an impeller. Hydrofoils have been reported to be good at resuspending particles, providing homogeneous fluid flow, and bulk fluid shear. It was decided that the hydrofoil impeller should also be implemented into the UTLAM diffusion cell, so that the stirring would mitigate known problems experienced in the compendial USP II apparatus. In this appendix computation fluid dynamics simulations of impeller geometry and its effect on bulk fluid shear, velocity, and mixing time scale were evaluated to determine the proper hydrofoil diameter for use in the UTLAM diffusion cell.

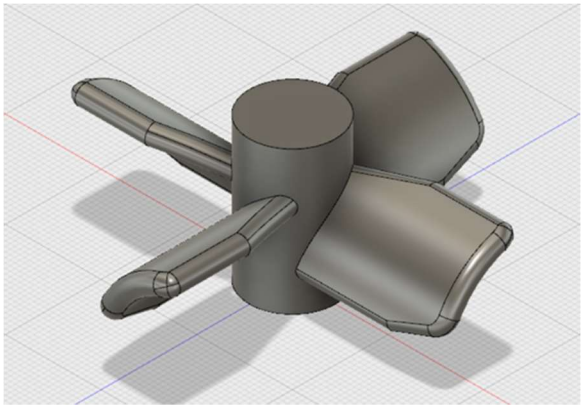

Figure A-1 Prototype Hydrofoil for UTLAM Diffusion Cell

Four blade hydrofoil originally considered for implementation in a 3D printed version of the UTLAM diffusion cell. The physical model was determined to chemically incompatible with lipophilic drugs.

A CAD representation of an ideal hydrofoil that was modelled using COMSOL mixer module's frozen rotor model. Early studies for the UTLAM diffusion cell also considered an anchor shaped impeller, however, the anchor impeller is a radial mixer and with the small volumes targeted in the UTLAM diffusion cell an axial mixer was

preferred. Below are the comparisons of the hydrofoil and anchor impeller. There is relatively little difference in the resulting computationally determined bulk fluid properties. This was not surprising because the anchor truly performs best with high viscosity solutions than water, yet the anchor is not noted in literature for its ability to resuspend particles.

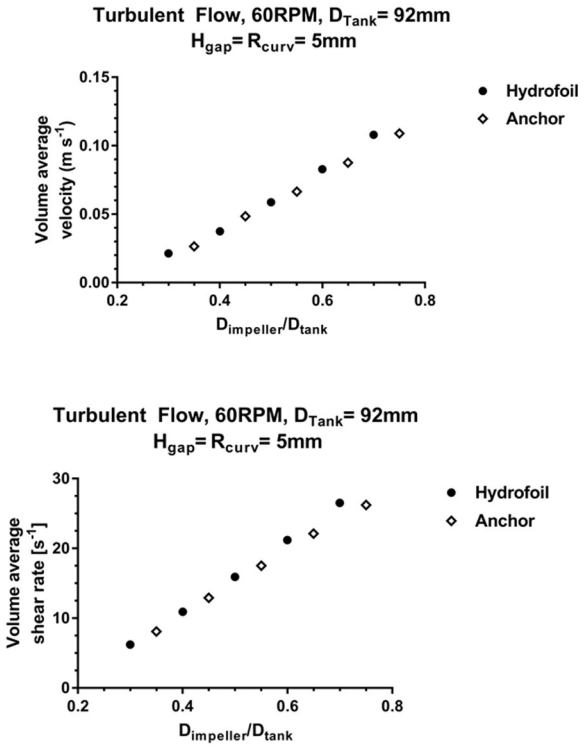

Figure A-2 Diameter Ratio of Impeller Study

In attempt to balance the need for sufficient velocity and shear for ideal particle resuspension and fluid mixing with selecting an impeller that would input the lowest amount of shear required (bulk fluid shear and the particle size determine the shear forces on the particle in fluid) to maintain those optimal mass transfer conditions, the diameter ratio between the tank and impeller were examined. Most commonly hydrofoils have a diameter ratio of 0.3-0.4. The UTLAM hydrofoil selected a diameter ratio of 0.5 to maximize velocity and minimize shear.

When the decision to move forward on selection of a hydrofoil, several diameter ratio designs were selected and simulated at various agitation rates to predict the bulk fluid properties. As we were concerned about the bulk fluid shear and its

influence on the local particle shear, the optimal candidate would produce a high fluid velocity with as little shear produced in the bulk fluid as possible. However, since shear and velocity are essentially proportional to each other, the compromise between the two seemed to be 50% of tank diameter.

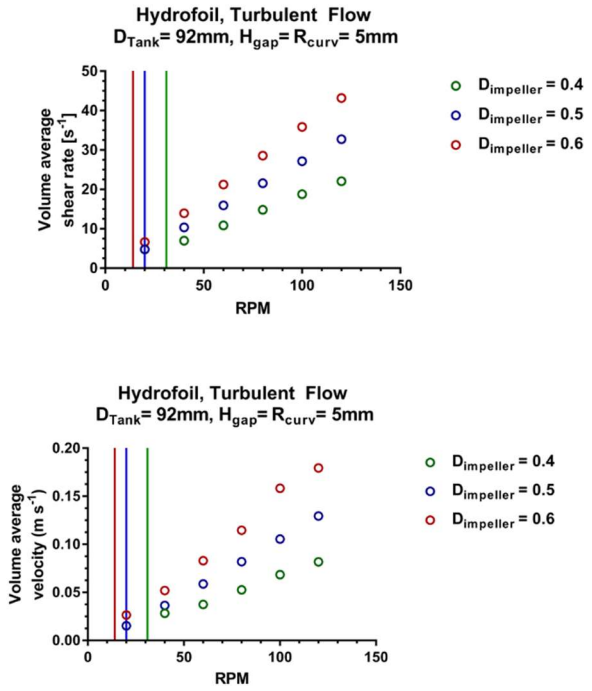

Figure A-3 Stirring Speed Study of Prototype Hydrofoil

The effect of stirring speed was estimated for the target diameter hydrofoil and 10% above and below. The vertical lines indicate the lower limit for valid simulation of turbulent flow based on the Reynolds number.

This ultimately led to the design of a final fabricable hydrofoil, with which the final diffusion cell could be design and characterized. As seen in the figure below, the height of the hydrofoil significantly affects the A/V ratio in this high aspect ratio tank (diameter larger than height).

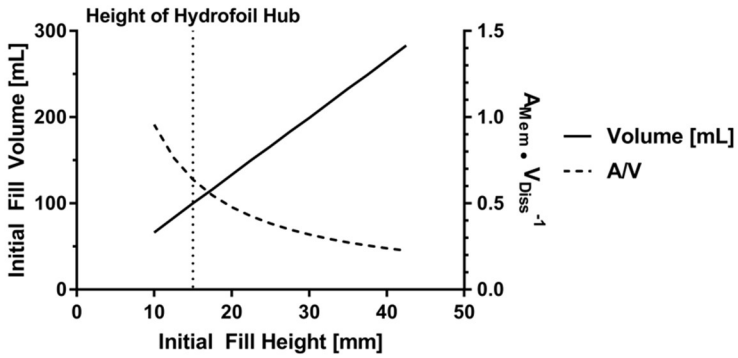

Figure A-4 Design Plot for UTLAM Diffusion Cell

Once a hydrofoil configuration was determined, the tank geometry was calculated and then the optimization of the A/V for the diffusion cell began. The A/V is limited by the height of the hydrofoil hub and effective blade height (linear projection onto the axial axis). Assuming that the hydrofoil hub was just barely covered with fluid, the impeller would function as desired within a certain range of agitation rates and maximize the geometric component of the absorption rate. The maximum stirring speed was qualitatively determined to be at or below the agitation rate which the vortex begins to form around the shaft at the fluid surface.

The final prototype UTLAM diffusion cell was created in CAD Fusion 360 and printed on a J750 Stratasys stereolithographic 3D printer. Due to high partitioning into the polymer used in the printing process, the prototype only served to gauge the ability of the support mesh to support experiment stress on the UTLAM. Additionally, the prototype allowed for significant experiential learning on how to operate the UTLAM diffusion cell.

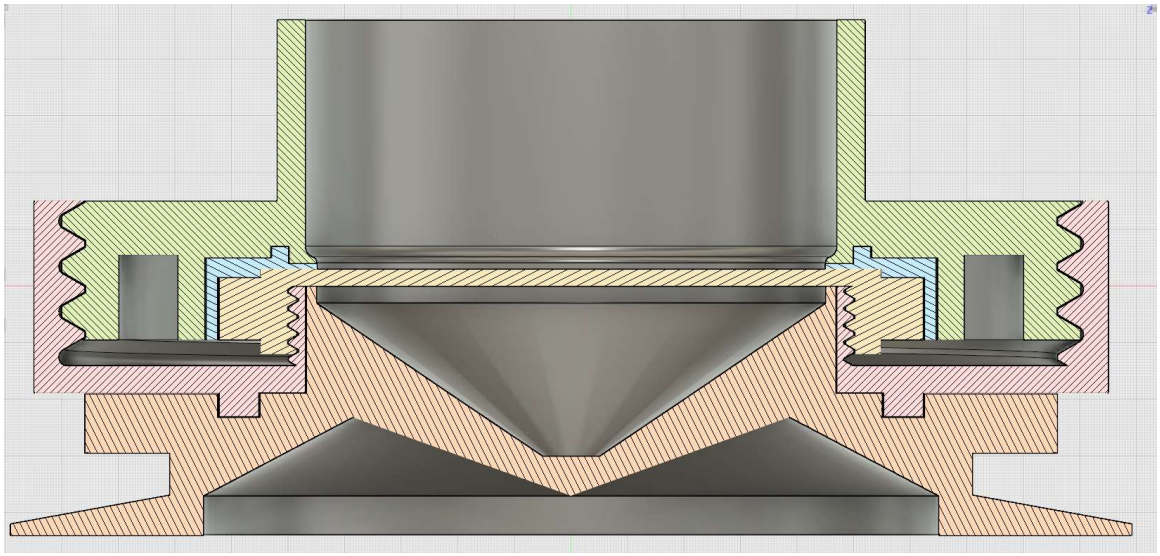

Figure A-5 Cross sectional view of the original UTLAM prototype dissolution device. Side view.

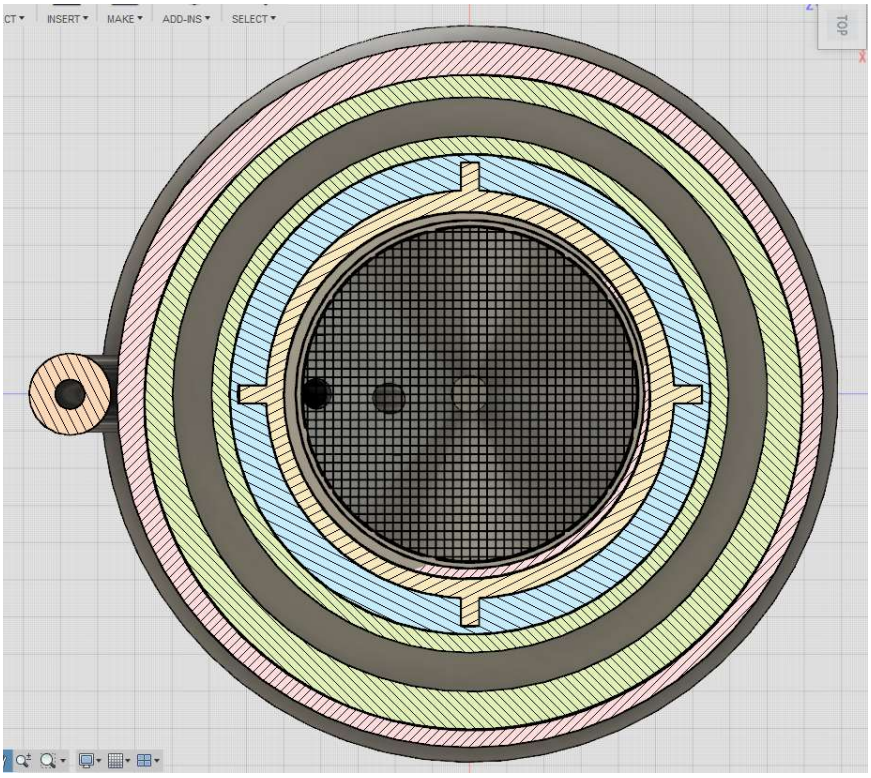

Figure A-6 Cross sectional view of the original UTLAM prototype dissolution apparatus with cut plane at the membrane surface.

APPENDIX B

MATLAB Code for Chapter 5

B. 1 Experimental Plots

```
clear all
close all
clc

%UTLAM Diffusion Cell Constants
AUTLAM = 21.8; %[cm2] exposed membrane surface area
hUTLAM = (12.5)*10^-4; %[cm] membrane thickness
hAqU = 39.5*10^-4; %[cm] Aqueous diffusion layer thickness
hAqUplus = hAqU+(4.53*10^-4); %[cm] ABL thickness plus StDev
hAqUminus = hAqU-(4.53*10^-4); %[cm] ABL thickness minus StDev
vrec = 219; %mL or cm3
vmUTLAM = AUTLAM*hUTLAM; %[cm3] membrane volume
hUTLAMplus = ((hUTLAM/10^-4)+0.2)*10^-4; %[cm] +95% CI membrane
thickness
vmUTLAMplus = AUTLAM*hUTLAMplus; %[cm3] membrane volume
hUTLAMminus = ((hUTLAM/10^-4)-0.2)*10^-4; %[cm] -95% CI membrane
thickness
vmUTLAMminus = AUTLAM*hUTLAMminus; %[cm3] membrane volume

%Rotating Diffusion Cell Constants
ARDC = 6.41; %[cm2] exposed membrane surface area
hRDC = 680*10^-4; %[cm] membrane thickness
hRDCplus = (838)*10^-4; %[cm] maximum measured thickness
hRDCminus = (596)*10^-4; %[cm] minimum measured thickness
vmRDC = ARDC*hRDC; %[cm3] membrane volume
vmRDCplus = ARDC*hRDCplus; %[cm3] membrane volume
vmRDCminus = ARDC*hRDCminus; %[cm3] membrane volume
hAqR = 36.1*10^-4; %[cm] Aqueous diffusion layer thickness
hAqRplus = hAqR+(3.97*10^-4); %[cm] ABL thickness plus (StDev same as
UTLAM)
hAqRminus = hAqR-(3.97*10^-4); %[cm] ABL thickness minus (StDev same as
UTLAM)
vrecRDC = 70; %[cm3] receiver side volume
%Ibuprofen Constants
PSANI = 37.3;%non-ionized polar surface area
%calculated using ChemAxon's chemicalize.org
PSAI = 40.13;%ionized polar surface area
%calculated using ChemAxon's chemicalize.org
DNI = 2.404*10^-7; %[cm2 s-1] Drug-PDMS non-ionized Diffusion
coefficent
```

```
%determined by rotating diffusino cell at 150RPM @pH 2 (sarah's data).
%first the Ppdms was determined, then KDpdms, then KD was divided by
the
%measured equilibrium K.
DI = 1.586*10^-8; %[cm2 s-1] Drug-PDMS ionized Diffusion coefficent
%was determined using the same method above, at pH 7 and 12 (sarah's
data)
pKa = 4.4; %drug pKa
PNI = 10^1.81; %non-ionized intrinsic parition coefficient
%Determined using an equilibrium partition experiment
PI = 0.245; %ionized intrinsic partition coefficient
%determined in the UTLAM at 150RPM at pH 7
DAq = 8.41*10^-6; %cm2/s
%ibuprofen aqueous diffusion coefficient (presumably the effective)

pH = (1:0.1:14);
fNI = 1./(1+10.^(pH-pKa));
%Wagner's Extraction Theory pH-partition model for rotating diffusion
cell and UTLAM diffucion cell
kUTLAM = (AUTLAM./(hUTLAM.*vmUTLAM)).*((DNI.*PNI*fNI)+(DI.*PI.*(1-
fNI))./(1.+(PNI.*fNI)+(PI.*(1-fNI)));
kUTLAMplus =
(AUTLAM./(hUTLAMplus.*vmUTLAMplus)).*((DNI.*PNI.*fNI)+(DI.*PI.*(1-
fNI))./(1.+(PNI.*fNI)+(PI.*(1-fNI)));
kUTLAMminus =
(AUTLAM./(hUTLAMminus.*vmUTLAMminus)).*((DNI.*PNI.*fNI)+(DI.*PI.*(1-
fNI))./(1.+(PNI.*fNI)+(PI.*(1-fNI)));

kRDC = (ARDC./(hRDC.*vmRDC)).*((DNI.*PNI.*fNI)+(DI.*PI.*(1-
fNI))./(1.+(PNI.*fNI)+(PI.*(1-fNI)));
kRDCplus = (ARDC./(hRDCplus.*vmRDCplus)).*((DNI.*PNI.*fNI)+(DI.*PI.*(1-
fNI))./(1.+(PNI.*fNI)+(PI.*(1-fNI)));
kRDCminus =
(ARDC./(hRDCminus.*vmRDCminus)).*((DNI.*PNI.*fNI)+(DI.*PI.*(1-
fNI))./(1.+(PNI.*fNI)+(PI.*(1-fNI)));

% Film Theory for UTLAM and RDC
%cm/s effective permeability through aqueous boundary layer
%UTLAM
PAqU = DAq/hAqU;
PAqUplus = DAq/hAqUplus;
PAqUminus = DAq/hAqUminus;
%RDC
PAqR = DAq/hAqR;
PAqRplus = DAq/hAqRplus;
PAqRminus = DAq/hAqRminus;

%cm/s Non-ionized permeability through membrane
%UTLAM
PmemNIU = (PNI.*DNI.*fNI)./hUTLAM;
PmemNIUplus = (PNI.*DNI.*fNI)./hUTLAMplus;
PmemNIUminus = (PNI.*DNI.*fNI)./hUTLAMminus;
%RDC
PmemNIR = (PNI.*DNI.*fNI)./hRDC;
PmemNIRplus = (PNI.*DNI.*fNI)./hRDCplus;
PmemNIRminus = (PNI.*DNI.*fNI)./hRDCminus;
```

```
%cm/s ionized permeability through membrane
%UTLAM
PmemIU = (PI.*DI.*(1-fNI))./hUTLAM;
PmemIUplus = (PI.*DI.*(1-fNI))./hUTLAMplus;
PmemIUminus = (PI.*DI.*(1-fNI))./hUTLAMminus;
%RDC
PmemIR = (PI.*DI.*(1-fNI))./hRDC;
PmemIRplus = (PI.*DI.*(1-fNI))./hRDCplus;
PmemIRminus = (PI.*DI.*(1-fNI))./hRDCminus;

%Total Permeability
%UTLAM
PmemTU = PmemNIU+PmemIU;
PmemTUplus = PmemNIUplus+PmemIUplus;
PmemTUminus = PmemNIUminus+PmemIUminus;
%RDC
PmemTR = PmemNIR+PmemIR;
PmemTRplus = PmemNIRplus+PmemIRplus;
PmemTRminus = PmemNIRminus+PmemIRminus;

%film theory Apparent Absorption Rate
kappUTLAM = (AUTLAM/vrec).*(((1./PAqU)+(1./PmemTU)).^-1);
kappUTLAMplus = (AUTLAM/vrec).*(((1./PAqUplus)+(1./PmemTUplus)).^-1);
kappUTLAMminus = (AUTLAM/vrec).*(((1./PAqUminus)+(1./PmemTUminus)).^-
1);

kappRDC = (ARDC/vrecRDC).*(((1./PAqR)+(1./PmemTR)).^-1);
kappRDCplus = (ARDC/vrecRDC).*(((1./PAqRplus)+(1./PmemTRplus)).^-1);
kappRDCminus = (ARDC/vrecRDC).*(((1./PAqRminus)+(1./PmemTRminus)).^-1);

%%pKa shift determination
%Varying hABL
syms x
x0 = [1 14]; %guess interval min, max
%Generating function for derivative
fUh0 =@(x)
((AUTLAM/vrec).*(((1./(DAq/hAqU))+(1./(((PNI.*DNI.*(1./(1+10.^(x-
pKa)))).*hUTLAM)+((PI.*DI.*(1-(1./(1+10.^(x-pKa))))).*hUTLAM)))).^-
1)).*((AUTLAM/vrec).*(((1./(DAq/hAqU))+(1./(((PNI.*DNI.*(1./(1+10.^(1-
pKa)))).*hUTLAM)+((PI.*DI.*(1-(1./(1+10.^(1-pKa))))).*hUTLAM)))).^-1));
fRh0 =@(x)
((ARDC/vrecRDC).*(((1./(DAq/hAqR))+(1./(((PNI.*DNI.*(1./(1+10.^(x-
pKa)))).*hRDC)+((PI.*DI.*(1-(1./(1+10.^(x-pKa))))).*hRDC)))).^-
1)).*((ARDC/vrecRDC).*(((1./(DAq/hAqR))+(1./(((PNI.*DNI.*(1./(1+10.^(1-
pKa)))).*hUTLAM)+((PI.*DI.*(1-(1./(1+10.^(1-pKa))))).*hRDC)))).^-1));
fUhw =@(x) ((AUTLAM./(hUTLAM.*vmUTLAM)).*((DNI.*PNI*(1./(1+10.^(x-
pKa)))+(DI.*PI.*(1-(1./(1+10.^(x-pKa)))))).*(1.+(PNI.*(1./(1+10.^(x-
pKa)))+(PI.*(1-(1./(1+10.^(x-
pKa))))))).*(AUTLAM./(hUTLAM.*vmUTLAM)).*((DNI.*PNI*(1./(1+10.^(1-
pKa)))+(DI.*PI.*(1-(1./(1+10.^(1-pKa)))))).*(1.+(PNI.*(1./(1+10.^(1-
pKa)))+(PI.*(1-(1./(1+10.^(1-pKa))))))));
fRhw =@(x) ((ARDC./(hRDC.*vmRDC)).*((DNI.*PNI.*(1./(1+10.^(x-
pKa)))+(DI.*PI.*(1-(1./(1+10.^(x-pKa)))))).*(1.+(PNI.*(1./(1+10.^(x-
pKa)))+(PI.*(1-(1./(1+10.^(x-
pKa))))))).*((ARDC./(hRDC.*vmRDC)).*((DNI.*PNI.*(1./(1+10.^(1-
```

```
pKa))))+(DI.*PI.*(1-(1./(1+10.^(1-pKa))))))./(1.+(PNI.*(1./(1+10.^(1-
pKa))))+(PI.*(1-(1./(1+10.^(1-pKa)))))));
%solve for second derivative
f_sd_Uh0 = matlabFunction(diff(fUh0(x),2));
f_sd_Rh0 = matlabFunction(diff(fRh0(x),2));
f_sd_Uhw = matlabFunction(diff(fUhw(x),2));
f_sd_Rhw = matlabFunction(diff(fRhw(x),2));
%Interpolate to find the inflection point (pKa_eff) d2y/dy2 = 0
pkaU = fzero(f_sd_Uh0,x0);
pkaR = fzero(f_sd_Rh0,x0);
pkaUw = fzero(f_sd_Uhw,x0);
pkaRw = fzero(f_sd_Rhw,x0);


%data ultra thin large area membrane diffusion cell
datayUTLAM = [2.48E-04
2.50E-04
2.46E-04
2.34E-04
2.14E-04
2.00E-04
1.89E-04
1.85E-04
2.70E-05
2.57E-05
2.26E-05
2.40E-05
2.31E-07
3.06E-07];
dataxUTLAM =
[1.968,1.958,1.954,1.981,4.449,4.445,4.45,4.428,6.435,6.431,6.44,6.428,
11.401,12.187];
%data rotating diffucion cell
datayRDC =[2.02E-05
2.10E-05
1.73E-05
2.01E-05
1.74E-05
1.27E-05
1.43E-05
1.19E-05
1.15E-05
9.16E-06
2.24E-05
8.04E-06
8.86E-06
9.24E-06
3.54E-06
3.40E-06
4.55E-06
1.50E-06
1.58E-06
2.46E-06
5.27E-07
5.33E-07
1.89E-07
```

```
1.86E-07
5.65E-08
5.17E-08
2.99E-08
1.11E-08];
dataxRDC =
[2,2,2,3,3,3.5,3.5,3.5,4,4,4,4.5,4.5,4.5,5,5,5,5.5,5.5,5.5,6,6,6.5,6.5,
7,7,12,12];
%Other Data
PKAx = [pKa pKa];
PKAy = [1E-9 1];
PKAxU = [pkaU pkaU];
PKAyU = [1E-9 1];
PKAxR = [pkaR pkaR];
PKAyR = [1E-9 1];
PKAxUw = [pkaUw pkaUw];
PKAyUw = [1E-9 1];
PKAxRw = [pkaRw pkaRw];
PKAyRw = [1E-9 1];

kABLU = (DAq/hAqU)*(AUTLAM/vrec);
kABLUx = [1 14];
kABLUy = [kABLU kABLU];

kABLR = (DAq/hAqR)*(ARDC/vrecRDC);
kABLRx = [1 14];
kABLRy = [kABLR kABLR];

%%Plots
figure
%predictions of Wagner's Extraction Theory
%against Film Theory based absorption rates for Aqueous vs Membrane
%controlled absorption
semilogy(pH,kRDC,'.r',...
    pH,kappRDC,'r',...
    kABLRx,kABLRy,'m')
hold on
semilogy(PKAx,PKAy,'-.m')
xlim([1 14])
ylim([1E-9 1])
xlabel('pH','FontSize',24,'Interpreter','tex','FontWeight','normal');
ylabel('Apparent Absorption Rate [s^-
^1]','FontSize',24,'Interpreter','tex','FontWeight','normal');
legend({'Extraction Theory RDC',...
'Film Theory RDC',...
'Aqueous Boundary Layer Absorption Rate',...
'Ibuprofen pKa'},'FontSize',13,'FontWeight','bold','location','best')
title('Membrane Controlled pH Dependent Absorption Rate-
Theoretical','FontSize',24,'Interpreter','tex','FontWeight','normal');
grid on

figure
%predictions of Wagner's Extraction Theory
%against Film Theory based absorption rates for Aqueous vs Membrane
%controlled absorption
semilogy(pH,kUTLAM,'.k',...
```

```
    pH,kappUTLAM,'k',...
    kABLUx,kABLUy,'m')
hold on
semilogy(PKAx,PKAy,'-.m')
xlim([1 14])
ylim([1E-9 1])
xlabel('pH','FontSize',24,'Interpreter','tex','FontWeight','normal');
ylabel('Apparent Absorption Rate [s^-
^1]','FontSize',24,'Interpreter','tex','FontWeight','normal');
legend({'Extraction Theory UTLAM',...
'Film Theory UTLAM',...
'Aqueous Boundary Layer Absorption Rate',...
'Ibuprofen pKa'},'FontSize',13,'FontWeight','bold','location','best')
title('Aqueous Controlled pH Dependent Absorption Rate-
Theoretical','FontSize',24,'Interpreter','tex','FontWeight','normal');
grid on

figure
%Experimental Data against Wagner's Extraction Theory
semilogy(pH,kUTLAM,'k',...
    pH,kUTLAMplus,'.k',...
    pH,kUTLAMminus,'.k',...
    pH,kRDC,'r',...
    pH,kRDCplus,'.r',...
    pH,kRDCminus,'.r',...
    kABLRx,kABLRy,'m')
hold on
semilogy(dataxUTLAM,datayUTLAM,'dk',...
    dataxRDC,datayRDC,'dr',...
    PKAxUw,PKAyUw,'-m',...
    PKAxRw,PKAyRw,'-.g',...
    PKAx,PKAy,'-.k','LineWidth',2)
xlim([1 14])
ylim([1E-9 1])
xlabel('pH','FontSize',24,'Interpreter','tex','FontWeight','normal');
ylabel('Apparent Absorption Rate [s^-
^1]','FontSize',24,'Interpreter','tex','FontWeight','normal');
legend({'UTLAM Avg','UTLAM +1StDev','UTLAM -1StDev',...
'RDC Avg','RDC +1StDev','RDC -1StDev',...
'Aqueous Boundary Layer Absorption Rate- RDC',...
'UTLAM Data- Hydrofoil, 150RPM, 37C',...
'RDC Data- RDC, 150RPM, 37C',...
'Effective pKa- UTLAM',...
'Effective pKa- RMDC',...
'Ibuprofen pKa'},'FontSize',13,'FontWeight','bold','location','best')
title('Aqueous vs Membrane Controlled pH Dependent Absorption Rate-
Extraction
Theory','FontSize',24,'Interpreter','tex','FontWeight','normal');
grid on


figure
%Experimental data against Film Theory
semilogy(pH,kappUTLAM,'k',...
    pH,kappUTLAMplus,'.k',...
    pH,kappUTLAMminus,'.k',...
```

```
    pH,kappRDC,'r',...
    pH,kappRDCplus,'.r',...
    pH,kappRDCminus,'.r',...
    kABLRx,kABLRy,'m')
hold on
semilogy(dataxUTLAM,datayUTLAM,'dk',...
    dataxRDC,datayRDC,'dr',...
    PKAxU,PKAyU,'-.m',...
    PKAxR,PKAyR,'-.g',...
    PKAx,PKAy,'-.k','LineWidth',2)
xlim([1 14])
ylim([1E-9 1])
xlabel('pH','FontSize',24,'Interpreter','tex','FontWeight','normal');
ylabel('Apparent Absorption Rate [s^-
^1]','FontSize',24,'Interpreter','tex','FontWeight','normal');
legend({'UTLAM Avg','UTLAM +1StDev','UTLAM -1StDev',...
'RDC Avg','RDC +1StDev','RDC -1StDev',...
'Aqueous Boundary Layer Absorption Rate- RDC',...
'UTLAM Data- Hydrofoil, 150RPM, 37C',...
'RDC Data- RDC, 150RPM, 37C',...
'Effective pKa- UTLAM',...
'Effective pKa- RMDC',...
'Ibuprofen pKa'},'FontSize',13,'FontWeight','bold','location','best')
title('Aqueous vs Membrane Controlled pH Dependent Absorption Rate-Film
Theory','FontSize',24,'Interpreter','tex','FontWeight','normal');
grid on
```

B. 2 Sensitivity Plots

```
clear all
close all
clc

%UTLAM Diffusion Cell Constants
AUTLAM = 21.8; %[cm2] exposed membrane surface area
hUTLAM = (12.5)*10^-4; %[cm] membrane thickness
hAqU = 39.5*10^-4; %[cm] Aqueous diffusion layer thickness
hAqUplus = hAqU+(4.53*10^-4); %[cm] ABL thickness plus StDev
hAqUminus = hAqU-(4.53*10^-4); %[cm] ABL thickness minus StDev
vrec = 219; %mL or cm3
vmUTLAM = AUTLAM*hUTLAM; %[cm3] membrane volume
hUTLAMplus = ((hUTLAM/10^-4)+4)*10^-4; %[cm] +95% CI membrane thickness
vmUTLAMplus = AUTLAM*hUTLAMplus; %[cm3] membrane volume
hUTLAMminus = ((hUTLAM/10^-4)-4)*10^-4; %[cm] -95% CI membrane
thickness
vmUTLAMminus = AUTLAM*hUTLAMminus; %[cm3] membrane volume

%Rotating Diffusion Cell Constants
ARDC = 6.41; %[cm2] exposed membrane surface area
hRDC = 680*10^-4; %[cm] membrane thickness
hRDCplus = (838)*10^-4; %[cm] maximum measured thickness
hRDCminus = (596)*10^-4; %[cm] minimum measured thickness
vmRDC = ARDC*hRDC; %[cm3] membrane volume
```

```
vmRDCplus = ARDC*hRDCplus; %[cm3] membrane volume
vmRDCminus = ARDC*hRDCminus; %[cm3] membrane volume
hAqR = 36.1*10^-4; %[cm] Aqueous diffusion layer thickness
hAqRplus = hAqR+(3.97*10^-4); %[cm] ABL thickness plus (StDev same as
UTLAM)
hAqRminus = hAqR-(3.97*10^-4); %[cm] ABL thickness minus (StDev same as
UTLAM)
vrecRDC = 70; %[cm3] receiver side volume

%Ibuprofen Constants
DNI = 2.404*10^-7; %[cm2 s-1] Drug-PDMS non-ionized Diffusion
coefficent
%determined by rotating diffusino cell at 150RPM @pH 2 (sarah's data).
%first the Ppdms was determined, then KDpdms, then KD was divided by
the
%measured equilibrium K.
DI = 1.586*10^-8; %[cm2 s-1] Drug-PDMS ionized Diffusion coefficent
%was determined using the same method above, at pH 7 and 12 (sarah's
data)
DAq = 8.41*10^-6; %cm2/s
%ibuprofen aqueous diffusion coefficient (presumably the effective)
pKa = 4.4; %drug pKa

PNIplus0 = 10^0;%non-ionized intrinsic parition coefficient
PNI = 10^1;
PNIplus = 10^2;
PNIplus1 = 10^3;
PNIplus2 = 10^4;
PNIplus3 = 10^5;
PNI05 = [PNIplus0 PNI PNIplus PNIplus1 PNIplus2 PNIplus3];

PI = 10^-1; %ionized intrinsic partition coefficient
PIplus = 10^-2;
PIplus1 = 10^-3;



pH = (1:0.1:14);
fNI = 1./(1+10.^(pH-pKa));
%Wagner's Extraction Theory pH-partition model for rotating diffusion
cell and UTLAM diffucion cell
kUTLAM = (AUTLAM./(hUTLAM.*vmUTLAM)).*((DNI.*PNI*fNI)+(DI.*PI.*(1-
fNI))./(1.+(PNI.*fNI)+(PI.*(1-fNI)));
kUTLAMplus =
(AUTLAM./(hUTLAMplus.*vmUTLAMplus)).*((DNI.*PNI.*fNI)+(DI.*PI.*(1-
fNI))./(1.+(PNI.*fNI)+(PI.*(1-fNI)));
kUTLAMminus =
(AUTLAM./(hUTLAMminus.*vmUTLAMminus)).*((DNI.*PNI.*fNI)+(DI.*PI.*(1-
fNI))./(1.+(PNI.*fNI)+(PI.*(1-fNI)));

kRDC = (ARDC./(hRDC.*vmRDC)).*((DNI.*PNI.*fNI)+(DI.*PI.*(1-
fNI))./(1.+(PNI.*fNI)+(PI.*(1-fNI)));
kRDCplus = (ARDC./(hRDCplus.*vmRDCplus)).*((DNI.*PNI.*fNI)+(DI.*PI.*(1-
fNI))./(1.+(PNI.*fNI)+(PI.*(1-fNI)));
kRDCminus =
(ARDC./(hRDCminus.*vmRDCminus)).*((DNI.*PNI.*fNI)+(DI.*PI.*(1-
fNI))./(1.+(PNI.*fNI)+(PI.*(1-fNI)));
```

```
% Film Theory for UTLAM and RDC
%cm/s effective permeability through aqueous boundary layer
%UTLAM
PAqU = DAq/hAqU;
%RDC
PAqR = DAq/hAqR;
%aqueous boundar layer variation study
hAq0 = 1*10^-4; % [cm]
hAq1 = 5*10^-4; % [cm]
hAq2 = 10*10^-4; % [cm]
hAq3 = 25*10^-4; % [cm]
hAq4 = 50*10^-4; % [cm]
hAq5 = 100*10^-4; % [cm]
hAq05 = [hAq0 hAq1 hAq2 hAq3 hAq4 hAq5];

PAqh0 = DAq/hAq0; %[cm/s]
PAqh1 = DAq/hAq1; %[cm/s]
PAqh2 = DAq/hAq2; %[cm/s]
PAqh3 = DAq/hAq3; %[cm/s]
PAqh4 = DAq/hAq4; %[cm/s]
PAqh5 = DAq/hAq5; %[cm/s]


%cm/s Non-ionized permeability through membrane
%UTLAM
PmemNIU = (PNI.*DNI.*fNI)./hUTLAM;
PmemNIUplus = (PNIplus.*DNI.*fNI)./hUTLAM;
PmemNIUplus1 = (PNIplus1.*DNI.*fNI)./hUTLAM;
PmemNIUplus2 = (PNIplus2.*DNI.*fNI)./hUTLAM;
PmemNIUplus3 = (PNIplus3.*DNI.*fNI)./hUTLAM;
PmemNIUplus0 = (PNIplus0.*DNI.*fNI)./hUTLAM;

%RDC
PmemNIR = (PNI.*DNI.*fNI)./hRDC;
PmemNIRplus = (PNIplus.*DNI.*fNI)./hRDC;
PmemNIRplus1 = (PNIplus1.*DNI.*fNI)./hRDC;
PmemNIRplus2 = (PNIplus2.*DNI.*fNI)./hRDC;
PmemNIRplus3 = (PNIplus3.*DNI.*fNI)./hRDC;
PmemNIRplus0 = (PNIplus0.*DNI.*fNI)./hRDC;

%cm/s ionized permeability through membrane
%UTLAM
PmemIU = (PI.*DI.*(1-fNI))./hUTLAM;
PmemIUplus = (PIplus.*DI.*(1-fNI))./hUTLAM;
PmemIUplus1 = (PIplus1.*DI.*(1-fNI))./hUTLAM;
%RDC
PmemIR = (PI.*DI.*(1-fNI))./hRDC;
PmemIRplus = (PIplus.*DI.*(1-fNI))./hRDC;
PmemIRplus1 = (PIplus1.*DI.*(1-fNI))./hRDC;

%Total Permeability
%UTLAM
PmemTU = PmemNIU+PmemIU;
PmemTUplus = PmemNIUplus+PmemIU;
```

```
PmemTUplus1 = PmemNIUplus1+PmemIU;
PmemTUplus2 = PmemNIUplus2+PmemIU;
PmemTUplus3 = PmemNIUplus3+PmemIU;
PmemTUplus0 = PmemNIUplus0+PmemIU;
XIU0 = PmemTUplus0./PAqU;
XIU1 = PmemTU./PAqU;
XIU2 = PmemTUplus./PAqU;
XIU3 = PmemTUplus1./PAqU;
XIU4 = PmemTUplus2./PAqU;
XIU5 = PmemTUplus3./PAqU;

%RDC
PmemTR = PmemNIR+PmemIR;
PmemTRplus = PmemNIRplus+PmemIR;
PmemTRplus1 = PmemNIRplus1+PmemIR;
PmemTRplus2 = PmemNIRplus2+PmemIR;
PmemTRplus3 = PmemNIRplus3+PmemIR;
PmemTRplus0 = PmemNIRplus0+PmemIR;
XIR0 = PmemTRplus0./PAqU;
XIR1 = PmemTR./PAqU;
XIR2 = PmemTRplus./PAqU;
XIR3 = PmemTRplus1./PAqU;
XIR4 = PmemTRplus2./PAqU;
XIR5 = PmemTRplus3./PAqU;

%film theory Apparent Absorption Rate
kappUTLAM = (AUTLAM/vrec).*(((1./PAqU)+(1./PmemTU)).^-1);
kappUTLAMplus = (AUTLAM/vrec).*(((1./PAqU)+(1./PmemTUplus)).^-1);
kappUTLAMplus1 = (AUTLAM/vrec).*(((1./PAqU)+(1./PmemTUplus1)).^-1);
kappUTLAMplus2 = (AUTLAM/vrec).*(((1./PAqU)+(1./PmemTUplus2)).^-1);
kappUTLAMplus3 = (AUTLAM/vrec).*(((1./PAqU)+(1./PmemTUplus3)).^-1);
kappUTLAMplus0 = (AUTLAM/vrec).*(((1./PAqU)+(1./PmemTUplus0)).^-1);

kappRDC = (ARDC/vrecRDC).*(((1./PAqR)+(1./PmemTR)).^-1);
kappRDCplus = (ARDC/vrecRDC).*(((1./PAqR)+(1./PmemTRplus)).^-1);
kappRDCplus1 = (ARDC/vrecRDC).*(((1./PAqR)+(1./PmemTRplus1)).^-1);
kappRDCplus2 = (ARDC/vrecRDC).*(((1./PAqR)+(1./PmemTRplus2)).^-1);
kappRDCplus3 = (ARDC/vrecRDC).*(((1./PAqR)+(1./PmemTRplus3)).^-1);
kappRDCplus0 = (ARDC/vrecRDC).*(((1./PAqR)+(1./PmemTRplus0)).^-1);

%film theory Absorption Function (normalized 0-1 by k/kmax)
AFUTLAM0 = kappUTLAMplus0./kappUTLAMplus0(1);
AFUTLAM1 = kappUTLAM./kappUTLAM(1);
AFUTLAM2 = kappUTLAMplus./kappUTLAMplus(1);
AFUTLAM3 = kappUTLAMplus1./kappUTLAMplus1(1);
AFUTLAM4 = kappUTLAMplus2./kappUTLAMplus2(1);
AFUTLAM5 = kappUTLAMplus3./kappUTLAMplus3(1);

AFRDC0 = kappRDCplus0./kappRDCplus0(1);
AFRDC1 = kappRDC./kappRDC(1);
AFRDC2 = kappRDCplus./kappRDCplus(1);
AFRDC3 = kappRDCplus1./kappRDCplus1(1);
AFRDC4 = kappRDCplus2./kappRDCplus2(1);
AFRDC5 = kappRDCplus3./kappRDCplus3(1);

%varying ABL thickness, constant K = 100
```

```
kappUTLAMh0 = (AUTLAM/vrec).*(((1./PAqh0)+(1./PmemTUplus)).^-1);
kappUTLAMh1 = (AUTLAM/vrec).*(((1./PAqh1)+(1./PmemTUplus)).^-1);
kappUTLAMh2 = (AUTLAM/vrec).*(((1./PAqh2)+(1./PmemTUplus)).^-1);
kappUTLAMh3 = (AUTLAM/vrec).*(((1./PAqh3)+(1./PmemTUplus)).^-1);
kappUTLAMh4 = (AUTLAM/vrec).*(((1./PAqh4)+(1./PmemTUplus)).^-1);
kappUTLAMh5 = (AUTLAM/vrec).*(((1./PAqh5)+(1./PmemTUplus)).^-1);

kappRDCh0 = (ARDC/vrecRDC).*(((1./PAqh0)+(1./PmemTRplus)).^-1);
kappRDCh1 = (ARDC/vrecRDC).*(((1./PAqh1)+(1./PmemTRplus)).^-1);
kappRDCh2 = (ARDC/vrecRDC).*(((1./PAqh2)+(1./PmemTRplus)).^-1);
kappRDCh3 = (ARDC/vrecRDC).*(((1./PAqh3)+(1./PmemTRplus)).^-1);
kappRDCh4 = (ARDC/vrecRDC).*(((1./PAqh4)+(1./PmemTRplus)).^-1);
kappRDCh5 = (ARDC/vrecRDC).*(((1./PAqh5)+(1./PmemTRplus)).^-1);

AFUTLAMh0 = kappUTLAMh0./kappUTLAMh0(1);
AFUTLAMh1 = kappUTLAMh1./kappUTLAMh1(1);
AFUTLAMh2 = kappUTLAMh2./kappUTLAMh2(1);
AFUTLAMh3 = kappUTLAMh3./kappUTLAMh3(1);
AFUTLAMh4 = kappUTLAMh4./kappUTLAMh4(1);
AFUTLAMh5 = kappUTLAMh5./kappUTLAMh5(1);

AFRDCh0 = kappRDCh0./kappRDCh0(1);
AFRDCh1 = kappRDCh1./kappRDCh1(1);
AFRDCh2 = kappRDCh2./kappRDCh2(1);
AFRDCh3 = kappRDCh3./kappRDCh3(1);
AFRDCh4 = kappRDCh4./kappRDCh4(1);
AFRDCh5 = kappRDCh5./kappRDCh5(1);

%%pKa shift determination
%Varying hABL
syms x
x0 = [1 14]; %guess interval min, max
%Generating function for derivative
fUh0 =@(x)
((AUTLAM/vrec).*(((1./(DAq/hAq0))+(1./(((PNIplus.*DNI.*(1./(1+10.^(x-
pKa)))./hUTLAM)+((PI.*DI.*(1-(1./(1+10.^(x-pKa))))./hUTLAM)))).^-
1))./((AUTLAM/vrec).*(((1./(DAq/hAq0))+(1./(((PNIplus.*DNI.*(1./(1+10.^
(1-pKa)))./hUTLAM)+((PI.*DI.*(1-(1./(1+10.^(1-pKa))))./hUTLAM)))).^-
1));
fUh1 =@(x)
((AUTLAM/vrec).*(((1./(DAq/hAq1))+(1./(((PNIplus.*DNI.*(1./(1+10.^(x-
pKa)))./hUTLAM)+((PI.*DI.*(1-(1./(1+10.^(x-pKa))))./hUTLAM)))).^-
1))./((AUTLAM/vrec).*(((1./(DAq/hAq1))+(1./(((PNIplus.*DNI.*(1./(1+10.^
(1-pKa)))./hUTLAM)+((PI.*DI.*(1-(1./(1+10.^(1-pKa))))./hUTLAM)))).^-
1));
fUh2 =@(x)
((AUTLAM/vrec).*(((1./(DAq/hAq2))+(1./(((PNIplus.*DNI.*(1./(1+10.^(x-
pKa)))./hUTLAM)+((PI.*DI.*(1-(1./(1+10.^(x-pKa))))./hUTLAM)))).^-
1))./((AUTLAM/vrec).*(((1./(DAq/hAq2))+(1./(((PNIplus.*DNI.*(1./(1+10.^
(1-pKa)))./hUTLAM)+((PI.*DI.*(1-(1./(1+10.^(1-pKa))))./hUTLAM)))).^-
1));
fUh3 =@(x)
((AUTLAM/vrec).*(((1./(DAq/hAq3))+(1./(((PNIplus.*DNI.*(1./(1+10.^(x-
pKa)))./hUTLAM)+((PI.*DI.*(1-(1./(1+10.^(x-pKa))))./hUTLAM)))).^-
1))./((AUTLAM/vrec).*(((1./(DAq/hAq3))+(1./(((PNIplus.*DNI.*(1./(1+10.^
```

```
(1-pKa)))./hUTLAM)+((PI.*DI.*(1-(1./(1+10.^(1-pKa))))./hUTLAM)))).^-
1));
fUh4 =@(x)
((AUTLAM/vrec).*(((1./(DAq/hAq4))+(1./(((PNIplus.*DNI.*(1./(1+10.^(x-
pKa)))./hUTLAM)+((PI.*DI.*(1-(1./(1+10.^(x-pKa))))./hUTLAM)))).^-
1))./((AUTLAM/vrec).*(((1./(DAq/hAq4))+(1./(((PNIplus.*DNI.*(1./(1+10.^
(1-pKa)))./hUTLAM)+((PI.*DI.*(1-(1./(1+10.^(1-pKa))))./hUTLAM)))).^-
1));
fUh5 =@(x)
((AUTLAM/vrec).*(((1./(DAq/hAq5))+(1./(((PNIplus.*DNI.*(1./(1+10.^(x-
pKa)))./hUTLAM)+((PI.*DI.*(1-(1./(1+10.^(x-pKa))))./hUTLAM)))).^-
1))./((AUTLAM/vrec).*(((1./(DAq/hAq5))+(1./(((PNIplus.*DNI.*(1./(1+10.^
(1-pKa)))./hUTLAM)+((PI.*DI.*(1-(1./(1+10.^(1-pKa))))./hUTLAM)))).^-
1));

fRh0 =@(x)
((ARDC/vrecRDC).*(((1./(DAq/hAq0))+(1./(((PNIplus.*DNI.*(1./(1+10.^(x-
pKa)))./hRDC)+((PI.*DI.*(1-(1./(1+10.^(x-pKa))))./hRDC)))).^-
1))./((ARDC/vrecRDC).*(((1./(DAq/hAq0))+(1./(((PNIplus.*DNI.*(1./(1+10.
^(1-pKa)))./hUTLAM)+((PI.*DI.*(1-(1./(1+10.^(1-pKa))))./hRDC)))).^-
1));
fRh1 =@(x)
((ARDC/vrecRDC).*(((1./(DAq/hAq1))+(1./(((PNIplus.*DNI.*(1./(1+10.^(x-
pKa)))./hRDC)+((PI.*DI.*(1-(1./(1+10.^(x-pKa))))./hRDC)))).^-
1))./((ARDC/vrecRDC).*(((1./(DAq/hAq1))+(1./(((PNIplus.*DNI.*(1./(1+10.
^(1-pKa)))./hUTLAM)+((PI.*DI.*(1-(1./(1+10.^(1-pKa))))./hRDC)))).^-
1));
fRh2 =@(x)
((ARDC/vrecRDC).*(((1./(DAq/hAq2))+(1./(((PNIplus.*DNI.*(1./(1+10.^(x-
pKa)))./hRDC)+((PI.*DI.*(1-(1./(1+10.^(x-pKa))))./hRDC)))).^-
1))./((ARDC/vrecRDC).*(((1./(DAq/hAq2))+(1./(((PNIplus.*DNI.*(1./(1+10.
^(1-pKa)))./hUTLAM)+((PI.*DI.*(1-(1./(1+10.^(1-pKa))))./hRDC)))).^-
1));
fRh3 =@(x)
((ARDC/vrecRDC).*(((1./(DAq/hAq3))+(1./(((PNIplus.*DNI.*(1./(1+10.^(x-
pKa)))./hRDC)+((PI.*DI.*(1-(1./(1+10.^(x-pKa))))./hRDC)))).^-
1))./((ARDC/vrecRDC).*(((1./(DAq/hAq3))+(1./(((PNIplus.*DNI.*(1./(1+10.
^(1-pKa)))./hUTLAM)+((PI.*DI.*(1-(1./(1+10.^(1-pKa))))./hRDC)))).^-
1));
fRh4 =@(x)
((ARDC/vrecRDC).*(((1./(DAq/hAq4))+(1./(((PNIplus.*DNI.*(1./(1+10.^(x-
pKa)))./hRDC)+((PI.*DI.*(1-(1./(1+10.^(x-pKa))))./hRDC)))).^-
1))./((ARDC/vrecRDC).*(((1./(DAq/hAq4))+(1./(((PNIplus.*DNI.*(1./(1+10.
^(1-pKa)))./hUTLAM)+((PI.*DI.*(1-(1./(1+10.^(1-pKa))))./hRDC)))).^-
1));
fRh5 =@(x)
((ARDC/vrecRDC).*(((1./(DAq/hAq5))+(1./(((PNIplus.*DNI.*(1./(1+10.^(x-
pKa)))./hRDC)+((PI.*DI.*(1-(1./(1+10.^(x-pKa))))./hRDC)))).^-
1))./((ARDC/vrecRDC).*(((1./(DAq/hAq5))+(1./(((PNIplus.*DNI.*(1./(1+10.
^(1-pKa)))./hUTLAM)+((PI.*DI.*(1-(1./(1+10.^(1-pKa))))./hRDC)))).^-
1));

%solve for second derivative
f_sd_Uh0 = matlabFunction(diff(fUh0(x),2));
f_sd_Uh1 = matlabFunction(diff(fUh1(x),2));
f_sd_Uh2 = matlabFunction(diff(fUh2(x),2));
```

```
f_sd_Uh3 = matlabFunction(diff(fUh3(x),2));
f_sd_Uh4 = matlabFunction(diff(fUh4(x),2));
f_sd_Uh5 = matlabFunction(diff(fUh5(x),2));

f_sd_Rh0 = matlabFunction(diff(fRh0(x),2));
f_sd_Rh1 = matlabFunction(diff(fRh1(x),2));
f_sd_Rh2 = matlabFunction(diff(fRh2(x),2));
f_sd_Rh3 = matlabFunction(diff(fRh3(x),2));
f_sd_Rh4 = matlabFunction(diff(fRh4(x),2));
f_sd_Rh5 = matlabFunction(diff(fRh5(x),2));

%Interpolate to find the inflection point (pKa_eff) d2y/dy2 = 0
pkaUh0 = fzero(f_sd_Uh0,x0);
pkaUh1 = fzero(f_sd_Uh1,x0);
pkaUh2 = fzero(f_sd_Uh2,x0);
pkaUh3 = fzero(f_sd_Uh3,x0);
pkaUh4 = fzero(f_sd_Uh4,x0);
pkaUh5 = fzero(f_sd_Uh5,x0);
pkaUh05 = [pkaUh0 pkaUh1 pkaUh2 pkaUh3 pkaUh4 pkaUh5];

pkaRh0 = fzero(f_sd_Rh0,x0);
pkaRh1 = fzero(f_sd_Rh1,x0);
pkaRh2 = fzero(f_sd_Rh2,x0);
pkaRh3 = fzero(f_sd_Rh3,x0);
pkaRh4 = fzero(f_sd_Rh4,x0);
pkaRh5 = fzero(f_sd_Rh5,x0);
pkaRh05 = [pkaRh0 pkaRh1 pkaRh2 pkaRh3 pkaRh4 pkaRh5];

%Varying K
%Generating function for derivative
fUK0 =@(x)
((AUTLAM/vrec).*(((1./(DAq/hAqU))+(1./(((PNIplus0.*DNI.*(1./(1+10.^(x-
pKa))))./hUTLAM)+((PI.*DI.*(1-(1./(1+10.^(x-pKa)))))./hUTLAM))))).^-
1))./((AUTLAM/vrec).*(((1./(DAq/hAqU))+(1./(((PNIplus0.*DNI.*(1./(1+10.
^(1-pKa))))./hUTLAM)+((PI.*DI.*(1-(1./(1+10.^(1-pKa)))))./hUTLAM))))).^-
1));
fUK1 =@(x)
((AUTLAM/vrec).*(((1./(DAq/hAqU))+(1./(((PNI.*DNI.*(1./(1+10.^(x-
pKa))))./hUTLAM)+((PI.*DI.*(1-(1./(1+10.^(x-pKa)))))./hUTLAM))))).^-
1))./((AUTLAM/vrec).*(((1./(DAq/hAqU))+(1./(((PNI.*DNI.*(1./(1+10.^(1-
pKa))))./hUTLAM)+((PI.*DI.*(1-(1./(1+10.^(1-pKa)))))./hUTLAM))))).^-1));
fUK2 =@(x)
((AUTLAM/vrec).*(((1./(DAq/hAqU))+(1./(((PNIplus.*DNI.*(1./(1+10.^(x-
pKa))))./hUTLAM)+((PI.*DI.*(1-(1./(1+10.^(x-pKa)))))./hUTLAM))))).^-
1))./((AUTLAM/vrec).*(((1./(DAq/hAqU))+(1./(((PNIplus.*DNI.*(1./(1+10.^
(1-pKa))))./hUTLAM)+((PI.*DI.*(1-(1./(1+10.^(1-pKa)))))./hUTLAM))))).^-
1));
fUK3 =@(x)
((AUTLAM/vrec).*(((1./(DAq/hAqU))+(1./(((PNIplus1.*DNI.*(1./(1+10.^(x-
pKa))))./hUTLAM)+((PI.*DI.*(1-(1./(1+10.^(x-pKa)))))./hUTLAM))))).^-
1))./((AUTLAM/vrec).*(((1./(DAq/hAqU))+(1./(((PNIplus1.*DNI.*(1./(1+10.
^(1-pKa))))./hUTLAM)+((PI.*DI.*(1-(1./(1+10.^(1-pKa)))))./hUTLAM))))).^-
1));
fUK4 =@(x)
((AUTLAM/vrec).*(((1./(DAq/hAqU))+(1./(((PNIplus2.*DNI.*(1./(1+10.^(x-
pKa))))./hUTLAM)+((PI.*DI.*(1-(1./(1+10.^(x-pKa)))))./hUTLAM))))).^-
```

```
1)).//((AUTLAM/vrec).*(((1./(DAq/hAqU))+(1./(((PNIplus2.*DNI.*(1./(1+10.
^(1-pKa)))).*hUTLAM)+((PI.*DI.*(1-(1./(1+10.^(1-pKa))))).*hUTLAM)))).^-
1));
fUK5 =@(x)
((AUTLAM/vrec).*(((1./(DAq/hAqU))+(1./(((PNIplus3.*DNI.*(1./(1+10.^(x-
pKa)))).*hUTLAM)+((PI.*DI.*(1-(1./(1+10.^(x-pKa))))).*hUTLAM)))).^-
1)).//((AUTLAM/vrec).*(((1./(DAq/hAqU))+(1./(((PNIplus3.*DNI.*(1./(1+10.
^(1-pKa)))).*hUTLAM)+((PI.*DI.*(1-(1./(1+10.^(1-pKa))))).*hUTLAM)))).^-
1));

fRK0 =@(x)
((ARDC/vrecRDC).*(((1./(DAq/hAqR))+(1./(((PNIplus0.*DNI.*(1./(1+10.^(x-
pKa)))).*hRDC)+((PI.*DI.*(1-(1./(1+10.^(x-pKa))))).*hRDC)))).^-
1)).//((ARDC/vrecRDC).*(((1./(DAq/hAqR))+(1./(((PNIplus0.*DNI.*(1./(1+10
.^(1-pKa)))).*hUTLAM)+((PI.*DI.*(1-(1./(1+10.^(1-pKa))))).*hRDC)))).^-
1));
fRK1 =@(x)
((ARDC/vrecRDC).*(((1./(DAq/hAqR))+(1./(((PNI.*DNI.*(1./(1+10.^(x-
pKa)))).*hRDC)+((PI.*DI.*(1-(1./(1+10.^(x-pKa))))).*hRDC)))).^-
1)).//((ARDC/vrecRDC).*(((1./(DAq/hAqR))+(1./(((PNI.*DNI.*(1./(1+10.^(1-
pKa)))).*hUTLAM)+((PI.*DI.*(1-(1./(1+10.^(1-pKa))))).*hRDC)))).^-1));
fRK2 =@(x)
((ARDC/vrecRDC).*(((1./(DAq/hAqR))+(1./(((PNIplus.*DNI.*(1./(1+10.^(x-
pKa)))).*hRDC)+((PI.*DI.*(1-(1./(1+10.^(x-pKa))))).*hRDC)))).^-
1)).//((ARDC/vrecRDC).*(((1./(DAq/hAqR))+(1./(((PNIplus.*DNI.*(1./(1+10.
^(1-pKa)))).*hUTLAM)+((PI.*DI.*(1-(1./(1+10.^(1-pKa))))).*hRDC)))).^-
1));
fRK3 =@(x)
((ARDC/vrecRDC).*(((1./(DAq/hAqR))+(1./(((PNIplus1.*DNI.*(1./(1+10.^(x-
pKa)))).*hRDC)+((PI.*DI.*(1-(1./(1+10.^(x-pKa))))).*hRDC)))).^-
1)).//((ARDC/vrecRDC).*(((1./(DAq/hAqR))+(1./(((PNIplus1.*DNI.*(1./(1+10
.^(1-pKa)))).*hUTLAM)+((PI.*DI.*(1-(1./(1+10.^(1-pKa))))).*hRDC)))).^-
1));
fRK4 =@(x)
((ARDC/vrecRDC).*(((1./(DAq/hAqR))+(1./(((PNIplus2.*DNI.*(1./(1+10.^(x-
pKa)))).*hRDC)+((PI.*DI.*(1-(1./(1+10.^(x-pKa))))).*hRDC)))).^-
1)).//((ARDC/vrecRDC).*(((1./(DAq/hAqR))+(1./(((PNIplus2.*DNI.*(1./(1+10
.^(1-pKa)))).*hUTLAM)+((PI.*DI.*(1-(1./(1+10.^(1-pKa))))).*hRDC)))).^-
1));
fRK5 =@(x)
((ARDC/vrecRDC).*(((1./(DAq/hAqR))+(1./(((PNIplus3.*DNI.*(1./(1+10.^(x-
pKa)))).*hRDC)+((PI.*DI.*(1-(1./(1+10.^(x-pKa))))).*hRDC)))).^-
1)).//((ARDC/vrecRDC).*(((1./(DAq/hAqR))+(1./(((PNIplus3.*DNI.*(1./(1+10
.^(1-pKa)))).*hUTLAM)+((PI.*DI.*(1-(1./(1+10.^(1-pKa))))).*hRDC)))).^-
1));

%solve for second derivative
f_sd_UK0 = matlabFunction(diff(fUK0(x),2));
f_sd_UK1 = matlabFunction(diff(fUK1(x),2));
f_sd_UK2 = matlabFunction(diff(fUK2(x),2));
f_sd_UK3 = matlabFunction(diff(fUK3(x),2));
f_sd_UK4 = matlabFunction(diff(fUK4(x),2));
f_sd_UK5 = matlabFunction(diff(fUK5(x),2));

f_sd_RK0 = matlabFunction(diff(fRK0(x),2));
f_sd_RK1 = matlabFunction(diff(fRK1(x),2));
```

```
f_sd_RK2 = matlabFunction(diff(fRK2(x),2));
f_sd_RK3 = matlabFunction(diff(fRK3(x),2));
f_sd_RK4 = matlabFunction(diff(fRK4(x),2));
f_sd_RK5 = matlabFunction(diff(fRK5(x),2));

%Interpolate to find the inflection point (pKa_eff) d2y/dy2 = 0
pkaUK0 = fzero(f_sd_UK0,x0);
pkaUK1 = fzero(f_sd_UK1,x0);
pkaUK2 = fzero(f_sd_UK2,x0);
pkaUK3 = fzero(f_sd_UK3,x0);
pkaUK4 = fzero(f_sd_UK4,x0);
pkaUK5 = fzero(f_sd_UK5,x0);
pkaUK05 = [pkaUK0 pkaUK1 pkaUK2 pkaUK3 pkaUK4 pkaUK5];

pkaRK0 = fzero(f_sd_RK0,x0);
pkaRK1 = fzero(f_sd_RK1,x0);
pkaRK2 = fzero(f_sd_RK2,x0);
pkaRK3 = fzero(f_sd_RK3,x0);
pkaRK4 = fzero(f_sd_RK4,x0);
pkaRK5 = fzero(f_sd_RK5,x0);
pkaRK05 = [pkaRK0 pkaRK1 pkaRK2 pkaRK3 pkaRK4 pkaRK5];


%Other Data
PKAx = [pKa pKa];
PKAy = [1E-10 1];

Xix = [1 14];
Xiy = [1 1];

kABLU = (DAq/hAqU)*(AUTLAM/vrec);% aqueous boundary layer absorption
rate
kABLUx = [1 14];
kABLUy = [kABLU kABLU];

kABLR = (DAq/hAqR)*(ARDC/vrecRDC);% aqueous boundary layer absorption
rate
kABLRx = [1 14];
kABLRy = [kABLR kABLR];

%%Plots
figure
% Film Theory variable K, aqueous controlled
semilogy(pH,kappUTLAMplus0,'ok',...
    pH,kappUTLAM,'-k',...
    pH,kappUTLAMplus,'--k',...
    pH,kappUTLAMplus1,':k',...
    pH,kappUTLAMplus2,'-.k',...
    pH,kappUTLAMplus3,'dk',...
    kABLUx,kABLUy,'-r')
    hold on
semilogy(PKAx,PKAy,'-m')
xlim([1 14])
ylim([1E-10 1E-2])
xlabel('pH','FontSize',24,'Interpreter','tex','FontWeight','normal');
```

```
ylabel('Apparent Absorption Rate [s^-
^1]','FontSize',24,'Interpreter','tex','FontWeight','normal');
legend({'K_N_-_I = 1','K_N_-_I = 10','K_N_-_I = 100','K_N_-_I =
1000',...
'K_N_-_I = 10,000','K = 100,000','Aqueous Boundary Layer Absorption
Rate- UTLAM',...
'Ibuprofen pKa'},'FontSize',13,'FontWeight','bold','location','best')
title('Aqueous Controlled pH Dependent Absorption Rate-Variable
K','FontSize',24,'Interpreter','tex','FontWeight','normal');
grid on

figure
% Film Theory variable K, aqueous controlled, Absorption Function
plot(pH,AFUTLAM0,'ok',...
    pH,AFUTLAM1,'-k',...
    pH,AFUTLAM2,'--k',...
    pH,AFUTLAM3,':k',...
    pH,AFUTLAM4,'-.k',...
    pH,AFUTLAM5,'dk')
    hold on
plot(PKAx,PKAy,'-m')
xlim([1 14])
ylim([0 1])
xlabel('pH','FontSize',24,'Interpreter','tex','FontWeight','normal');
ylabel('Absorption
Function','FontSize',24,'Interpreter','tex','FontWeight','normal');
legend({'K_N_-_I = 1','K_N_-_I = 10','K_N_-_I = 100','K_N_-_I =
1000',...
'K_N_-_I = 10,000','K_N_-_I = 100,000',...
'Ibuprofen pKa'},'FontSize',13,'FontWeight','bold','location','best')
title('Aqueous Controlled Absorption Function as a Function of
K','FontSize',24,'Interpreter','tex','FontWeight','normal');
grid on

figure
% Film Theory variable K, membrane controlled
semilogy(pH,kappRDCplus0,'ok',...
    pH,kappRDC,'-k',...
    pH,kappRDCplus,'--k',...
    pH,kappRDCplus1,':k',...
    pH,kappRDCplus2,'-.k',...
    pH,kappRDCplus3,'dk',...
    kABLUx,kABLUy,'-r')
    hold on
semilogy(PKAx,PKAy,'-m')
xlim([1 14])
ylim([1E-10 1E-2])
xlabel('pH','FontSize',24,'Interpreter','tex','FontWeight','normal');
ylabel('Apparent Absorption Rate [s^-
^1]','FontSize',24,'Interpreter','tex','FontWeight','normal');
legend({'K_N_-_I = 1','K_N_-_I = 10','K_N_-_I = 100','K_N_-_I =
1000',...
'K_N_-_I = 10,000','K_N_-_I = 100,000','Aqueous Boundary Layer
Absorption Rate- UTLAM',...
'Ibuprofen pKa'},'FontSize',13,'FontWeight','bold','location','best')
```

```
title('Membrane Controlled pH Dependent Absorption Rate-Variable
K','FontSize',24,'Interpreter','tex','FontWeight','normal');
grid on

figure
% Film Theory variable K, Membrane controlled, Absorption Function
plot(pH,AFRDC0,'ok',...
    pH,AFRDC1,'-k',...
    pH,AFRDC2,'--k',...
    pH,AFRDC3,':k',...
    pH,AFRDC4,'-.k',...
    pH,AFRDC5,'dk')
    hold on
plot(PKAx,PKAy,'-m')
xlim([1 14])
ylim([0 1])
xlabel('pH','FontSize',24,'Interpreter','tex','FontWeight','normal');
ylabel('Absorption
Function','FontSize',24,'Interpreter','tex','FontWeight','normal');
legend({'K_N_-_I = 1','K_N_-_I = 10','K_N_-_I = 100','K_N_-_I =
1000',...
'K_N_-_I = 10,000','K_N_-_I = 100,000',...
'Ibuprofen pKa'},'FontSize',13,'FontWeight','bold','location','best')
title('Membrane Controlled Absorption Function as a Function of
K','FontSize',24,'Interpreter','tex','FontWeight','normal');
grid on

figure
% Film Theory variable hAq, Aqueous controlled, Absorption rate
semilogy(pH,kappUTLAMh0,'ok',...
    pH,kappUTLAMh1,'-k',...
    pH,kappUTLAMh2,'--k',...
    pH,kappUTLAMh3,':k',...
    pH,kappUTLAMh4,'-.k',...
    pH,kappUTLAMh5,'dk')
    hold on
semilogy(PKAx,PKAy,'-m')
xlim([1 14])
ylim([1E-10 1E-2])
xlabel('pH','FontSize',24,'Interpreter','tex','FontWeight','normal');
ylabel('Apparent Absorption Rate (s^-
^1)','FontSize',24,'Interpreter','tex','FontWeight','normal');
legend({'h_A_q = 1\mum','h_A_q = 5\mum','h_A_q = 10\mum','h_A_q =
25\mum',...
'h_A_q = 50\mum','h_A_q = 100\mum',...
'Ibuprofen pKa'},'FontSize',13,'FontWeight','bold','location','best')
title('Aqueous Controlled Apparent Absorption Rate as a Function of
ABL','FontSize',24,'Interpreter','tex','FontWeight','normal');
grid on

figure
% Film Theory variable hAq, Membrane controlled, Absorption rate
semilogy(pH,kappRDCh0,'ok',...
    pH,kappRDCh1,'-k',...
    pH,kappRDCh2,'--k',...
    pH,kappRDCh3,':k',...
```

```
    pH,kappRDCh4,'-.k',...
    pH,kappRDCh5,'dk')
    hold on
semilogy(PKAx,PKAy,'-m')
xlim([1 14])
ylim([1E-10 1E-2])
xlabel('pH','FontSize',24,'Interpreter','tex','FontWeight','normal');
ylabel('Apparent Absorption Rate (s^-
^1)','FontSize',24,'Interpreter','tex','FontWeight','normal');
legend({'h_A_q = 1\mum','h_A_q = 5\mum','h_A_q = 10\mum','h_A_q =
25\mum',...
'h_A_q = 50\mum','h_A_q = 100\mum',...
'Ibuprofen pKa'},'FontSize',13,'FontWeight','bold','location','best')
title('Membrane Controlled Apparent Absorption Rate as a Function of
ABL','FontSize',24,'Interpreter','tex','FontWeight','normal');
grid on

figure
% Film Theory variable hAq, Aqueous controlled, Absorption Function
plot(pH,AFUTLAMh0,'ok',...
    pH,AFUTLAMh1,'-k',...
    pH,AFUTLAMh2,'--k',...
    pH,AFUTLAMh3,':k',...
    pH,AFUTLAMh4,'-.k',...
    pH,AFUTLAMh5,'dk')
    hold on
plot(PKAx,PKAy,'-m')
xlim([1 14])
ylim([0 1])
xlabel('pH','FontSize',24,'Interpreter','tex','FontWeight','normal');
ylabel('Absorption
Function','FontSize',24,'Interpreter','tex','FontWeight','normal');
legend({'h_A_q = 1\mum','h_A_q = 5\mum','h_A_q = 10\mum','h_A_q =
25\mum',...
'h_A_q = 50\mum','h_A_q = 100\mum',...
'Ibuprofen pKa'},'FontSize',13,'FontWeight','bold','location','best')
title('Aqueous Controlled Absorption Function as a Function of
ABL','FontSize',24,'Interpreter','tex','FontWeight','normal');
grid on

figure
% Film Theory variable hAq, Membrane controlled, Absorption Function
plot(pH,AFRDCh0,'ok',...
    pH,AFRDCh1,'-k',...
    pH,AFRDCh2,'--k',...
    pH,AFRDCh3,':k',...
    pH,AFRDCh4,'-.k',...
    pH,AFRDCh5,'dk')
    hold on
plot(PKAx,PKAy,'-m')
xlim([1 14])
ylim([0 1])
xlabel('pH','FontSize',24,'Interpreter','tex','FontWeight','normal');
ylabel('Absorption
Function','FontSize',24,'Interpreter','tex','FontWeight','normal');
```

```
legend({'h_A_q = 1\mum','h_A_q = 5\mum','h_A_q = 10\mum','h_A_q =
25\mum',...
'h_A_q = 50\mum','h_A_q = 100\mum',...
'Ibuprofen pKa'},'FontSize',13,'FontWeight','bold','location','best')
title('Membrane Controlled Absorption Function as a Function of
ABL','FontSize',24,'Interpreter','tex','FontWeight','normal');
grid on

figure
%Shift in the effective pKa varying hAq
plot(hAq05.*10^4,pkaUh05,'-.ok',...
     hAq05.*10^4,pkaRh05,':dk')
    hold on
%plot(PKAx,PKAy,'-m')
xlim([0 125])
ylim([4 6])
xlabel('Aqueous Boundary Layer Thickness
[\mum]','FontSize',24,'Interpreter','tex','FontWeight','normal');
ylabel('Effective
pKa','FontSize',24,'Interpreter','tex','FontWeight','normal');
legend({'Aqueous Boundary Layer Controlled',...
'Membrane
Controlled'},'FontSize',13,'FontWeight','bold','location','best')
title('Shift in Effective pKa as a Function of ABL
Thickness','FontSize',24,'Interpreter','tex','FontWeight','normal');
grid on

figure
%Shift in the effective pKa varying K
semilogx(PNI05,pkaUK05,'-.ok',...
     PNI05,pkaRK05,':dk')
    hold on
%plot(PKAx,PKAy,'-m')
xlim([10^0 10^6])
ylim([4 9])
xlabel('Non-Ionized Partition
Coefficient','FontSize',24,'Interpreter','tex','FontWeight','normal');
ylabel('Effective
pKa','FontSize',24,'Interpreter','tex','FontWeight','normal');
legend({'Aqueous Boundary Layer Controlled',...
'Membrane
Controlled'},'FontSize',13,'FontWeight','bold','location','best')
title('Shift in Effective pKa as a Function of Non-Ionized Partition
Coefficient','FontSize',24,'Interpreter','tex','FontWeight','normal');
grid on

figure
% Film Theory variable K, XI, Mem vs Aq control in UTLAM
semilogy(pH,XIU0,'ok',...
    pH,XIU1,'-k',...
    pH,XIU2,'--k',...
    pH,XIU3,':k',...
    pH,XIU4,'-.k',...
    pH,XIU5,'dk')
    hold on
semilogy(Xix,Xiy,'-m')
```

```
xlim([1 14])
ylim([1E-5 1E4])
xlabel('pH','FontSize',24,'Interpreter','tex','FontWeight','normal');
ylabel('\Xi','FontSize',36,'Interpreter','tex','FontWeight','normal');
legend({'K_N_-_I = 1','K_N_-_I = 10','K_N_-_I = 100','K_N_-_I =
1000',...
'K_N_-_I = 10,000','K_N_-_I = 100,000',...
'P_m_e_m = P_A_q'},'FontSize',13,'FontWeight','bold','location','best')
title('\Xi as a Function of pH in UTLAM Diffusion
Cell','FontSize',24,'Interpreter','tex','FontWeight','normal');
grid on

figure
% Film Theory variable K, XI, Mem vs Aq control in RDC
semilogy(pH,XIR0,'ok',...
    pH,XIR1,'-k',...
    pH,XIR2,'--k',...
    pH,XIR3,':k',...
    pH,XIR4,'-.k',...
    pH,XIR5,'dk')
    hold on
semilogy(Xix,Xiy,'-m')
xlim([1 14])
ylim([1E-5 1E4])
xlabel('pH','FontSize',24,'Interpreter','tex','FontWeight','normal');
ylabel('\Xi','FontSize',36,'Interpreter','tex','FontWeight','normal');
legend({'K_N_-_I = 1','K_N_-_I = 10','K_N_-_I = 100','K_N_-_I =
1000',...
'K_N_-_I = 10,000','K_N_-_I = 100,000',...
'P_m_e_m = P_A_q'},'FontSize',13,'FontWeight','bold','location','best')
title('\Xi as a Function of pH in Rotating Diffusion
Cell','FontSize',24,'Interpreter','tex','FontWeight','normal');
grid on
```

APPENDIX C

MATLAB Code for Chapter 6

```
%%This program calculates the the theoretical max and diffusion limited
%%fluxs in
%%addition to the monodisperse particle size flux dependence for a
%%particular drug.  These predictions are based off of the rotating
PDMS
%%membrane flux apparatus. Created by Patrick D. Sinko 10/07/2016
%%Assumption that the membrane permeability is so high that it is
ignored
%%in the calculation
clear all
close all
clc

%%Model Constants
ViscosityH20 = 6.92*10^-1; %[cp, @37C]
MolVol = 263.4; %[ibuprofen molecular volume predicted by atomic
volume]
HLC = 13.26*10^-5; %[Hayduk-Laudie Constant for diffusion coefficients]
p = 0.9933; %density of water at 37C g/cc
RPM = 150; % [selected rotational speed of motor]
TransArea = 21.8; %[cm^2] Area of flat circular opening on diffusion
cell Seive support
TransAreaSS = 25.2;%[cm^2] Area of flat circular opening on diffusion
cell Laser Cut 316SS support
DrugDensity = 1.18; %[g/mL(cm^3)]
LogKpdms = 1.81; %PDMS log partition coefficient
DrugSol = 68; %[ug/mL] Membrane surface concentration **Measure
Ibuprofen solubility with 0.9mM SDS**
%of drug in micrograms per milliliter
VolD = 90; %[mL] Donor side volume
hUTLAMS = (12.5)*10^-4; %[cm] membrane thickness from pH studies
hUTLAM = (11.2)*10^-4; %[cm] membrane thickness from particle size dose
% studies
DNI = 2.404*10^-7; %[cm2 s-1] Drug-PDMS non-ionized Diffusion
coefficent
%determined by rotating diffusino cell at 150RPM @pH 2 (sarah's data).
%first the Ppdms was determined, then KDpdms, then KD was divided by
the
%measured equilibrium K.
DI = 1.586*10^-8; %[cm2 s-1] Drug-PDMS ionized Diffusion coefficent
PNI = 10^1.81; %non-ionized intrinsic parition coefficient
%Determined using an equilibrium partition experiment
PI = 0.245; %ionized intrinsic partition coefficient
```

```
DAq = 8.41*10^-6; %cm2/s
%ibuprofen aqueous diffusion coefficient (presumably the effective)
pH = 2;
pKa = 4.4;
fNI = 1./(1+10.^(pH-pKa));
S = DrugSol; %[micrograms]
AvgParticleR = 1*10^-4; %[cm] D50 of drug particle radius
AvgParticleR1 = 3.1*10^-4; %[cm] D50 of drug particle radius
%Opt Mass = 3.32; Opt Num = 1.20; MS Num = ;
AvgParticleR2 = 5.1*10^-4; %[cm] D50 of drug particle radius
%Opt Mass = 18.28; Opt Num = 5.39; MS Num = ;
AvgParticleR3 = 80*10^-4; %[cm] D50 of drug particle radius
%Opt Mass = 117.58; Opt Num = 64.35; MS Num = 77.3;

DOSE = (6.12:10^-1:5*10^4); %[mg/mL] % 6.12 = 68*90/1000
CONC = (10^-4:10^-4:S/1000); %mg/mL for solution flux
%%Calculation of Model Constants


%OMEGA = (2*pi*RPM)/60; %[cm/s] rotational speed
%HLDC = (HLC)/((ViscosityH20^1.4)*(MolVol^0.589)); %[cm^2/s] drug
diffusion coefficient
HLDC =DAq;
ABLh = 39.5*10^-4;% measured average ABL in pH 2 150 RPM in seive
support experiments (confirmed with pH-absorption experiments)
ABLhSS1 = 29.45*10^-4; % measured average ABL in pH 2 150 RPM
experiments for UTLAM 1 Laser cut 316SS
ABLhSS2 = 38.92*10^-4; % measured average ABL in pH 2 150 RPM
experiments for UTLAM 2 Laser cut 316SS
% ABLhSS2 = 150*10^-4;
%1.61*((ViscosityH20/(100*p))^(1/6))*(HLDC^(1/3))*(1/sqrt(OMEGA)); %
[cm] Levich Model Calculation of Aqueous Boundary Layer thickness based
of off of Rotating disk

PermAqDonor = (HLDC/ABLh); % [cm/sec]Permeability of the Drug through
the aqueous donor phase ABL
PermAqDonorSS1 = HLDC/ABLhSS1;
PermAqDonorSS2 = HLDC/ABLhSS2;

PermMemS = ((PNI*DNI*fNI)/hUTLAMS)+((PI*DI*(1-
fNI))/hUTLAMS);%Permeability of PDMS Membrane cm/s
PermMem = ((PNI*DNI*fNI)/hUTLAM)+((PI*DI*(1-fNI))/hUTLAM);%Permeability
of PDMS Membrane cm/s
%%Calculation of the maximum flux (upper limit)
%If the concentration at the surface of the membrane is equal to the
%solubility of the drug in the donor phase than C'S1 is DrugSol and if
the
%Receiver phase is under sink conditions then C'B2 = 0;
Jb = (1./PermAqDonor);
JbSS1 = (1./PermAqDonorSS1);
JbSS2 = (1./PermAqDonorSS2);
Jc = (1./PermMem);
JcS = (1./PermMemS);

Jmax = (1/(Jc))*S; %[ug*cm^(-2)*s^(-1)] Maximum Flux through membrane
%%Calculation of the diffusion limited flux (lower Limit)
```

```
%Assuming sink conditions in the receiver phase C'B2 = 0 and the flux
is
%dependent on the diffusion from the particle
%pinned particles
Ja= (TransArea*DrugDensity*(AvgParticleR^2))./(3*DOSE/1000*HLDC);
% HSWS
JaSShsws=
(TransAreaSS*DrugDensity*(AvgParticleR1^2))./(3*DOSE/1000*HLDC);
%5363
JaSS5363=
(TransAreaSS*DrugDensity*(AvgParticleR2^2))./(3*DOSE/1000*HLDC);
%150250
JaSS150250=
(TransAreaSS*DrugDensity*(AvgParticleR3^2))./(3*DOSE/1000*HLDC);

%%%%%%%%%%%%%%%pinned particles%%%%%%%%%%%%%%%%%
Jmin = S*(1./(Ja+Jb+Jc));%[g*cm^(-2)*s^(-1)] Diffusion limited flux for
suspensions through membrane
JminS = 1000.*CONC.*(((1./PermAqDonor)+(1./PermMemS)).^-1);%[g*cm^(-
2)*s^(-1)] Diffusion limited flux for solutions through membrane
%Calculating dose dependent transitional flux
LAMBDA = sqrt((3.*(DOSE./1000))./(AvgParticleR^2.*DrugDensity.*VolD));
P_A = LAMBDA.^2/HLDC;
pRegC = (Jc)^-1; % in UTLAM Diffusion Cell pH 2 --> pH 12+ Region C is
membrane only (ignore receiver ABL for well stirred system)
A = (LAMBDA.*S.*HLDC);
a = P_A/HLDC;
b = pRegC/HLDC;
%establishing C1 & C2 for Seive mesh
%Seive Mesh
C1 = -
b.*(a+LAMBDA).^2.*exp(2.*LAMBDA.*ABLh)./(exp(2.*LAMBDA.*ABLh).*(a+LAMBD
A).*(b+LAMBDA).*(a-LAMBDA)+((-b+LAMBDA).*(-a+LAMBDA).^2));
C2 = b.*(a+LAMBDA)./(exp(2.*LAMBDA.*ABLh).*(a+LAMBDA).*(b+LAMBDA)+((-
b+LAMBDA).*(-a+LAMBDA)));
JdoseDep =A.*(C2-C1);

%%%%%%%%%%%%%%%%%%%%HSWS particles%%%%%%%%%%%%%%%%%%%%5
Jmin_SS1hsws = S*(1./(JaSShsws+JbSS1+Jc));%[g*cm^(-2)*s^(-1)] Diffusion
limited flux for suspensions through membrane in 316 SS 3mm Mesh
Jmin_SS2hsws = S*(1./(JaSShsws+JbSS2+Jc));%[g*cm^(-2)*s^(-1)] Diffusion
limited flux for suspensions through membrane in 316 SS 3mm Mesh
JminS_SS1hsws = 1000.*CONC.*(((1./PermAqDonorSS1)+(1./PermMemS)).^-
1);%[g*cm^(-2)*s^(-1)] Diffusion limited flux for solutions through
membrane in 316 SS 3mm Mesh
JminS_SS2hsws = 1000.*CONC.*(((1./PermAqDonorSS2)+(1./PermMemS)).^-
1);%[g*cm^(-2)*s^(-1)] Diffusion limited flux for solutions through
membrane in 316 SS 3mm Mesh
%%Calculating dose dependent transitional flux
LAMBDAhsws =
sqrt((3.*(DOSE./1000))./(AvgParticleR1^2.*DrugDensity.*VolD));
P_Ahsws = LAMBDAhsws.^2/HLDC;
pRegC = (Jc)^-1; % in UTLAM Diffusion Cell pH 2 --> pH 12+ Region C is
membrane only (ignore receiver ABL for well stirred system)
Ahsws = (LAMBDAhsws.*S.*HLDC);
ahsws = P_Ahsws/HLDC;
```

```
b = pRegC/HLDC;
%establishing C1 & C2 for UTLAM SS1, UTLAM SS2
%SS1
C1hsws1 = -
b.*(ahsws+LAMBDAhsws).^2.*exp(2.*LAMBDAhsws.*ABLhSS1)./(exp(2.*LAMBDAhs
ws.*ABLhSS1).*(ahsws+LAMBDAhsws).*(b+LAMBDAhsws).*(ahsws-
LAMBDAhsws)+((-b+LAMBDAhsws).*(-ahsws+LAMBDAhsws).^2));
C2hsws1 =
b.*(ahsws+LAMBDAhsws)./(exp(2.*LAMBDAhsws.*ABLhSS1).*(ahsws+LAMBDAhsws)
.*(b+LAMBDAhsws)+((-b+LAMBDAhsws).*(-ahsws+LAMBDAhsws)));
JdoseDephswsSS1 =Ahsws.*(C2hsws1-C1hsws1);
%SS2
C1hsws2 = -
b.*(ahsws+LAMBDAhsws).^2.*exp(2.*LAMBDAhsws.*ABLhSS2)./(exp(2.*LAMBDAhs
ws.*ABLhSS2).*(ahsws+LAMBDAhsws).*(b+LAMBDAhsws).*(ahsws-
LAMBDAhsws)+((-b+LAMBDAhsws).*(-ahsws+LAMBDAhsws).^2));
C2hsws2 =
b.*(ahsws+LAMBDAhsws)./(exp(2.*LAMBDAhsws.*ABLhSS2).*(ahsws+LAMBDAhsws)
.*(b+LAMBDAhsws)+((-b+LAMBDAhsws).*(-ahsws+LAMBDAhsws)));
JdoseDephswsSS2 =Ahsws.*(C2hsws2-C1hsws2);

%%%%%%%%%%%%%%%%%%%%53-63 particles%%%%%%%%%%%%%%%%%%%5
Jmin_SS15363 = S*(1./(JaSS5363+JbSS1+Jc));%[g*cm^(-2)*s^(-1)] Diffusion
limited flux for suspensions through membrane in 316 SS 3mm Mesh
Jmin_SS25363 = S*(1./(JaSS5363+JbSS2+Jc));%[g*cm^(-2)*s^(-1)] Diffusion
limited flux for suspensions through membrane in 316 SS 3mm Mesh
JminS_SS15363 = 1000.*CONC.*(((1./PermAqDonorSS1)+(1./PermMemS)).^-
1);%[g*cm^(-2)*s^(-1)] Diffusion limited flux for solutions through
membrane in 316 SS 3mm Mesh
JminS_SS25363 = 1000.*CONC.*(((1./PermAqDonorSS2)+(1./PermMemS)).^-
1);%[g*cm^(-2)*s^(-1)] Diffusion limited flux for solutions through
membrane in 316 SS 3mm Mesh
%%Calculating dose dependent transitional flux
LAMBDA5363 =
sqrt((3.*(DOSE./1000))./(AvgParticleR2^2.*DrugDensity.*VolD));
P_A5363 = LAMBDA5363.^2/HLDC;
pRegC = (Jc)^-1; % in UTLAM Diffusion Cell pH 2 --> pH 12+ Region C is
membrane only (ignore receiver ABL for well stirred system)
A5363 = (LAMBDA5363.*S.*HLDC);
a5363 = P_A5363/HLDC;
b = pRegC/HLDC;
%establishing C1 & C2 for UTLAM SS1, UTLAM SS2
%SS1
C153631 = -
b.*(a5363+LAMBDA5363).^2.*exp(2.*LAMBDA5363.*ABLhSS1)./(exp(2.*LAMBDA53
63.*ABLhSS1).*(a5363+LAMBDA5363).*(b+LAMBDA5363).*(a5363-
LAMBDA5363)+((-b+LAMBDA5363).*(-a5363+LAMBDA5363).^2));
C253631 =
b.*(a5363+LAMBDA5363)./(exp(2.*LAMBDA5363.*ABLhSS1).*(a5363+LAMBDA5363)
.*(b+LAMBDA5363)+((-b+LAMBDA5363).*(-a5363+LAMBDA5363)));
JdoseDep5363SS1 =A5363.*(C253631-C153631);
%SS2
C153632 = -
b.*(a5363+LAMBDA5363).^2.*exp(2.*LAMBDA5363.*ABLhSS2)./(exp(2.*LAMBDA53
63.*ABLhSS2).*(a5363+LAMBDA5363).*(b+LAMBDA5363).*(a5363-
LAMBDA5363)+((-b+LAMBDA5363).*(-a5363+LAMBDA5363).^2));
```

```
C253632 =
b.*(a5363+LAMBDA5363)./(exp(2.*LAMBDA5363.*ABLhSS2).*(a5363+LAMBDA5363)
.*(b+LAMBDA5363)+((-b+LAMBDA5363).*(-a5363+LAMBDA5363)));
JdoseDep5363SS2 =A5363.*(C253632-C153632);

%%%%%%%%%%%%%%%%%%% 150-250 particles%%%%%%%%%%%%%%%%%%
Jmin_SS1150250 = S*(1./(JaSS150250+JbSS1+Jc));%[g*cm^(-2)*s^(-1)]
Diffusion limited flux for suspensions through membrane in 316 SS 3mm
Mesh
Jmin_SS2150250 = S*(1./(JaSS150250+JbSS2+Jc));%[g*cm^(-2)*s^(-1)]
Diffusion limited flux for suspensions through membrane in 316 SS 3mm
Mesh
JminS_SS1150250 = 1000.*CONC.*(((1./PermAqDonorSS1)+(1./PermMemS)).^-
1);%[g*cm^(-2)*s^(-1)] Diffusion limited flux for solutions through
membrane in 316 SS 3mm Mesh
JminS_SS2150250 = 1000.*CONC.*(((1./PermAqDonorSS2)+(1./PermMemS)).^-
1);%[g*cm^(-2)*s^(-1)] Diffusion limited flux for solutions through
membrane in 316 SS 3mm Mesh
%%Calculating dose dependent transitional flux
LAMBDA150250 =
sqrt((3.*(DOSE./1000))./(AvgParticleR3^2.*DrugDensity.*VolD));
P_A150250 = LAMBDA150250.^2/HLDC;
pRegC = (Jc)^-1; % in UTLAM Diffusion Cell pH 2 --> pH 12+ Region C is
membrane only (ignore receiver ABL for well stirred system)
A150250 = (LAMBDA150250.*S.*HLDC);
a150250 = P_A150250/HLDC;
b = pRegC/HLDC;
%establishing C1 & C2 for UTLAM SS1, UTLAM SS2
%SS1
C11502501 = -
b.*(a150250+LAMBDA150250).^2.*exp(2.*LAMBDA150250.*ABLhSS1)./(exp(2.*LA
MBDA150250.*ABLhSS1).*(a150250+LAMBDA150250).*(b+LAMBDA150250).*(a15025
0-LAMBDA150250)+((-b+LAMBDA150250).*(-a150250+LAMBDA150250).^2));
C21502501 =
b.*(a150250+LAMBDA150250)./(exp(2.*LAMBDA150250.*ABLhSS1).*(a150250+LAM
BDA150250).*(b+LAMBDA150250)+((-b+LAMBDA150250).*(-
a150250+LAMBDA150250)));
JdoseDep150250SS1 =A150250.*(C21502501-C11502501);
%SS2
C11502502 = -
b.*(a150250+LAMBDA150250).^2.*exp(2.*LAMBDA150250.*ABLhSS2)./(exp(2.*LA
MBDA150250.*ABLhSS2).*(a150250+LAMBDA150250).*(b+LAMBDA150250).*(a15025
0-LAMBDA150250)+((-b+LAMBDA150250).*(-a150250+LAMBDA150250).^2));
C21502502 =
b.*(a150250+LAMBDA150250)./(exp(2.*LAMBDA150250.*ABLhSS2).*(a150250+LAM
BDA150250).*(b+LAMBDA150250)+((-b+LAMBDA150250).*(-
a150250+LAMBDA150250)));
JdoseDep150250SS2 =A150250.*(C21502502-C11502502);

%monodisperse flux vs radius
dose_p =[10^-1,10^0,10^1,10^2,10^3,10^4];%mg/mL
R = (0.1*10^-4:10^-6:1000*10^-4); %cm

Jp =zeros(length(dose_p),length(R));
LAMBDAp = zeros(length(dose_p),length(R));
P_Ap = zeros(length(dose_p),length(R));
```

```
Ap = zeros(length(dose_p),length(R));
ap = zeros(length(dose_p),length(R));
C1p = zeros(length(dose_p),length(R));
C2p = zeros(length(dose_p),length(R));
JdoseDep_p = zeros(length(dose_p),length(R));
for i = 1:length(dose_p)
    for j = 1:length(R)
    Jp(i,j)=
S.*((TransArea.*DrugDensity.*(R(j).^2))./(3.*dose_p(i)./1000.*HLDC)).^-
1;

    %%Calculating dose dependent transitional flux
    LAMBDAp(i,j) =
sqrt((3.*(dose_p(i)./1000))./(R(j)^2.*DrugDensity.*VolD));
    P_Ap(i,j) = LAMBDAp(i,j).^2/HLDC;

    Ap(i,j) = (LAMBDAp(i,j).*S.*HLDC);
    ap(i,j) = P_Ap(i,j)/HLDC;
    b = pRegC/HLDC;
    C1p(i,j) = -
b.*(ap(i,j)+LAMBDAp(i,j)).^2.*exp(2.*LAMBDAp(i,j).*ABLh)./(exp(2.*LAMBD
Ap(i,j).*ABLh).*(ap(i,j)+LAMBDAp(i,j)).*(b+LAMBDAp(i,j)).*(ap(i,j)-
LAMBDAp(i,j))+((-b+LAMBDAp(i,j)).*(-ap(i,j)+LAMBDAp(i,j)).^2));
    C2p(i,j) =
b.*(ap(i,j)+LAMBDAp(i,j))./(exp(2.*LAMBDAp(i,j).*ABLh).*(ap(i,j)+LAMBDA
p(i,j)).*(b+LAMBDAp(i,j))+((-b+LAMBDAp(i,j)).*(-
ap(i,j)+LAMBDAp(i,j))));
    JdoseDep_p(i,j) =Ap(i,j).*(C2p(i,j)-C1p(i,j));
    end
end

J_Jx = R(1);
J_Jx1 = R(29991);
JoJx = [J_Jx*10^4 J_Jx1*10^4];
J_Jy = JdoseDep_p(29991)/JdoseDep_p(1);
JoJy = [J_Jy J_Jy];
%%%%%%Calculating the actual flux per fraction of particles in
experimental
%%%%%%bins size


%Experimental Data
%Seive Mesh (0.9-18mm)
dose3=[24.32,24.22,95.92,96.02,185.82,186.12];
dose=[25.02,25.120,24.320,30.22,184.02,184.520,187.040,186.720,9000,900
0,9000,9000];
dose2=[188.12,188.12,188.92,186.42,9000,9000,9000,9000];
dose3x=[0.2077,0.2463,0.3689,0.3168,0.3603,0.6181];
dosex=[0.1467,0.1994,0.1413,0.2171,0.3457,0.3405,0.2609,0.4105,0.6591,0
.6932,0.8372,0.7082];
dose2x=[0.2171,0.2625,0.2185,0.2598,0.6039,0.5768,0.5763,0.6165];
meshsolnx=[0.05,0.05,0.05,0.05,0.05];
meshsolny=[0.0886,0.0836,0.0989,0.0871,0.0780];
%UTLAM 1 Data
SS1solnx=[0.0447, 0.0449]; %ABL exp
SS1solny=[0.1041, 0.1041];%ABL exp
```

```
SS1PSDxHSWS=[0.264, 1.08, 10.1];
SS1PSDyHSWS=[0.1109, 0.1433, 0.2398];
SS1PSDx5363=[0.369, 1.07, 10.2, 40.3];
SS1PSDy5363=[0.0991, 0.1370, 0.2068, 0.3199];
SS1PSDx150250=[0.202, 0.99, 10.0, 40.3];
SS1PSDy150250=[0.0268, 0.0438, 0.1728, 0.2155];
%UTLAM 2 Data
SS2solnx=[0.0449, 0.0444];%ABL exp
SS2solny=[0.0828, 0.0818];%ABL exp
SS2PSDxHSWS=[0.211, 1.04, 10.4, 40.3];
SS2PSDyHSWS=[0.0937, 0.1500, 0.2527, 0.4510];
SS2PSDx5363=[0.291, 1.14, 10.1];
SS2PSDy5363=[0.0826, 0.1238, 0.1745];
SS2PSDx150250=[0.201, 0.99, 10.1];
SS2PSDy150250=[0.0249, 0.0595, 0.1929];

%%%%%Pinned Particle Experiments%%%%%
figure('name','Flux vs. Dose/V_{D} 0.9-1.8mm Seive mesh Support
Experiments') % 0.9-1.8mm Seive mesh Support Experiments
semilogx(DOSE./VolD, JdoseDep,'m',...
        DOSE./VolD, Jmin,':k',...
        CONC, JminS,'-.b',...
        [68/1000, 10^4], [Jmax, Jmax],'k',...
        [68/1000, 68/1000], [0, Jmax],'c',...
        dose3./VolD, dose3x,'og',...%suspension pH 2 150 RPM data (4
micron HSWS)
        dose./VolD, dosex,'ok',...%suspension pH 2 150 RPM data (53-63
micron seive)
        dose2./VolD, dose2x,'or',...%suspension pH 2 150 RPM data (150-
250 micron seive)
        meshsolnx,meshsolny,'dk')%solution pH 2 150 RPM data
hold on
xlabel('Dose/Donor Volume
(mg/mL)','FontSize',24,'Interpreter','tex','FontWeight','normal');
ylabel('Flux [\mug cm^-^2s^-
^1]','FontSize',24,'Interpreter','tex','FontWeight','normal');
legend('Convection Diffusion Model, Dissolution in the ABL',...
'Diffusion Limited Maximum Flux-With Particles',...
'Diffusion Limited Flux-With Solutions in Seive Mesh UTLAM',...
'Maximum Flux',...
'Ibuprofen Solubility at 37C',...
        '2\mum radius High Shear Wet Seive Susp.',...
        '53-63\mum seive cut Susp.',...
        '150-250\mum seive cut Susp.',...
        '53-63\mum seive cut Sol.',...
    'location','best')
grid minor
title('Monodisperse Flux for Trapped Particle Experiments
','FontSize',24,'Interpreter','tex','FontWeight','normal');
hold off


%%%%%%%%%%%%HSWS particle Experiments%%%%%%%%%%%%%%%
figure('name','Flux vs. Dose/V_{D} UTLAM 1 & 2 LCSS Support High Shear
Wet Sieved Experiments') % UTLAM SS1/2 Experiments
semilogx(DOSE./VolD, JdoseDephswsSS1,'-.r',...
```

```
    DOSE./VolD, JdoseDephswsSS2,'-.b',...
    DOSE./VolD, Jmin_SS1hsws,':r',...
    DOSE./VolD, Jmin_SS2hsws,':b',...
    CONC, JminS_SS1hsws,'-r',...
    CONC, JminS_SS2hsws,'-b',...
    [68/1000, 10^4], [Jmax, Jmax],'k',...
    [68/1000, 68/1000], [0, Jmax],'m',...
    SS1solnx,SS1solny,'or',...
    SS2solnx,SS2solny,'ob',...
  SS1PSDxHSWS,SS1PSDyHSWS,'dr',...
  SS2PSDxHSWS,SS2PSDyHSWS,'db')
hold on
xlabel('Dose/Donor Volume
(mg/mL)','FontSize',24,'Interpreter','tex','FontWeight','normal');
ylabel('Flux [\mug cm^-^2s^-
^1]','FontSize',24,'Interpreter','tex','FontWeight','normal');
legend('Convection Diffusion Model, Dissolution in SS1',...
'Convection Diffusion Model, Dissolution in SS2',...
'Diffusion Limited Maximum Flux-With Particles in SS1',...
'Diffusion Limited Maximum Flux-With Particles in SS2',...
'Diffusion Limited Flux-With Solutions in SS1',...
'Diffusion Limited Flux-With Solutions in SS2',...
'Maximum Flux',...
'Ibuprofen Solubility at 37C',...
'SS1 Solution Data','SS2 Solution Data',...
'SS1 High Shear Wet Sieved Particles','SS2 High Shear Wet Sieved
Particles',...
'location','best')
grid minor
title('Monodisperse Flux for 3.1{\mu}m Radius Particles
','FontSize',24,'Interpreter','tex','FontWeight','normal');
hold off

%%%%%%%%%%%%53-63 particle Experiments%%%%%%%%%%%%%%%
figure('name','Flux vs. Dose/V_{D} UTLAM 1 & 2 LCSS Support 52-63\mum
Experiments') % UTLAM SS1/2 Experiments
semilogx(DOSE./VolD, JdoseDep5363SS1,'-.r',...
    DOSE./VolD, JdoseDep5363SS2,'-.b',...
    DOSE./VolD, Jmin_SS15363,':r',...
    DOSE./VolD, Jmin_SS25363,':b',...
    CONC, JminS_SS15363,'-r',...
    CONC, JminS_SS25363,'-b',...
    [68/1000, 10^4], [Jmax, Jmax],'k',...
    [68/1000, 68/1000], [0, Jmax],'m',...
    SS1solnx,SS1solny,'or',...
    SS2solnx,SS2solny,'ob',...
    SS1PSDx5363,SS1PSDy5363,'dr',...
    SS2PSDx5363,SS2PSDy5363,'db')
hold on
xlabel('Dose/Donor Volume
(mg/mL)','FontSize',24,'Interpreter','tex','FontWeight','normal');
ylabel('Flux [\mug cm^-^2s^-
^1]','FontSize',24,'Interpreter','tex','FontWeight','normal');
legend('Convection Diffusion Model, Dissolution in SS1',...
'Convection Diffusion Model, Dissolution in SS2',...
'Film Theory Diffusion Ltd Max. Flux With Particles in SS1',...
'Film Theory Diffusion Ltd Max. Flux With Particles in SS2',...
```

```
'Film Theory Diffusion Ltd Max. Flux With Solutions in SS1',...
'Film Theory Diffusion Ltd Max. Flux With Solutions in SS2',...
'Maximum Flux',...
'Ibuprofen Solubility at 37C',...
'SS1 Solution Data','SS2 Solution Data',...
'SS1 53-63\mum Sieved Particles','SS2 53-63\mum Sieved Particles',...
'location','best')
grid minor
title('Monodisperse Flux for 5.1{\mu}m Average Radius Particles
','FontSize',24,'Interpreter','tex','FontWeight','normal');
hold off

%%%%%%%%%%%%150-250 micron particle Experiments%%%%%%%%%%%%%%%
figure('name','Flux vs. Dose/V_{D} UTLAM 1 & 2 LCSS Support 150-250
\mum Experiments') % UTLAM SS1/2 Experiments
semilogx(DOSE./VolD, JdoseDep150250SS1,'-.r',...
    DOSE./VolD, JdoseDep150250SS2,'-.b',...
    DOSE./VolD, Jmin_SS1150250,':r',...
    DOSE./VolD, Jmin_SS2150250,':b',...
    CONC, JminS_SS1150250,'-r',...
    CONC, JminS_SS2150250,'-b',...
    [68/1000, 10^4], [Jmax, Jmax],'k',...
    [68/1000, 68/1000], [0, Jmax],'m',...
    SS1solnx,SS1solny,'or',...
    SS2solnx,SS2solny,'ob',...
  SS1PSDx150250,SS1PSDy150250,'dr',...
  SS2PSDx150250,SS2PSDy150250,'db')
hold on
xlabel('Dose/Donor Volume
(mg/mL)','FontSize',24,'Interpreter','tex','FontWeight','normal');
ylabel('Flux [\mug cm^-^2s^-
^1]','FontSize',24,'Interpreter','tex','FontWeight','normal');
legend('Convection Diffusion Model, Dissolution in SS1',...
'Convection Diffusion Model, Dissolution in SS2',...
'Film Theory Diffusion Ltd Max. Flux With Particles in SS1',...
'Film Theory Diffusion Ltd Max. Flux With Particles in SS2',...
'Film Theory Diffusion Ltd Max. Flux With Solutions in SS1',...
'Film Theory Diffusion Ltd Max. Flux With Solutions in SS2',...
'Maximum Flux',...
'Ibuprofen Solubility at 37C',...
'SS1 Solution Data','SS2 Solution Data',...
'SS1 150-250\mum Sieved Particles','SS2 150-250\mum Sieved
Particles',...
'location','best')
grid minor
title('Monodisperse Flux for 80{\mu}m Average Radius Particles
','FontSize',24,'Interpreter','tex','FontWeight','normal');
hold off

figure('name','Particle Radius vs Particle Flux UTLAM 1 & 2 LCSS
Experiments') % UTLAM SS1/2 Experiments
semilogx(R*10^4,JdoseDep_p./JdoseDep_p(1),'k',...
    JoJx,JoJy,':k');
hold on
xlabel('Spherical Radius
(\mum)','FontSize',24,'Interpreter','tex','FontWeight','normal');
```

```
ylabel('J(r) / J_M_a_x
','FontSize',24,'Interpreter','tex','FontWeight','normal');
legend('variable dose monodisperse particle flux',...
    'minimum flux',...
'location','best')
grid minor
title('Monodisperse Flux of Particles at different
doses','FontSize',24,'Interpreter','tex','FontWeight','normal');
hold off

figure('name','Particle Radius vs Total UTLAM 1 & 2 LCSS Experiments')
% UTLAM SS1/2 Experiments
semilogx(R*10^4,JdoseDep_p,'k',...
[0.1 300], [Jmax, Jmax],'g');
hold on
xlim([10^-1 10^3])
ylim([0 1])
xlabel('Average Spherical Radius
(\mum)','FontSize',24,'Interpreter','tex','FontWeight','normal');
ylabel('J(r) (\mug cm^-^2 s^-
^1)','FontSize',24,'Interpreter','tex','FontWeight','normal');
legend('Dose = 9 * 10^-^3 mg/mL',...
    'Dose = 9 * 10^-^2 mg/mL',...
    'Dose = 9 * 10^-^1 mg/mL',...
    'Dose = 9 * 10^0 mg/mL',...
    'Dose = 9 * 10^1 mg/mL',...
    'Dose = 9 * 10^2 mg/mL',...
    'Maximum Flux','location','best')
grid minor
title('Total Monodisperse Flux of Particles at different
doses','FontSize',24,'Interpreter','tex','FontWeight','normal');
hold off

%%%%%%%%%%%%all data%%%%%%%%%%%%%%%
figure('name','Flux vs. Dose/V_{D} UTLAM 1 & 2 LCSS Support High Shear
Wet Sieved Experiments') % UTLAM SS1/2 Experiments
semilogx(SS1solnx,SS1solny,'or',...
    SS2solnx,SS2solny,'ob',...
  SS1PSDxHSWS,SS1PSDyHSWS,'dr',...
  SS2PSDxHSWS,SS2PSDyHSWS,'db',...
  SS1PSDx5363,SS1PSDy5363,'sr',...
  SS2PSDx5363,SS2PSDy5363,'sb',...
  SS1PSDx150250,SS1PSDy150250,'pr',...
  SS2PSDx150250,SS2PSDy150250,'pb')
%ylim([0 1]);
hold on
xlabel('Dose/Donor Volume
(mg/mL)','FontSize',24,'Interpreter','tex','FontWeight','normal');
ylabel('Flux [\mug cm^-^2s^-
^1]','FontSize',24,'Interpreter','tex','FontWeight','normal');
legend('SS1 Solution Data','SS2 Solution Data',...
'SS1 High Shear Wet Sieved Particles','SS2 High Shear Wet Sieved
Particles',...
'SS1 53-63\mum Sieved Particles','SS2 53-63\mum Sieved Particles',...
'SS1 150-250\mum Sieved Particles','SS2 150-250\mum Sieved
Particles',...
```

```
'location','best')
grid minor
title('Experimental
Data','FontSize',24,'Interpreter','tex','FontWeight','normal');
hold off
```

REFERENCE

1. Shi, Y.; Erickson, B.; Jayasankar, A.; Lu, L. J.; Marsh, K.; Menon, R.; Gao, P. Assessing Supersaturation and Its Impact on In Vivo Bioavailability of a Low-Solubility Compound ABT-072 With a Dual pH, Two-Phase Dissolution Method. *J. Pharm. Sci.* **2016,** *105*, (9), 2886-2895.
2. Amidon, G. E., Pharmaceutical Product Development. University of Michigan, 2015; pp 1-41.
3. Turner, M. J. The current state of drug discovery and what it might take to improve drug discovery outcomes and approval successes. *Drug Discovery Today* **2015,** *0*, (0), 1-3.
4. Mudie, D. M.; Amidon, G. L.; Amidon, G. E. Physiological Parameters for Oral Delivery and in Vitro Testing. *Mol. Pharm.* **2010,** *7*, (5), 1388-1405.
5. Mudie, D. M.; Shi, Y.; Ping, H. L.; Gao, P.; Amidon, G. L.; Amidon, G. E. Mechanistic analysis of solute transport in an in vitro physiological two-phase dissolution apparatus. *Biopharm. Drug Dispos.* **2012,** *33*, (7), 378-402.
6. Shi, Y.; Gao, P.; Gong, Y. C.; Ping, H. L. Application of a Biphasic Test for Characterization of In Vitro Drug Release of Immediate Release Formulations of Celecoxib and Its Relevance to In Vivo Absorption. *Mol. Pharm.* **2010,** *7*, (5), 1458-1465.
7. HIguchi, W. I.; HIguchi, T. Theoretical Analysis of Diffusional Movement Heterogeneous Barriers. *Journal of the American Pharmaceutical Association* **1959,** *49*, (9), 598-607.
8. Higuchi, T. Rate of Release of Medicaments from Ointment Bases Containing Drugs in Suspension. *J. Pharm. Sci.* **1961,** *50*, (10), 874-875.
9. Shefter, E.; Higuchi, T. Dissolution Behavior of Crystalline Solved and Nonsolvated Forms of Some Pharmaceuticals. *J. Pharm. Sci.* **1962,** *52*, (8), 781-792.
10. Amidon, G. L.; Sinko, P. J.; Fleischer, D. Estimating Human Oral Fraction Dose Absorbed: A Correlation Using Rat Intestinal Membrane Permeability for Passive and Carrier-Mediated Compounds. *Pharmaceutical Research* **1988,** *5*, (10).
11. Sinko, P. J.; Leesman, G. D.; Amidon, G. L. Predicting Fraction Dose Absorbed in Humans Using a Macroscopic Mass Balance Approach. *Pharmaceutical Research* **1991,** *8*, (8).
12. Amidon, G. L.; Lennernas, H.; Shah, V. P.; Crison, J. R. A Theoretical Basis for a Biopharmaceutic Drug Classification: The Correlation of in vitro Drug Product Dissolution and in vivo Bioavailability. *Pharmaceutical Research* **1995,** *12*, (3).

13. Pouton, C. W. Formulation of poorly water-soluble drugs for oral administration: Physicochemical and physiological issues and the lipid formulation classification system. *Eur. J. Pharm. Sci.* **2006,** *29*, (3-4), 278-287.

14. Lionberger, R. A. FDA critical path initiatives: Opportunities for generic drug development. *Aaps Journal* **2008,** *10*, (1), 103-109.

15. Carstensen, J. T.; Wright, J. L.; Blessel, K. W.; Sheridan, J. USP DISSOLUTION TEST .2. SIGMOID DISSOLUTION PROFILES FROM DIRECTLY COMPRESSED TABLETS. *J. Pharm. Sci.* **1978,** *67*, (1), 48-50.

16. Cohen, J. L.; Hubert, B. B.; Leeson, L. J.; Rhodes, C. T.; Robinson, J. R.; Roseman, T. J.; Shefter, E. The Development of USP Dissolution and Drug Release Standards. *Pharmaceutical Research* **1990,** *7*, (10), 983-987.

17. Vertzoni, M.; Dressman, J.; Butler, J.; Hempenstall, J.; Reppas, C. Simulation of fasting gastric conditions and its importance for the in vivo dissolution of lipophilic compounds. *Eur. J. Pharm. Biopharm.* **2005,** *60*, (3), 413-417.

18. Kostewicz, E. S.; Abrahamsson, B.; Brewster, M.; Brouwers, J.; Butler, J.; Carlert, S.; Dickinson, P. A.; Dressman, J.; Holm, R.; Klein, S.; Mann, J.; McAllister, M.; Minekus, M.; Muenster, U.; Müllertz, A.; Verwei, M.; Vertzoni, M.; Weitschies, W.; Augustijns, P. In vitro models for the prediction of in vivo performance of oral dosage forms. *Eur. J. Pharm. Sci.* **2014,** *57*, 342-366.

19. Fuchs, A.; Leigh, M.; Kloefer, B.; Dressman, J. B. Advances in the design of fasted state simulating intestinal fluids: FaSSIF-V3. *Eur. J. Pharm. Biopharm.* **2015,** *94*, 229-240.

20. Bergström, C. A. S.; Holm, R.; Jørgensen, S. A.; Andersson, S. B. E.; Artursson, P.; Beato, S.; Borde, A.; Box, K.; Brewster, M.; Dressman, J.; Feng, K.-I.; Halbert, G.; Kostewicz, E.; McAllister, M.; Muenster, U.; Thinnes, J.; Taylor, R.; Mullertz, A. Early pharmaceutical profiling to predict oral drug absorption: Current status and unmet needs. *Eur. J. Pharm. Sci.* **2014,** *57*, 173-199.

21. Markopoulos, C.; Andreas, C. J.; Vertzoni, M.; Dressman, J.; Reppas, C. In-vitro simulation of luminal conditions for evaluation of performance of oral drug products: Choosing the appropriate test media. *Eur. J. Pharm. Biopharm.* **2015,** *93*, 173-182.

22. Augustijns, P.; Wuyts, B.; Hens, B.; Annaert, P.; Butler, J.; Brouwers, J. A review of drug solubility in human intestinal fluids: Implications for the prediction of oral absorption. *Eur. J. Pharm. Sci.* **2014,** *57*, 322-332.

23. Lennernäs, H.; Aarons, L.; Augustijns, P.; Beato, S.; Bolger, M.; Box, K.; Brewster, M.; Butler, J.; Dressman, J.; Holm, R.; Julia Frank, K.; Kendall, R.; Langguth, P.; Sydor, J.; Lindahl, A.; McAllister, M.; Muenster, U.; Müllertz, A.; Ojala, K.; Pepin, X.; Reppas, C.; Rostami-Hodjegan, A.; Verwei, M.; Weitschies, W.; Wilson, C.; Karlsson, C.; Abrahamsson, B. Oral biopharmaceutics tools – Time for a new initiative – An introduction to the IMI project OrBiTo. *Eur. J. Pharm. Sci.* **2014,** *57*, 292-299.

24. Klein, S. The Use of Biorelevant Dissolution Media to Forecast the In Vivo Performance of a Drug. *The AAPS Journal* **2010,** *12*, (3), 397-406.

25. Garbacz, G.; Wedemeyer, R.-S.; Nagel, S.; Giessmann, T.; Mönnikes, H.; Wilson, C. G.; Siegmund, W.; Weitschies, W. Irregular absorption profiles observed from diclofenac

extended release tablets can be predicted using a dissolution test apparatus that mimics in vivo physical stresses. *Eur. J. Pharm. Biopharm.* **2008,** *70*, (2), 421-428.

26. Dressman, J. B.; Amidon, G. L.; Reppas, C.; Shah, V. P. Dissolution Testing as a Prognostic Tool for Oral Drug Absorption: Immediate Release Dosage Forms. *Pharmaceutical Research* **1998,** *15*, (1), 11-22.

27. Mudie, D. M.; Murray, K.; Hoad, C. L.; Pritchard, S. E.; Garnett, M. C.; Amidon, G. L.; Gowland, P. A.; Spiller, R. C.; Amidon, G. E.; Marciani, L. Quantification of Gastrointestinal Liquid Volumes and Distribution Following a 240 mL Dose of Water in the Fasted State. *Mol. Pharm.* **2014,** *11*, (9), 3039-3047.

28. Behafarid, F., Brasseur, J.G., Vijayakumar, G., Jayaraman, B., Wang, Y., Computational Studies of Drug Release, Transport and Absorption in the Human Intestines. Bull. Amer. Phys. Soc., 2016.

29. Behafarid, F., Vijayakumar, G., Brasseur, J.G., The Interplay between Pharmaceutical Dissolution and Absorption In the Human Gut studied with Computer Simulation. American Association of Pharmaceutical Scientists (AAPS) Annual Meeting Denver, CO, 2016.

30. Brasseur, J. G., Behafarid, F., Wang, Y., Mudie, D., Amidon, G., Hydrodynamic Influences on Drug Dissolution and Absorption In Vitro and In Vivo, quantified with Mathematical Models and Computer Simulation. 6th Pharmaceutical Sciences World Congress (FIP PSWC 2017), 2017.

31. Hens, B.; Tsume, Y.; Bermejo, M.; Paixao, P.; Koenigsknecht, M. J.; Baker, J. R.; Hasler, W. L.; Lionberger, R.; Fan, J.; Dickens, J.; Shedden, K.; Wen, B.; Wysocki, J.; Loebenberg, R.; Lee, A.; Frances, A.; Amidon, G.; Yu, A.; Benninghoff, G.; Salehi, N.; Talattof, A.; Sun, D.; Amidon, G. L. Low Buffer Capacity and Alternating Motility along the Human Gastrointestinal Tract: Implications for in Vivo Dissolution and Absorption of Ionizable Drugs. *Mol. Pharm.* **2017,** *14*, (12), 4281-4294.

32. Noyes, A. A.; Whitney, W. R. The rate of Solution of Solid Substances in their own Solutions. *Journal of the American Chemical Society* **1897,** *19*, 932-934.

33. Higuchi, W. I.; Hiestand, E. N. DISSOLUTION RATES OF FINELY DIVIDED DRUG POWDERS .1. EFFECT OF A DISTRIBUTION OF PARTICLE SIZES IN A DIFFUSION-CONTROLLED PROCESS. *J. Pharm. Sci.* **1963,** *52*, (1), 67-&.

34. Higuchi, W. I.; Hiestand, E. N.; Rowe, E. L. DISSOLUTION RATES OF FINELY DIVIDED DRUG POWDERS .2. MICRONIZED METHYLPREDNISOLONE. *J. Pharm. Sci.* **1963,** *52*, (2), 162-&.

35. Day, M. A. The No-Slip Condition of Fluid Dynamics. *Erkenntnis (1975-)* **1990,** *33*, (3), 285-296.

36. Barrat, J. L.; Bocquet, L. Large slip effect at a nonwetting fluid-solid interface. *Physical Review Letters* **1999,** *82*, (23), 4671-4674.

37. Neto, C.; Evans, D. R.; Bonaccurso, E.; Butt, H. J.; Craig, V. S. J. Boundary slip in Newtonian liquids: a review of experimental studies. *Reports on Progress in Physics* **2005,** *68*, (12), 2859-2897.

38. Hintz, R. J.; Johnson, K. C. THE EFFECT OF PARTICLE-SIZE DISTRIBUTION ON DISSOLUTION RATE AND ORAL ABSORPTION. *Int. J. Pharm.* **1989,** *51*, (1), 9-17.

39. Niebergall, P. J.; Milosovich, G.; Goyan, J. E. Dissolution rate studies II. Dissolution of particles under conditions of rapid agitation. *J. Pharm. Sci.* **1963,** *52*, (3), 236-241.

40. Sheng, J. J.; Sirois, P. J.; Dressman, J. B.; Amidon, G. L. Particle diffusional layer thickness in a USP dissolution apparatus II: A combined function of particle size and paddle speed. *J. Pharm. Sci.* **2008,** *97*, (11), 4815-4829.

41. Sugano, K. Theoretical comparison of hydrodynamic diffusion layer models used for dissolution simulation in drug discovery and development. *Int. J. Pharm.* **2008,** *363*, (1), 73-77.

42. Aissa, A.; Abdelouahab, M.; Noureddine, A.; El Ganaoui, M.; Pateyron, B. Ranz and Marshall Correlations Limits on Heat Flow Between a Sphere and its Surrounding Gas at High Temperature. *Thermal Science* **2015,** *19*, (5), 1521-1528.

43. Wang, Y.; Abrahamsson, B.; Lindfors, L.; Brasseur, J. G. Comparison and Analysis of Theoretical Models for Diffusion Controlled Dissolution. *Mol. Pharm.* **2012,** *9*, 1052-1066.

44. Wang, Y.; Abrahamsson, B.; Lindfors, L.; Brasseur, J. G. Analysis of Diffusion-Controlled Dissolution from Polydisperse Collections of Drug Particles with an Assessed Mathematical Model. *J. Pharm. Sci.* **2015,** *104*, (9), 2998-3017.

45. Wang, Y.; Brasseur, J. G. Enhancement of mass transfer from particles by local shear-rate and correlations with application to drug dissolution. *AIChE Journal* **2019,** *0*, (0), e16617.

46. Ranz, W. E.; Marshall, W. R. EVAPORATION FROM DROPS .1. *Chem. Eng. Prog.* **1952,** *48*, (3), 141-146.

47. Ranz, W. E.; Marshall, W. R. EVAPORATION FROM DROPS .2. *Chem. Eng. Prog.* **1952,** *48*, (4), 173-180.

48. Sun, D., Introduction to PK and Biopharmaceutics In *Route of Drug Administration and Oral Absorption*, Duxin Sun, Professor and Instructor of PharmSci 700: Pharmacokinetics and Biopharmaceutics: University of Michigan, 2014.

49. Sugano, K. Possible reduction of effective thickness of intestinal unstirred water layer by particle drifting effect. *Int. J. Pharm.* **2010,** *387*, (1), 103-109.

50. Doyle-McCullough, M.; Smyth, S. H.; Moyes, S. M.; Carr, K. E. Factors influencing intestinal microparticle uptake in vivo. *Int. J. Pharm.* **2007,** *335*, (1), 79-89.

51. Hodges, G. M.; Carr, E. A.; Hazzard, R. A.; Carr, K. E. Uptake and translocation of microparticles in small intestine. *Digestive Diseases and Sciences* **1995,** *40*, (5), 967-975.

52. LIMPANUSSORN, J.; SIMON, L.; DAYAN, A. D. Transepithelial Transport of Large Particles in Rat: a New Model for the Quantitative Study of Particle Uptake. *Journal of Pharmacy and Pharmacology* **1998,** *50*, (7), 753-760.

53. Norris, D. A.; Puri, N.; Sinko, P. J. The effect of physical barriers and properties on the oral absorption of particulates. *Adv. Drug Deliv. Rev.* **1998,** *34*, (2), 135-154.

54. Amidon, G. E. Rotating Membrane Diffusion Studies of Micellar and Suspension Systems. University of Michigan, Ann Arbor, 1979.

55. Talattof, A.; Price, J. C.; Amidon, G. L. Gastrointestinal Motility Variation and Implications for Plasma Level Variation: Oral Drug Products. *Mol. Pharm.* **2016,** *13*, (2), 557-567.

56. Gao, P.; Shi, Y. Characterization of Supersaturatable Formulations for Improved Absorption of Poorly Soluble Drugs. *Aaps Journal* **2012,** *14*, (4), 703-713.

57. Locher, K.; Borghardt, J. M.; Frank, K. J.; Kloft, C.; Wagner, K. G. Evolution of a mini-scale biphasic dissolution model: Impact of model parameters on partitioning of dissolved API and modelling of in vivo-relevant kinetics. *Eur. J. Pharm. Biopharm.* **2016,** *105*, 166-175.

58. Frank, K. J.; Locher, K.; Zecevic, D. E.; Fleth, J.; Wagner, K. G. In vivo predictive mini-scale dissolution for weak bases: Advantages of pH-shift in combination with an absorptive compartment. *Eur. J. Pharm. Sci.* **2014,** *61*, 32-39.

59. Stein, P. C.; di Cagno, M.; Bauer-Brandl, A. A Novel Method for the Investigation of Liquid/Liquid Distribution Coefficients and Interface Permeabilities Applied to the Water-Octanol-Drug System. *Pharmaceutical Research* **2011,** *28*, (9), 2140-2146.

60. Takano, R.; Kataoka, M.; Yamashita, S. Integrating drug permeability with dissolution profile to develop IVIVC. *Biopharm. Drug Dispos.* **2012,** *33*, (7), 354-365.

61. Kataoka, M.; Sugano, K.; da Costa Mathews, C.; Wong, J. W.; Jones, K. L.; Masaoka, Y.; Sakuma, S.; Yamashita, S. Application of Dissolution/Permeation System for Evaluation of Formulation Effect on Oral Absorption of Poorly Water-Soluble Drugs in Drug Development. *Pharmaceutical Research* **2012,** *29*, (6), 1485-1494.

62. Kataoka, M.; Yano, K.; Hamatsu, Y.; Masaoka, Y.; Sakuma, S.; Yamashita, S. Assessment of absorption potential of poorly water-soluble drugs by using the dissolution/permeation system. *Eur. J. Pharm. Biopharm.* **2013,** *85*, (3), 1317-1324.

63. Miyaji, Y.; Fujii, Y.; Takeyama, S.; Kawai, Y.; Kataoka, M.; Takahashi, M.; Yamashita, S. Advantage of the Dissolution/Permeation System for Estimating Oral Absorption of Drug Candidates in the Drug Discovery Stage. *Mol. Pharm.* **2016,** *13*, (5), 1564-1574.

64. Kataoka, M.; Masaoka, Y.; Yamazaki, Y.; Sakane, T.; Sezaki, H.; Yamashita, S. In Vitro System to Evaluate Oral Absorption of Poorly Water-Soluble Drugs: Simultaneous Analysis on Dissolution and Permeation of Drugs. *Pharmaceutical Research* **2003,** *20*, (10), 1674-1680.

65. Yano, K.; Masaoka, Y.; Kataoka, M.; Sakuma, S.; Yamashita, S. Mechanisms of Membrane Transport of Poorly Soluble Drugs: Role of Micelles in Oral Absorption Processes. *J. Pharm. Sci.* **2010,** *99*, (3), 1336-1345.

66. Kataoka, M.; Itsubata, S.; Masaoka, Y.; Sakuma, S.; Yamashita, S. In Vitro Dissolution/Permeation System to Predict the Oral Absorption of Poorly Water-Soluble Drugs: Effect of Food and Dose Strength on It. *Biological and Pharmaceutical Bulletin* **2011,** *34*, (3), 401-407.

67. Buckley, S. T.; Fischer, S. M.; Fricker, G.; Brandl, M. In vitro models to evaluate the permeability of poorly soluble drug entities: Challenges and perspectives. *Eur. J. Pharm. Sci.* **2012,** *45*, (3), 235-250.

68. Adson, A.; Burton, P. S.; Raub, T. J.; Barsuhn, C. L.; Audus, K. L.; Ho, N. F. H. Passive Diffusion of Weak Organic Electrolytes across Caco-2 Cell Monolayers: Uncoupling the Contributions of Hydrodynamic, Transcellular, and Paracellular Barriers. *J. Pharm. Sci.* **1995,** *84*, (10), 1197-1204.

69. Kansy, M.; Senner, F.; Gubernator, K. Physicochemical High Throughput Screening: Parallel Artificial Membrane Permeation Assay in the Description of Passive Absorption Processes. *Journal of Medicinal Chemistry* **1998,** *41*, (7), 1007-1010.

70. Di, L.; Kerns, E. H.; Fan, K.; McConnell, O. J.; Carter, G. T. High throughput artificial membrane permeability assay for blood–brain barrier. *European Journal of Medicinal Chemistry* **2003,** *38*, (3), 223-232.

71. Ottaviani, G.; Martel, S.; Carrupt, P.-A. Parallel Artificial Membrane Permeability Assay: A New Membrane for the Fast Prediction of Passive Human Skin Permeability. *Journal of Medicinal Chemistry* **2006,** *49*, (13), 3948-3954.

72. Mensch, J.; Melis, A.; Mackie, C.; Verreck, G.; Brewster, M. E.; Augustijns, P. Evaluation of various PAMPA models to identify the most discriminating method for the prediction of BBB permeability. *Eur. J. Pharm. Biopharm.* **2010,** *74*, (3), 495-502.

73. Seo, P. R.; Teksin, Z. S.; Kao, J. P. Y.; Polli, J. E. Lipid composition effect on permeability across PAMPA. *Eur. J. Pharm. Sci.* **2006,** *29*, (3), 259-268.

74. Kerns, E. H.; Di, L.; Petusky, S.; Farris, M.; Ley, R.; Jupp, P. Combined Application of Parallel Artificial Membrane Permeability Assay and Caco-2 Permeability Assays in Drug Discovery. *J. Pharm. Sci.* **2004,** *93*, (6), 1440-1453.

75. Avdeef, A.; Nielsen, P. E.; Tsinman, O. PAMPA—a drug absorption in vitro model. *Eur. J. Pharm. Sci.* **2004,** *22*, (5), 365-374.

76. Ulbricht, M. Advanced Functional Polymer Membranes. *Polymer* **2006,** *47*, 2217-2262.

77. Meylan, W. M.; Howard, P. H. ATOM FRAGMENT CONTRIBUTION METHOD FOR ESTIMATING OCTANOL-WATER PARTITION-COEFFICIENTS. *J. Pharm. Sci.* **1995,** *84*, (1), 83-92.

78. Breindl, A.; Beck, B.; Clark, T.; Glen, R. C. Prediction of the n-octanol/water partition coefficient, logP, using a combination of semiempirical MO-calculations and a neural network. *J. Mol. Model.* **1997,** *3*, (3), 142-155.

79. Kah, M.; Brown, C. D. LogD: Lipophilicity for ionisable compounds. *Chemosphere* **2008,** *72*, (10), 1401-1408.

80. Kerns, E. H.; Di, L.; Petusky, S.; Kleintop, T.; Huryn, D.; McConnell, O.; Carter, G. Pharmaceutical profiling method for lipophilicity and integrity using liquid chromatography-mass spectrometry. *J. Chromatogr. B* **2003,** *791*, (1-2), 381-388.

81. Sinko, P. D.; Gidley, D.; Vallery, R.; Lamoureux, A.; Amidon, G. L.; Amidon, G. E. In Vitro Characterization of the Biomimetic Properties of Poly(dimethylsiloxane) To Simulate Oral Drug Absorption. *Mol. Pharm.* **2017,** *14*, (12), 4661-4674.

82. Linnankoski, J.; Ranta, V.-P.; Yliperttula, M.; Urtti, A. Passive oral drug absorption can be predicted more reliably by experimental than computational models- Fact or Myth. *Eur. J. Pharm. Sci.* **2008,** *34*, 129-139.

83. Winiwarter, S.; Bonham, N. M.; Ax, F.; Hallberg, A.; Lennernas, H.; Karlen, A. Correlation of human jejunal permeability (in vivo) of drugs with experimentally and theoretically derived parameters. A multivariate data analysis approach. *Journal of Medicinal Chemistry* **1998,** *41*, (25), 4939-4949.

84. Krieg, B. J.; Taghavi, S. M.; Amidon, G. L.; Amidon, G. E. In Vivo Predictive Dissolution: Comparing the Effect of Bicarbonate and Phosphate Buffer on the Dissolution of Weak Acids and Weak Bases. *J. Pharm. Sci.* **2015,** *104*, (9), 2894-2904.

85. Krieg, B. J.; Taghavi, S. M.; Amidon, G. L.; Amidon, G. E. In Vivo Predictive Dissolution: Transport Analysis of the CO2, Bicarbonate In Vivo Buffer System. *J. Pharm. Sci.* **2014,** *103*, (11), 3473-3490.

86. Siepmann, J.; Gopferich, A. Mathematical Modeling of Bioerodible, polymeric drug delivery systems. *Adv. Drug Deliv. Rev.* **2001,** *48*, 229-247.

87. Sperling, L. H., *Introduction to Physical Polymer Science*. 4th ed.; John Wiley & Sons: Hoboken, New Jersey, 2006.

88. Efimenko, K.; Wallace, W. E.; Genzer, J. Surface modification of Sylgard-184 poly(dimethyl siloxane) networks by ultraviolet and ultraviolet/ozone treatment. *J. Colloid Interface Sci.* **2002,** *254*, (2), 306-315.

89. Dattelbaum, D. M.; Jensen, J. D.; Schwendt, A. M.; Kober, E. M.; Lewis, M. W.; Menikoff, R. A novel method for static equation-of state-development: Equation of state of a cross-linked poly(dimethylsiloxane) (PDMS) network to 10 GPa. *J. Chem. Phys.* **2005,** *122*, (14), 12.

90. Garrett, E. R.; Chemburkar, P. B. EVALUATION CONTROL AND PREDICTION OF DRUG DIFFUSION THROUGH POLYMERIC MEMBRANES .3. DIFFUSION OF BARBITURATES PHENYLALKYLAMINES DEXTROMETHORPHAN PROGESTERONE AND OTHER DRUGS. *J. Pharm. Sci.* **1968,** *57*, (8), 1401-+.

91. Gidley, D. W.; Peng, H. G.; Vallery, R. S., Positron annihilation as a method to characterize porous materials. In *Annual Review of Materials Research*, Annual Reviews: Palo Alto, 2006; Vol. 36, pp 49-79.

92. Vallery, R. S.; Zitzewitz, P. W.; Gidley, D. W. Resolution of the orthopositronium-lifetime puzzle. *Physical Review Letters* **2003,** *90*, (20), 4.

93. Kajcsos, Z.; Liszkay, L.; Duplatre, G.; Varga, L.; Lohonyai, L.; Paszti, F.; Szilagyi, E.; Lazar, K.; Kotai, E.; Pal-Borbely, G.; Beyer, H. K.; Caullet, P.; Patarin, J.; Azenha, M. E.; Gordo, P. M.; Gil, C. L.; de Lima, A. P.; Margues, M. F. F. Positronium trapping in porous solids: Means and limitations for structural studies. *Acta Phys. Pol. A* **2005,** *107*, (5), 729-737.

94. Eldrup, M.; Lightbody, D.; Sherwood, J. N. THE TEMPERATURE-DEPENDENCE OF POSITRON LIFETIMES IN SOLID PIVALIC ACID. *Chem. Phys.* **1981,** *63*, (1-2), 51-58.

95. Fragiadakis, D.; Pissis, P.; Bokobza, L. Glass transition and molecular dynamics in poly (dimethylsiloxane)/silica nanocomposites. *Polymer* **2005,** *46*, (16), 6001-6008.

96. Dahan, A.; Wolk, O.; Kim, Y. H.; Ramachandran, C.; Crippen, G. M.; Takagi, T.; Bermejo, M.; Amidon, G. L. Purely in Silico BCS Classification: Science Based Quality Standards for the World's Drugs. *Mol. Pharm.* **2013,** *10*, (11), 4378-4390.

97. Wagner, J. G.; Sedman, A. J. Quantitaton of rate of gastrointestinal and buccal absorption of acidic and basic drugs based on extraction theory. *Journal of Pharmacokinetics and Biopharmaceutics* **1973,** *1*, (1), 23-50.

98. Crank, J., *The mathematics of diffusion*. Clarendon Press: Oxford, [Eng], 1975; p viii, 414 p.

99. Siegel, R. A. A laplace transform technique for calculating diffusion time lags. *Journal of Membrane Science* **1986,** *26*, (3), 251-262.

100. Winne, D. Shift of pH-absorption curves. *Journal of Pharmacokinetics and Biopharmaceutics* **1977,** *5*, (1), 53-94.

101. Hayduk, W.; Laudie, H. Prediction of Diffusion Coefficients for nonelectrolytes in dilute aqueous solutions. *A.I.Ch.E. Journal* **1974,** *20*, (3), 610-615.

102. Wang, Z. Polydimethylsiloxane Mechanical Properties Measured by Macroscopic Compression and Nanoindentation Techniques. University of South Florida, 2011.

103. Gao, J. S.; Guo, D. Z.; Santhanam, S.; Fedder, G. K. Material Characterization and Transfer of Large-Area Ultra-Thin Polydimethylsiloxane Membranes. *J. Microelectromech. Syst.* **2015,** *24*, (6), 2170-2177.

104. Ng, J. M. K.; Gitlin, I.; Stroock, A. D.; Whitesides, G. M. Components for integrated poly(dimethylsiloxane) microfluidic systems. *ELECTROPHORESIS* **2002,** *23*, (20), 3461-3473.

105. Gray, V.; Kelly, G.; Xia, M.; Butler, C.; Thomas, S.; Mayock, S. The Science of USP 1 and 2 Dissolution: Present Challenges and Future Relevance. *Pharmaceutical Research* **2009,** *26*, (6), 1289-1302.

106. Shore, P. A.; Brodie, B. B.; Hogben, C. A. M. THE GASTRIC SECRETION OF DRUGS - A PH PARTITION HYPOTHESIS. *Journal of Pharmacology and Experimental Therapeutics* **1957,** *119*, (3), 361-369.

107. Singh, A.; Worku, Z. A.; Van den Mooter, G. Oral formulation strategies to improve solubility of poorly water-soluble drugs. *Expert Opinion on Drug Delivery* **2011,** *8*, (10), 1361-1378.

108. Cao, F.; Rodriguez-Hornedo, N.; Amidon, G. E. Mechanistic Analysis of Cocrystal Dissolution, Surface pH, and Dissolution Advantage as a Guide for Rational Selection. *J. Pharm. Sci.* **2019,** *108*, (1), 243-251.

109. Alonzo, D. E.; Zhang, G. G. Z.; Zhou, D.; Gao, Y.; Taylor, L. S. Understanding the Behavior of Amorphous Pharmaceutical Systems during Dissolution. *Pharmaceutical Research* **2010,** *27*, (4), 608-618.

110. Torchilin, V. P. Structure and design of polymeric surfactant-based drug delivery systems. *J. Control. Release* **2001,** *73*, (2), 137-172.

111. Levich, V. G., Convective Diffusion in Liquids. In *Physicochemical Hydrodynamics*, Prentice-Hall, Inc.: Englewood Cliffs, N.J., 1962.

112. Sahoo, P.; Wilkins, C.; Yeager, J. Threshold selection using Renyi's entropy. *Pattern Recognition* **1997,** *30*, (1), 71-84.

113. Ridler, T. W.; Calvard, S. Picture Thresholding Using an Iterative Selection Method. *IEEE Transactions on Systems, Man, and Cybernetics* **1978,** *8*, (8), 630-632.

114. Plackett, R. L.; Burman, J. P. The Design of Optimum Multifactorial Experiments. *Biometrika* **1946,** *33*, (4), 305-325.

115. Stowe, R. A.; Mayer, R. P. EFFICIENT SCREENING OF PROCESS VARIABLES. *Industrial & Engineering Chemistry* **1966,** *58*, (2), 36-40.

116. Vanaja, K.; Shobha Rani, R. H. Design of Experiments: Concept and Applications of Plackett Burman Design. *Clinical Research and Regulatory Affairs* **2007,** *24*, (1), 1-23.

117. Melchels, F. P. W.; Feijen, J.; Grijpma, D. W. A review on stereolithography and its applications in biomedical engineering. *Biomaterials* **2010,** *31*, (24), 6121-6130.

118. Pham, D. T.; Gault, R. S. A comparison of rapid prototyping technologies. *Int. J. Mach. Tools Manuf.* **1998,** *38*, (10-11), 1257-1287.

119. Gross, B. C.; Erkal, J. L.; Lockwood, S. Y.; Chen, C.; Spence, D. M. Evaluation of 3D Printing and Its Potential Impact on Biotechnology and the Chemical Sciences. *Analytical Chemistry* **2014,** *86*, (7), 3240-3253.

120. Wang, J.; Goyanes, A.; Gaisford, S.; Basit, A. W. Stereolithographic (SLA) 3D printing of oral modified-release dosage forms. *Int. J. Pharm.* **2016,** *503*, (1), 207-212.

121. Goyanes, A.; Kobayashi, M.; Martínez-Pacheco, R.; Gaisford, S.; Basit, A. W. Fused-filament 3D printing of drug products: Microstructure analysis and drug release characteristics of PVA-based caplets. *Int. J. Pharm.* **2016,** *514*, (1), 290-295.

122. Alhijjaj, M.; Belton, P.; Qi, S. An investigation into the use of polymer blends to improve the printability of and regulate drug release from pharmaceutical solid dispersions prepared via fused deposition modeling (FDM) 3D printing. *Eur. J. Pharm. Biopharm.* **2016,** *108*, (Supplement C), 111-125.

123. Melocchi, A.; Parietti, F.; Maroni, A.; Foppoli, A.; Gazzaniga, A.; Zema, L. Hot-melt extruded filaments based on pharmaceutical grade polymers for 3D printing by fused deposition modeling. *Int. J. Pharm.* **2016,** *509*, (1), 255-263.

124. Sadia, M.; Sośnicka, A.; Arafat, B.; Isreb, A.; Ahmed, W.; Kelarakis, A.; Alhnan, M. A. Adaptation of pharmaceutical excipients to FDM 3D printing for the fabrication of patient-tailored immediate release tablets. *Int. J. Pharm.* **2016,** *513*, (1), 659-668.

125. Pietrzak, K.; Isreb, A.; Alhnan, M. A. A flexible-dose dispenser for immediate and extended release 3D printed tablets. *Eur. J. Pharm. Biopharm.* **2015,** *96*, (Supplement C), 380-387.

126. Goyanes, A.; Chang, H.; Sedough, D.; Hatton, G. B.; Wang, J.; Buanz, A.; Gaisford, S.; Basit, A. W. Fabrication of controlled-release budesonide tablets via desktop (FDM) 3D printing. *Int. J. Pharm.* **2015,** *496*, (2), 414-420.

127. Goyanes, A.; Buanz, A. B. M.; Basit, A. W.; Gaisford, S. Fused-filament 3D printing (3DP) for fabrication of tablets. *Int. J. Pharm.* **2014,** *476*, (1), 88-92.

128. Martinez, P. R.; Goyanes, A.; Basit, A. W.; Gaisford, S. Fabrication of drug-loaded hydrogels with stereolithographic 3D printing. *Int. J. Pharm.* **2017,** *532*, (1), 313-317.